



# Durham E-Theses

---

## *Defects in MgO and ZnSe*

Russell, G. J.

### How to cite:

---

Russell, G. J. (1976) *Defects in MgO and ZnSe*, Durham theses, Durham University. Available at Durham E-Theses Online: <http://etheses.dur.ac.uk/8142/>

### Use policy

---

The full-text may be used and/or reproduced, and given to third parties in any format or medium, without prior permission or charge, for personal research or study, educational, or not-for-profit purposes provided that:

- a full bibliographic reference is made to the original source
- a [link](#) is made to the metadata record in Durham E-Theses
- the full-text is not changed in any way

The full-text must not be sold in any format or medium without the formal permission of the copyright holders.

Please consult the [full Durham E-Theses policy](#) for further details.

DEFECTS IN MgO AND ZnSe

by

G. J. RUSSELL, B.Sc., M.Phil.

The copyright of this thesis rests with the author.  
No quotation from it should be published without  
his prior written consent and information derived  
from it should be acknowledged.

Presented in Candidature for the Degree of  
Doctor of Philosophy in the University of Durham

April 1976



*To my wife Margaret*

*and daughters*

*Joanne and Nicola*

### ACKNOWLEDGEMENTS

It is a pleasure to express my thanks to friends and colleagues who have been most closely associated with the studies recorded in this thesis: in particular to my supervisor, Dr. J. Woods, for his encouragement and efforts which have made it possible to present this work for the degree of Doctor of Philosophy and to several members of the Basic Ceramics Group at Harwell, especially Dr. D.H. Bowen, who not only provided the stimulus for the investigation of radiation damage in MgO, but also supplied me with the crystals used in this study.

I am grateful to Professor D.A. Wright for permitting the use of his laboratory facilities, and to the workshop staff headed by Mr. F. Spence for their helpful support. I am also grateful to Dr. M.H. Lewis of the University of Warwick for allowing me to perform the annealing treatments of MgO in his research laboratory.

For experimental assistance I am indebted to Messrs. J.R. Cutter and N.F. Thompson who have grown the crystals of ZnSe and ZnS/Se studied in this work, and to Mr. E.A.E. Ammar for his valuable help in performing the electron spin resonance measurements.

Finally I wish to express my appreciation to Mrs. J. Henderson for her careful typing of this thesis.

ABSTRACT

This thesis describes the transmission electron microscope investigations of two unrelated materials, namely MgO and ZnSe. As-grown crystals of MgO have been found to contain several interesting configurations of precipitates on grown-in dislocations. An arrangement not previously reported has been found in which precipitates are located at the  $\langle 100 \rangle$  extremities in the  $[100]$  projection of a prismatic dislocation loop on a  $\{110\}$  plane. Some of the platelet-shaped precipitates have been identified by electron diffraction as calcium stabilised zirconia in agreement with earlier work, but the identity of the spherical ones has still not been established. The application of reflection electron microscopy to the study of etched surfaces is demonstrated. A study of neutron damaged MgO is reported in which the effects of post-irradiation annealing treatment in the temperature range from 1100 to 1800°C are described. The most important finding of this aspect of the work concerns the growth of cuboidal cavities in material irradiated with a dose exceeding  $10^{20}$  nvt. These defects are nucleated on annealing at 1500°C for an hour in an ambient of argon and most of their growth does not occur until the annealing temperature exceeds about 1600°C. Electron spin resonance studies of the same samples indicate that the nucleation of cavities is accompanied by a conversion of iron ions from the divalent to the trivalent state in octahedral symmetry and that most of the cavity growth does not occur until these trivalent ions become associated with vacancies. A mechanism to account for the role of iron in the cavity growth process is proposed.

In the second part of this work it is shown that the major defects occurring in ZnSe are long thin ortho-twins. This study is supplemented by an investigation of zinc sulpho-selenide crystals which are found to contain narrower twins and, in addition, groups of long intrinsic stacking faults, and some polytypic regions. The fact that the stacking faults in mixed crystals are exclusively intrinsic in nature and that they usually occur in groups in which each fault has the same slip vector suggests that they owe their origin to a slip process arising from post-growth stress. An explanation based on the more covalent nature of the bonding in ZnSe and involving a stress relieving mechanism is proposed to account for the long ortho-twins being favoured in this material. Some preliminary results of ion beam damage in ZnSe samples prepared by ion thinning are discussed.

## CONTENTS

CHAPTER 1	INTRODUCTION	
1.1	BACKGROUND TO THESIS	1
1.2	SCOPE OF THESIS	2
CHAPTER 2	THE TRANSMISSION ELECTRON MICROSCOPE	
2.1	INTRODUCTION	4
2.2	HISTORICAL DEVELOPMENT	4
2.3	THE INSTRUMENT AND ITS PRINCIPLES OF OPERATION	6
2.3.1	The Illumination System	7
2.3.2	The Imaging System	8
2.3.3	Recording System	11
2.3.4	Other Operational Features	13
2.4	MODES OF OPERATION	17
2.4.1	Bright Field Microscopy	17
2.4.2	Dark Field Microscopy	18
2.4.3	Selected Area Diffraction	19
2.4.4	Reflection Electron Diffraction	20
2.5	CALIBRATION	20
2.5.1	Magnification	21
2.5.2	Camera Length	22
2.5.3	Relative Rotation	25
CHAPTER 3	ELECTRON DIFFRACTION AND THE INTERPRETATION OF MICROGRAPHS OF THIN FOILS	
3.1	INTRODUCTION	27
3.2	ELECTRON WAVELENGTHS	27
3.3	SCATTERING PROCESSES AND BRAGG'S LAW	29
3.4	ATOMIC SCATTERING	31
3.5	STRUCTURE FACTOR	32
3.6	REPRESENTATION OF DIFFRACTION PATTERNS	36
3.7	KINEMATICAL THEORY OF DIFFRACTION CONTRAST	40
3.7.1	Perfect Crystals	40
3.7.2	Imperfect Crystals	43
3.8	CONCLUDING REMARKS	45

CHAPTER 4	THE CRYSTAL STRUCTURES OF MAGNESIUM OXIDE AND ZINC SELENIDE AND SOME OF THE DEFECTS IN THESE MATERIALS	
4.1	CRYSTAL STRUCTURES	47
4.2	POINT DEFECTS	50
4.3	DISLOCATIONS	52
4.4	STACKING FAULTS AND TWINS	54
CHAPTER 5	AS GROWN MAGNESIUM OXIDE	
5.1	INTRODUCTION	57
5.2	SPECIMEN PREPARATION	58
5.2.1	Chemical Polishing	58
5.2.2	Extraction Replicas	59
5.2.3	Surface Etching	60
5.3	OBSERVATIONS OF DEFECTS IN AS-GROWN MAGNESIUM OXIDE	61
5.3.1	Damage Introduced by Specimen Handling	61
5.3.2	Dislocations and Precipitates in As-Grown Material	63
5.3.3	Etching at Precipitate Sites	67
5.3.4	Identification of Precipitates	69
5.4	SUMMARY	75
CHAPTER 6	NEUTRON IRRADIATED AND ANNEALED MAGNESIUM OXIDE	
6.1	GENERAL INTRODUCTION	76
6.2	THEORY OF NEUTRON DAMAGE	77
6.2.1	Ionic Displacement	77
6.2.2	Transmutations	81
6.3	EXPERIMENTAL DETAILS	83
6.4	TRANSMISSION ELECTRON MICROSCOPE OBSERVATIONS	84
6.4.1	As-Irradiated Material	84
6.4.2	Samples Annealed below 1500°C	86
6.4.3	Samples Annealed above 1500°C	86
6.5	ELECTRON SPIN RESONANCE	92
6.6	DISCUSSION OF CAVITY GROWTH MECHANISM	94
6.7	CONCLUSIONS	98

CHAPTER 7	AS-GROWN ZINC SELENIDE AND ZINC SULPHO-SELENIDE	
7.1	GENERAL INTRODUCTION	99
7.2	SPECIMEN PREPARATION	100
7.2.1	Crystal Growth	100
7.2.2	Chemical Polishing	101
7.2.3	Ion Beam Thinning	102
7.3	OBSERVATIONS OF DEFECTS	104
7.3.1	As-Grown Zinc Selenide	104
7.3.2	As-Grown Zinc Sulpho-Selenide	107
7.3.3	Ion Beam Thinned Zinc Selenide	111
7.4	DISCUSSION	113
7.4.1	As-Grown Zinc Selenide and Zinc Sulpho-Selenide	113
7.4.2	Ion Beam Damage in Zinc Selenide	119
CHAPTER 8	SUMMARY OF CONCLUSIONS	
8.1	AS-GROWN AND NEUTRON IRRADIATED MAGNESIUM OXIDE	121
8.2	ZINC SELENIDE AND ZINC SULPHO-SELENIDE	123
8.3	FUTURE WORK	124
REFERENCES		127

CHAPTER 1

INTRODUCTION

1.1 BACKGROUND TO THESIS

This thesis is slightly unusual in that it is concerned with electron microscope studies of two unrelated materials, MgO and ZnSe. The reasons for this are that the work on MgO was done during the period 1970-73 when the author was an Experimental Officer on the staff of Portsmouth Polytechnic, while the work on ZnSe was done from 1973 to the present in the Department of Applied Physics and Electronics, University of Durham, where the author is now employed as a Senior Experimental Officer.

The work at Portsmouth was supervised by Dr. K J Martin and was carried out in conjunction with Dr. D H Bowen, then of the Materials Development Division, A.E.R.E., Harwell. MgO was of specific interest to members of this group at Harwell because it was considered to be of potential use in nuclear reactors, either as an oxide fuel dispersant or as a material for fuel element sleeves. To evaluate the effects of neutron damage in this material, an extensive radiation damage study was undertaken at Harwell in the mid 1960's. Some of the results of this earlier work showed that material irradiated to doses in excess of  $10^{20}$  nvt exhibited discontinuities in curves of density and lattice parameter versus annealing temperature at annealing temperatures greater than  $1500^{\circ}\text{C}$ . In addition, transmission electron microscopy demonstrated that cuboidal cavities were formed by a vacancy condensation process at elevated temperatures. The aim of the study of MgO reported here was to establish whether or not the growth of cavities could be explained in terms of the independent measurements made at A.E.R.E., Harwell, of the variation of density and lattice parameter.



The work in Durham has been concerned with defects in crystals of ZnSe grown from the vapour phase, and Dr. J Woods has acted as supervisor. This particular II-VI compound semiconductor has been extensively studied at Durham in recent years, mainly because of its interesting luminescent properties. As some defects such as twin boundaries and stacking faults are thought to play an important role in certain forms of luminescence, it is important to investigate the defect structures of the single crystal boules used in studies of luminescence. In addition, a knowledge of the nature and extent of defects in crystals can lead to improvements in the method of crystal growth. It was with these points in mind that the investigation of ZnSe reported here was carried out.

## 1.2 SCOPE OF THESIS

The two studies which form the basis of this work were primarily concerned with transmission electron microscopy. A description is therefore given in Chapter 2 of a conventional transmission instrument. The treatment is based not only on the cited literature, but also on the writer's personal experience of two commercial instruments. It is biased towards the underlying principles of the operation of a microscope rather than its physical design and construction, and comparisons are made with its optical counterpart.

To assist with an understanding of the electron micrographs and the electron diffraction patterns presented in this thesis, Chapter 3 contains an account of the fundamental principles of the kinematical theory of electron diffraction which are used to explain the formation of image contrast. Also, since the studies reported here were confined to crystalline samples, the crystal structures of the materials examined are described in Chapter 4 together with some of their more common defects.

The results of the investigation of MgO are contained in Chapters 5 and 6. Chapter 5 is concerned with as-grown material and includes a summary of an extensive study of the precipitates which decorate grown-in dislocations. In Chapter 6 an account is given of an investigation of neutron irradiated material and, in particular, of the effect on the damage of annealing treatments at temperatures in excess of 1500°C. The results of electron spin resonance measurements have helped to clarify the processes which occur during annealing.

In the second part of this work, observations made on single crystals of ZnSe and zinc sulpho-selenide grown from the vapour phase are described in Chapter 7. The different types of defect observed in these two related materials are discussed in relation to the slightly different nature of the bonding of the zincblende and wurtzite structures. Chapter 7 also includes some preliminary observations of ion beam damage in ion thinned ZnSe samples.

CHAPTER 2

THE TRANSMISSION ELECTRON MICROSCOPE

2.1 INTRODUCTION

The purpose of this chapter is to describe a conventional transmission electron microscope drawing attention to the principles that it has in common with the optical microscope. No attempt is made to discuss the principles of electron optics and lens design, as these topics have been treated extensively elsewhere (see for example the literature cited by Thomas 1964a and by Hirsch et al 1965a). In this chapter the historical development of the electron microscope is described. This is followed by a description of the principles of operation of a conventional instrument and an outline of the method by which contrast is produced. The chapter ends with an account of the calibration methods which are in common use and which have been employed in the present work to calibrate both of the instruments used.

2.2 HISTORICAL DEVELOPMENT

Although de Broglie postulated the wave nature of a beam of moving particles in 1924 and shortly afterwards Busch (1926) produced a theoretical analysis of the use of a suitable axial magnetic field to focus an electron beam, it was not until 1939 that the first transmission electron microscope, as we now know it, was commercially produced by Siemens in Berlin (see for instance von Borries and Ruska 1939). In the intervening years there were several independent attempts to produce such an instrument and thus improve on the best resolution of the optical microscope which is limited by the wavelength of visible light. The limit of resolution of an optical instrument is  $\frac{0.61 \lambda}{N.A.}$ , where  $\lambda$  is the wavelength of the illumination and N.A. is the numerical aperture of

the microscope which has a maximum possible value of nearly unity. Thus, the very short wavelength of an electron beam combined with the possibility of deflecting it during its transit through a magnetic field, opened the way for a new branch of microscopy.

After the manufacture of the first commercial instrument, at least a further ten years elapsed before any practical application was made to metallurgical problems. This was due partly to the fact that the manufacture of the first electron microscope closely preceded the second war and consequently no instruments were sold outside Germany, and partly to the problems associated with the development of techniques of preparing suitable samples. In fact the first successful preparation of a metal sample was made by Heidenreich (1949) who thinned aluminium from the bulk material by electrolytic polishing. Later, better results were obtained with aluminium by Hirsch et al (1956). These early results indicated the potential of transmission microscopy and by this time a number of commercial instruments were available. While electron microscopes have been produced throughout the world since the war, it is perhaps worth noting the important contributions made by the English and Japanese scientists in the development of this instrument. This is evidenced both by the large number of microscopes manufactured and sold in England and Japan and by the amount of work carried out using these instruments. By the early 1960's the physical processes involved in image formation had been elucidated in terms of what are now known as the kinematical and dynamical theories of electron diffraction. These theories are now widely established and have been published in book form (see for example Hirsch et al 1965b).

To complete this brief chronological account of the development of the transmission electron microscope it is worth mentioning some

of the major developments that have taken place in the field over the past decade or so. These include:

- (i) the introduction of high voltage electron microscopes, i.e. instruments designed to operate at accelerating voltages of 1 MV and above.
- (ii) an increase in the use of analytical techniques which is mainly due to the introduction of, and subsequent rapid technological developments associated with, the energy dispersive x-ray spectrometer.
- (iii) the adoption of the conventional transmission electron microscope to permit a scanning mode of operation in transmission (see Crewe 1972).

The work in this thesis however is not concerned with these more recent developments in electron microscopy, but with the conventional transmission instrument, the design of which will now be described.

### 2.3 THE INSTRUMENT AND ITS PRINCIPLES OF OPERATION

While they are very different in external physical appearance, the electron and optical microscopes are very similar in the respect that they both employ the same basic principles. This is illustrated schematically in figure 2.1, which shows that the electron microscope operates using a source of electrons with condenser, objective and projector lenses performing the same function as their light-optical counterparts. The principal differences that arise from using a beam of electrons instead of a beam of light are associated with the different instrumentation of the electron microscope. For instance the source of illumination is provided by an electron gun, the lenses are electromagnetic and the microscope is evacuated to a pressure of about  $10^{-5}$  torr to minimise absorption of the electron beam by residual gases.

These are a few of the features which contribute to the much larger size and more especially to the different technology of the electron microscope which is described below.

### 2.3.1 The Illumination System

In the schematic diagram of the electron microscope shown in Figure 2.1, the illumination system is seen to consist of an electron gun and a condenser lens arrangement. A schematic diagram illustrating the gun of a modern microscope is shown in Figure 2.2. The gun comprises three electrodes, namely a V-shaped tungsten filament or cathode, a Wehnelt cylinder or grid and an anode. The filament emits electrons thermionically and is surrounded by the Wehnelt cylinder, which is biased negatively with respect to the filament by the small current flowing ( $\sim 100 \mu\text{A}$ ) through the variable resistor  $R$  ( $\sim 1 \text{ M}\Omega$ ). In this self-biasing arrangement, the magnitude of the bias on the Wehnelt cylinder can be adjusted by varying  $R$ . Since the Wehnelt cylinder acts as a converging electro-static lens the strength of which can be controlled, the convergence of the electron beam can obviously be adjusted. This convergence results in the cross-over of the electron beam in the region of the anode. Although it is not shown as such in Figure 2.2, this cross-over forms an effective source with a smaller area than the filament and it is this effective source which is imaged by the condenser lens system.

The condenser systems of most commercial instruments employ two lenses as shown in Figure 2.3. The first of these is a strong lens which demagnifies the cross-over and produces a further reduction in the diameter of the effective source to about  $1 \mu\text{m}$ . The second condenser lens projects this image, which is located in the back focal plane of the first condenser lens, on to the specimen with a

magnification of about two times. The spot size at the specimen plane is therefore approximately 2  $\mu\text{m}$  in diameter. Some of the advantages of the small spot size, produced by a double condenser arrangement, compared with the larger spot size of a single condenser lens system, are as follows:

- (i) The higher beam current density produced in the smaller spot permits better penetration of the beam through thin samples.
- (ii) Only the area being examined is exposed to the electron beam so that nearby areas are not contaminated by the cracking action of the electron beam on the vapour from the diffusion pump oil.
- (iii) Charging effects, which can occur particularly with non-conducting samples, are reduced by using a small spot size.
- (iv) The high beam current density can be used to follow the annealing behaviour of certain defects in some materials (see for example Section 5.3.1).
- (v) The small spot size is associated with a small beam divergence, i.e. the conditions of parallel illumination are approached more closely. This gives rise to better image resolution and sharper diffraction spots.

### 2.3.2 The Imaging System

The imaging system illustrated in Figure 2.1 consists simply of an objective and projector lens. In practice however, most modern microscopes incorporate three stages of magnification, the third being provided by an intermediate lens or lens assembly situated between the other two lenses of the imaging system. Thus, after three successive stages of enlargement, an image of the object is projected on to the fluorescent screen of the microscope. This is illustrated in Figure 2.4 which is a diagram of the ray paths in the imaging system under microscopy conditions.

The first stage of magnification is produced by the objective lens which is a strong lens of very short focal length ( $\sim 1 \rightarrow 2$  mm). This is the most important part of the microscope because, in addition to being largely magnified, the image produced by this lens must be free from defects such as spherical aberration, astigmatism and chromatic aberration, because these would be further magnified in the subsequent stages of image enlargement. It is necessary therefore to machine the pole pieces to a very high degree of tolerance ( $< 0.2 \mu\text{m}$  variation in the diameter of the holes through the pole pieces) and to keep them free from contamination. Further, the objective lens current must be stabilised and, in order to give optimum performance and stability, this lens is usually designed to operate at almost constant current, giving a magnification of about 25 X.

In addition to the above requirements, the design of the objective stage must be such that it can accommodate a specimen in the region of its front focal plane and it must be possible to translate this specimen in two perpendicular directions which are mutually perpendicular to the electron-optic axis. These specifications have led to the development of two basic methods of specimen loading in commercial instruments. The more common of these employs a cartridge which contains the specimen and which is loaded through the bore of the upper pole piece of the objective lens. With this system, which is used in the JEM 120 instrument, the upper and lower pole pieces of the lens cannot be symmetrical because the bore of the lower pole piece is necessarily smaller than that of the upper one in order to attain the short focal length required. In the other system, which is used in the goniometer stage of the Philips EM 300 instrument, a side entry method of specimen loading is employed. Specimens are mounted on a thin and flat blade at the end of a rod and can be

introduced between closely spaced and symmetrical objective pole pieces. In passing, it is to be noted that with both systems, air-lock assemblies are invariably incorporated to minimise the time taken to interchange samples.

The second stage of magnification is provided by the intermediate lens or lens system. While similar in design to the objective lens, it differs in the respect that it has a longer focal length ( $\sim 2$  cm). The function of this lens is usually to provide the complete range of working magnifications of the instrument. It is designed in such a way that its shortest focal length corresponds to the maximum total magnification of the microscope. As its focal length is increased the first intermediate image produced by the objective lens must be moved along the electron-optic axis of the microscope from a position just in front of the intermediate lens in the direction towards the objective lens (see Figure 2.4). This results in a reduction in the magnifications produced by both the intermediate and objective lenses and thereby provides a continuous range of working magnifications, the lower limit of which is set by distortion of the image. This distortion is due to the increasing divergence of beams from the objective lens as the first intermediate image moves towards it. The intermediate lens thus provides the second stage of magnification which is typically of the order of 10 X.

The projector lens, like the objective, is a strong lens and is usually designed to operate at a constant optimum excitation. Also like the objective lens, its function is to form a highly magnified image at a large image distance of an object, which in this case is the second intermediate image (see Figure 2.4), located at its front focal plane. However this lens differs from the objective in the following important ways:

- (i) The whole extent of the magnetic field contributes to the image formation process. This contrasts with the objective lens in which the upper half of the field, i.e. above the specimen, is effective only in changing the path of the illuminating beam.
- (ii) The aperture of the image forming rays from a given object point is much smaller at the projector lens than it is at the objective. Consequently the effects of aberrations in the projector lens are less serious and the tolerances in the dimensions of its pole pieces are far less critical than they are for the objective lens.
- (iii) As the projector does not have to accommodate a specimen, it can be made symmetrical and more compact than the objective with the result that it can have a shorter focal length.

For these reasons it is usual for the projector to produce the largest stage magnification and this can have a value in the region of 100 X .

Thus a typical total enlargement of 25,000 X (= 25 x 10 x 100) is obtained on the viewing screen and this is a convenient magnification for the examination of many defects in crystalline materials.

### 2.3.3 Recording System

The final electron image produced by the imaging system is projected, as stated above, on to a viewing screen. As electron beams are not themselves visible, it is necessary to convert part of their energy into visible light and this is done by a screen coated with a fluorescent material which is usually a mixture of the sulphides of cadmium and zinc containing small quantities of 'activator'. This

fluorescent screen is usually made to give high light output and good contrast rather than high resolution. As it is viewed directly by eye its spectral response to the electron beam is selected to be of the colour to which the eye is most sensitive, namely green.

In addition to the large viewing ports for direct observation of the image on the screen, most microscopes have the facilities of a further stage of magnification of the image which is provided by a telescope. This aid is essential for accurate focussing and for correcting objective lens astigmatism in the image prior to photographic recording. Optical magnifications of up to 10 X can be employed without being limited by the grain size of the fluorescent layer on the screen.

Before mentioning the use of cameras which are necessary to provide a permanent record of an image, an important fundamental difference between the electron and optical microscopes should be pointed out. This concerns the depths of field and of focus of the two instruments relative to the specimen dimensions used. The depth of field,  $D$ , is defined as the distance by which the objective lens may be out of focus on either side of the object before the blurring of the image becomes comparable with the attained resolution  $\delta$ . The depth of focus  $D'$ , is the corresponding distance in image space. Thus  $D$  is the short distance between two planes symmetrically displaced about the object plane and  $D'$  is the counterpart of this in image space.  $D$  and  $D'$  are related to the objective semi-aperture angle  $\alpha$ , to the operative magnification  $M$  and to  $\delta$  by the following relationships:

$$D = \frac{2\delta}{\alpha} \quad \text{and} \quad D' = \frac{2\delta M^2}{\alpha}$$

(see for instance Thomas 1964b).

The full implications of these expressions become apparent when the magnitude of  $D$  and  $D'$  are evaluated for an actual working condition. For instance, when  $\delta = 20 \text{ \AA}$ ,  $\alpha = 5 \times 10^{-3}$  rad and  $M = 10,000 \text{ X}$ , then  $D = 8000 \text{ \AA}$  and  $D' = 8 \times 10^3 \text{ cm}$ . Thus in most practical cases, the whole thickness of a foil sufficiently thin for examination by transmission microscopy is in focus at once and the depth of focus can be regarded as being infinite. This is completely different from the situation in the optical microscope where, because of the much larger objective semi-aperture, the depths of field and of focus are comparatively very small.

As a consequence of the large depth of focus of the electron microscope, it is possible to position the camera for photographic recording of the image either below the fluorescent screen or just below the projector lens without necessitating any adjustment of the objective lens focussing. Cameras employing cassettes which contain sheet film and which are located below the fluorescent screen are the most widely used type, though some instruments have been designed to accommodate a 35 mm roll film camera at the top of the projection chamber. Regarding photographic emulsions, the most suitable for image recording are relatively slow with a small grain size and give high contrast. It is important to note that their contrast and resolution is always better than that of the fluorescent screen.

#### 2.3.4 Other Operational Features

In the above account of the working principles of the electron microscope, many features essential to the operation of the instrument were not discussed. For completeness these are mentioned briefly below.

##### (i) Vacuum System

The vacuum employed in an electron microscope is usually of the order of  $10^{-4}$  to  $10^{-5}$  torr and is produced by an oil diffusion pump backed by a rotary pump. In some instruments all valves are operated

manually while others incorporate automatic systems. In order to produce a good vacuum in the more important regions of the microscope, direct connections are usually made between the pumping system and the electron gun chamber and the specimen stage. Another feature of the vacuum system is the use of specimen and camera air-locks to enable the specimen or the plate camera to be removed without letting the whole of the system up to atmospheric pressure.

(ii) Apertures

Each of the electromagnetic lenses has an aperture or aperture system associated with it. Some of these are fixed while the positions of others can be adjusted from outside the vacuum system. The adjustable ones usually form part of a rod assembly containing up to three individual apertures, any one of which may be moved to allow the direct beam to pass through it. The most important aperture from the point of view of image formation is that associated with the objective lens. As this aperture is small, with a diameter in the range 20 to 50  $\mu\text{m}$ , and as it is used to produce image contrast (see Section 2.4.1), it is particularly important for it to be made with a high degree of precision and for it to be cleaned regularly to remove organic contaminations arising from polymerisation of the diffusion pump oil vapours in the electron beam. The condenser lens apertures are also usually of the adjustable type. As the function of these is to reduce the diameter of the beam and thereby provide a source of nearly parallel illumination, these apertures are prone to more severe contamination than the objective lens ones, even though their diameters are typically ten times as large. Consequently they have to be cleaned regularly. The final aperture to be mentioned is that used in the technique of selected area diffraction (see Section 2.4.3). This is situated at the position of the first intermediate image and again is of the adjustable kind. It is only introduced

into the path of the beam when the instrument is operated in the diffraction mode. This, together with its location, makes it far less prone to contamination than the others described above.

(iii) Astigmator Coils

Both the objective and condenser lens systems of most instruments are usually fitted with two sets of mutually perpendicular coils which are used to deflect the beam electro-magnetically in such a way as to correct for astigmatism in the image of the source of illumination and in the image of the specimen. Correct adjustment of the objective astigmators is of prime importance in the formation of images of good quality, particularly at high magnifications. For the initial setting of these astigmators, a circular hole in a specially prepared carbon film is usually used as a standard object. This setting involves the formation of a Fresnel fringe which is uniformly displaced from the edge of the hole around its complete circumference in a slightly over-focussed image. Figure 2.5 illustrates an example of astigmatism in an over-focussed image of cuboidal cavities in MgO (see Section 6.4.3). The image of the same area after correcting for astigmatism and focussing properly is shown in Figure 2.6. These figures demonstrate the importance of correcting for astigmatism. Inadequate correction accounts for the incorrectly identified diffraction contrast effects observed by Bowen (1970, private communication).

(iv) Beam Tilt Device

This device, like the astigmator coils just mentioned, comprises a set of coils for deflecting the electron beam. These coils are usually situated in the upper bore of the objective lens between the specimen and the illumination system, and their function is to enable the illuminating beam to be tilted through an angle of up to about  $5^{\circ}$

about any desired azimuth. This facility is required for the purpose of dark field microscopy (see Section 2.4.2).

(v) Goniometer stage

In order to perform many contrast experiments such as those associated with the determination of the Burgers vector of a dislocation, it is necessary to be able to tilt the sample through relatively large angles. This facility is provided by the goniometer stage of the electron microscope. As each commercial instrument has an objective stage and a specimen chamber with their own special characteristics, goniometer stages are designed individually. They usually come under the classification of instrumental attachments and are used in place of the standard objective stage. Independently of their method of specimen loading, they do however utilise one of two basic principles of operation. In one type the specimen is tilted about two orthogonal axes which are mutually perpendicular to the direction of the electron beam, while in the other the specimen is only tilted about one such axis, the other degree of freedom being provided by rotation about an axis parallel to the electron beam. With each system the specimen can be tilted about any azimuth to provide a degree of tilt which is limited by the design of the objective stage and in particular by the focal length of the objective lens. In fact as a consequence of providing this tilting facility, the maximum magnification that can be attained by the instrument is always reduced, typically by a factor of  $\frac{1}{2}$ . However this is rarely of importance in the study of defects in crystalline materials, which is the main use for which the goniometer is designed.

(vi) Alignment

As with any optical system, all the components of an electron

microscope must be aligned with respect to a specific axis, and this is referred to as the electron-optic axis. It is defined as the imaginary line drawn between the centres of two fixed components, usually the screen and the objective lens. Every instrument has its own procedure for alignment, but basically each involves the accurate alignment of the illumination system with the imaging system. This is achieved by a sequence of mechanical or electromagnetic adjustments of each component in both systems with respect to the electron-optic axis. Parts of the sequence are repetitive because of the interaction of one part of the system with another. The main features of good overall alignment are simply that the part of the image at the centre of the screen does not move as the image rotates when the magnification is swept through its full working range, and that simultaneously, no electromagnetic deflection of the illuminating spot is necessary.

## 2.4 MODES OF OPERATION

The method by which the image is formed in an electron microscope was described in Section 2.3.2. It is now necessary to consider how contrast is produced in this image and in doing this the concept of electron diffraction is introduced. This section is thus concerned with the modes of operation of the instrument that are most frequently encountered in the study of crystalline specimens.

### 2.4.1 Bright Field Microscopy

It can be seen from Figure 2.4 that under microscopy conditions the parallel beam of illumination is scattered by the specimen and that this scattered beam is used to form an enlarged image of the specimen on the screen. In the case of crystalline specimens the scattering takes the form of Bragg diffracted beams at angles of less

than a few degrees to the direction of the transmitted beam. Furthermore these diffracted beams give rise to a diffraction pattern in the back focal plane of the objective lens. By inserting an objective aperture of suitable size (see for instance Thomas 1964c) in this plane, as shown in Figure 2.7, so that only the directly transmitted and low angle inelastically scattered electrons are allowed to pass, an image of the specimen is produced by these undeviated electrons alone. This is called a "bright field image." The contrast that it exhibits therefore arises from the differences in intensities of electrons diffracted into Bragg reflections from various regions of the specimen and is therefore known as "diffraction contrast." Thus regions of the specimen that diffract electrons strongly into Bragg reflections appear as regions of dark contrast in a bright field image.

#### 2.4.2 Dark Field Microscopy

The other microscopic mode of operation which is frequently employed is achieved either by displacing the objective aperture laterally to receive one of the diffracted beams such as that at A in Figure 2.7, or by tilting the illumination system so that the required diffracted beam passes along the electron-optic axis of the microscope as shown in Figure 2.8. The latter of these methods is favoured, particularly when working at high magnification, because the image forming beam of electrons is then retained along the electron-optic axis of the objective lens and spherical and chromatic aberrations are then minimised. The image formed from this diffracted beam is called a "dark field image." Those regions of the specimen which appear in dark contrast in the bright field image due to the fact that electrons are strongly diffracted into a particular Bragg reflection exhibit light contrast in the dark field image formed from this reflection.

As electrons are usually diffracted into more than one diffracted beam, only parts of a dark field image exhibit contrast reversal with respect to the corresponding bright field image.

In addition to its invaluable use in fault analysis, this mode of operation has another advantage over bright field microscopy in that the beam used to form an image does not contain a component of inelastically scattered electrons as does the directly transmitted one. This results in dark field images which are sharper, but of lower intensity, than their bright field counterparts.

#### 2.4.3 Selected Area Diffraction

As stated earlier the Bragg diffracted beams from the specimen form a diffraction pattern in the back focal plane of the objective. By reducing the strength of the intermediate lens the diffraction pattern can be imaged on the screen as shown in the ray path diagram of Figure 2.9. Further, by inserting an aperture of diameter  $D$  in the plane of the first intermediate image as shown in this figure, only those electrons passing through an area of diameter  $D/M$  on the specimen are allowed to contribute to the final diffraction pattern, where  $M$  is the magnification of the objective lens. In practice a typical value for  $D$  is  $30\ \mu\text{m}$  and that for  $M$  is  $\times 25$ , so the area of specimen selected is defined by a spot of about  $1\ \mu\text{m}$  in diameter. This technique is termed "selected area diffraction" and was first employed by Le Poole (1947). It enables diffraction patterns to be obtained from very small areas of specimen and is used extensively in relating the nature of defects to crystal structure. For the accurate selection of a desired area, it is of paramount importance that the first intermediate image and the diffraction aperture should be coincident (see Figure 2.9).

#### 2.4.4 Reflection Electron Diffraction

In contrast to the above three modes of operation which are usually employed in conjunction with one another to examine defects in thin crystals, reflection electron diffraction is a technique which can be used for the study of thick, bulk samples. Electron diffraction patterns are obtained from surfaces of crystals and, as a consequence of the small value of Bragg angle, the surface from which diffraction is to be obtained must lie almost parallel to the electron beam.

With this technique the specimen can be placed in either of two positions, each of which necessitates a modification of the instrument to enable it to accommodate an attachment or specimen holder with tilting facilities. One of these positions is situated just below the projector lens in the place where the 35 mm roll film camera would be located and the other is in the same position as that which is normally occupied by specimens for study by transmission. While the latter has the disadvantage of only being suitable for small specimens, it does have the one special advantage that the imaging system of the microscope can be used, as in the case of transmission microscopy, to form a magnified image (see Section 5.3.3).

#### 2.5 CALIBRATION

As a consequence of its suitability for diffraction studies, the calibration of the electron microscope is more complex than that of its optical counterpart. In fact three separate experiments must be performed to calibrate the instrument for use in the study of crystalline specimens. These include the determinations of the final image magnifications and the camera lengths (see Section 2.5.2) and the measurement of the relative rotation of the microscope image with respect to its corresponding diffraction pattern throughout the range

of normal working conditions. This relative rotation arises from the reduced strength of the intermediate lens in the diffraction mode of operation. To conclude this chapter each of the calibration procedures will be described.

### 2.5.1 Magnification

Although most manufacturers of electron microscopes provide their customers with calibration charts for their instruments, it is often useful to be able to check these and this is usually done by employing one of the reference objects listed below:

- (i) a diffraction grating replica
- (ii) polystyrene latex particles
- (iii) crystal lattice planes of known spacing .

The last of these three samples is only of use at the very top end of the range of working magnifications and is thus primarily employed as a reference in studies involving direct lattice resolution. For the work recorded in this thesis the other two reference objects are more suitable.

Carbon replicas of ruled diffraction gratings with up to 55,000 lines per inch and shadowed with a heavy metal to provide contrast can be obtained commercially (from, for instance, E.F. Fullam, Inc., Schenectady, New York, U.S.A.). An electron-micrograph recorded from such a replica is shown in Figure 2.10. Calibration of the microscope is performed by recording images such as this and determining their individual magnifications throughout the entire working range of the microscope. In some cases, as with the Philips EM300, this range is provided by a stepped current regulator in the intermediate lens circuit while in others, the JEM120 for instance, the range is continuous and a graph of intermediate lens current versus magnification must be derived. Similarly the magnification range can also be calibrated by

using latex spheres, like those shown in Figure 2.11, as reference objects. The ones in this micrograph have a diameter of  $1900 \text{ \AA}$  and were obtained from the Dow Chemical Company, Midland, Michigan, U.S.A. Of these two reference objects the diffraction grating replica is considered to be the more reliable for the following reasons:

- (i) Latex particles can change in shape and size when subjected to large beam current densities for long periods.
- (ii) Independently made measurements have revealed a considerable variation in the size of similar latex spheres (see Agar, 1965). This is attributed to slight differences in their preparation.

#### 2.5.2 Camera Length

Although the electron microscope produces an enlarged image of the electron intensity distribution in the back focal plane of the objective lens when it is operated in the diffraction mode, it is not realistic to think in terms of magnification as there is no tangible object with which the final diffraction image can be directly related. Consequently it is necessary to introduce a more meaningful parameter to define the effective magnification of a diffraction pattern. As operation in the diffraction mode essentially uses the microscope as an electron diffraction camera, the parameter chosen is that of camera length,  $L$ , and this is defined as the "effective" distance between the specimen and the final diffraction image. The significance of the camera length can be understood from the following considerations.

The condition for diffraction to occur is defined by the Bragg equation:

$$\lambda = 2 d_{(hkl)} \sin \theta \dots \dots (2.1)$$

where  $\lambda$  is the wavelength of the electron beam

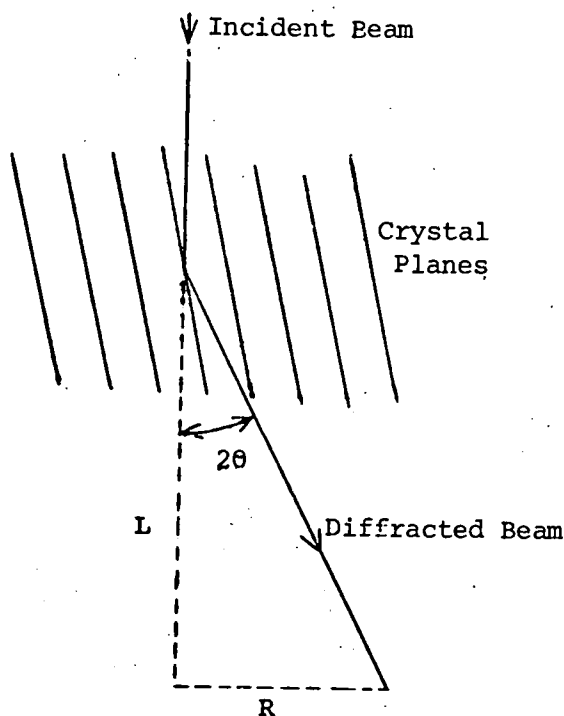
$d_{(hkl)}$  is the interplanar spacing of the  $(hkl)$  planes

$\theta$  is the Bragg angle.

Now the wavelength of 100 KeV electrons is  $0.037 \text{ \AA}$  and the interplanar spacing of planes of low index is of the order of  $2 \text{ \AA}$  for most crystals. Therefore  $\theta$  has a value of about  $1^\circ$  for most reflections and  $\sin \theta$  can be approximated to  $\theta$ . Thus equation 2.1 becomes:

$$\lambda = 2d_{(hkl)} \theta \dots \dots (2.2)$$

The fulfilment of the Bragg condition in the electron microscope is shown schematically below, where R represents the distance between the undeviated and diffracted beams at the camera level.



From the diagram it can be seen that:

$$R = L \tan 2\theta \dots \dots (2.3)$$

But since  $\tan 2\theta \approx 2\theta$

$$R = L 2\theta \dots \dots \dots (2.4)$$

Eliminating  $\theta$  from equations 2.2 and 2.4 yields:

$$\lambda L = R d_{(hkl)} \dots \dots \dots (2.5)$$

This is known as the "camera equation". Its use requires a known value of  $\lambda$  from the electron energy, a calibrated value of  $L$  and a measured value of  $R$  to enable an unknown interplanar spacing  $d_{(hkl)}$  to be calculated.

Returning to the calibration of the camera length, it is obvious that this parameter varies with the intermediate lens current which consequently must usually be set at a fixed and reproducible value when operating the instrument in the diffraction mode. The calibration is performed by taking a diffraction pattern from a material of known lattice parameter. In the course of this work evaporated gold films have been used as reference samples and Figure 2.12 shows a diffraction pattern from one such sample. As gold has the face-centred cubic structure, the allowed reflections in this pattern, starting with the ring of smallest diameter, are associated with reflections from planes with  $(hkl)$  values in the sequence:  $(111)$ ,  $(200)$ ,  $(220)$ ,  $(311)$ ,  $(222)$  ..... (see Section 3.5). Further, since they arise from a cubic material, these reflections are associated with interplanar spacings of the form:

$$d_{(hkl)} = a_0 / (h^2 + k^2 + l^2)^{1/2} \dots \dots \dots (2.6)$$

where  $a_0$  is the lattice parameter of the material.

Thus, by taking the value of  $a_0$  given in tables (see for instance Barrett 1943), the  $d_{hkl}$  values for the reference material can be

calculated, and from measurements of the corresponding values of R, the camera length can be determined using equation 2.5.

Three experimental aspects of the calibration procedure are:

- (i) For the determination of L, only measurements of reflections with an R value  $\geq$  to that associated with the  $d_{(311)}$  planes have been considered. The primary reasons for this was to reduce the experimental error incurred by only measuring relatively large values of R.
- (ii) Only diffraction patterns free from astigmatism have been used. This was ensured by establishing that the diameter of a particular diffraction ring was constant when measured about any azimuth.
- (iii) Measurements of an unknown interplanar spacing were always made from a print of approximately x5 photographic enlargement. To avoid possible errors arising from the determination of the actual magnitude of this enlargement, calculations were made with respect to a diffraction pattern from the reference material which had been subjected to the same photographic enlargement.

### 2.5.3 Relative Rotation

To permit the crystallography of defects to be studied it is necessary to be able to relate diffraction patterns directly to their corresponding images, and this requires the relative rotation between the two to be known. A method frequently used to determine the magnitude of this rotation is now described.

Small crystal flakes of molybdenum trioxide are produced in a test tube, for example, by subliming a crystal of ammonium molybdate in the flame of a bunsen burner. These flakes are liberated as a cloud of fine particles which are just visible to the naked eye.

By placing electron microscope grids coated with carbon support films at suitable positions in the test tube, some of these small crystalline particles can be collected for examination in the electron microscope.

The method of calibrating the relative rotation involves recording images of a molybdenum trioxide crystal, each with a superimposed electron diffraction pattern, over the entire range of working magnifications. One such image is shown in Figure 2.13. The main reason for using these particular crystals which have the rhombohedral structure is that their long straight edges are known to be perpendicular to the [100] direction in the crystal and can thus be related to the [100] direction in the indexed diffraction pattern. The relative rotation,  $\theta$ , can therefore be directly measured for each setting of magnification and a calibration curve, similar to that shown in Figure 2.14 for the JEM 120 microscope, can be derived.

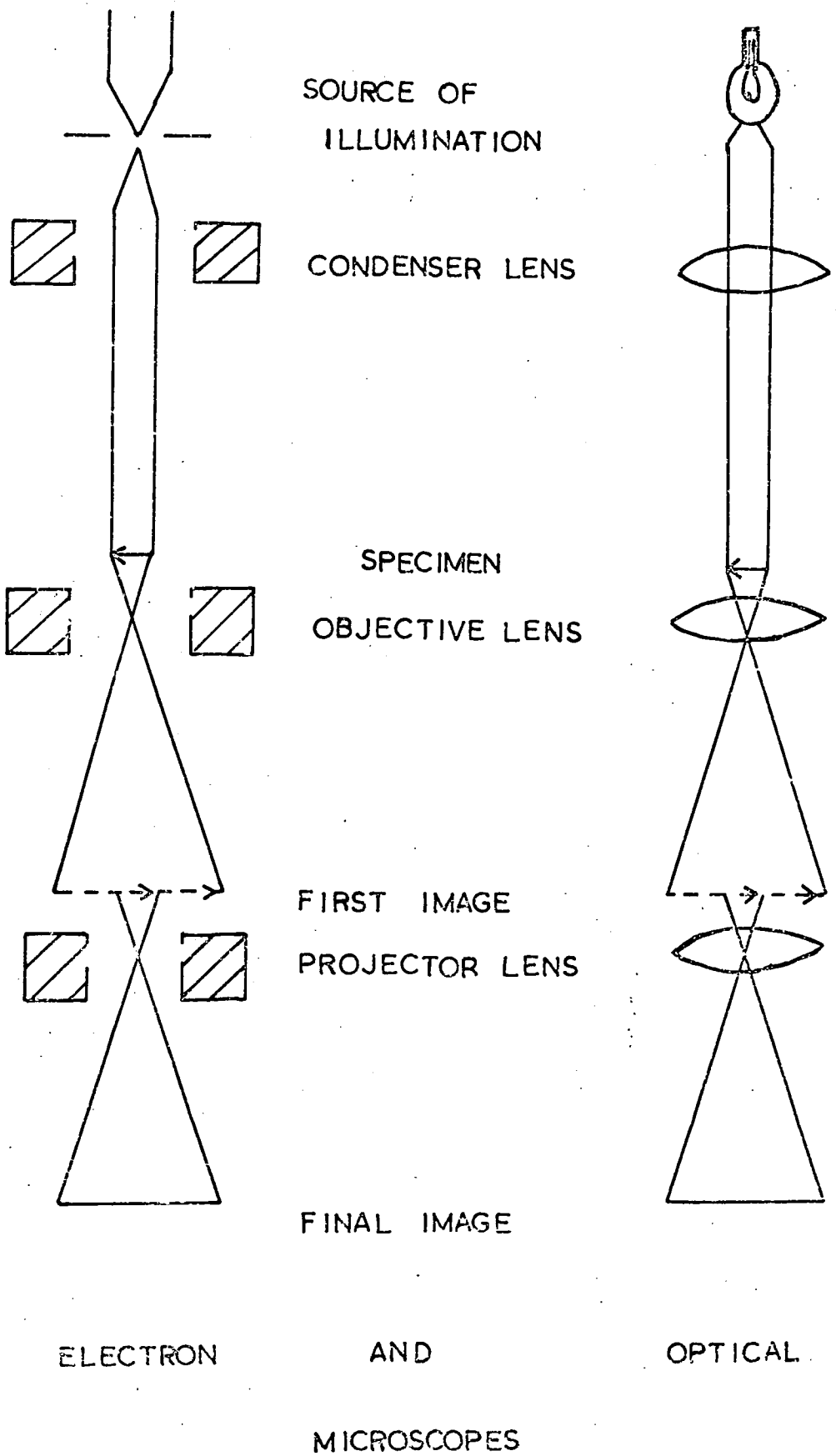


FIGURE 2.1

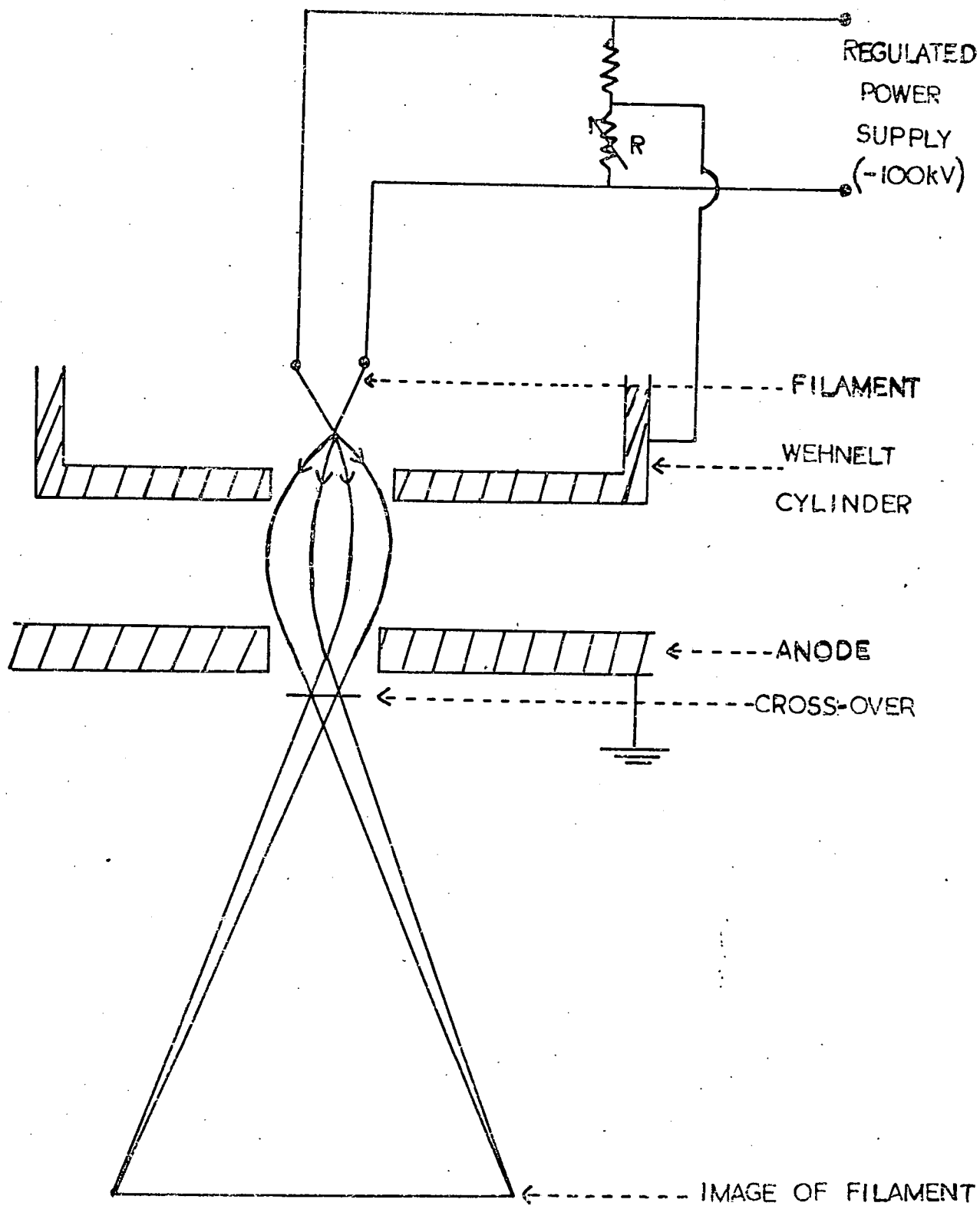


FIGURE 2.2 THE ELECTRON GUN

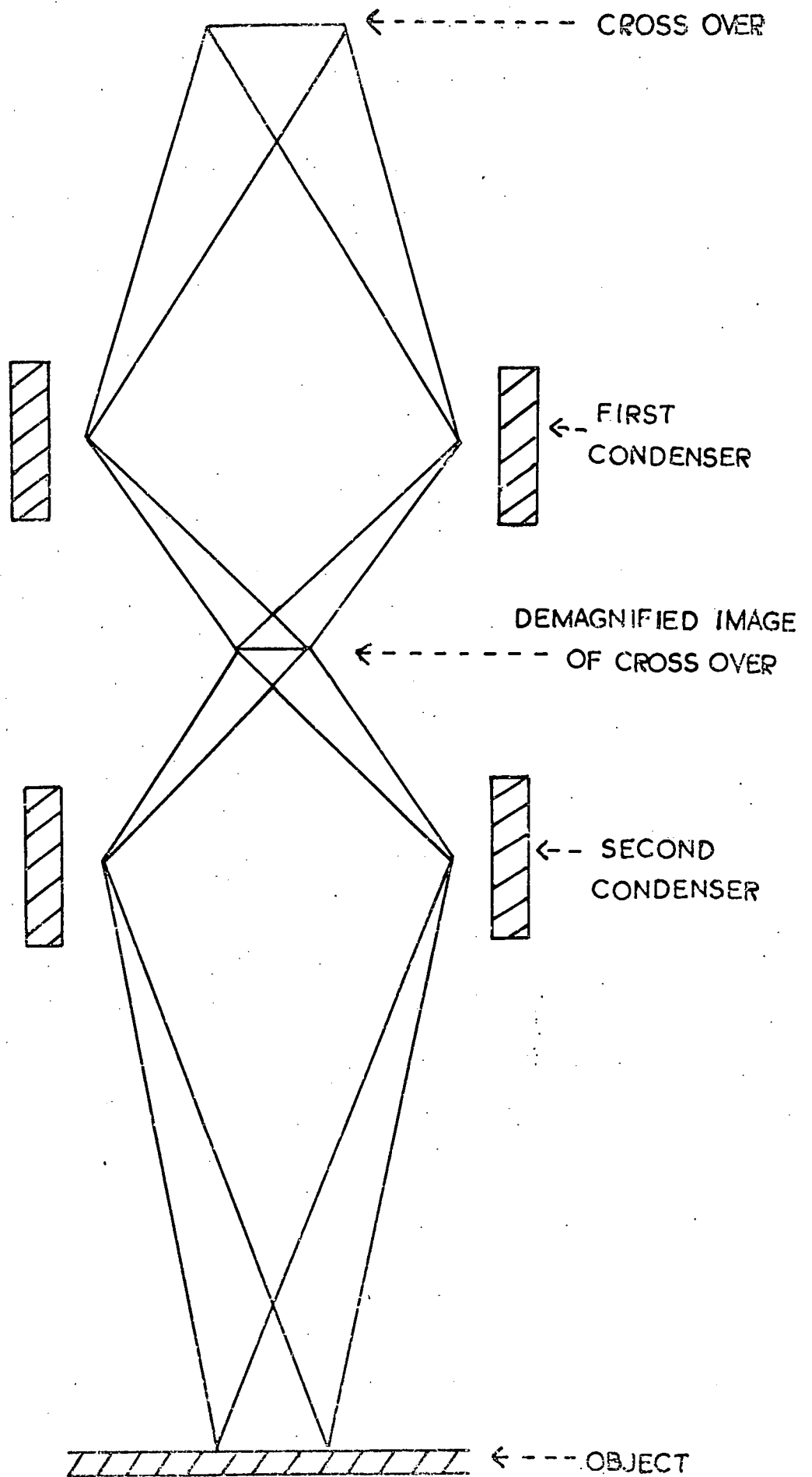


FIGURE 2.3 THE CONDENSER SYSTEM

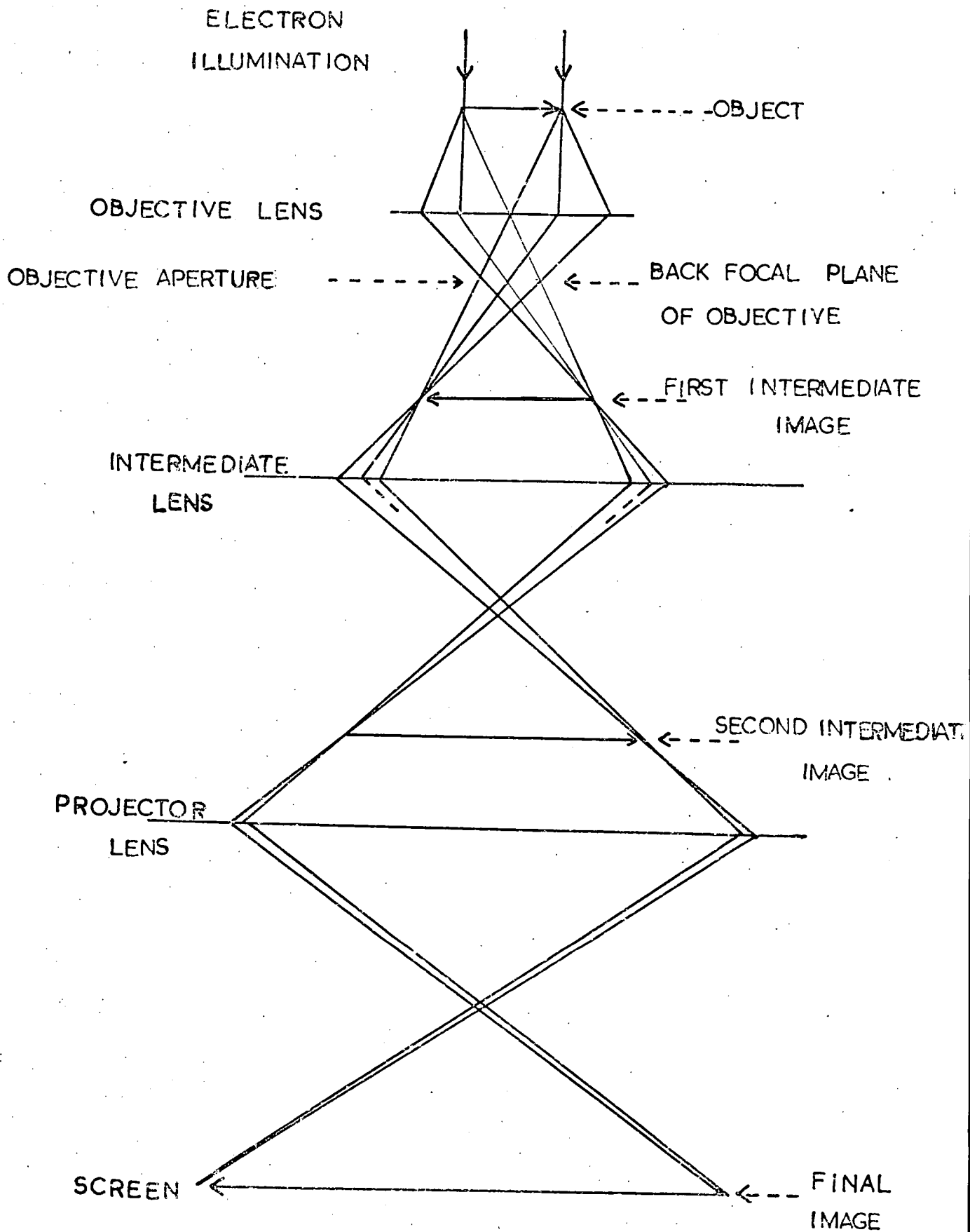


FIGURE 2.4 RAY PATHS UNDER MICROSCOPY CONDITIONS

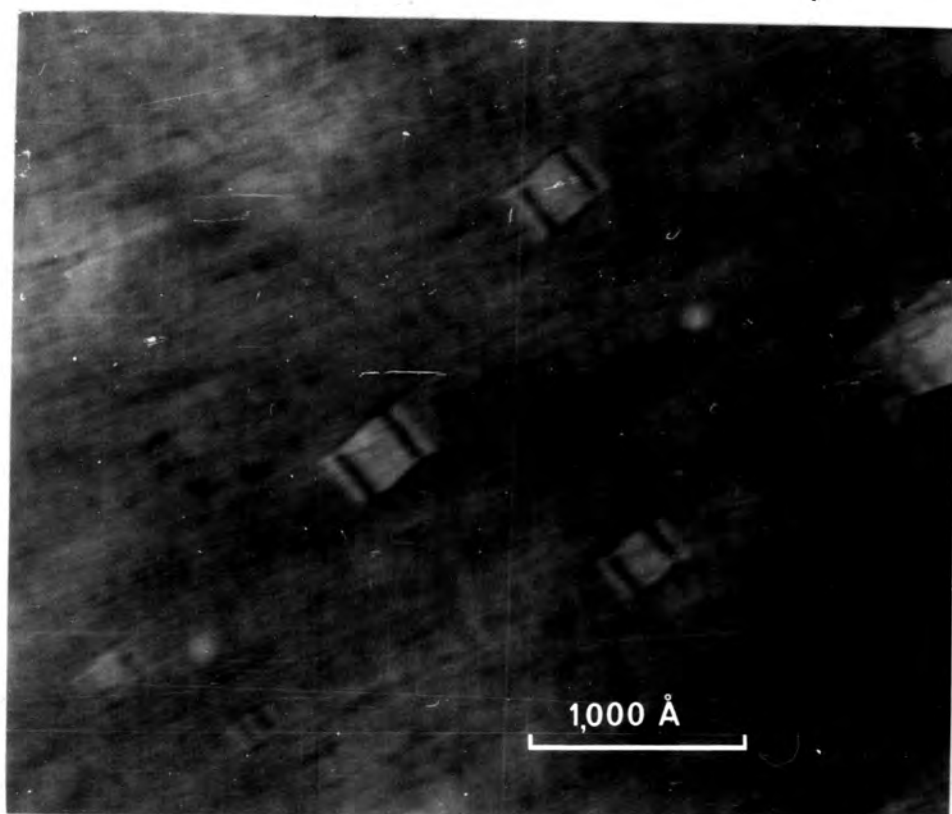


FIGURE 2.5  
FRESNEL FRINGES IN AN ASTIGMATIC IMAGE OF CAVITIES

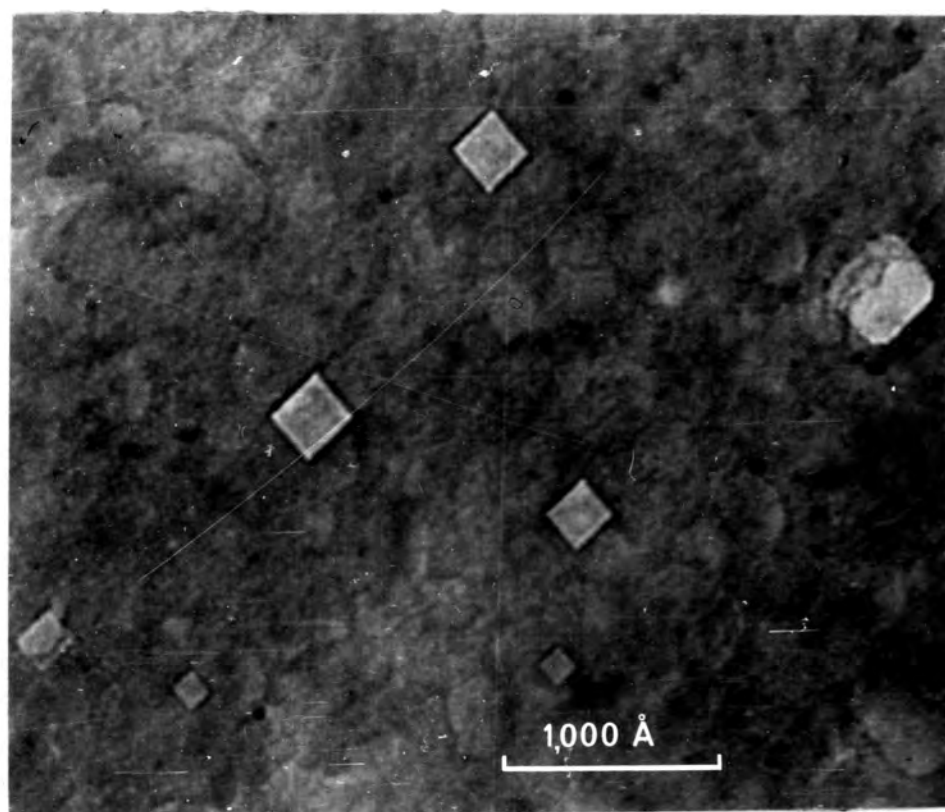


FIGURE 2.6  
AS ABOVE AFTER CORRECTING FOR ASTIGMATISM AND REFOCUSING

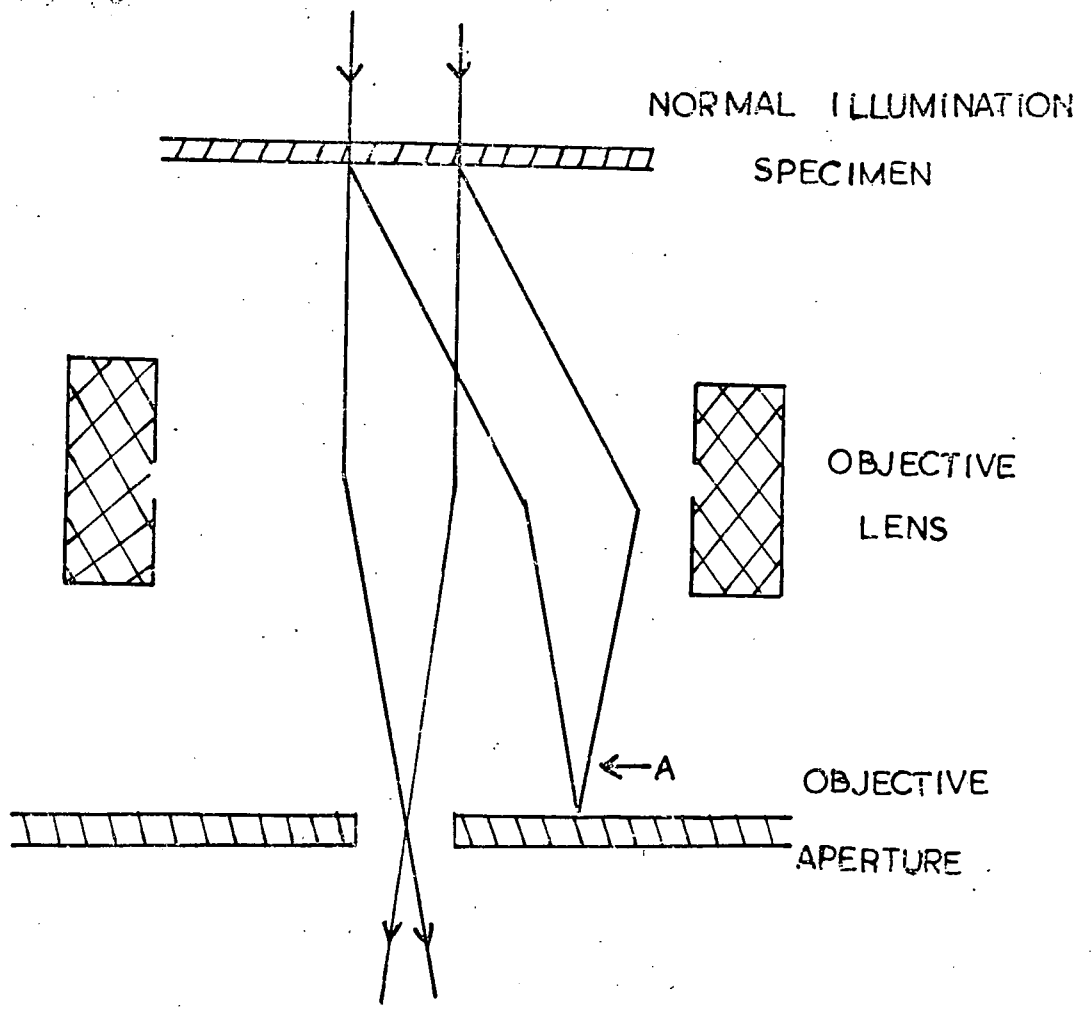


FIGURE 2.7 BRIGHT FIELD MICROSCOPY

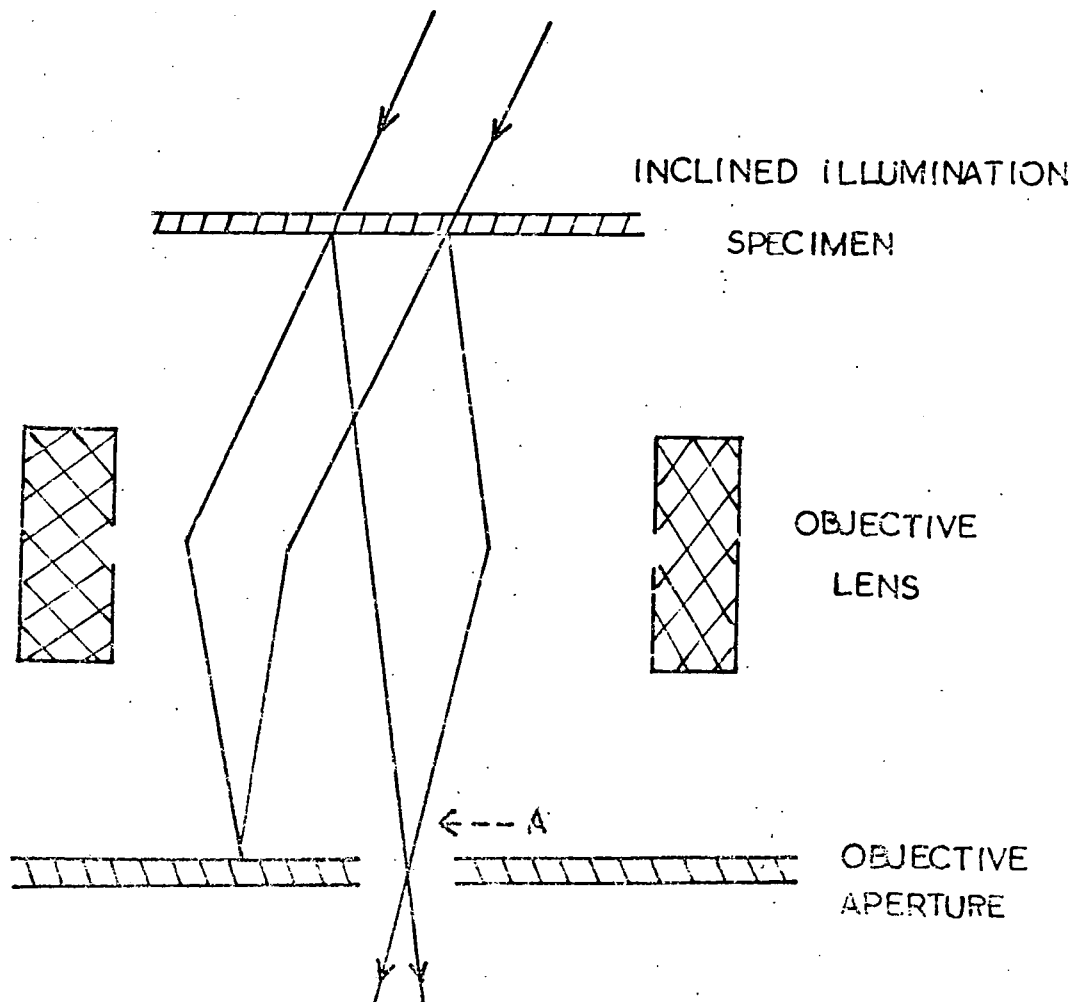


FIGURE 2.8 DARK FIELD MICROSCOPY

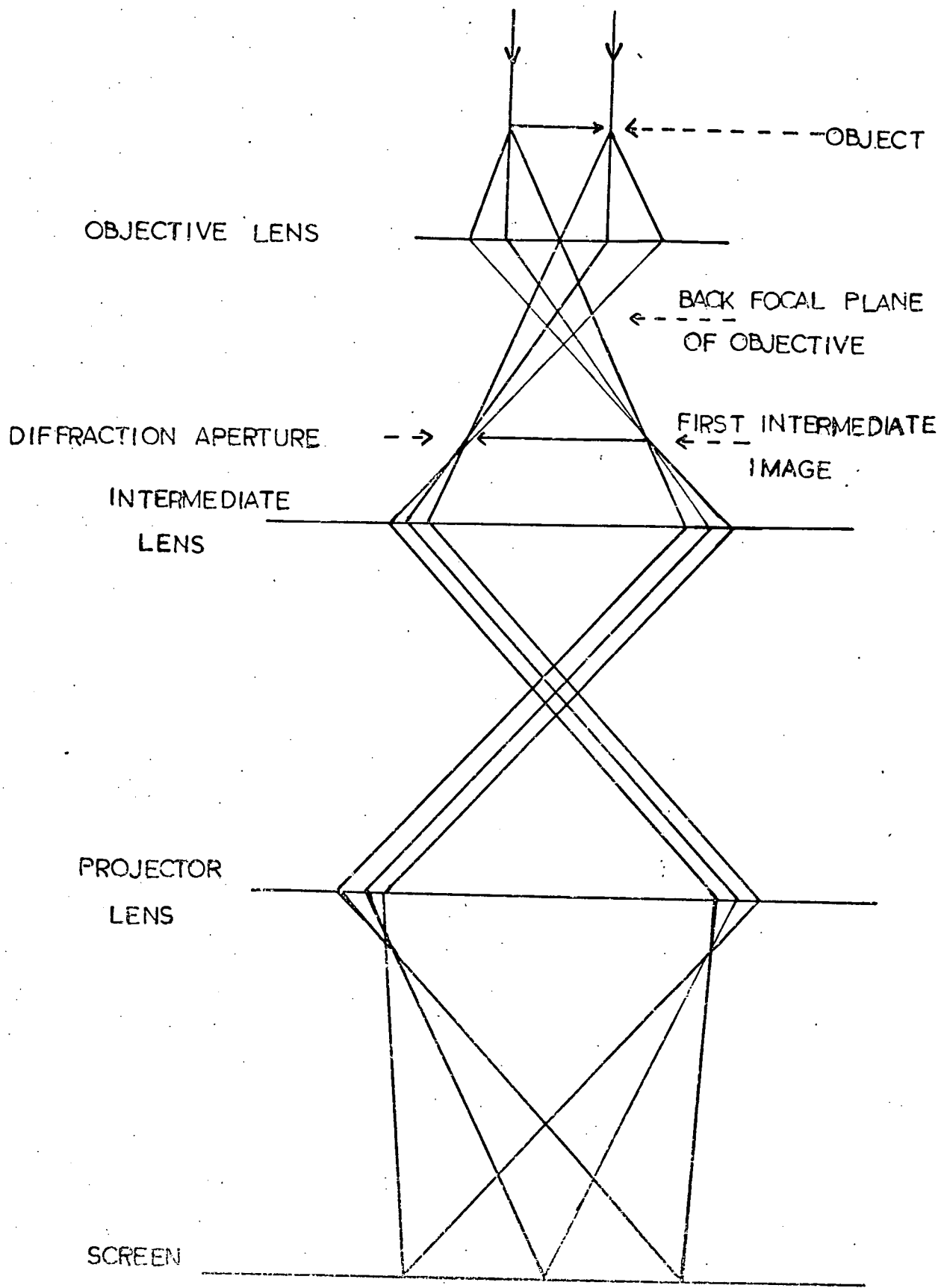


FIGURE 2.9 RAY PATHS UNDER DIFFRACTION CONDITIONS

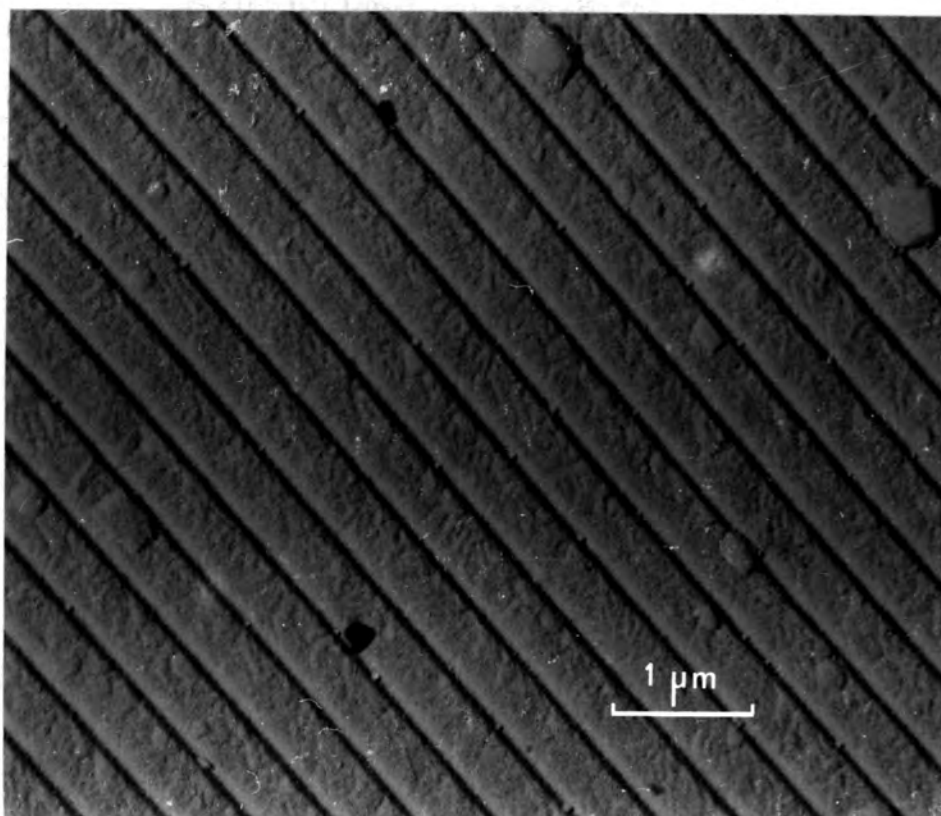


FIGURE 2.10  
DIFFRACTION GRATING REPLICA HAVING 55000 LINES PER INCH

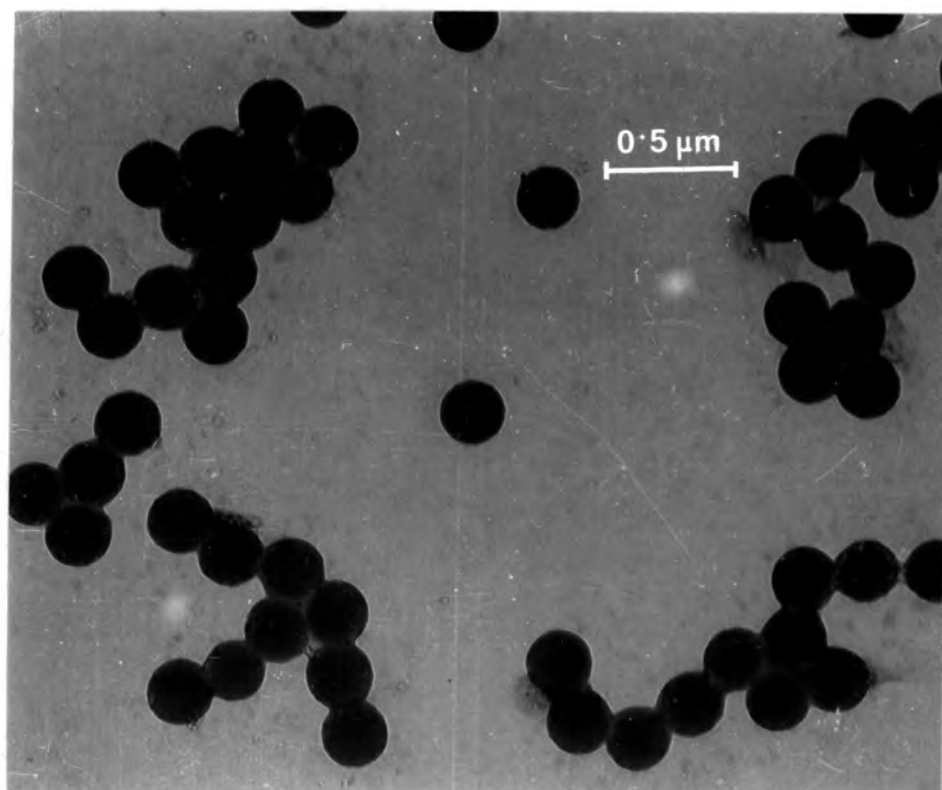


FIGURE 2.11  
LATEX SPHERES 1900 Å IN DIAMETER

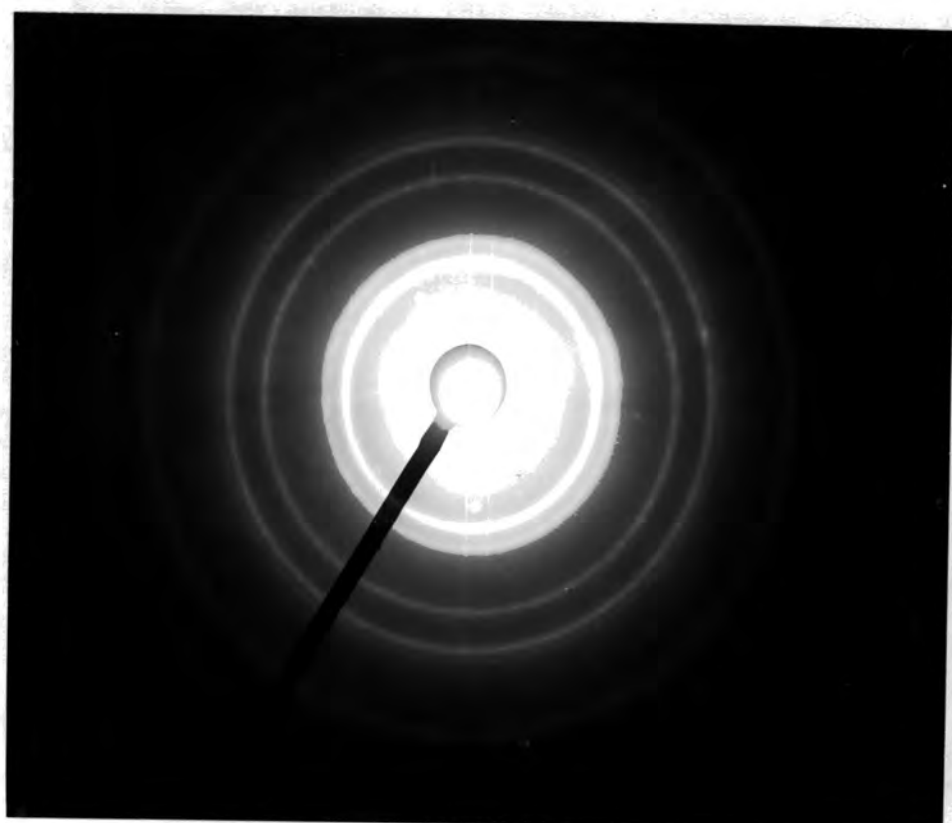


FIGURE 2.12  
TRANSMISSION DIFFRACTION PATTERN FROM POLYCRYSTALLINE GOLD

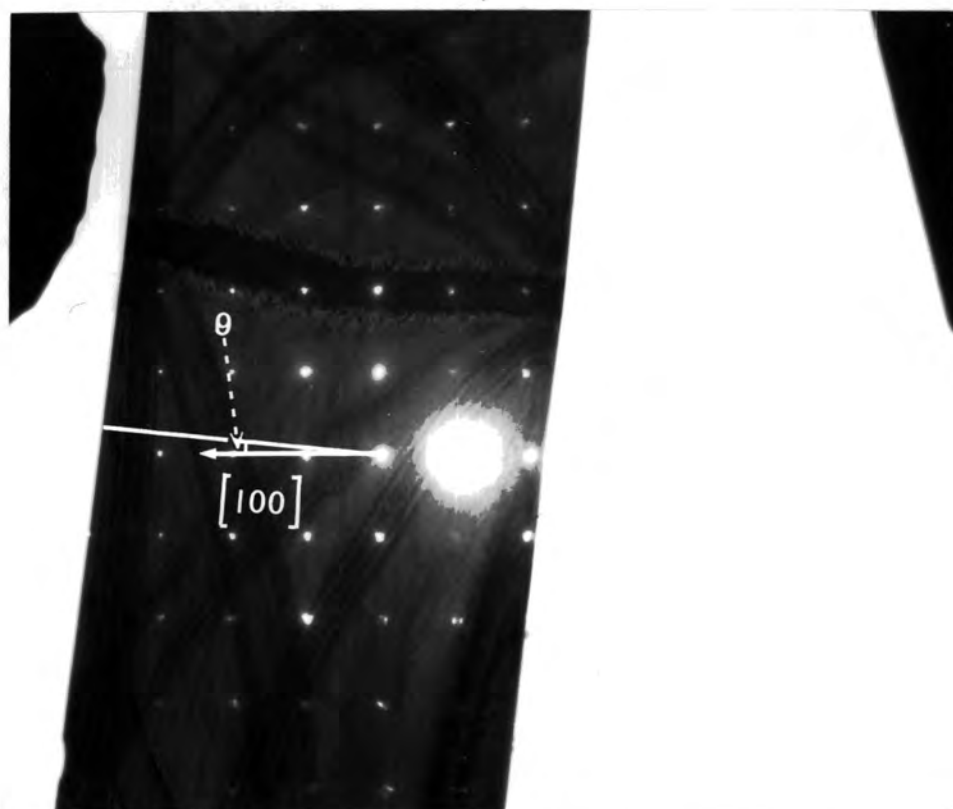


FIGURE 2.13  
MICROGRAPH WITH SUPERIMPOSED DIFFRACTION PATTERN FROM  $\text{MoO}_3$  CRYSTAL

ACTUAL CLOCKWISE ROTATION OF IMAGE WITH RESPECT TO DIFFRACTION PATTERN

- O ≡ 80 kV measurement
- + ≡ 100 kV measurement
- X ≡ 120 kV measurement

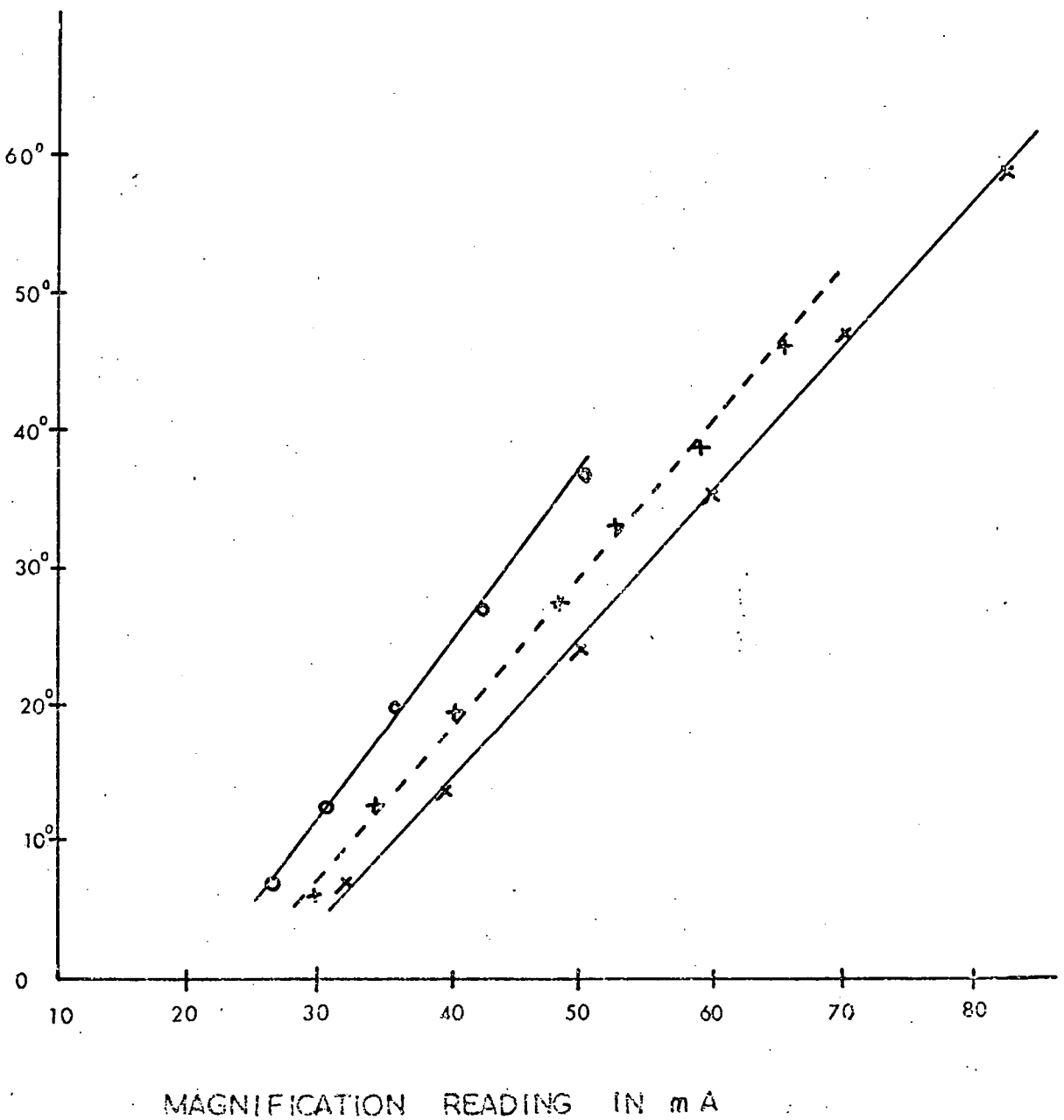


FIGURE 2 14 RELATIVE ROTATION CALIBRATION

### CHAPTER 3

#### ELECTRON DIFFRACTION AND THE INTERPRETATION

##### OF MICROGRAPHS OF THIN FOILS

### 3.1 INTRODUCTION

In electronmicroscope studies of biological materials and surface replicas, image contrast is produced by heavy metal atoms which are used to stain or shadow specimens respectively. The scattering of electrons by atoms is proportional to the square of their atomic number (see for example Thomas 1964d), so high local concentrations of heavy metal atoms give rise to regions of dark contrast in the image and yield information concerning the topography of the specimen. In crystalline specimens however the phenomenon of diffraction of electrons by crystal planes leads to a completely different and more complex form of image contrast. This is called diffraction contrast and was briefly mentioned when the modes of operation of the electron microscope were discussed in Section 2.4. As the interpretation of this contrast depends on an understanding of electron diffraction and of the intensities of electrons in diffracted beams, the purpose of this chapter is to provide an account of the theory of electron diffraction and its role in image formation. Because of the extent and mathematical complexity of this subject, the account given here is necessarily confined to the basic principles involved with a view to providing an adequate background for the understanding of most of the micrographs and diffraction patterns reported in this thesis.

### 3.2 ELECTRON WAVELENGTHS

In order to account for the diffraction of electrons by crystals it is necessary to associate a wave motion with a beam of

electrons. This is in accordance with de Broglie's hypothesis (1924) which states that the wavelength,  $\lambda$ , of a moving particle is related to its momentum by the relationship:

$$\lambda = \frac{h}{mv} \quad \dots \quad \dots \quad \dots (3.1)$$

where  $h$  is Planck's constant  
 $m$  is the mass of the particle, and  
 $v$  is the velocity of the particle.

Now for a beam of electrons accelerated through a potential  $V$ , the kinetic energy of each electron is given by:

$$Ve = \frac{1}{2} m v^2 \quad \dots \quad \dots \quad \dots (3.2)$$

where  $e$  is the electronic charge.

Eliminating  $v$  from this equation gives

$$Ve = \frac{1}{2} \frac{h^2}{m \lambda^2} \quad \dots \quad \dots \quad \dots (3.3a)$$

This can be rewritten as

$$\lambda = \frac{h}{\sqrt{2m Ve}} \quad \dots \quad \dots \quad \dots (3.3b)$$

However, the mass,  $m$ , varies with the velocity of the electron and therefore a relativistic correction must be applied. Using Einstein's relativity equation, the kinetic energy of the electron is related to its rest mass,  $m_0$ , by the expression:

$$Ve = m c^2 - m_0 c^2 \quad \dots \quad \dots (3.4)$$

where  $c$  is the velocity of light.

Substituting the value of  $m$  derived from equation 3.4 into equation 3.3b yields:

$$\lambda = \frac{h}{\left[ 2m_0 Ve \left( 1 + \frac{Ve}{2m_0 c^2} \right) \right]^{1/2}} \dots \dots (3.5a)$$

When the numerical values of the constants are inserted, the expression becomes

$$\lambda = \frac{12.26}{\left[ V \left( 1 + 0.9788 \times 10^{-6} V \right) \right]^{1/2}} \text{ \AA} \dots \dots (3.5b)$$

where V is in volts.

The factor  $(1 + 0.9788 \times 10^{-6} V)$  provides the relativistic correction and for an accelerating voltage of 100 KV amounts to about 5%. The electron wavelength is calculated to be 0.037  $\text{\AA}$  for an accelerating potential of 100 KV. This is much smaller than the wavelengths normally associated with X-rays used in diffraction studies and is responsible for the major differences between electron and X-ray diffraction.

### 3.3 SCATTERING PROCESSES AND BRAGG'S LAW

While an electron beam can be used in the same way as X-rays, or a beam of neutrons, to obtain information relating to crystal structures, an electron beam differs from the other two forms of radiation in that the strength of its interaction with crystalline material is greater. For instance neutrons interact only with the nuclei of atoms and X-ray photons only with the electron clouds. An electron beam, however, interacts with both the nucleus and the extra-nuclear electrons of an atom. The effect of the positively charged nucleus is to change the direction of the incident electron only, thus causing it to suffer no energy loss. Such electrons are said to be elastically scattered. On the other hand, those incident electrons which interact with the electron clouds of atoms lose energy which is

released in the form of heat, excitation, ionisation, secondary emission and X-rays. This interaction contributes to the inelastic component of the scattered electrons. The elastically scattered component is the more important in image formation and contrast in crystalline materials and is discussed below in more detail.

Consider a plane wave of electrons with a wave front AA', incident upon a set of atomic planes as shown in Figure 3.1. Assuming that elastic scattering by nuclei gives rise to secondary waves, then the condition for these to reinforce one another in constructive interference is that the difference in the path lengths for rays diffracted by successive crystal planes must be equal to an integral number of wavelengths. Thus, the distance RQS must equal one wavelength or an integral multiple of it. From Figure 3.1 it can be seen that:

$$RQ = QS = d \sin\theta$$

Thus the condition for reinforcement of the diffracted rays is:

$$n\lambda = 2d \sin\theta \quad \dots \quad \dots \quad \dots (3.6a)$$

where n is an integer and

$\lambda$  is the electron wavelength .

This is Bragg's Law and the integer n, which gives the number of wavelengths in the difference in path lengths for waves from successive planes, is the order of reflection. It is usual practice in problems involving crystallography to incorporate n in the parameter d. Thus, if the diffracting planes have Miller indices hkl, then

$$n \lambda = 2 d_{(hkl)} \sin \theta$$

or 
$$\lambda = 2 d_{n(hkl)} \sin \theta$$

or 
$$\lambda = 2 d_{(h'k'l')} \sin \theta \quad \dots \quad \dots \quad (3.6b)$$

where  $h' = nh$

$$k' = nk$$

$$l' = nl$$

The phase difference of course is  $2\pi/\lambda$  times the path difference between waves scattered from successive atomic planes, so that the condition for reinforcement is that the phase difference between successively scattered waves must be a multiple of  $2\pi$ .

Because of the small values of the electron wavelength the values of  $\theta$  are correspondingly small. For instance diffraction of 100 KeV electrons by the (200) planes of aluminium occurs when

$$\sin \theta = 0.0183 \quad \text{or} \quad \theta \approx 1^\circ$$

Thus a characteristic of electron diffraction (using electrons of this energy) is that the atomic planes which give rise to Bragg reflection lie approximately parallel to the incident electron beam.

### 3.4 ATOMIC SCATTERING

The other factor which determines the intensity of an elastically scattered beam of electrons is the efficiency of the scattering produced by individual atoms. In the case of X-ray diffraction, a measure of this efficiency is provided by the atomic scattering factor,  $f_x$ , and for a particular atom this is defined as:

$$f_x = \frac{\text{amplitude of a wave scattered by an atom}}{\text{amplitude of a wave scattered by a free electron}}$$

However for an incident wave of unit amplitude, the amplitude of the wave scattered by an electron is  $e^2/m_0 c^2$ , with the terminology used earlier in this chapter. Therefore the amplitude of a wave scattered by an atom is

$$\frac{e^2}{m_0 c^2} f_x \dots \dots \dots (3.7)$$

The counterpart of this in electron diffraction is the atomic scattering amplitude,  $f(\theta)$ , and this represents the amplitude of the electron spherical wave scattered by an atom and is usually expressed in the form (see for example Hirsch et al 1965c)

$$f(\theta) = \frac{K (Z - f_x)}{\sin^2 \theta/\lambda} \dots \dots \dots (3.8)$$

where  $K = m_0 e^2/2h^2$ .

The first term in brackets arises from nuclear scattering of the electrons, while the second one accounts for the interaction of the electrons with the extra nuclear electron cloud. The  $\sin^2 \theta/\lambda$  term shows that the value of  $f(\theta)$  increases rapidly to a maximum as  $\theta$  decreases towards  $0^\circ$ . For a typical low index reflection  $\sin\theta/\lambda$  is of the order of  $0.2 \text{ \AA}^{-1}$  and the value of  $f_x$  is such that  $f(\theta) / \left( \frac{e^2}{m_0 c^2} f_x \right)$  is about  $10^4$ . Thus the scattering power of atoms for electrons is very much greater than for X-rays. This accounts for the qualitative observation that a thin foil of material scatters electrons strongly but has little effect on a beam of X-rays.

### 3.5 STRUCTURE FACTOR

In the previous section the scattering from an individual atom was discussed. It is now necessary to investigate the combined effect

of the scattering produced by a group of atoms in a crystalline material. This is determined both by the crystal structure and the type of atoms present. For this purpose the group of atoms considered is that which defines the unit cell. In computing the sum of all the scattered amplitudes from all the atoms in the unit cell, i.e. the structure factor  $F_{hkl}$ , the phase difference  $\phi$  between waves from successive scattering points must be taken into account. However before this can be done, the form of the amplitude must be discussed.

Any wave of wavelength  $\lambda$ , with plane surfaces of constant amplitude and phase, travelling in the  $x$  direction can be represented by the wave function

$$\psi = A \exp \left[ 2\pi i x/\lambda \right] \dots \dots \dots (3.9a)$$

where  $A$  represents the amplitude of the wave.

For a system of spherical co-ordinates this can be rewritten as

$$\psi = A \exp \left[ 2\pi i \underline{k} \cdot \underline{r} \right] \dots \dots \dots (3.9b)$$

where  $|\underline{k}| = \frac{1}{\lambda}$

In the case of a wave scattered by an atom at the position  $\underline{r}$ , the constant  $A$  can be replaced by the atomic scattering factor  $f(\theta)$ , while  $2\pi \underline{k} \cdot \underline{r}$  represents the phase difference  $\phi$  of the surface of the wave-front with respect to an atom at the origin. Thus the equation for the scattered wave can be written as

$$\psi = f(\theta) \exp \left[ i \phi \right] \dots \dots \dots (3.9c)$$

Now the phase difference between waves scattered from different points can be obtained by considering a wave incident at angles of  $\alpha_1$ ,  $\beta_1$ ,  $\gamma_1$ , with respect to the crystal axes  $a$ ,  $b$ ,  $c$  and scattered in the

direction making angles  $\alpha_2, \beta_2, \gamma_2$ , with these axes as shown in Figure 3.2. The path difference between rays scattered at the origin and from the lattice point  $Z'$  is  $(Z'P - OQ)$  or  $c (\cos \gamma_1 - \cos \gamma_2)$  with respect to the  $c$  axis. Similarly the path differences with respect to the  $a$  and  $b$ -axes for scattering from points at  $X'$  and  $Y'$  relative to the origin are  $a (\cos \alpha_1 - \cos \alpha_2)$  and  $b (\cos \beta_1 - \cos \beta_2)$ . The condition for reinforcement of the wave is that the path difference with respect to each axis must equal a whole number of wavelengths.

Thus

$$a (\cos \alpha_1 - \cos \alpha_2) = h \lambda \quad \dots \quad \dots \quad (3.10)$$

$$b (\cos \beta_1 - \cos \beta_2) = k \lambda \quad \dots \quad \dots \quad (3.11)$$

$$c (\cos \gamma_1 - \cos \gamma_2) = \ell \lambda \quad \dots \quad \dots \quad (3.12)$$

where  $h, k$  and  $\ell$  are integers.

These are called the Laue equations. Their sum yields a value for the total path difference of  $\lambda (h + k + \ell)$  for the wave scattered by the atom at  $R$  (in Figure 3.2) with respect to the origin. So the phase angle  $\phi$  corresponding to this condition is  $2\pi (h + k + \ell)$ . This is the phase angle for the specific case of an atom with co-ordinates  $(a, b, c)$  where  $a, b$  and  $c$  are the unit cell dimensions. Thus for an atom in the generalised position with co-ordinates  $(u, v, w)$ , where  $u, v$  and  $w$  are expressed in units of the unit cell dimensions, the phase difference with respect to the origin is given by  $2\pi (h u + k v + \ell w)$ . Thus the amplitude of the wave scattered by a unit cell containing one lattice point at the position  $(u, v, w)$  is obtained by plotting the amplitude-phase diagram as shown in Figure 3.3. In this case the structure factor  $(F_{hkl})$  is equal to the atomic scattering

factor ( $f(\theta)$ ) and the amplitude of the diffracted wave is given by

$$\psi = f(\theta) \exp 2\pi i (hu + kv + lw) \dots \dots (3.9d)$$

However when the unit cell contains  $N$  lattice points, the structure factor is the sum of all the scattered amplitudes as shown in Figure 3.4. By resolving the vector quantities  $f_1(\theta) \rightarrow f_n(\theta)$  into components parallel and perpendicular to the incident wave,  $F_{hkl}$  is found to be given by

$$\begin{aligned} |F_{hkl}|^2 &= (f_1(\theta) \cos \phi_1 + f_2(\theta) \cos \phi_2 \dots \dots f_n(\theta) \cos \phi_n)^2 \\ &+ (f_1(\theta) \sin \phi_1 + f_2(\theta) \sin \phi_2 \dots \dots f_n(\theta) \sin \phi_n)^2 \end{aligned} \quad (3.13a)$$

where  $f_1(\theta), f_2(\theta) \dots \dots f_n(\theta)$  are the scattering factors of the different atoms in the unit cell.

This equation can be written more compactly in the form

$$F_{hkl} = \sum_{n=1}^N f_n(\theta) \exp \left[ 2\pi i (h u_n + k v_n + l w_n) \right] \dots \dots (3.13b)$$

The intensity resulting from all of the scattering points in the unit cell is given by  $|F_{hkl}|^2$ . For each scattering point the intensity depends on the scattering angle and the indices  $h, k, l$ . For a unit cell with a centre of symmetry at the origin, each of the sine terms of equation 3.13a is zero so this equation can be rewritten as

$$F_{hkl} = \sum_{n=1}^N f_n(\theta) \cos 2\pi i (h u_n + k v_n + l w_n) \dots \dots (3.13c)$$

To illustrate the effect of the structure factor on diffraction, consider the unit cell of a monatomic fcc structure. The four lattice points are located at  $000, \frac{1}{2}\frac{1}{2}0, \frac{1}{2}0\frac{1}{2}$  and  $0\frac{1}{2}\frac{1}{2}$ . Thus from equation 3.13c

$$F_{hkl} = f(\theta) \left[ 1 + \cos \pi (h+k) + \cos \pi (k+l) + \cos \pi (h+l) \right]$$

Therefore, unless  $hkl$  are all even or all odd,  $F_{hkl} = 0$  and the reflection  $hkl$  is absent and is described as a systematic absence.

The reflections which do occur have  $F_{hkl} = 4 f(\theta)$  and values of  $hkl$  which lie in the sequence:

111, 200, 220, 311, 222, 400, 331, 420 .....

Similar analyses give the conditions for reflection for all crystal structures.

### 3.6 REPRESENTATION OF DIFFRACTION PATTERNS

From the preceding sections it can be deduced that there are two separate conditions that must be met for reinforcement of a wave from a set of crystal planes designated by the Miller indices  $hkl$ . Firstly the Laue equations (which are equivalent to Bragg's law) must be simultaneously satisfied and secondly the structure factor of this set of planes must not be zero. It is now necessary to consider what happens when both of these conditions are fulfilled.

The Laue equations (equations 3.10 to 3.12) define the geometrical conditions necessary for reinforcement to occur. Each equation represents a family of cones of diffracted intensity. The angles at the apices of these cones correspond to  $2\alpha_2$ ,  $2\beta_2$  and  $2\gamma_2$  in Figure 3.2 and the families of cones arise from the different possible values of  $\alpha_2$ ,  $\beta_2$  and  $\gamma_2$  which are determined by the integral values of  $h$ ,  $k$  and  $l$ .

Now consider the specific case of a beam of electrons incident along one of the  $\langle 100 \rangle$  axes of a crystal with the simple cubic structure. The set of cones arising from the row of atoms that are parallel to the beam intersects the plane normal to the beam to produce a family of

circles as shown in Figure 3.5. The other two families of course, with their axes coincident with the other two  $\langle 100 \rangle$  axes of the crystal, intersect this plane to form two sets of hyperbolae as illustrated schematically in Figure 3.5. Since the wavelength of 100 KeV electrons is so small, these hyperbolae approximate to straight lines in practice. In principle, for reinforcement of the diffracted wave to occur, all three Laue equations must be satisfied simultaneously, i.e. an intensity maximum only arises where the point of intersection of two hyperbolae coincide with a circle. In practice, however, this is not such an unlikely event as Figure 3.5 might suggest. This is because of the effect of a fundamental phenomenon of diffraction which is that the resolution of an intensity maximum in a diffracted wave improves (or becomes sharper) as the number of diffracting centres contributing to the maximum increases. In the electron microscope, diffraction is usually obtained from a slab of material which is thin in the direction of the electron beam. Therefore the intensity maxima of the diffracted waves are sharp in directions which are perpendicular to the beam but are elongated and not so well resolved in the direction parallel to the beam. This represents a relaxation of the Laue condition corresponding to the row of diffracting centres lying parallel to the beam such that the rings in Figure 3.5 are broad and diffuse, in marked contrast to the clearly defined hyperbolae. Consequently electron diffraction patterns effectively arise in general from the intersection of the two families of hyperbolae only, to produce a two dimensional array of spots as indicated in Figure 3.5. These spot patterns are most conveniently interpreted using the concepts of the reciprocal lattice and the reflecting sphere as described below.

The reciprocal lattice comprises a set of points each of which represents a reflecting plane in the crystal and which has the same

indices as this plane. The reciprocal lattice is constructed from the real lattice by drawing a line from each crystal plane such that the line is perpendicular to its corresponding plane and also passes through the origin. The reciprocal lattice point corresponding to each  $(hkl)$  plane is located at a distance  $1/d_{hkl}$  from the origin along such a line. In this way a space lattice of reciprocal lattice points can be formed for any crystal structure.

The use of the concept of the reciprocal lattice in crystallography becomes apparent when the reflecting sphere construction shown in Figure 3.6 is considered. In this figure a wave with wave vector  $\underline{k}$  where  $|\underline{k}| = 1/\lambda$  is incident at an angle of  $\theta$  upon the  $(hkl)$  plane of a crystal at  $O$ . The sphere of radius  $|\underline{k}|$  which is drawn with its centre at a position  $-\underline{k}$  from  $O$  is called the reflecting sphere. Now consider the case when the reciprocal lattice point corresponding to the  $(hkl)$  plane lies on the surface of this sphere, i.e.

$|\underline{g}| = 1/d_{hkl}$ . Then from elementary geometric considerations

$$\sin \theta = |\underline{g}|/2|\underline{k}| \quad \text{or} \quad \sin \theta = \lambda/2d_{hkl}$$

This is Bragg's Law (see Section 3.3) which can be rewritten as

$$\underline{k}' - \underline{k} = \underline{g} \quad \dots \quad \dots \quad \dots \quad (3.14)$$

where  $\underline{k}'$  is the diffracted wave vector.

Thus the reflecting sphere construction in Figure 3.6 provides a geometrical representation of the conditions necessary for crystal planes to give rise to diffraction and forms a basis for the interpretation of electron as well as X-ray diffraction patterns.

In its application to electron diffraction there are two important features to note:-

(i) As the wavelength of 100 KeV electrons is only  $0.037 \text{ \AA}$ , the radius of the reflecting sphere is about  $27 \text{ \AA}^{-1}$  in reciprocal space. This is to be compared with the value of  $|g|$  for a typical reflection, for instance from the (200) plane of an aluminium crystal, which is about  $0.5 \text{ \AA}^{-1}$ . Therefore the reflecting sphere can be approximated to a plane over a region containing a considerable number of reciprocal lattice points.

(ii) Because of the relaxation of the Laue condition associated with the row of atoms lying parallel to the direction of the electron beam, the reciprocal lattice "points" are extended in this direction, to form spikes, the lengths of which are inversely proportional to the specimen thickness. This effect further increases the probability of a reciprocal lattice "point" coinciding with the reflecting sphere, especially when the curvature of the latter is taken into account. This is illustrated in Figure 3.7 which also shows the intensity distribution along the spikes (see Section 3.7).

As a consequence of these two effects, electron diffraction patterns containing many orders of reflections can be obtained more easily than their X-ray counterparts. With crystals of high symmetry, such as those belonging to the cubic and hexagonal systems, the two dimensional arrays of diffraction spots can generally be indexed simply by comparing them with standard patterns corresponding to orientations of low index (see for instance Hirsch et al 1965d). Patterns arising from crystals of lower symmetry are more difficult to analyse and it is usually necessary to have some a priori knowledge of their structures.

### 3.7 KINEMATICAL THEORY OF DIFFRACTION CONTRAST

#### 3.7.1 Perfect Crystals

In the above discussion of the effect of the relaxation of the Laue condition corresponding to the row of atoms parallel to the electron beam, it was stated that the intensity distribution along reciprocal lattice points had the form shown in Figure 3.7 but no attempt was made to justify this. The explanation requires the application of the kinematical theory of electron diffraction to account for the origin of some image contrast effects in crystalline samples.

One of the main assumptions made in the kinematical approach is that a two-beam condition is operating, that is to say there is only one diffracted beam in addition to the directly transmitted one. Another assumption is that the planes giving rise to this diffracted beam are not exactly in the Bragg reflecting condition, see Figure 3.8. As a result of this slight angular deviation, which is measured by the deviation parameter  $\underline{s}$ , successive unit cells along the column AB do not scatter in phase. Since  $\underline{k}' - \underline{k} = \underline{g} + \underline{s}$  in this case (see equation 3.14) the phase angle is  $2\pi(\underline{g} + \underline{s}) \cdot \underline{r}$  (see equation 3.9c). For the column AB which consists of N unit cells each containing one scattering point with an atomic scattering factor  $f_n(\theta)$  at a position  $\underline{r}_n$ , the total amplitude of the scattered wave is found from equation 3.9c to be

$$\psi_T = \sum_{n=1}^N f_n(\theta) \exp \left[ 2\pi i (\underline{g} + \underline{s}) \cdot \underline{r}_n \right] \dots \dots (3.15)$$

If all of the atoms have the same atomic scattering factor then  $f_n(\theta)$  can be taken outside the summation and equation 3.15 can be approximated to an integral. Thus, by taking the origin, 0, at the middle

of the column and neglecting the atomic scattering factor, the diffracted amplitude can be written as

$$\psi_T \approx \int_{-t/2}^{t/2} \exp \left[ 2\pi i (\underline{g} + \underline{s}) \cdot \underline{r}_n \right] dr \quad \dots \quad \dots \quad (3.16a)$$

Since  $\underline{g}$  is a reciprocal lattice vector and  $\underline{r}_n$  is a real lattice vector, then  $\underline{g} \cdot \underline{r}_n$  is integral so that  $\exp (2\pi i \underline{g} \cdot \underline{r}_n)$  has the value of unity.

Therefore equation 3.16a can be rewritten as

$$\psi_T \approx \int_{-t/2}^{t/2} \exp \left[ 2\pi i \underline{s} \cdot \underline{r} \right] dr \quad \dots \quad \dots \quad (3.16b)$$

On integrating and substituting limits it is found that

$$\psi_T \approx \frac{\sin \pi t |\underline{s}|}{\pi |\underline{s}|} \quad \dots \quad \dots \quad \dots \quad (3.16c)$$

so that the diffracted intensity,  $I_D$ , is given by

$$I_D \approx \frac{\sin^2 \pi t |\underline{s}|}{(\pi |\underline{s}|)^2} \quad \dots \quad \dots \quad \dots \quad (3.17a)$$

In terms of double angles this can be rewritten as

$$I_D \approx \frac{(1 - \cos 2\pi t |\underline{s}|)}{2(\pi |\underline{s}|)^2} \quad \dots \quad \dots \quad \dots \quad (3.17b)$$

The same result is obtained by using an amplitude phase diagram (see Figure 3.4) in which the amplitudes scattered by successive unit cells in the column AB are summed.

Equation 3.17b shows that the intensity of the diffracted wave varies periodically both with  $|\underline{s}|$  and with  $t$ . First consider the variation of intensity with  $|\underline{s}|$  which is illustrated in Figure 3.7.

This shows that the intensity spike in reciprocal space is of length  $1/t$ , which corresponds to the width of the central maximum. The length of this spike is determined by the magnitude of  $d\theta$  as shown in Figure 3.8. From the diagram,  $d\theta = \frac{1}{t/|g|}$ . However  $|g| = 1/d_{hkl}$ , so  $d\theta = d_{hkl}/t$ . Therefore the length of the diffraction spike decreases for smaller values of  $d_{hkl}$  and larger values of  $t$ , i.e. for larger angles of diffraction and for thicker crystals respectively (accepting the limitation of the kinematical theory to thin crystals only).

Now consider equation 3.17b from the viewpoint of the periodic variation of the diffracted intensity with specimen thickness. The intensity of the diffracted beam oscillates from minimum to maximum values as the beam traverses the crystal. One complete period of oscillation corresponds to the extinction distance,  $t_0$ , for the particular reflection in a specific material. From equation 3.17a it can be inferred that  $t_0 = \frac{1}{|s|}$

Next notice that the total intensity,  $I_I$ , incident on the specimen is equal to the sum of the transmitted,  $I_T$ , and diffracted intensity,  $I_D$ , i.e.

$$I_I = I_D + I_T \quad \dots \quad \dots \quad \dots \quad (3.18)$$

Therefore the transmitted intensity also varies periodically with thickness so that it is a minimum when the diffracted intensity is at a maximum and vice versa, i.e. the diffracted wave is  $\pi/2$  out of phase with the transmitted one, as shown in Figure 3.9.

As a consequence of this periodic variation in intensity with orientation and thickness, easily recognisable contrast effects occur in electron micrographs. In a perfect crystal the contrast

manifests itself in the form of extinction contours. In bright field images these appear as broad dark bands which are contours of constant  $|\underline{s}|$  (inclination contours) or of constant  $t$  (thickness contours). The origin of thickness contours at the edge of a wedge shaped sample is shown in Figure 3.9.

### 3.7.2 Imperfect Crystals

In imperfect crystals, in addition to the extinction contours, the discontinuities in the crystal structure which occur at crystal defects introduce local modifications to the phase angle of the wave emerging from the lower surface of the specimen and give rise to additional contrast effects. The range in the image over which this contrast occurs is largely determined by the nature of the discontinuity associated with the defect in the crystal, i.e. by the extent of the strain field. The expression for the amplitude of a wave scattered from an imperfect crystal is no longer given by equation 3.15 but by

$$\psi_T = \sum_{n=1}^N f_n(\theta) \exp \left[ 2\pi i (\underline{g} + \underline{s}) \cdot (\underline{r}_n + \underline{R}_n) \right] \dots \dots (3.19a)$$

where  $\underline{R}_n$  is the displacement of the  $n^{\text{th}}$  cell from its proper position in a perfect crystal.

Applying a treatment similar to that used above, equation 3.19a can be written as an integral of the form

$$\psi_T = \int_0^t \exp \left[ 2\pi i (\underline{g} + \underline{s}) \cdot (\underline{r} + \underline{R}) \right] dr \dots \dots (3.19b)$$

where  $\underline{R}$  is the displacement of the unit cell at  $\underline{r}$ .

The term  $\underline{s} \cdot \underline{R}$  is nearly zero and can be neglected. Also  $\underline{g} \cdot \underline{r}$  has an integral value as before, so the above expression approximates to

$$\psi_T \approx \int_0^t \left[ \exp(2\pi i \underline{g} \cdot \underline{R}) \exp(2\pi i \underline{s} \cdot \underline{r}) \right] dr \dots \quad (3.19c)$$

By comparing this with the amplitude of a wave diffracted by a perfect crystal (see equation 3.16b), it is evident that the effect of the fault is to introduce an additional phase factor of magnitude  $\exp(2\pi i \underline{g} \cdot \underline{R})$ . Thus contrast arises through a phase contrast mechanism where the phase difference is produced by the atomic displacements  $\underline{R}$ .

One of the important effects of this additional phase factor on the contrast produced by defects is as follows. When the product  $\underline{g} \cdot \underline{R} = 0$ , i.e. when the atomic displacements are perpendicular to the diffraction vector and therefore lie in the plane containing the direction of the electron beam, the expression in 3.19c reduces to the same form as that for the amplitude of a wave diffracted by a perfect crystal (see equation 3.16b). Consequently in this condition no contrast is produced by the atomic displacement  $\underline{R}$ . This invisibility criterion is used to determine the Burgers vectors of dislocations (see Section 4.3) and the slip vectors of other defects, such as stacking faults (see Section 4.4). The application of the principle is clearly illustrated by the following example.

Figure 3.10 shows a bright field image of a grown-in dislocation decorated with precipitates in MgO (see Section 5.3.2). The plane of the foil is (001) and the two-beam diffraction condition corresponding to Figure 3.10 is shown in Figure 3.11 in which there is no relative rotation with respect to the micrograph. As the dislocation is long in comparison with the thickness of the foil, it must lie approximately in the plane of the specimen. Now MgO has the NaCl structure (see Section 4.1), the slip system of which is  $\{110\} \langle \bar{1}\bar{1}0 \rangle$ . The dislocation

in Figure 3.10 must therefore lie along the  $[\bar{1}\bar{1}0]$  direction in one of the two  $\{110\}$  planes that are perpendicular to the plane of the foil. Further, if this dislocation is predominantly either of edge or screw character, its Burgers vector must also lie in one of these planes. As it gives rise to contrast when the diffraction conditions in Figure 3.11 are operative, the product  $\underline{g} \cdot \underline{b}$  (where  $\underline{b}$  is the Burgers vector of the dislocation and replaces the displacement vector  $\underline{R}$  in equation 3.19c) has a non-zero value in this case. Therefore  $\underline{b}$  does not lie in the  $[\bar{1}\bar{1}0]$  direction which is parallel to the length of the dislocation. By tilting the specimen to produce the two-beam condition in which the  $(\bar{2}20)$  plane gives rise to Bragg reflection, the micrograph in Figure 3.12 is obtained. The diffraction pattern corresponding to this is shown in Figure 3.13 and as with Figures 3.10 and 3.11, there is no relative rotation of the diffraction pattern with respect to the image. In this diffraction condition the dislocation does not give rise to any contrast and its position is only evidenced by the location of the precipitates. Thus for the  $(\bar{2}20)$  reflection operating,  $\underline{g} \cdot \underline{b} = 0$ . Consequently  $\underline{b}$  is of the form  $a_0/2 [\bar{1}10]$ , where  $a_0$  is the lattice parameter of MgO, and the dislocation is of edge type (see Section 4.3).

The determination of the Burgers vector just described was very straightforward. In many instances, when the slip system is not known, it is usual to make up a table with all the possible Burgers vectors and to evaluate the product  $\underline{g} \cdot \underline{b}$  for a number of intuitively chosen two-beam cases.

### 3.8 CONCLUDING REMARKS

While the kinematical theory of electron diffraction outlined in this chapter provides a practical and convenient method for

explaining the contrast effects observed in the images of crystals, it is only strictly applicable when the following conditions are fulfilled:-

- (i) the specimen is sufficiently thin to allow rescattering and absorption processes to be neglected.
- (ii) there is only one diffracted beam in addition to the directly transmitted one.
- (iii) the Bragg condition for the diffracted beam is not exactly satisfied so that the intensity of this beam is small compared with that of the directly transmitted one.

For a more precise explanation of contrast effects, especially in specimens greater than a few hundred Å thick, the application of the more rigorous and much more complex dynamical theory of electron diffraction is necessary. This theory involves the interaction of the direct and diffracted beams. For a comprehensive treatment of it, reference should be made to Chapters 8 to 12 of the book by Hirsch et al (1965c). However, in spite of the limitations of the kinematical theory, its main qualitative features are similar to those of the dynamical theory and its use therefore is justified for most purposes in electron microscopy (see for example Hirsch et al 1960).



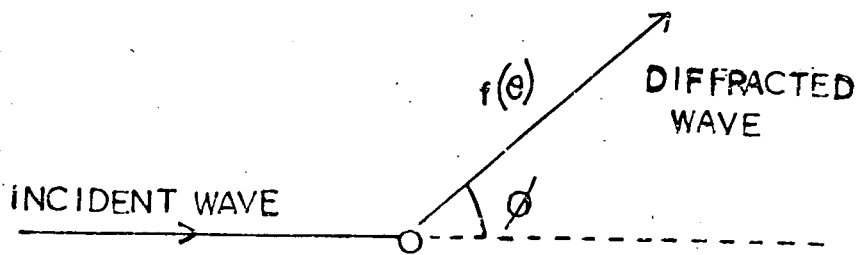


FIGURE 3.3 THE AMPLITUDE PHASE DIAGRAM FOR SCATTERING FROM A UNIT CELL CONTAINING ONE LATTICE POINT

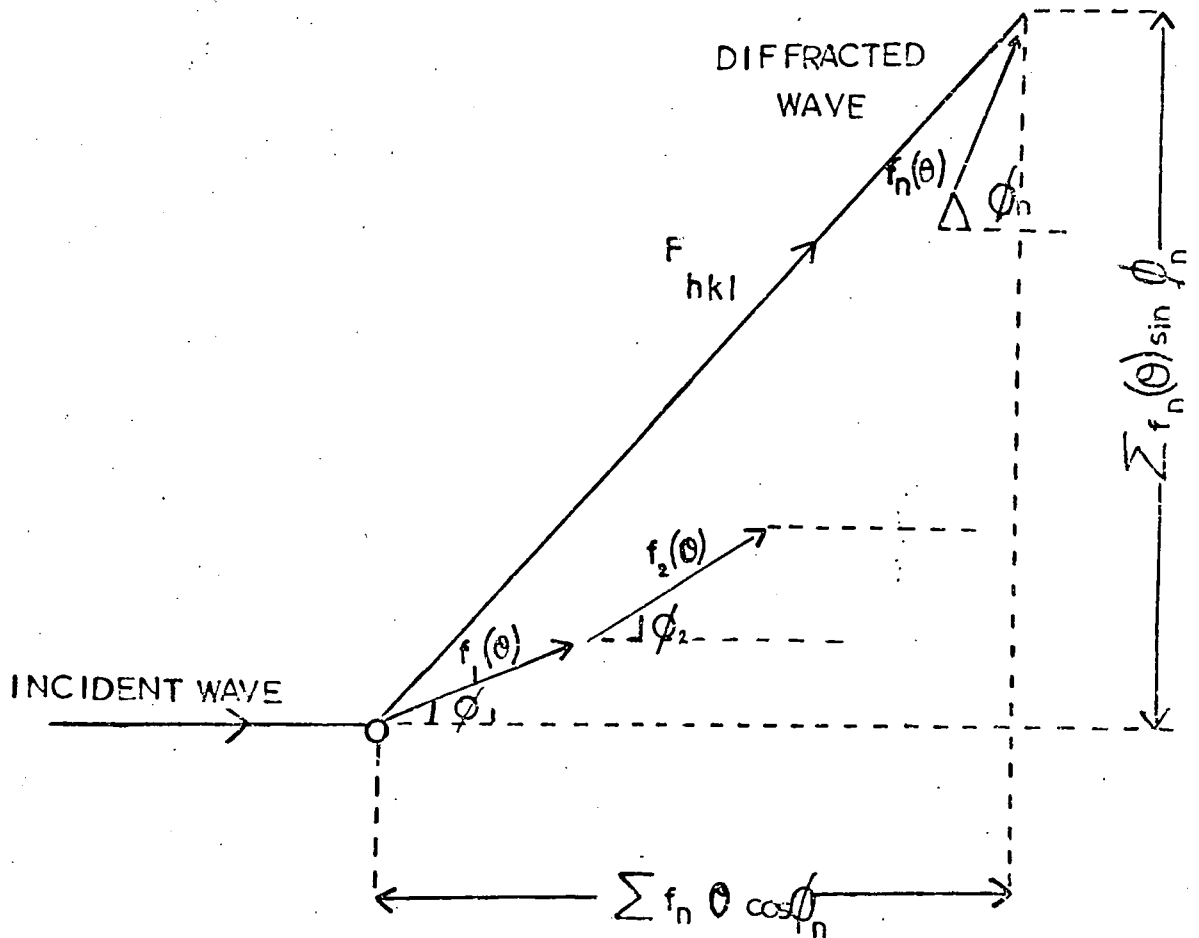


FIGURE 3.4 AMPLITUDE PHASE DIAGRAM FOR SCATTERING FROM A UNIT CELL CONTAINING  $n$  ATOMS

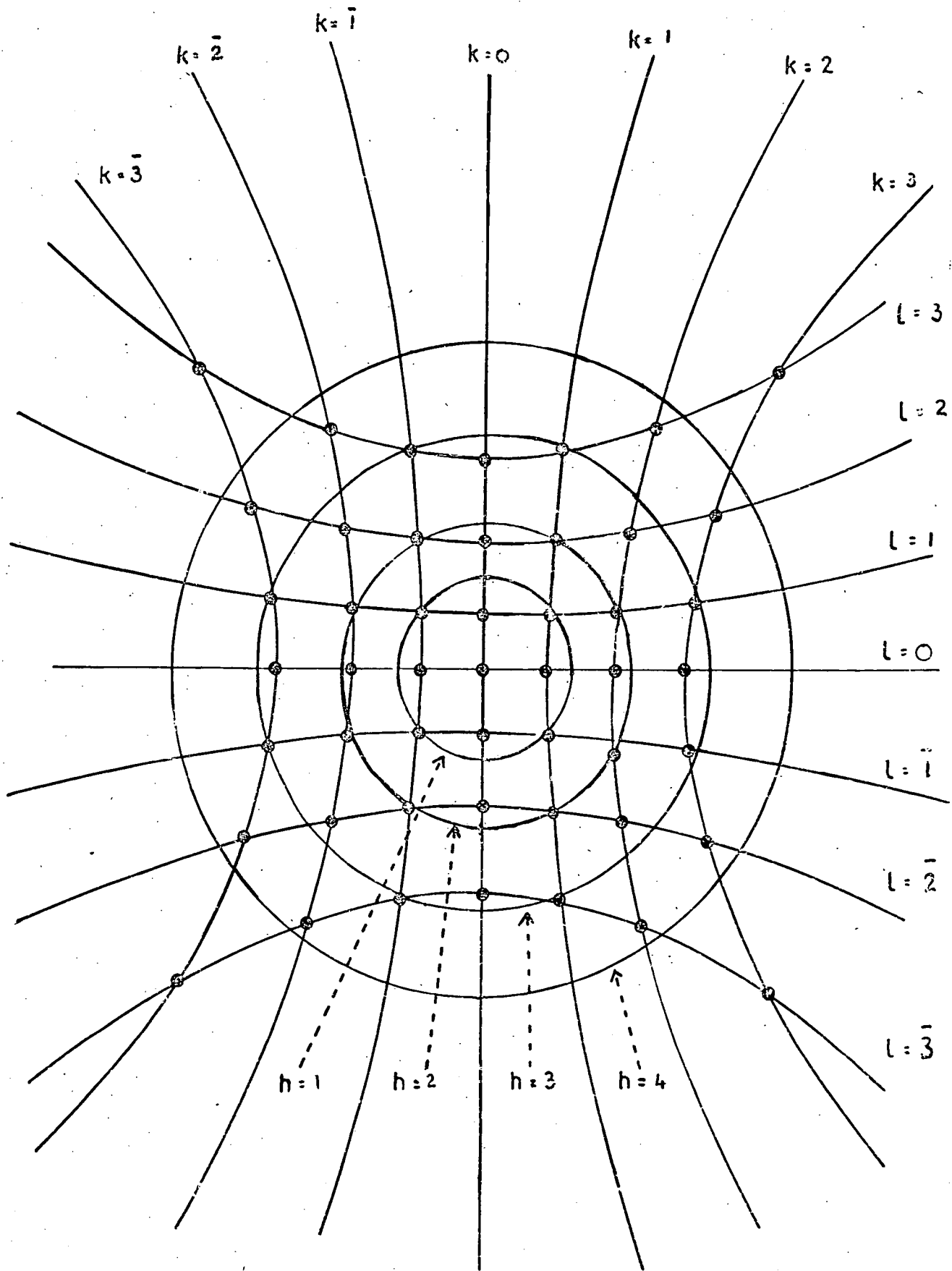


FIGURE 3.5 SCHEMATIC REPRESENTATION OF THE THREE LAUE CONDITIONS FOR A CUBIC CRYSTAL

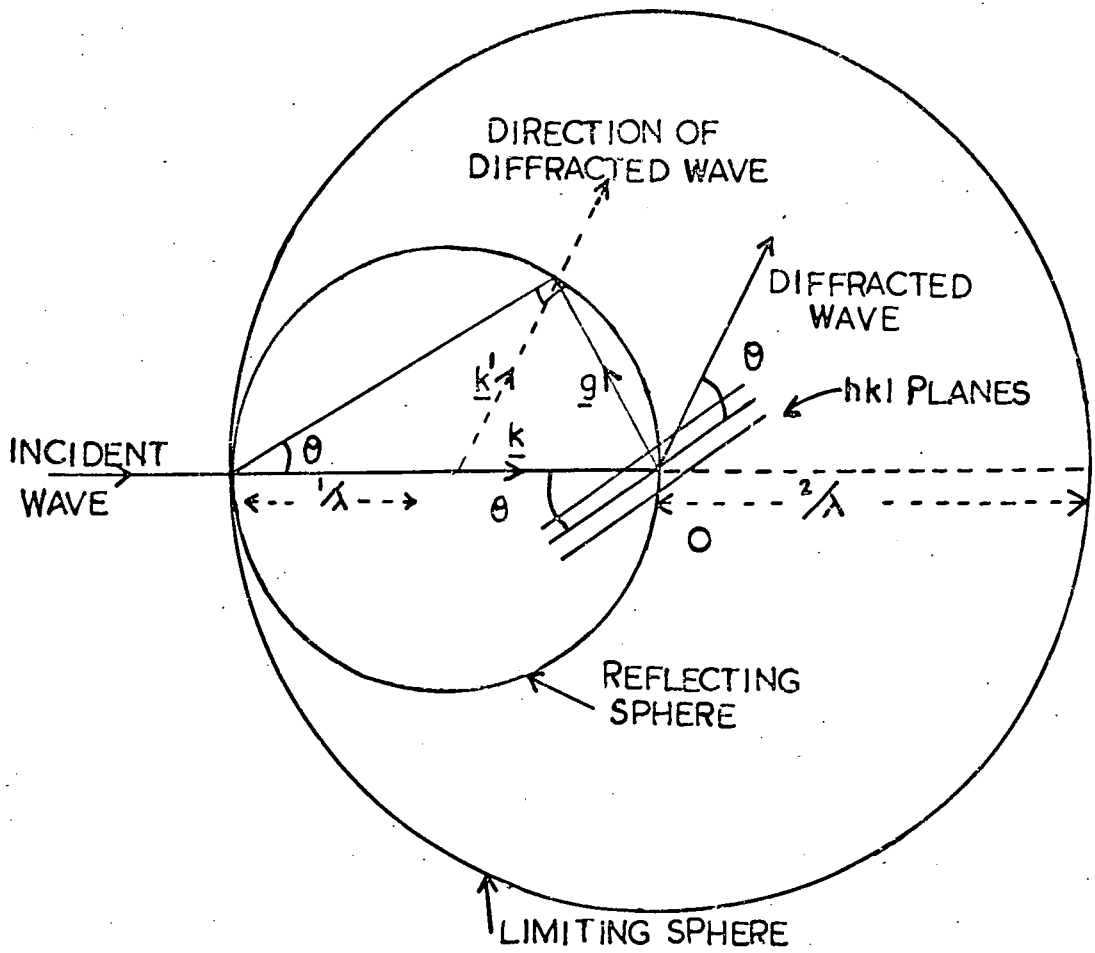


FIGURE 3.6 REFLECTING SPHERE CONSTRUCTION

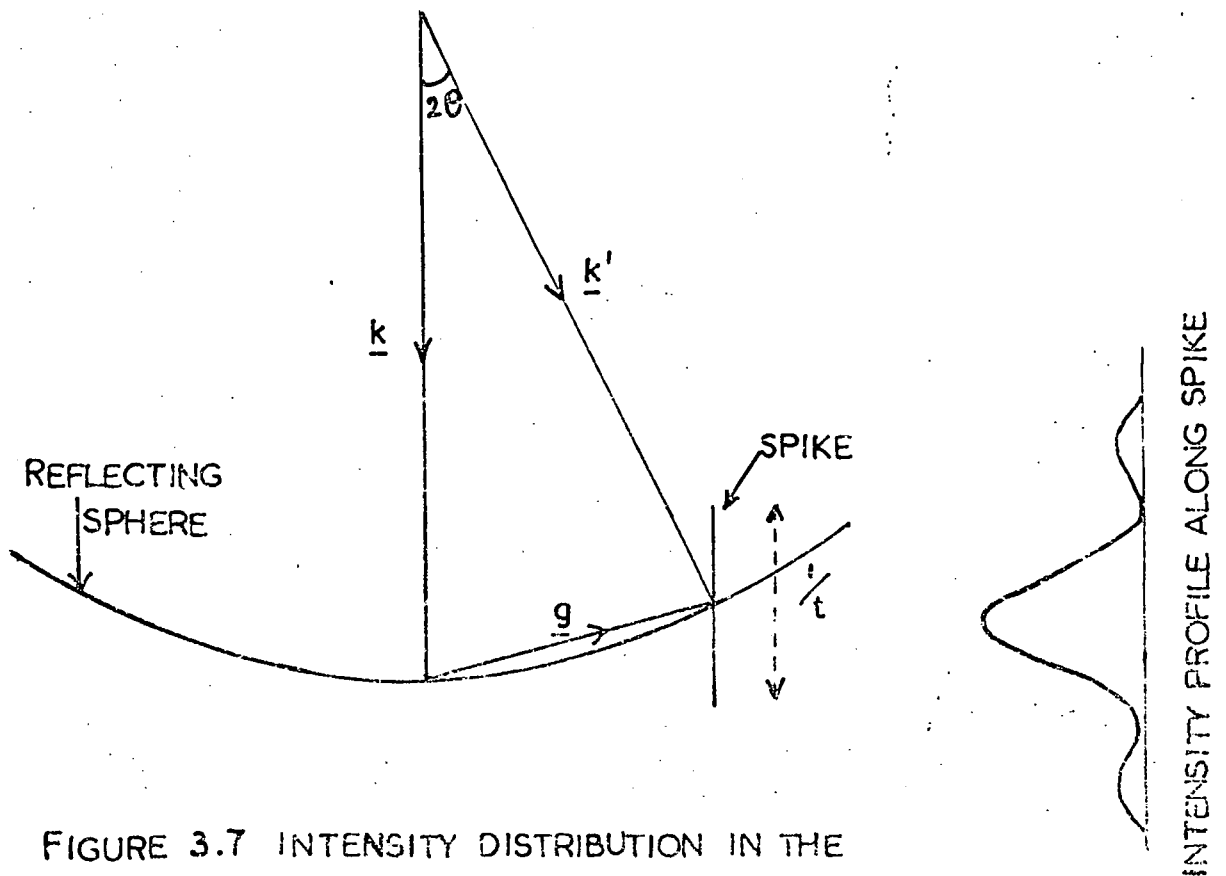


FIGURE 3.7 INTENSITY DISTRIBUTION IN THE FORM OF A SPIKE

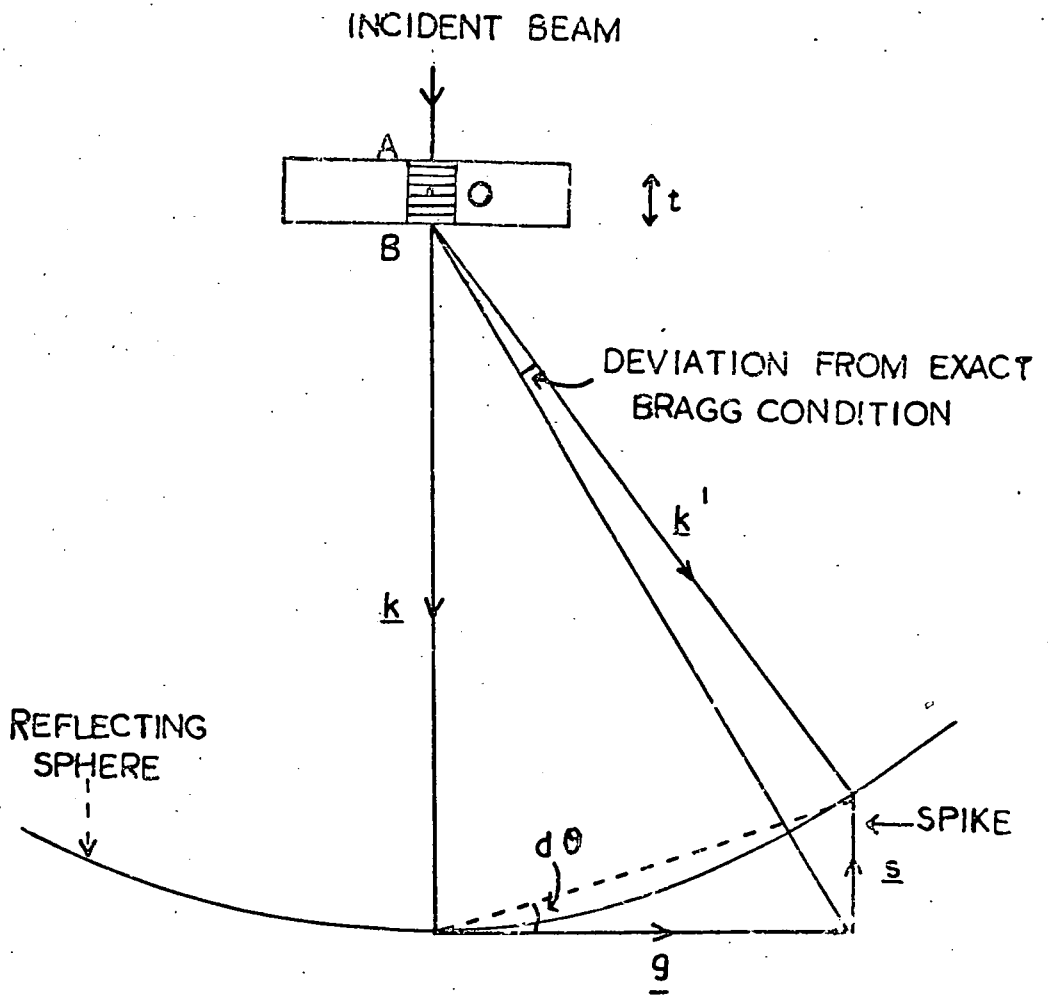


FIGURE 3.8 ILLUSTRATING REFLECTING SPHERE CONSTRUCTION FOR KINEMATICAL CONDITIONS (EXAGGERATED)

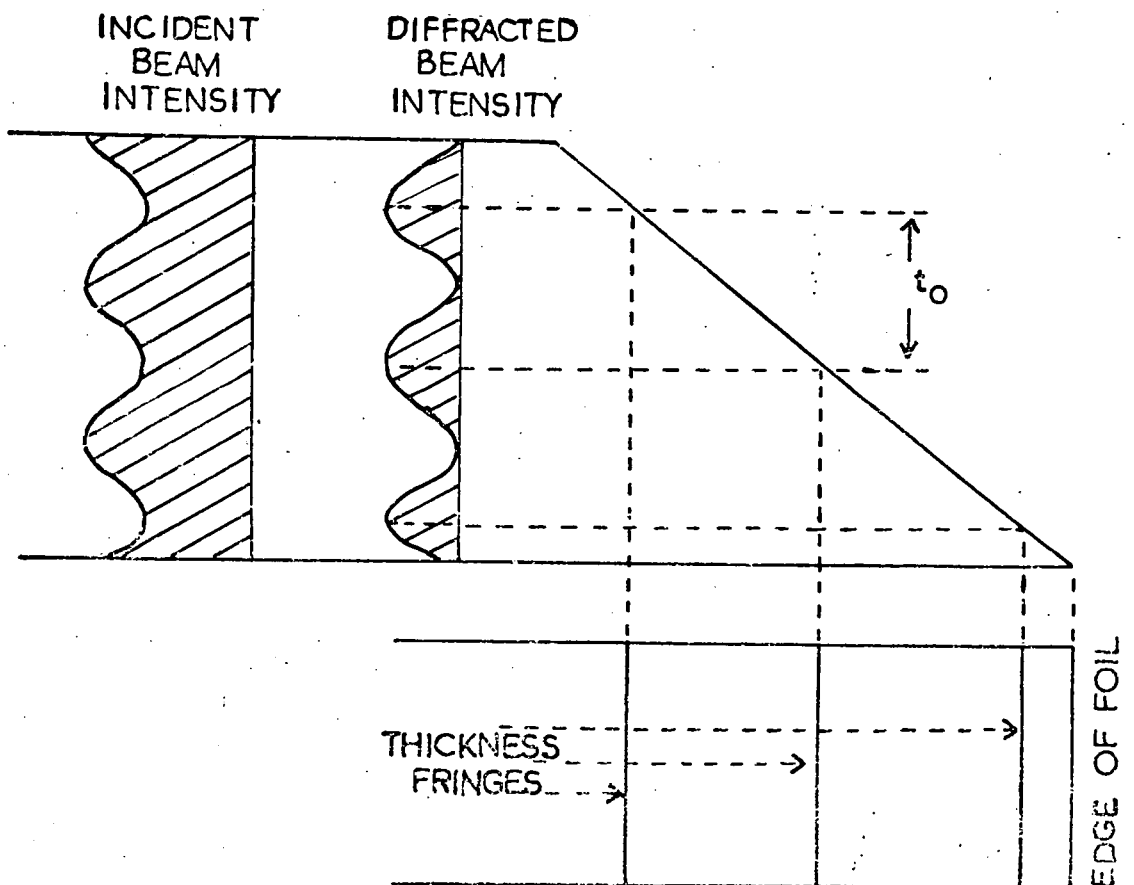


FIGURE 3.9 SCHEMATIC ILLUSTRATION OF THE ORIGIN OF THICKNESS FRINGE CONTRAST

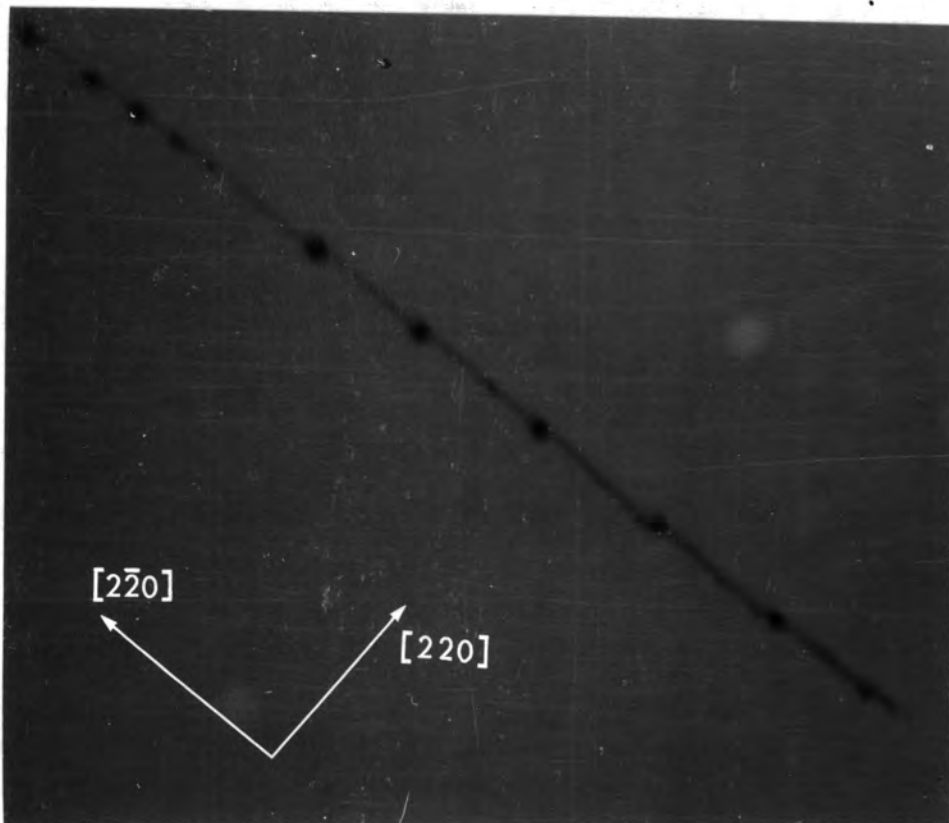


FIGURE 3.10  
A BRIGHT FIELD IMAGE OF A DISLOCATION IN  $MgO$

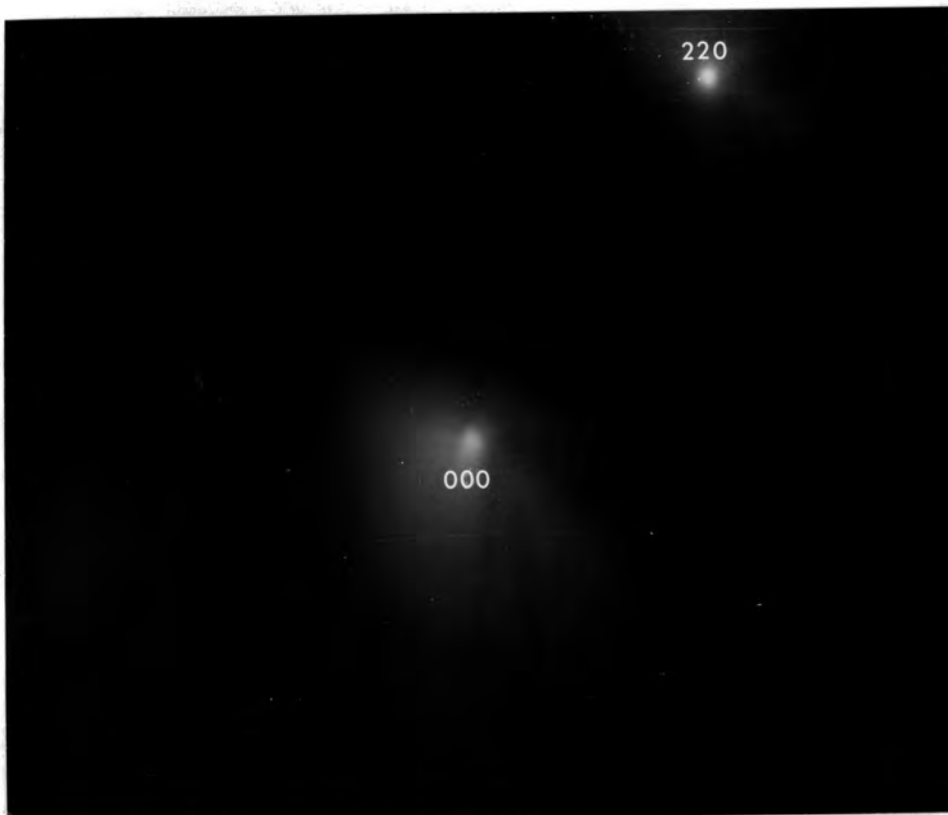


FIGURE 3.11  
THE TWO-BEAM DIFFRACTION CONDITION CORRESPONDING TO FIG. 3.10

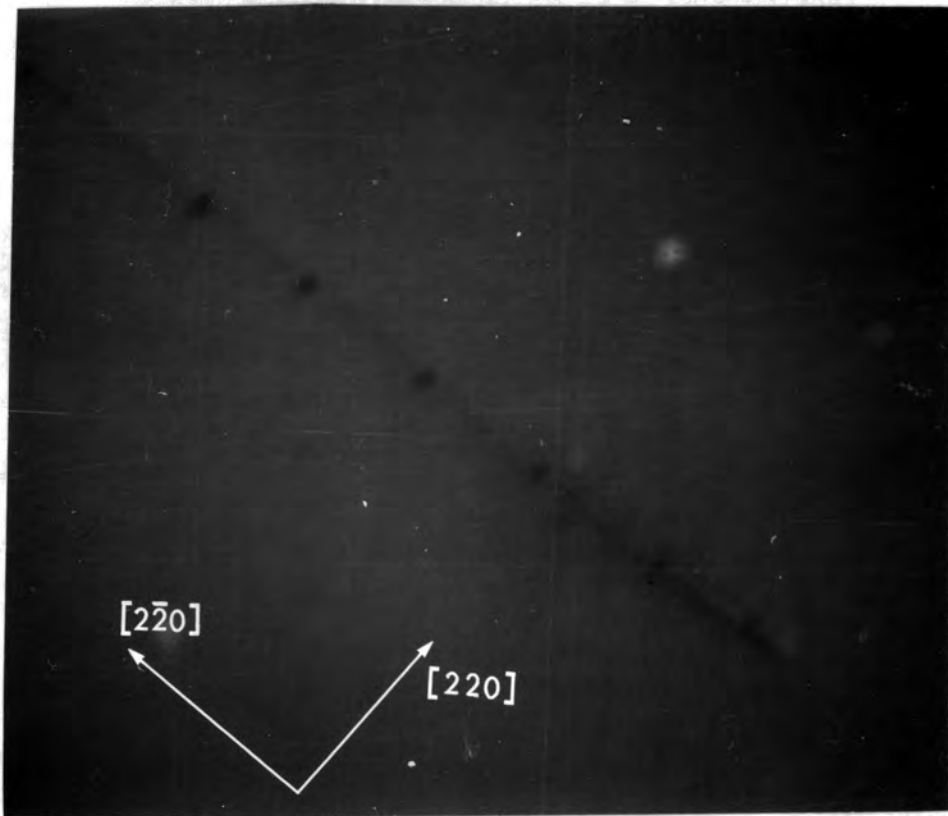


FIGURE 3.12  
THE SAME AREA AS IN FIG. 3.10 AFTER TILTING

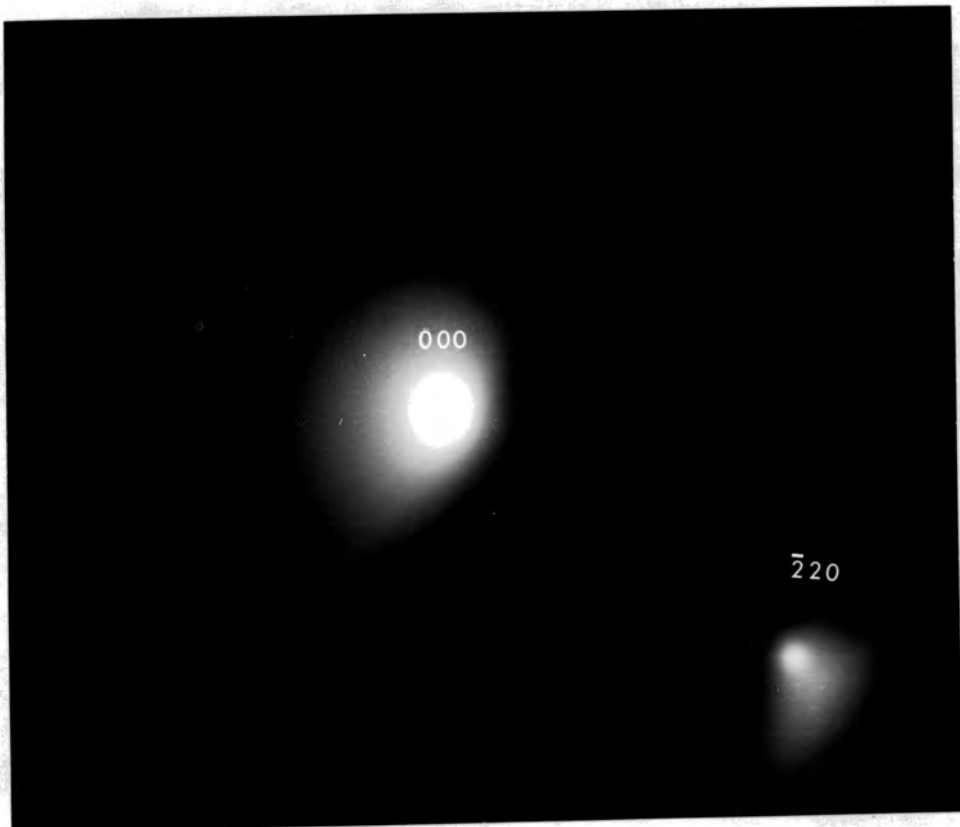


FIGURE 3.13  
THE TWO-BEAM DIFFRACTION CONDITION CORRESPONDING TO FIG. 3.12

CHAPTER 4

THE CRYSTAL STRUCTURES OF MAGNESIUM OXIDE AND ZINC SELENIDE  
AND SOME OF THE DEFECTS IN THESE MATERIALS

The purpose of this chapter is to provide an abbreviated account of the topics of crystal structure and crystal defects as a background against which to understand the results reported in this thesis. As numerous book-length reviews have been written on these two topics (see for example Brown and Forsyth 1973 on crystalline structures and Henderson 1972 on crystal defects), the account given here is necessarily limited in its scope. It is of course confined to the crystal structures of MgO and ZnSe and to those defects in these materials which can be detected by TEM. Nevertheless it includes a description of many of the defects in crystalline materials which are most commonly observed using this technique.

4.1 CRYSTAL STRUCTURES

MgO is an alkaline earth oxide having the simple rocksalt (NaCl) structure shown in Figure 4.1. This consists of two interpenetrating face-centred cubic lattices, one made up of anions which are shown as filled circles and the other of cations which are shown as open circles. The two sublattices are displaced from one another by a distance equal to half the lattice parameter along one of the cube edges. The unit cell contains four molecules with four metal ions at  $0,0,0$ ;  $\frac{1}{2},\frac{1}{2},0$ ;  $\frac{1}{2},0,\frac{1}{2}$ ;  $0,\frac{1}{2},\frac{1}{2}$  and four halogen ions at  $\frac{1}{2},\frac{1}{2},\frac{1}{2}$ ;  $0,0,\frac{1}{2}$ ;  $0,\frac{1}{2},0$ ;  $\frac{1}{2},0,0$ .

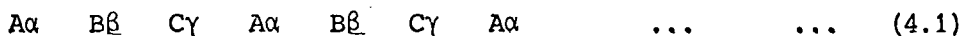
ZnSe belongs to a different family of materials known as the zinc chalcogenides. It usually forms crystals with the zincblende (sphalerite) structure. This crystal structure, like that of rocksalt,

is based on a face-centred cubic Bravais lattice and consists of interpenetrating face-centred cubic sublattices of different atoms displaced from one another along a body diagonal by one quarter the length of the body diagonal of the unit cell (see Figure 4.2). The unit cell of the zincblende structure, like that of rocksalt, contains four molecules with four metal atoms at  $0,0,0$ ;  $0, \frac{1}{2}, \frac{1}{2}$ ;  $\frac{1}{2}, 0, \frac{1}{2}$ ;  $\frac{1}{2}, \frac{1}{2}, 0$  and four non-metal atoms at  $\frac{1}{4}, \frac{1}{4}, \frac{1}{4}$ ;  $\frac{1}{4}, \frac{3}{4}, \frac{3}{4}$ ;  $\frac{3}{4}, \frac{1}{4}, \frac{3}{4}$ ;  $\frac{3}{4}, \frac{3}{4}, \frac{1}{4}$ .

The following features of the zincblende structure should be mentioned.

(i) The sites occupied by atoms are such that if both kinds of atom were the same, the arrangement would be identical with the diamond structure. Consequently the sites have tetrahedral symmetry and this leads to a basic difference between the rocksalt and zincblende structures which owes its origin to the nature of the bonding. While the bonding of the rocksalt structure is almost wholly ionic, that of the diamond structure is covalent. The bonding of materials with the zincblende structure is intermediate between these two extremes.

(ii) The displacement of one atomic sublattice from the other by  $\frac{1}{4} \langle 111 \rangle$  gives rise to a unit cell which has no centre of symmetry or inversion. Thus the double (metal and non-metal) atomic layers which are stacked along the  $\langle 111 \rangle$  directions have unique orientations, i.e. crystals with this structure are polar and opposed  $(hkl)$  and  $(\bar{h}\bar{k}\bar{l})$  planes and opposed  $[hkl]$  and  $[\bar{h}\bar{k}\bar{l}]$  directions can be associated with different physical and chemical properties (see Roth 1967). For many of these properties, the most important polar directions are those with the lowest indices, i.e.  $\langle 111 \rangle$  and  $\langle \bar{1}\bar{1}\bar{1} \rangle$ . The stacking sequence along these directions is of the form



where A, B and C represent zinc layers and  $\alpha$ ,  $\beta$  and  $\gamma$  represent selenium layers. If the  $\langle 111 \rangle$  axis is vertical, the atoms of any layer lie vertically above the atoms of lower-lying planes designated by the same letter. The occurrence of the double atomic layers indicated in the above stacking sequence leads to the designation of the opposite faces of a  $\{111\}$  crystal platelet as the metal or  $\{111\}$  and the non-metal or  $\{\bar{1}\bar{1}\bar{1}\}$  surfaces respectively.

The final crystal structure to be described in this section is that of wurtzite. This is included firstly because it is closely related to the zinblende structure and secondly because defects such as stacking faults in the zinblende structure give rise to thin regions with this hexagonal arrangement (see Section 7.4.1). The wurtzite structure is conveniently described by reference to the stacking of double atomic layers in the  $\langle 111 \rangle$  directions of the zinblende structure (see the stacking sequence 4.1). Using the same notation as above, the stacking of atomic layers in the wurtzite structure is of the form



The stacking sequence of the close packed planes in wurtzite is different from that in zinblende in that the positions of the atoms are repeated after every second double atomic layer instead of every third. The unit cell of the structure is shown in Figure 4.3. The atomic arrangement consists of two interpenetrating hexagonal close packed lattices, one based on metal atoms and the other on non-metal ones. The unit cell contains two molecules with two metal atoms at  $0,0,0$ ;  $\frac{1}{3}, \frac{2}{3}, \frac{1}{2}$  and two non-metal atoms at  $0,0,u$ ;  $\frac{1}{3}, \frac{2}{3}, \frac{1}{2} + u$ , with  $u \approx \frac{3}{8}$  (see for example Fuller 1929).

There are two important differences between this structure and zincblende. Firstly wurtzite has only one polar axis compared with the four of zincblende and secondly the structure occurs for materials where the proportion of ionic relative to covalent bonding is slightly higher. Evidence supporting the latter point is provided by the calculated values of the Madelung constant for the two arrangements, these being 1.638 and 1.641 for zincblende and wurtzite respectively (see Sherman 1932). Since the Madelung constant for the rocksalt structure is 1.7476 (see for example Companion 1964), the bonding of the wurtzite structure is slightly more ionic than that of zincblende.

#### 4.2 POINT DEFECTS

As the strain fields of isolated point defects only extend a few atomic diameters beyond their lattice positions, these defects are not usually detected by TEM. However, since these are the simplest form of crystal defect, and as many larger defects arise from their agglomeration, it is relevant to include a brief description of their properties.

The common types of point defect in a crystal lattice are:-

- (i) a vacancy, i.e. a proper site from which an atom or ion is missing,
- (ii) an interstitial, where an extra atom or ion is inserted in a position between atoms or ions in their proper lattice sites,
- (iii) a substitutional impurity, where an atom or ion of the crystal is replaced by some foreign atom or ion. Interstitial impurities are obviously also possible.

In each of these three cases there is a distortion of the lattice in the immediate vicinity of the defect. In particular, the presence

of a vacancy or an interstitial leads to an interesting effect on the properties of the lattice. For instance, while it is difficult for an atom or ion to move from its lattice site in a perfect crystal, it is relatively easy for it to move from one vacancy or interstitial position to another. The concentration of point defects therefore has marked effects on diffusion and allied properties of a material.

Point defects are usually classified in the following three groups:

- (i) Schottky defects
- (ii) anti-Schottky defects
- (iii) Frenkel defects.

In a monatomic crystal a Schottky defect is simply a vacancy which is present with no corresponding interstitial and an anti-Schottky defect is the interstitial counterpart of this. However in an ionic material like MgO, it is usual to consider these defects to occur in pairs of metal and non-metal vacancies or interstitials and the defects are then referred to as Schottky or anti-Schottky pairs. The Frenkel defect also consists of a pair of point defects, but in this case one is a vacancy and the other is an interstitial where there is no particular relationship between their positions.

In any real crystal there will generally be some of each of these defects present and their concentration will be determined by thermodynamic considerations. At any given temperature there exists a dynamic equilibrium in which the number of defects of any particular kind being created per second is equal to the number being annihilated per second. This is a very elementary explanation of what amounts to a complex thermodynamic subject (see for example Kelly and Groves 1970).

As a consequence of charge compensation in ionic materials, the presence of vacancies leads to another important group of point defects known as colour centres. These are most frequently met in the alkali halides though they have been studied extensively in some II-VI compounds, notably MgO. While they have not been the subject of the investigation reported here, their importance in this material justifies the mention of their existence. The most extensively studied member of this group is the F centre which consists simply of an electron trapped at a cation vacancy. The antimorph of this is the V centre which consists of an anion vacancy with a trapped hole. There are several other more complex configurations of trapped electron and trapped hole centres and for a comprehensive treatment of these the reader is referred to the classic text by Schulman and Compton (1963).

#### 4.3 DISLOCATIONS

The concept of dislocations in crystals was introduced by Orowan (1934), Polanyi (1934) and Taylor (1934) to account for a difference of approximately three orders of magnitude between the experimentally observed and theoretically calculated values of the yield strengths of crystals. It was proposed that the low observed values could be explained by line defects, namely dislocations, which could move relatively easily across slip planes in a perfect crystal. The movement of large numbers of dislocations on a slip plane accounts for the experimentally observed slip bands. Many powerful techniques were eventually developed for both the direct and indirect observation of dislocations, one of the more important of which is TEM. The resultant observations have substantiated the early theories and have contributed significantly to the present understanding of many of the physical properties of the crystalline solid state.

Dislocations are classified according to the relative orientation of their slip, or Burgers vector, and their length. In one extreme the line defect has a Burgers vector perpendicular to its length in which case it is defined as an edge dislocation, and in the other it has a Burgers vector parallel to its length and is then designated as a screw dislocation. Schematic diagrams of these two types of dislocation are shown in Figures 4.4 and 4.5. Many dislocations, or parts of them, are neither purely edge nor purely screw in character, that is to say, their Burgers vectors are neither perpendicular nor parallel to their lengths. Such dislocations are said to be of mixed character with an edge and a screw component. A specific example of this type occurs in the zinblende structure with what is termed a  $60^\circ$  dislocation on account of the angle between its Burgers vector and its length (see for example Holt 1962).

The Burgers vector of a dislocation can be determined by performing what is called a Burgers circuit operation. In this, an atom to atom path is taken such that a closed circuit would have been obtained in a perfect crystal. However, when a similar path containing the same number of atom to atom steps is taken around a dislocation, the circuit fails to close. The closure failure (the vector required to close the circuit) is the Burgers vector,  $\underline{b}$ , of the dislocation and this is illustrated for the pure edge and pure screw dislocations in Figures 4.4 and 4.5. In these two cases the closure failure is a lattice vector and the defects are said to be perfect dislocations.

Normally as dislocations move through crystals, they glide over preferred planes in specific crystallographic directions which are energetically favourable. These planes and directions constitute the slip system of a particular structure, and a knowledge of this system facilitates the interpretation of electron micrographs containing

dislocations. The slip system of MgO is  $\{110\} \langle \bar{1}\bar{1}0 \rangle$  and that of ZnSe is  $\{111\} \langle \bar{1}\bar{1}0 \rangle$  and inspection of the crystal structures of these materials in Figures 4.1 and 4.2 reveals that the displacement of an atom or ion to its nearest neighbour position in these directions only requires the replacement of one atom or ion by another of the same type.

#### 4.4 STACKING FAULTS AND TWINS

The above discussion was confined to perfect dislocations, the movement of which leaves a crystal unchanged in its atomic arrangement other than in the immediate vicinity of the dislocation lines. In contrast, the movement of partial dislocations, which have Burgers vectors that are less than a unit lattice vector in magnitude, can leave areas across which the regular atomic stacking sequence is interrupted. These areas are called stacking faults and they are formed when a perfect dislocation dissociates into two partial dislocations which separate and leave a ribbon of stacking fault between them. For a face-centred cubic material with a lattice parameter  $a$ , this dissociation leads to a reduction in the elastic strain energy of perfect dislocations and takes the form:

$$\frac{a}{2} \left[ 110 \right] \longrightarrow \frac{a}{6} \left[ 211 \right] + \frac{a}{6} \left[ 12\bar{1} \right]$$

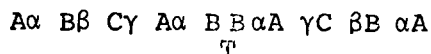
The stacking fault between these partial dislocations is so called because of the stacking disorder of the close packed  $\{111\}$  plane on which it lies. This is illustrated schematically in Figures 4.6 and 4.7 for a face-centred cubic metal. The two diagrams show the two types of stacking fault which can occur and which are called intrinsic and extrinsic. The intrinsic fault is equivalent to the removal of part of a close packed layer of atoms which results in a

stacking sequence of the form  $ABCACABC$ , where A, B and C represent layers of atoms on a  $\{111\}$  plane as before (see Section 4.1), and where T denotes the position of a twin boundary (see below). On the other hand, the extrinsic stacking fault consists of part of an extra layer of atoms inserted between two layers of atoms on a close packed plane so that the stacking sequence is of the form  $ABCABACABC$ . From these stacking sequences an interesting feature of stacking faults is apparent. This concerns the atomic arrangement in the vicinity of these defects which is such that the stacking sequences contain local regions of hexagonal material.

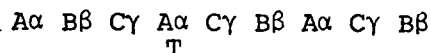
The other common defect in face-centred cubic materials which involves interruptions of the stacking sequence of close packed planes is the twin boundary. The main characteristic of this fault is that all of the lattice sites occupied by atoms on one of its sides are in the mirror image positions of atoms on the other side. This can be seen from the stacking sequence which is of the form  $ABCABCBCBACBA$  where T denotes the position of a twin boundary as above. Twin boundaries frequently occur in pairs on the same  $\{111\}$  plane and the region between them is called a twin. Twins that are very thin but more than two atomic layers thick are called microtwins. This minimum thickness is necessary in this definition because examination of the stacking sequences of the extrinsic and intrinsic stacking faults reveals that these faults are equivalent to pairs of twin boundaries on alternate and adjacent atomic layers respectively.

To extend this account to include stacking faults and twins in the zincblende structure it is necessary simply to replace each single atomic layer by a double one. For instance A, B and C are replaced by  $A\alpha$ ,  $B\beta$  and  $C\gamma$  using the same terminology employed in Section 4.1. This leads to one interesting property of twins in the zincblende

structure which is that they can occur in two different forms (see for instance Holt 1966). These are the ortho and the para-twin and they are illustrated in Figures 4.8 and 4.9. The true twin boundary across which the atoms are mirror-image related is the para type and this is characterised by an array of wrong bonds which may be either metal to metal or non-metal to non-metal. The stacking sequence of this boundary is of the form



The energetically more favourable and the more frequently encountered twin boundary (see Section 7.3.1) which occurs in the zincblende structure is the ortho-twin. While the atom sites are mirror-image related across this boundary, the types of atoms are different in the mirror-image positions. The stacking sequence of this boundary is



From these two sequences it can also be seen that the two types of twin boundary differ in the respect that the crystallographic polarity remains the same across the ortho-twin boundary but the polar direction changes from a  $\langle 111 \rangle$  to a  $\langle \bar{1}\bar{1}\bar{1} \rangle$  axis across the para-twin one.

In conclusion it should be noted that the defects described in this section can arise not only from the movement of partial dislocations in relieving stress in grown crystals, but also as a result of incidental growth at the crystal interface occurring during crystal growth.

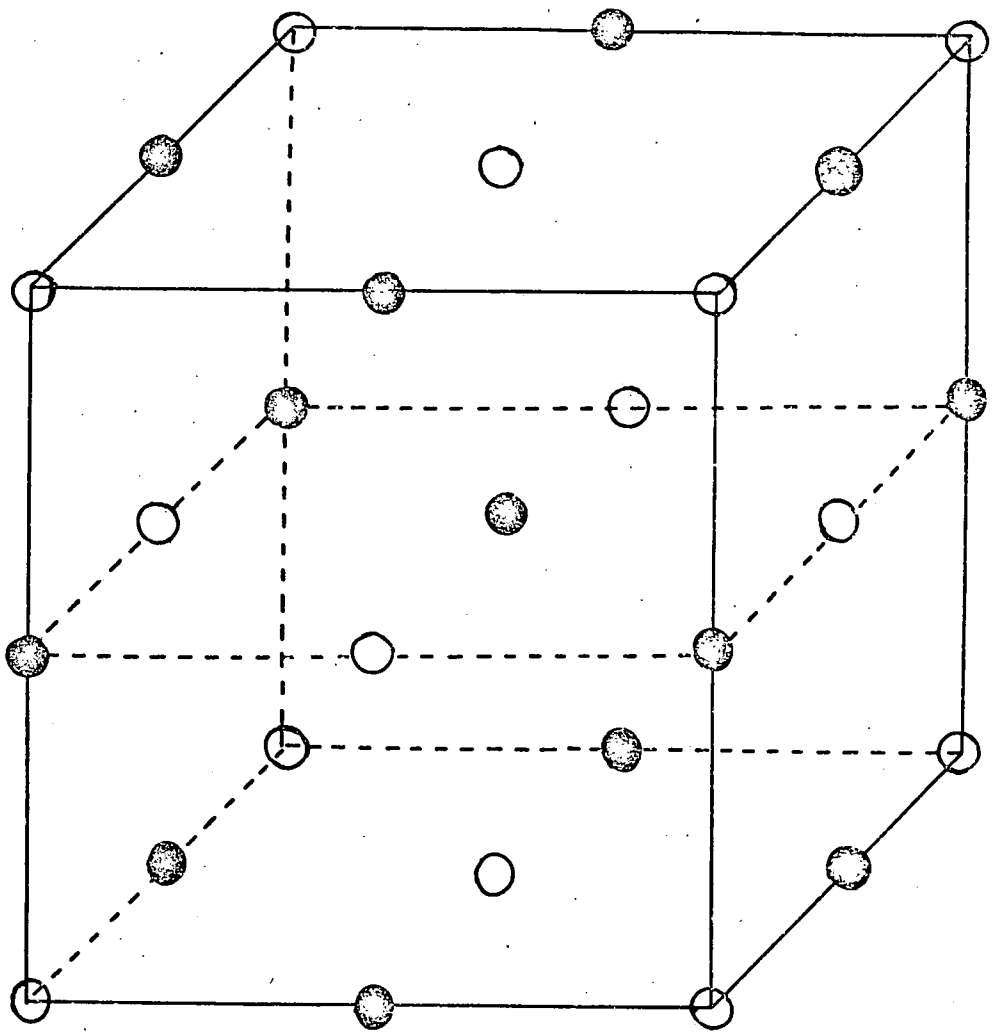


FIGURE 4.1 THE ROCKSALT STRUCTURE

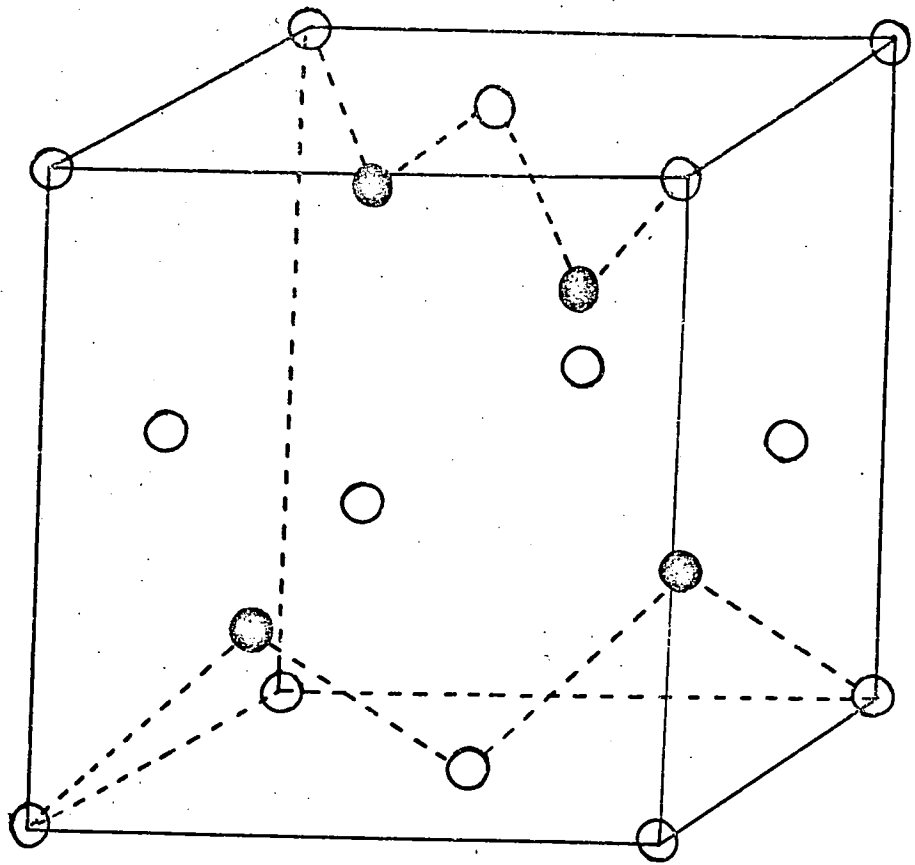


FIGURE 4.2 THE ZINCBLLENDE STRUCTURE

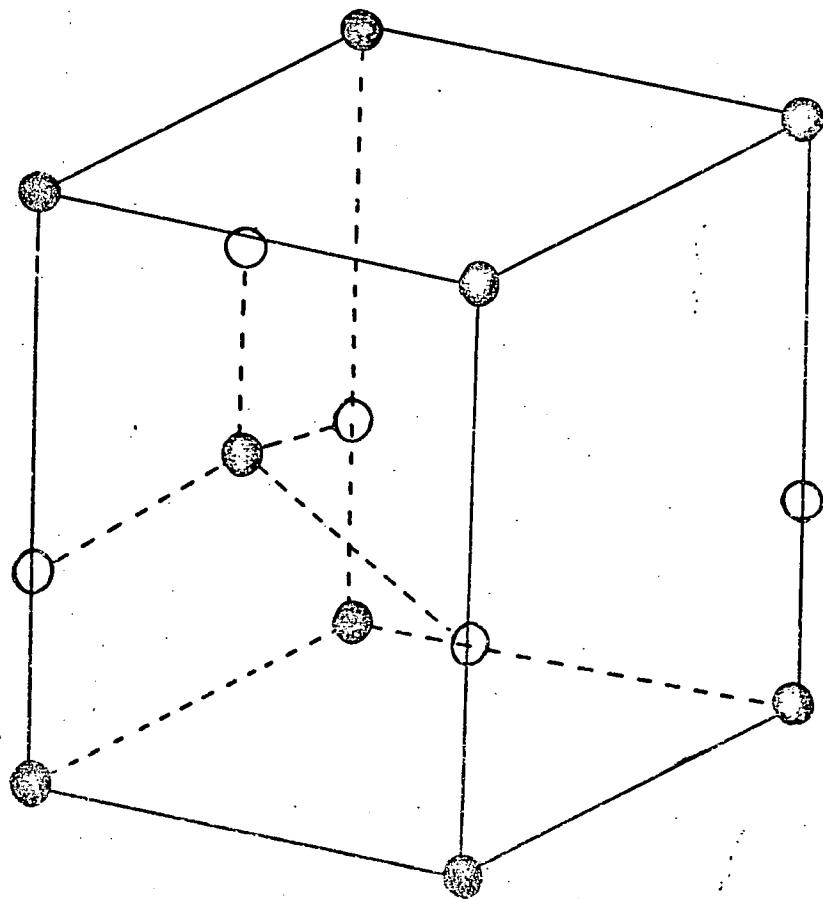


FIGURE 4.3 THE WURTZITE STRUCTURE

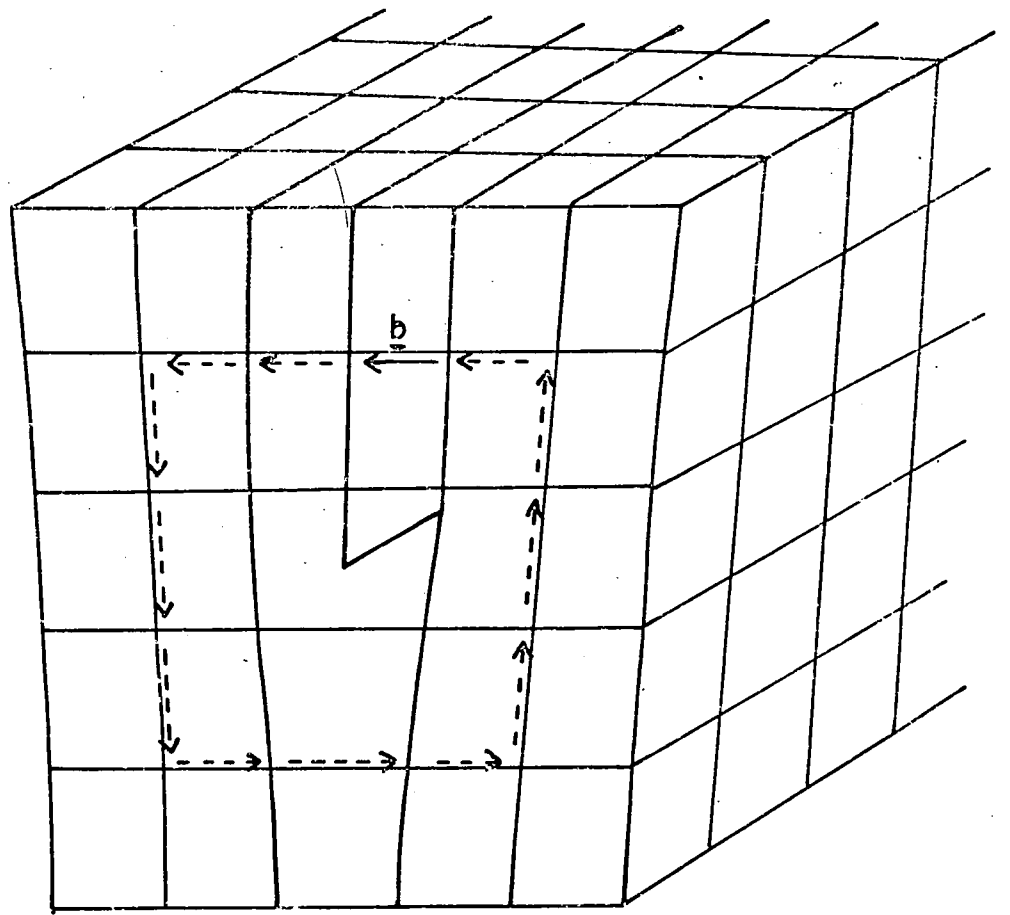


FIGURE 4.4 THE EDGE DISLOCATION

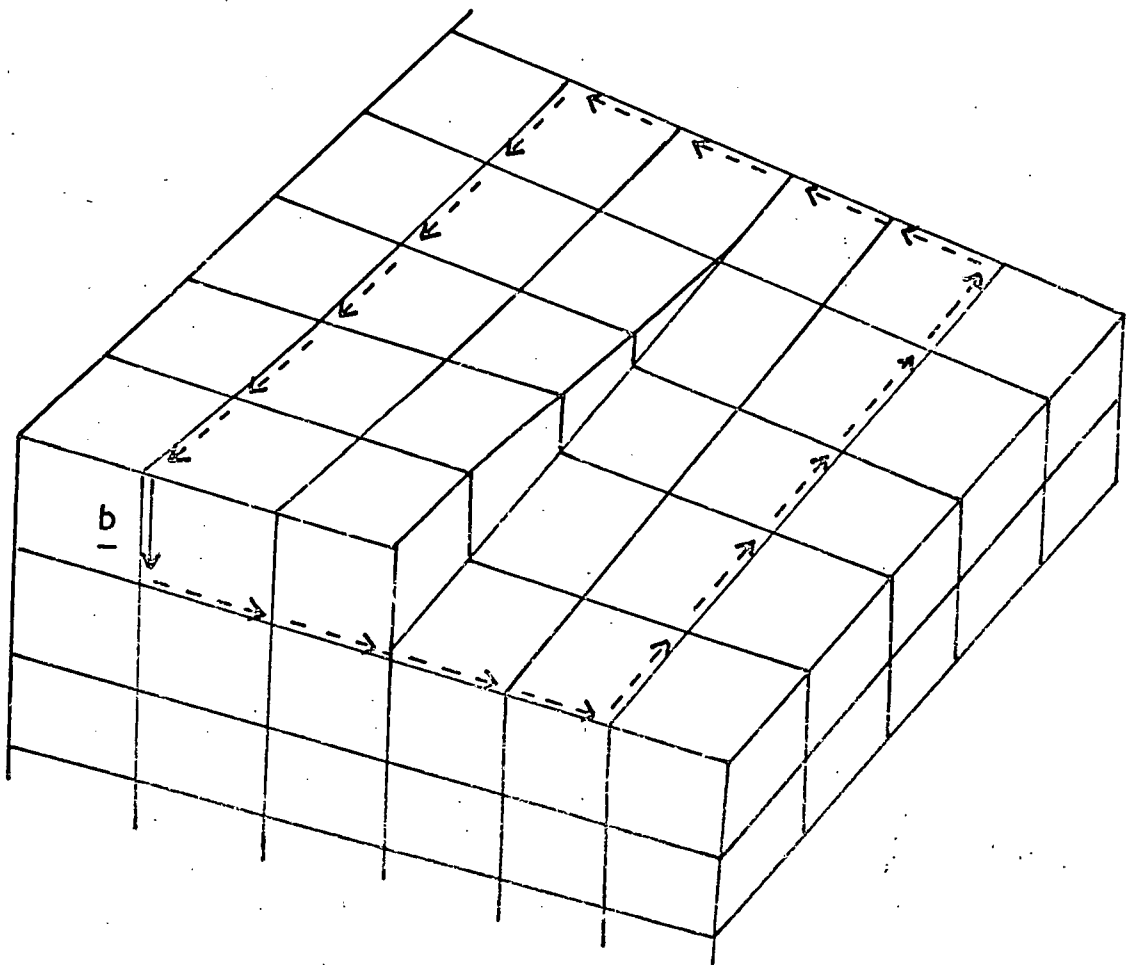


FIGURE 4.5 THE SCREW DISLOCATION

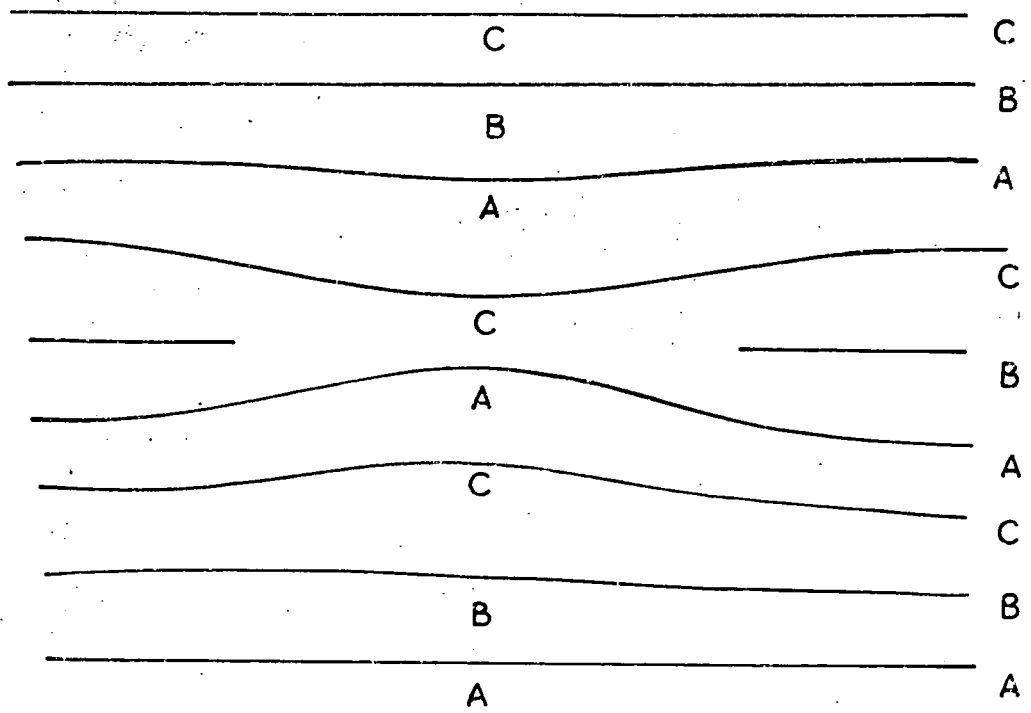


FIGURE 4.6 AN INTRINSIC STACKING FAULT

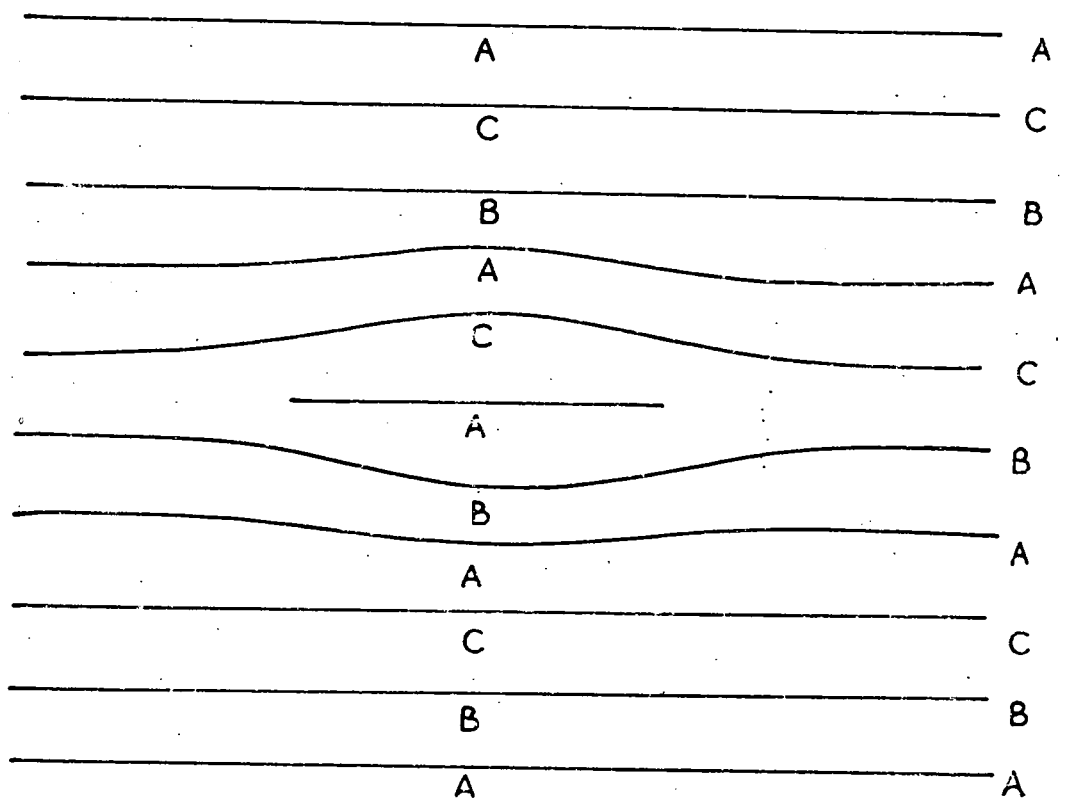


FIGURE 4.7 AN EXTRINSIC STACKING FAULT

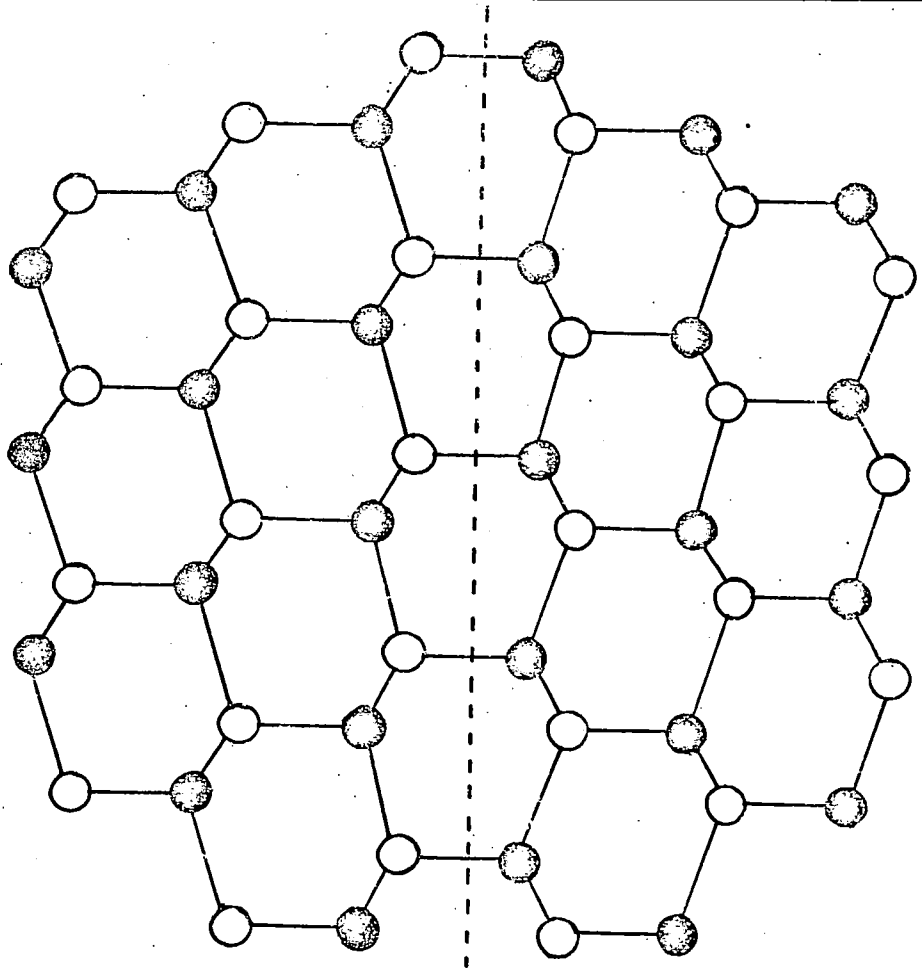


FIGURE 4.8 THE ORTHO-TWIN BOUNDARY

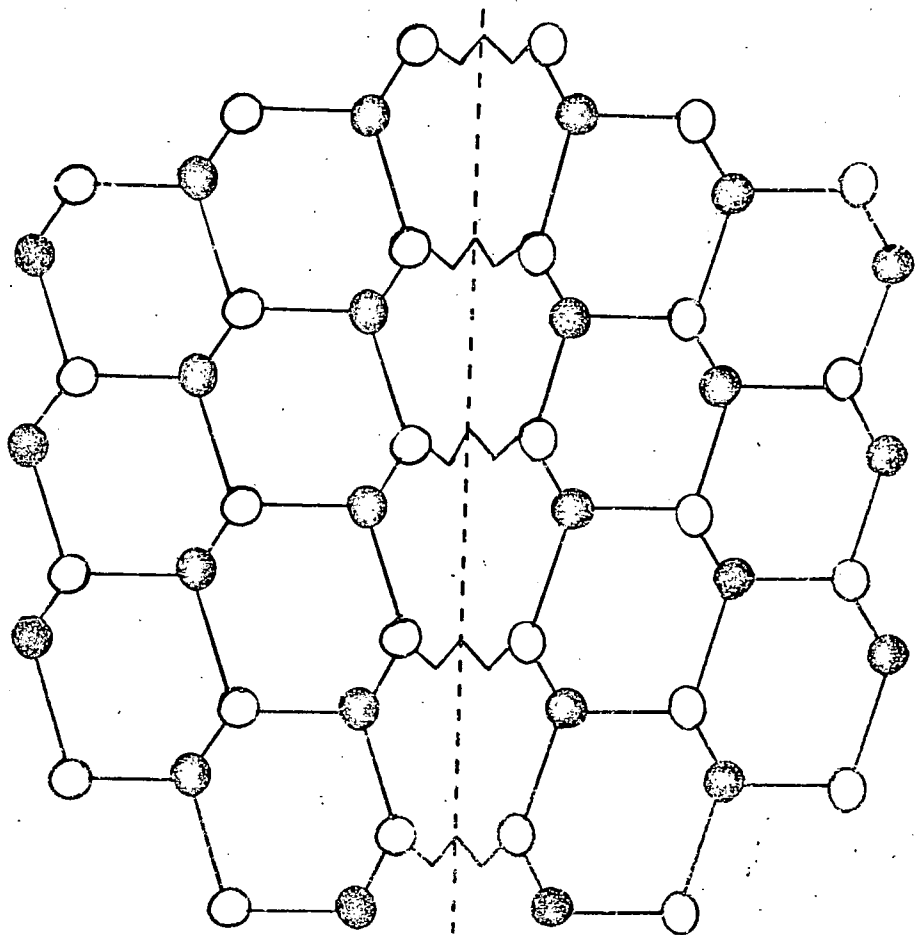


FIGURE 4.9 THE PARA-TWIN BOUNDARY

CHAPTER 5

AS GROWN MAGNESIUM OXIDE

5.1 INTRODUCTION

The impurity precipitates present in nominally pure MgO have been discussed by several workers. Particular interest has been concentrated on the precipitates which decorate as-grown dislocations, and which were first reported by Venables (1961) who later identified them as consisting of calcium stabilised zirconia using the techniques of X-ray and reflection electron diffraction (see Venables 1963). Much of this interest was stimulated by the fact that the abundance of these precipitates would suggest a much larger concentration of zirconium as an impurity in MgO than was found by spectrographic techniques (see for instance Bowen 1963, Henderson 1964) and neutron activation analysis (see for instance Venables 1963, Miles 1965). In fact calculations made by Venables (1963) showed, that if all of the precipitates observed by transmission electron microscopy (TEM) were of zirconia, it would be necessary for all of the zirconium atoms present to be concentrated in the observed precipitates, leaving none dispersed in solution in the MgO matrix. Another interesting feature of these precipitates which is recorded in some of the above cited literature is the crystallographic configurations in which they are found. In this chapter, observations which are in the main similar to those reported previously, but which include one unusual crystallographic arrangement of precipitates on as-grown dislocations, are discussed. These observations were made on as-grown Norton MgO using the techniques of TEM, extraction replication and reflection electron diffraction and microscopy (see Russell and Woods 1976).

## 5.2 SPECIMEN PREPARATION

### 5.2.1 Chemical Polishing

Cleaved flakes of material with dimensions of the order of  $1 \times 0.5 \times 0.02 \text{ cm}^3$  were coated around the edges with a thin layer of acid resistant paint. They were then supported by a corner clamped between two glass slides and were individually chemically thinned in phosphoric acid at about  $160^\circ\text{C}$ . The polishing depended quite critically on the maintenance of a continuous flow of acid over the surface of the specimens and, for this reason, samples were agitated quite vigorously throughout the process. When a specimen had been reduced to less than half of its initial thickness, it was removed from the polishing agent and washed, first in distilled water and then in methanol. After it had been dried under a tungsten lamp, the protective layer of paint was carefully removed from its edges using a pair of tweezers. The purpose of this step was twofold; firstly it was easier to remove the paint without damaging the specimen at this stage than it was when the thinning had been completed, and secondly, by removing the paint, the flow of the polishing agent around the sample edges in the final stages of thinning was less restricted. Next the specimen was remounted between the glass slides and polishing was continued.

The progress of the thinning was followed by observing light reflected from the crystal surface. Immediately a hole appeared in a specimen, polishing was discontinued and the sample was thoroughly rinsed, first in distilled water and then in methanol before being dried. Having produced one hole, it was often possible to increase the useful specimen area by partially re-immersing the sample in the polishing agent until another hole was formed in the vicinity of the first one.

After the final washing process, all specimens were examined under normal illumination in an optical microscope. Around the edges of holes, regions which were thin enough for examination by TEM were identified by the presence of interference fringes. A typical example is shown in Figure 5.1. Such regions were subsequently fractured from the crystal flake by applying pressure, at a distance from the hole, using the fine point of a pair of tweezers. Sections which were less than 3 mm in diameter, and which contained thin regions, were placed between two 100-mesh copper grids in the specimen holder of the electron microscope.

#### 5.2.2 Extraction Replicas

Flakes of material  $1 \times 1 \times 0.1 \text{ cm}^3$  in size were etched in phosphoric acid at about  $100^\circ\text{C}$ . This etching occurred when a specimen was not agitated and its effect was to leave precipitates on hillocks standing in relief on a crystal surface. The etched samples were washed carefully in distilled water, so as not to disturb the precipitates, and were then rinsed in methanol.

Extraction replicas of etched surfaces were prepared as follows. The etched specimens were placed in a vacuum coating unit and carbon was evaporated normally on to them to a thickness of about  $1000 \text{ \AA}$  in the manner described by Bradley (1965a). The carbon film was subsequently removed from the crystal surface by slowly immersing the specimen at a shallow angle, with the evaporated film uppermost, into phosphoric acid at about  $100^\circ\text{C}$ . In this way the acid was allowed gradually to dissolve the crystal at the carbon film/crystal interface and thereby release the carbon film together with the precipitates which stood in relief on the etched surface. The strength of the acid on which the carbon film was floating was then reduced to less than one tenth of its

initial concentration. This was achieved by removing most of it from its container using a pipette, while taking special care not to disturb the floating film, and then replenishing the container with distilled water. Electron microscope specimen grids were next dropped on to the carbon replicas to utilise the maximum possible area. Using the point of a pair of tweezers, the carbon film was broken around the rim of each grid thus separating each one from the rest of the film and from each other. The grids were then picked up individually by carefully immersing them in the diluted acid, inverting them to bring the replica uppermost on the grid and then lifting them free from the acid surface. Excess acid remaining on the replica and grid was removed by gently dripping water from a pipette and allowing it to flow over the surface of the sample. After the replicas had been dried on filter paper under a tungsten lamp, they were shadowed with gold in a coating unit. The shadowing angle was 15 degrees, and the process was carried out at a pressure less than  $10^{-4}$  torr. The purpose of this shadowing was two-fold. Firstly it provided information concerning the three dimensional morphology of precipitates and secondly, the diffraction patterns from the gold film could be used as a reference to give direct measurement of interplanar spacings for diffracted beams from extracted precipitates.

### 5.2.3 Surface Etching

While phosphoric acid is a chemical polish for MgO at temperatures between about 140 and 160°C, at lower temperatures it is an etch, particularly when samples are not agitated. However Bowen (1962) has shown that more extensive etching is produced by fuming nitric acid and the specimens for examination by the techniques of reflection electron microscopy and diffraction were prepared using this etchant. Cleaved

flakes of as-grown material with dimensions of  $0.3 \times 0.3 \times 0.02 \text{ cm}^3$  were etched for periods of up to ten minutes. They were then washed in distilled water and in methanol. After being dried, the samples were attached to specimen studs using colloidal graphite and were then ready for examination in the electron microscope.

### 5.3 OBSERVATIONS OF DEFECTS IN AS-GROWN MAGNESIUM OXIDE

#### 5.3.1 Damage Introduced by Specimen Handling

During the preparation of specimens minute fragments were frequently observed to have become detached from thin edges as can be seen at A in Figure 5.1. A cleavage crack associated with a similar fractured edge is shown in an electron micrograph in Figure 5.2. In this transmission micrograph, as in all others recording features of MgO samples in this work, unless stated to the contrary, a  $\{100\}$  plane was approximately perpendicular to the electron beam. This, together with the known  $\langle 110 \rangle \{1\bar{1}0\}$  slip system and  $\{100\}$  cleavage of MgO, makes the interpretation of dislocation images straightforward in comparison with metals. The dislocations situated beyond the end of the  $\{100\}$  cleavage crack in Figure 5.2 closely resemble those of screw character which lie on one of the planes designated as  $45^\circ$  planes by Washburn et al (1960). They are pinned at opposite surfaces of the foil and because of the known slip system they provide a direct means of measurement of specimen thickness.

In regions like that shown in Figure 5.2 another type of dislocation was commonly observed to have been introduced following specimen handling. An example is shown in Figure 5.3. From the observations that these dislocations were generally long compared with the thickness of the foil, and that they were in the main parallel to

cleavage cracks, it can be inferred that they were approximately in the plane of the foil and thus lay in a  $\langle 100 \rangle$  direction. Consequently their Burgers vectors, which must have a  $\langle 110 \rangle$  orientation, cannot be parallel to the dislocations themselves, and it follows that these dislocations are predominantly edge in character. In contrast to the behaviour of the screw dislocations which were pinned on opposite sides of the specimen and which were never observed to move during examination in the electron microscope, these dislocations were readily annealed out by electron beam heating. This annealing was such that one of the points where the dislocation intersected the specimen surface was observed to move discontinuously towards the other until the dislocation was completely removed. This observation indicated that each of the ends of these dislocations was pinned on the same side of the foil.

While Figures 5.2 and 5.3 show separate examples of screw and edge dislocations, it should be pointed out that in the region of cleavage cracks it was usual to observe a selection of both types. This is illustrated in Figure 5.4. Most of the screw dislocations in this area of the specimen, which is more severely damaged than that shown in Figure 5.2, intersect the foil surfaces in two lines which are parallel to the  $[100]$  direction, and which are situated at equal distances and on opposite sides of the cleavage crack. From this observation it is suggested that these dislocations lie in slip traces on either side of the cleavage crack. The fact that a few dislocations like that at A do not intersect the foil surface at the same distance from the cleavage crack as do the others is attributed to the climb of these dislocations out of the slip plane.

Finally in discussing damage introduced by specimen handling it should be noted that no dislocations lying in one of the  $\{110\}$

planes which are perpendicular to the plane of the foil have been observed. Such dislocations, either of edge or screw character would have Burgers vectors parallel to the plane of the foil. However it is considered that in preparing specimens for the electron microscope it would be likely that any component of applied stress resolved in this plane would be small compared with that resolved along one of the {110} planes which make an angle of  $45^{\circ}$  with the foil surface. Thus the absence of the dislocations just mentioned is not surprising.

### 5.3.2 Dislocations and Precipitates in As-Grown Material

In this electron microscope study of as-grown material, attention has been focussed on "grown-in" dislocations, and the precipitates which were observed to be distributed along their lengths. These precipitates were also occasionally observed as isolated particles but then they were usually found to be near other precipitates which were associated with dislocations. A similar observation has been made by Bowen (1963) who suggested that most, if not all, of the isolated precipitates must have been associated with grown-in dislocations before the material was chemically polished.

One of the two most common arrangements of precipitates encountered was that of a decorated "hairpin" dislocation, an example of which is shown in Figure 5.5. As reported by Miles (1965) this type of dislocation was always found to exhibit the orientation shown in the micrograph, that is, the loops of the hairpin were symmetrical about a  $\langle 100 \rangle$  direction. Another feature of these dislocations, which has not been discussed elsewhere, was that the loops were usually pinned by relatively large precipitates as in Figure 5.5. This might be due to pipe diffusion of impurity atoms along dislocations in the

presence of thermal gradients during crystal growth. In fact Morgan and Bowen (1967) suggested that pipe diffusion processes are more likely to be operative in ionic solids than in metals because of the larger size of dislocation cores in the former class of materials.

The second arrangement that was frequently observed involved straight dislocations. In general these were approximately parallel to either a  $\langle 100 \rangle$  or a  $\langle 110 \rangle$  direction in the plane of the foil, so that, for the reasons discussed in Section 5.3.1, they were mainly either edge or screw in character respectively. An example of the edge type is shown in Figure 5.6 and one of the screw type in Figure 5.7. It is possible that the straight edge dislocation is a section of a hairpin dislocation lying in a  $\{100\}$  plane perpendicular to the plane of the foil. The straight screw dislocation cannot be accounted for in the same way. It was also different from the edge type in that the precipitates decorating it were generally slightly smaller than those on the edge dislocations. This is in agreement with the observations of Bowen (1963), though the origin of this difference remains unknown.

Another configuration of precipitates in an as-grown sample is shown in Figure 5.8. Dislocation loops on  $\{110\}$  planes have been produced by annealing both cold worked (see Groves and Kelly 1962) and neutron irradiated MgO (see Groves and Kelly 1963, Bowen and Clarke 1964). However as far as the present writer is aware, Figure 5.8 is the only recorded example of the observation of similar dislocations decorated with precipitates in as-grown material. This makes this feature a rare observation considering the large quantity of work published on the topic of decorated dislocations in MgO. However, although it is not typical of as-grown MgO, its unusual nature justifies its inclusion here. The structure sensitivity of the precipitation

process is demonstrated by the approximately symmetrical location of the precipitates on the larger dislocation loop in Figure 5.8. Just as the precipitates formed at the  $\langle 100 \rangle$  extremities of the hairpin dislocation in the most favourable regions for precipitation, those in Figure 5.8 are situated at the  $\langle 100 \rangle$  extremities in the  $\langle 001 \rangle$  projection of the larger loop. These and all the other precipitates observed decorating grown-in dislocations are thought to have been formed as a result of the dislocations acting as sinks for migrating impurity atoms. However it is to be noted that in contrast to all other grown-in dislocations, which were probably produced by thermal stresses or by vacancy condensation during growth from the melt, the dislocation loops in Figure 5.8 appear to have arisen as a direct consequence of stress associated with the large precipitate at the centre of the loops. Narayan (1973) has attributed the formation of similar but smaller and undecorated loops in MgO to the presence of  $\text{MgAl}_2\text{O}_4$  precipitates. The material studied in the present work, although from a different source, contained a comparable concentration of aluminium impurity, i.e. about 150 p.p.m., which suggests that the dislocation loops in Figure 5.8 are probably similar in origin and nature to those observed by Narayan.

Not all of the precipitates were spherical in shape as might be inferred from the micrographs shown above. Some were rod like and lay along the length of dislocations as shown in Figure 5.9. These precipitates were usually much smaller than the spherical ones with lengths ranging from about 0.01 to 0.5  $\mu\text{m}$ . From the fact that their other dimensions were much smaller than this, it is probable that many similar ones were obscured by the contrast from dislocations. Bowen (1963) also pointed out that if the structure factors of the precipitates were such that electrons were diffracted less strongly than from

the MgO matrix then the precipitates would not be seen.

Another feature of the spherical precipitates (described incidentally by Venables (1961) as ball shaped) which was occasionally observed was their apparent transparency, as illustrated at A in Figure 5.9. This characteristic has been reported previously by Bowen and Clarke (1963) who attributed it to a diffraction contrast effect. Bowen (1963) subsequently found that the transparent areas increased in size during examination. He associated this effect with the diffusion of atoms from the particle as a result of electron beam heating of the specimen. However attempts to reproduce this effect in the present study have been unsuccessful. This may be due to a failure to repeat the experiment under the same conditions of specimen thickness and distance of the precipitates from the surface of the foil.

While the identity or presence of all the precipitates discussed above could not be revealed using the technique of selected area diffraction, fine structure effects were observed in the diffraction patterns from some as-grown samples. An example is shown in Figure 5.10 where it is seen that some of the diffraction spots are approximately square in shape. In fact, these spots are slightly extended in  $\langle 110 \rangle$  directions and it is suggested that their origin is associated with the presence of partially coherent precipitates which are not detected by transmission microscopy. The fact that the magnitude of the spot broadening increases with increasing deviation from an exact zone axis, as seen at A, is in agreement with this suggestion. Further, the presence of such precipitates in this material has been demonstrated by etching experiments, see Section 5.3.3. However it is emphasised that this diffraction effect was only

encountered on three occasions during the examination of a few dozen thinned samples.

Another similar diffraction effect was observed in selected area patterns taken from two overlapping crystals similar to those shown at B in the optical photomicrograph of Figure 5.1. This effect which is illustrated by the diffraction pattern in Figure 5.11 was readily reproducible. The magnitude of the spot broadening did not appear to depend on the angle between the two crystals, or on the size of the smaller section of crystal fractured from the edge of the sample. If diffraction patterns such as that in Figure 5.11 are regarded as two separate orthogonal matrices of spots, then reflections in only one of these matrices will exhibit the effect in question. Hence the effect is thought to be associated with double diffraction. One possible explanation is that the spatial distribution of intensity within the beams diffracted from the small section of crystal is a function of the dimensions of this section. Consequently, when these beams act as primary beams for the main crystal, a fine structure effect arising from the shape of the small section of crystal is produced in each of the doubly diffracted beams. The effect is almost certainly not related to the similar one which was observed occasionally when no overlapping of crystals was involved and which is illustrated in Figure 5.10. Finally it should perhaps be noted that the selected area diffraction aperture used was circular so that the observed effects were not associated with the electron optics.

### 5.3.3 Etching at Precipitate Sites

While phosphoric acid acts as a chemical polish for MgO within the temperature range 140 to 160°C, at temperatures below about 130°C,

it etches as-grown material at precipitate sites. This etching, which gives rise to pyramidal hillocks, was first associated with precipitate particles independently by Ghosh and Clarke (1961) and by Venables (1961). The correspondence between precipitates and hillocks was subsequently examined extensively by Bowen (1963) who discovered that fuming nitric acid produced a greater surface density of etch hillocks than phosphoric acid (see Bowen 1962). A detailed investigation of this etching was not pursued in the present study but examples showing characteristics of the pyramidal hillocks observed by transmission and reflection electron microscopy are recorded.

In transmission, etch hillocks usually appeared as regions of darker contrast than the background because of higher absorption. This is shown in Figure 5.12 which is an example of a specimen etched by phosphoric acid. However when the orientation of this region was changed so that an extinction contour passed close to the hillocks, thickness fringe contrast was exhibited by the hillocks, see Figure 5.13. While it can be inferred from Figure 5.12 that the etch features were hillocks and not pits because of their enhanced electron absorption, more conclusive evidence for this suggestion is provided by Figure 5.14 which shows an etch feature at the edge of a thin specimen. An important feature is that there are small regions of dark contrast in the middle of the images of the etch hillocks in Figures 5.13 and 5.14 which are believed to be associated with precipitates.

Comparison of the sizes of the hillocks in Figures 5.13 and 5.14 raises the question discussed by Bowen (1963) as to whether the size of a pyramid be taken as an indication of the size of the precipitate that nucleated it. Bowen concluded that there was such a correlation but the problem was complicated by the fact that the pyramid size

was also a function of the distance of the precipitate from the surface of the sample being etched. The correlation was thus only significant when comparing size distributions of pyramids from two or more different specimens etched under identical conditions.

Another characteristic of etch hillocks which is apparent in Figures 5.13 and 5.14 is the  $\langle 110 \rangle$  orientation of their bases. This aspect has also been investigated by Bowen (1963) who concluded, from measurements made on pyramids cleaved through a diagonal, that their faces lay close to  $\{111\}$  planes.

Pyramidal hillocks produced by etching MgO in fuming nitric acid are shown in the reflection electron micrograph in Figure 5.15. This image was obtained using the technique first employed by Halliday and Newman (1960) in which diffracted rather than scattered electrons are used to form an image. The procedure involved taking a dark field image from a low index spot in a reflection electron diffraction pattern. By comparing Figure 5.15 with the transmission micrographs of samples etched with phosphoric acid, it is obvious that a much larger surface density of hillocks was obtained when fuming nitric acid was employed as an etchant. Bowen (1963) attributed this difference to the greater reactivity of fuming nitric acid with the large number of different impurity ions in MgO.

#### 5.3.4 Identification of Precipitates

As mentioned in Section 5.3.2, attempts to identify precipitates in as-grown material using selected area diffraction were unsuccessful. In order to overcome this difficulty, the two different diffraction techniques employed by Venables (1963) and by Bowen (1970, private communication) in the study of this material have been investigated.

The techniques were those of:-

- (i) reflection electron diffraction from bulk specimens, and
- (ii) selected area diffraction from extraction replicas.

It was shown in Section 5.3.3 that the effect of etching was to produce an array of precipitates standing in relief on a crystal surface. Such an array is ideally suited to examination by the technique of reflection electron diffraction because an electron beam can be diffracted by a relatively large number of precipitates without having to penetrate the parent material. The experiment was performed using a reflection electron diffraction attachment. This was located below the projector lens with the result that the lens system could only be used to control the illumination of the specimen and the camera length could only be changed by varying the accelerating voltage.

A typical reflection electron diffraction pattern from an MgO sample which had been etched for five minutes in fresh fuming nitric acid is shown in Figure 5.16. The specimen was approximately in a  $\langle 100 \rangle$  orientation and the diffraction pattern exhibits two main features. Firstly, several of the matrix reflections show a form of "streaking" in  $\langle 110 \rangle$  directions and secondly a few extra reflections of low intensity are present. The streaking effect consists of intensity maxima situated around the positions of the matrix spots. The diffraction arises of course from a surface containing a large number of small hillocks, like those shown earlier in Figure 5.15. Furthermore, Bowen (1963) has shown that the four elevated faces of these etch features lie close to  $\{111\}$  planes. Diffracting centres with this geometry would give rise to intensity spikes through reciprocal lattice points in directions perpendicular to the facets. It is suggested that the pairs of spikes on that side of the matrix reflection which is closer to the specimen

surface are more prominent than the pairs on the other side because of an asymmetrical intensity distribution along these spikes. This is attributed to the fact that each hillock is bounded by the same set of four {111} planes. Hillocks bounded by the other set of four {111} planes only occur on the opposite surface of the sample which is not exposed to the electron beam. Thus asymmetry in the intensity distribution of spikes through reciprocal lattice points would occur about the plane of the specimen surface.

The other important feature of the diffraction pattern in Figure 5.16 is the set of extra reflections, one of which can be seen at A. These are of low intensity relative to those of the parent matrix and were always observed to form a square array. Hence it was concluded that they arose from a precipitate of cubic rather than tetragonal structure. Further it can be inferred from the positions of the precipitate reflections that the cube edges of the precipitate material lay parallel to those of the parent matrix. The MgO reflections were used to determine the camera constant from which the lattice parameter of the precipitate material was found to be 5.12 Å. Similar precipitate material was observed by Venables (1963) who reported a lattice parameter of 5.14 Å. Venables showed that only three of the known impurities in MgO could be identified as having this value of lattice parameter. These were SiO ( $a_0 = 5.16 \text{ \AA}$ ), SrO ( $a_0 = 5.14 \text{ \AA}$ ) and ZrO<sub>2</sub> ( $a_0 = 5.07 \text{ \AA}$ ). The fact that each of these materials has a different crystal structure enabled Venables to make an unambiguous identification of the precipitates. He did this by stripping a sufficiently large number of them from etched MgO surfaces using support films, to allow an x-ray powder photograph to be taken. The relative intensities of the diffraction rings obtained showed that

the precipitate material had the fluorite structure and it was consequently identified as  $ZrO_2$ . However Venables considered that the difference between his measured and the reported values of the lattice parameter was too large to be attributable to experimental error. This he explained in the following way. The presence of certain impurities in  $ZrO_2$  can produce a wide variation in its lattice parameter. For instance Duwez et al (1952) showed that the introduction of 30 mole % of CaO increased the lattice parameter to nearly  $5.15 \text{ \AA}$  and that the introduction of a similar amount of MgO decreased it to about  $5.065 \text{ \AA}$ . From this Venables concluded that the  $ZrO_2$  precipitates in as-grown MgO contained a relatively large proportion of the calcium impurity atoms also in the host crystal. He thus identified the precipitates as calcium stabilised  $ZrO_2$ . Since there is no evidence in the present work to conflict with this reasoning, it is concluded that the precipitate reflections seen in Figure 5.16 also arise from calcium stabilised  $ZrO_2$ .

Finally in discussing Figure 5.16 there remains one diffraction spot of low intensity at B, which still needs to be explained. Measurements suggest that it arises from a double diffraction effect between the parent and precipitate materials. The (002) matrix reflection probably acts as a primary beam which undergoes diffraction at the precipitate material to give rise to this extra reflection.

As well as being convenient for reflection electron diffraction investigations, the precipitates standing in relief on etched surfaces of as-grown MgO were equally suited to examination by the method of extraction replication. Using this technique it is possible to obtain diffraction patterns from small particles, the diffraction effects of which are normally completely masked by those of the parent material,

when the latter is examined by TEM (see for example Hale and Batson 1965). A few observations of precipitates on extraction replicas are recorded to complete this study of as-grown material.

A feature which was frequently seen in extraction replicas prepared by the method described in Section 5.2.2 is shown in Figure 5.17. This linear array of particles probably marks the site of a straight dislocation similar to those observed in transmission microscopy of bulk material (see Figure 5.9). As the extraction replica was taken from a {100} surface, this suggestion is consistent with the observation that many grown-in dislocations were approximately parallel to  $\langle 100 \rangle$  directions (see Section 5.3.2).

In contrast to the unsuccessful attempts to obtain electron diffraction effects from precipitates in bulk specimens, diffraction patterns were observed with these extraction precipitates as shown in Figure 5.18. The diffraction rings arise from polycrystalline gold which was employed as a shadowing material. Using these as a standard for calibration of the camera length of the microscope, the three different inter-planar spacings associated with the diffraction spots were found to be 2.91, 1.81 and 1.55 Å. The ratios of these spacings suggest that the crystal system of the precipitate material is cubic. Thus the single lattice parameter ( $a_0$ ) can be calculated and was found to be 5.12 Å. This identifies the rod shaped precipitates with the calcium stabilised  $ZrO_2$  detected by reflection electron diffraction.

While the long axes of most of these thin platelet particles were straight, a few exhibited the morphology shown in Figure 5.19. This particle is similar in appearance to the precipitate at C in Figure 2 of the paper by Venables 1963. The latter was extracted

from a zirconium doped MgO sample and was thought to be one of the larger precipitates pinning grown-in dislocations. It is suggested that the particle in Figure 5.19 is of similar origin and that its form is directly related to both the orientation of the dislocation with which it had previously been associated and the crystal structure of MgO. In fact a precipitate of similar morphology is thought to be present at B on the dislocation in Figure 5.9.

In addition to these platelet shaped precipitates, others with a spherical form as shown in Figure 5.20 were observed in extraction replicas. These resembled the ball shaped precipitates observed in TEM of bulk material. However unlike the platelet ones, these did not give rise to any diffraction effects even when extracted from the parent material. Consequently they remain unidentified and, in contrast with the view expressed by Venables (1963), no evidence has been found here to identify the ball precipitates as calcium stabilised  $ZrO_2$ .

The extracted ball precipitates did however exhibit the following two interesting characteristics. Firstly, while they appeared in general as dark images on the screen of the microscope, parts of them were observed to be light. This feature can be seen in Figure 5.20 which is a negative print necessary to demonstrate the effect of shadowing (see for instance Bradley 1965b), and this exhibits reverse contrast to that on the screen. It will be recalled that a similar effect was observed in ball precipitates when they were examined in bulk material (see Section 5.3.2). Secondly the precipitates showed a tendency to aggregate into clusters as demonstrated in Figure 5.21. This feature has been observed independently by Bowen (1970, private communication). The clusters were probably formed during the washing process before the carbon film was evaporated on to the crystal

surface. It is expected that the origin of the clustering is associated with closely spaced spherical precipitates on a dislocation lying parallel to the etched surface of the MgO.

#### 5.4 SUMMARY

Two types of precipitate have been observed in as-grown MgO. One was platelet shaped and has been identified by electron diffraction as consisting of calcium stabilised  $ZrO_2$ . Using reflection electron diffraction it has been shown that these precipitates exhibit an orientational relationship with respect to the parent material as observed by Venables (1963). The second precipitate was spherical in appearance and remains unidentified because no diffraction effects were observed. In fact Bowen (1963) was unable to identify these precipitates by electron probe microanalysis due to their small size. Thus it is concluded that, while the topic of impurity precipitates in MgO has been extensively studied since the original observation of "ball and chain" precipitates by Venables (1961), the literature still lacks a conclusive identification of ball shaped precipitates.

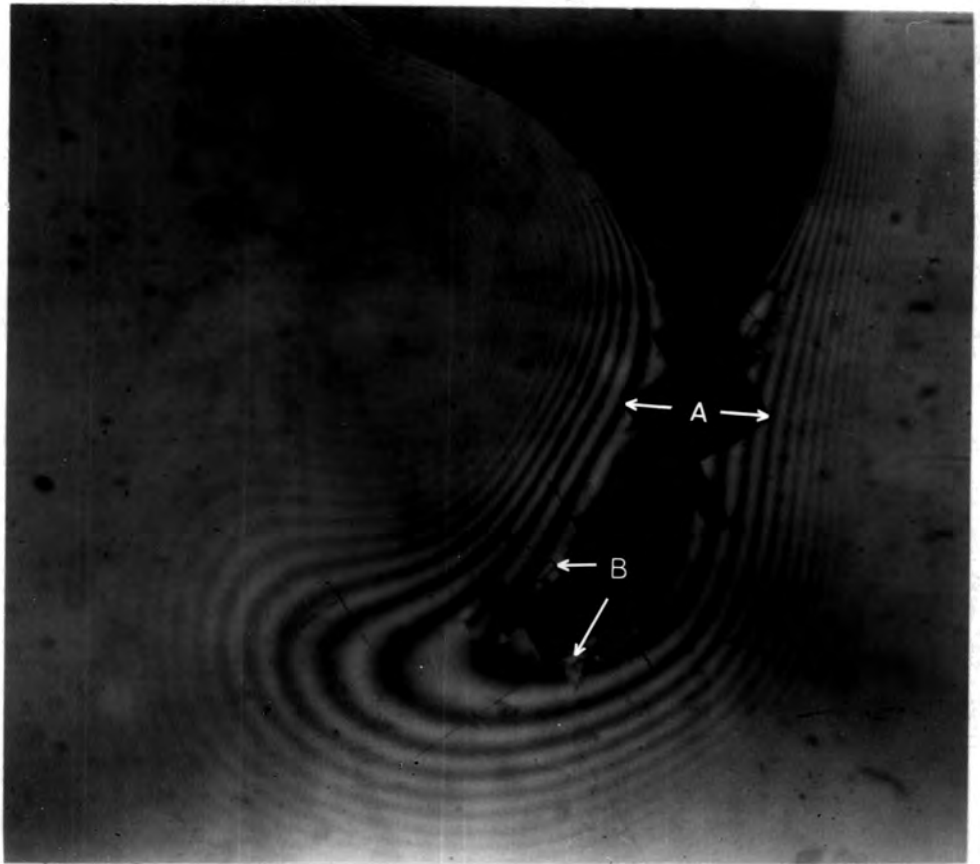


Figure 5.1: Photomicrograph of thinned MgO showing interference fringes x 200

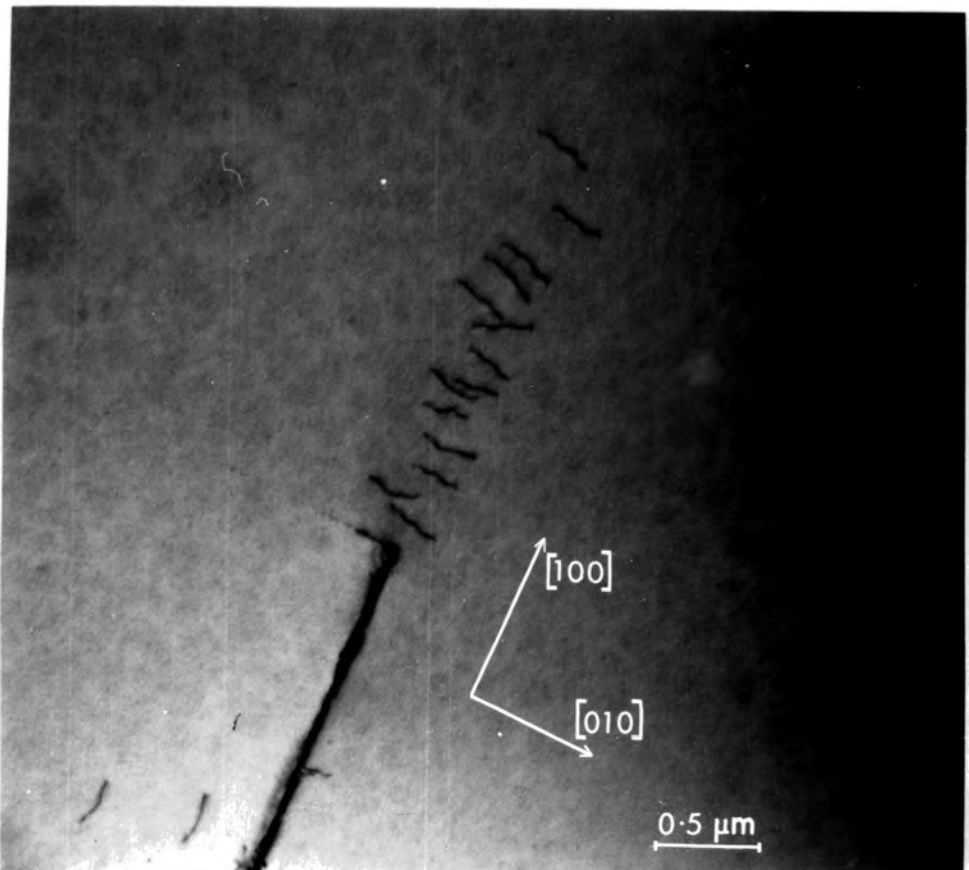


Figure 5.2: Dislocations at the end of a cleavage crack

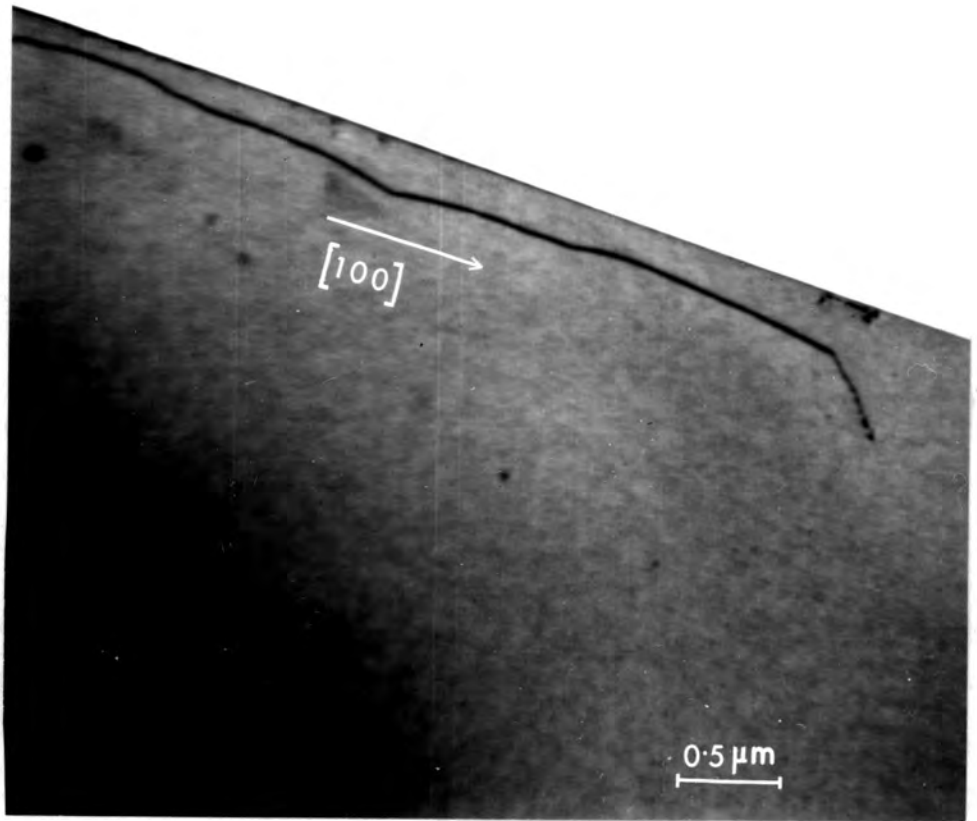


Figure 5.3: An edge dislocation lying parallel to a fractured edge of a specimen

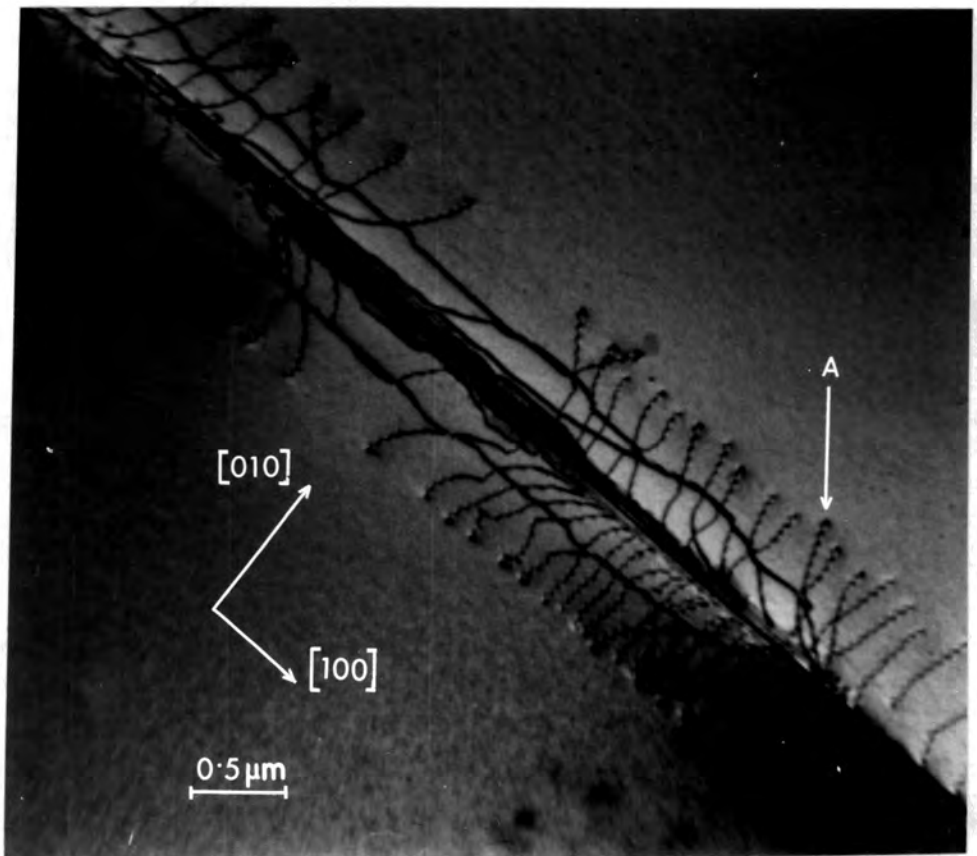


Figure 5.4: A cleavage crack showing edge and screw dislocations

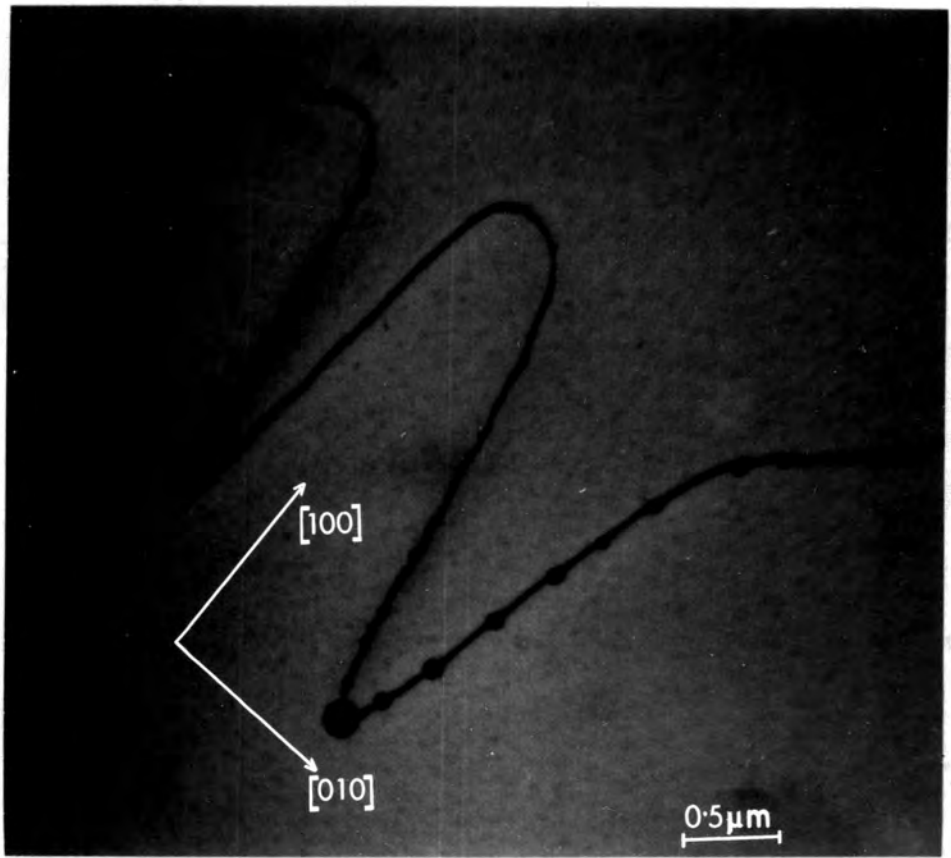


Figure 5.5: A 'hairpin' dislocation decorated with precipitates

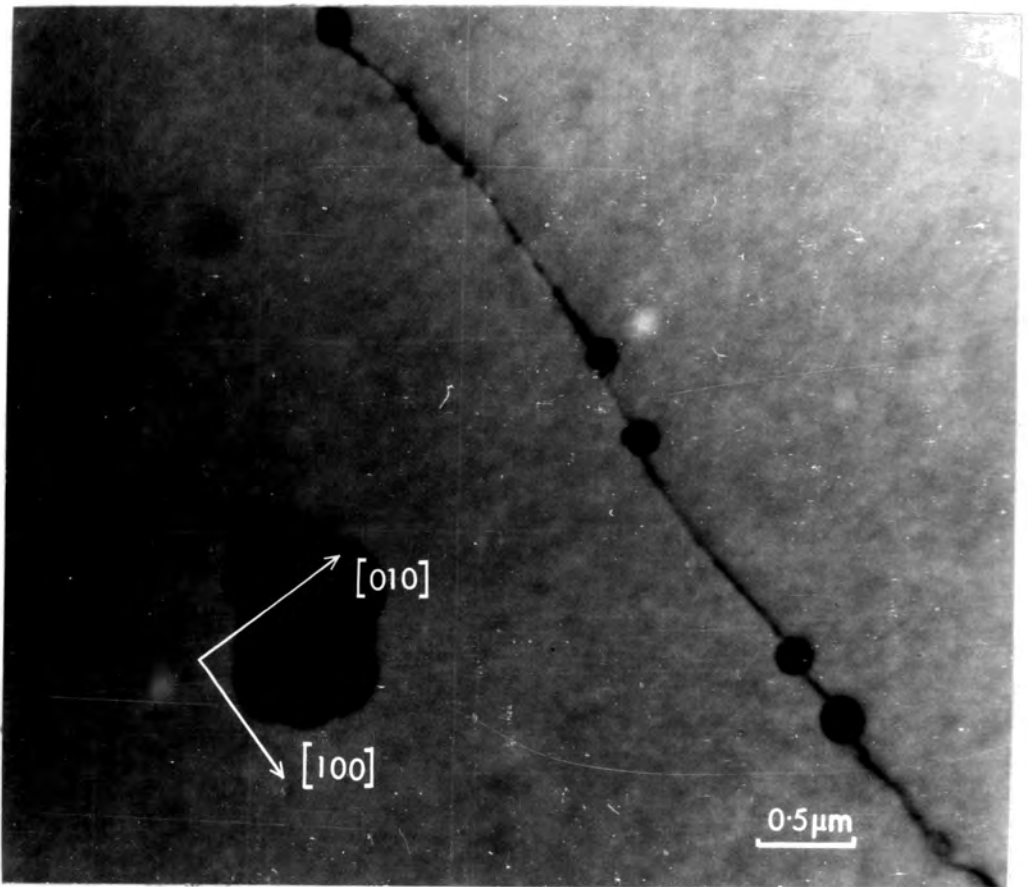


Figure 5.6: A straight dislocation of edge character

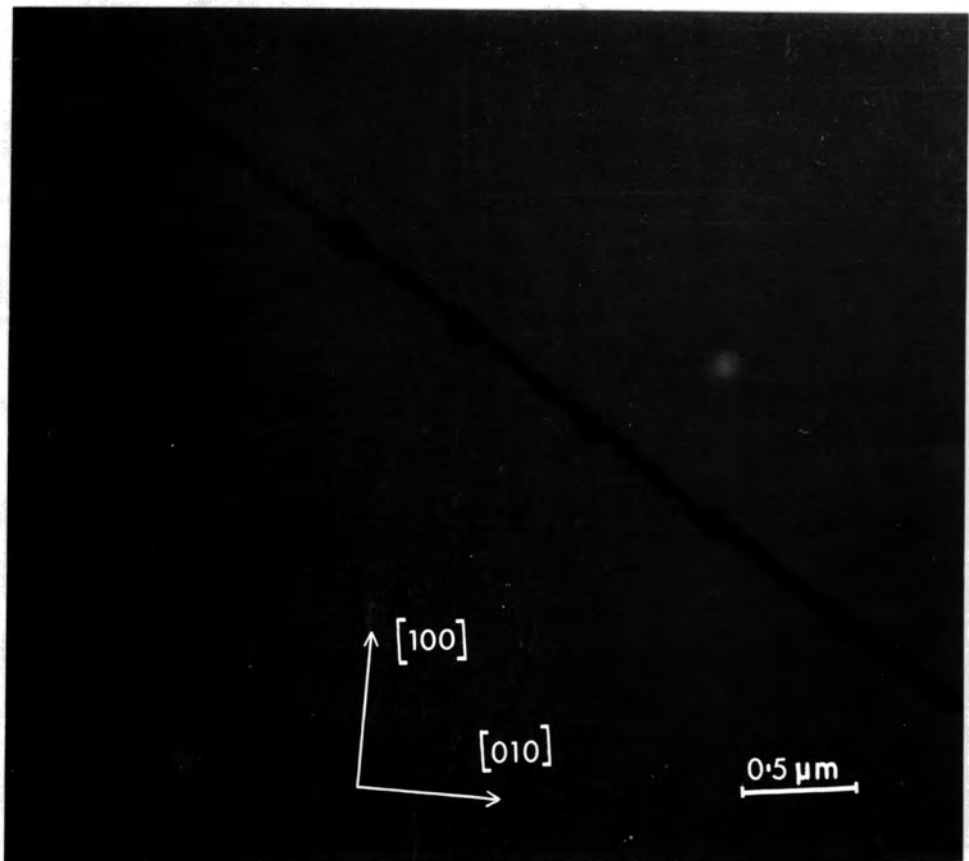


Figure 5.7: A straight dislocation of screw character

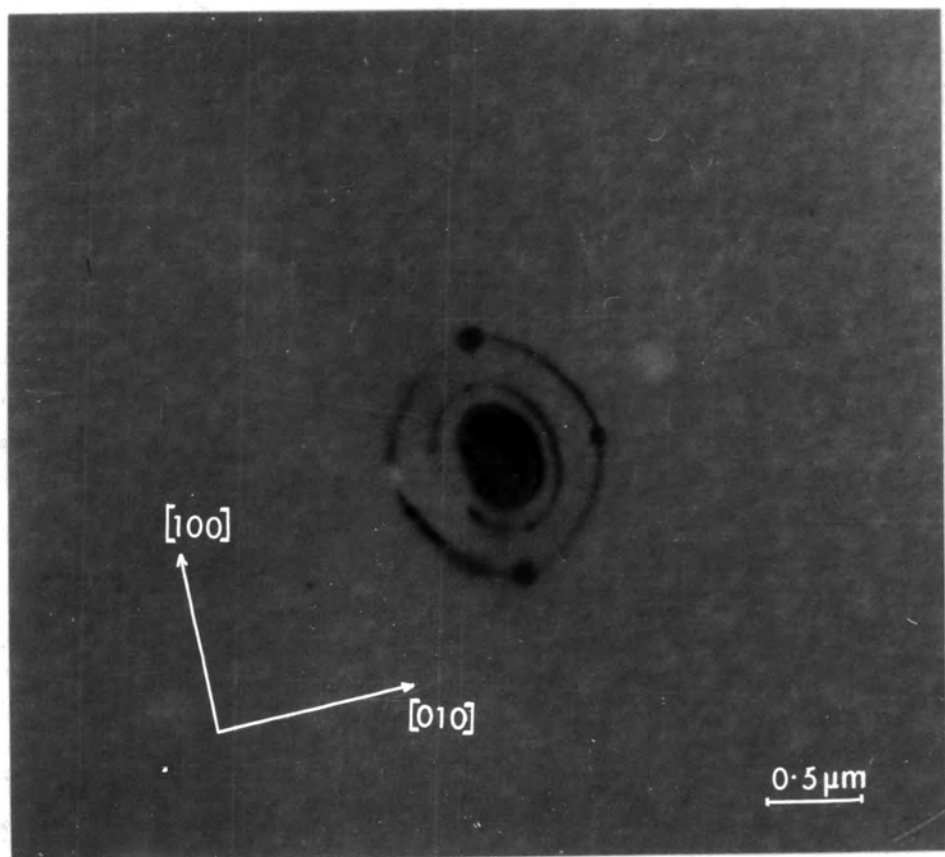


Figure 5.8: Dislocation loops decorated with precipitates

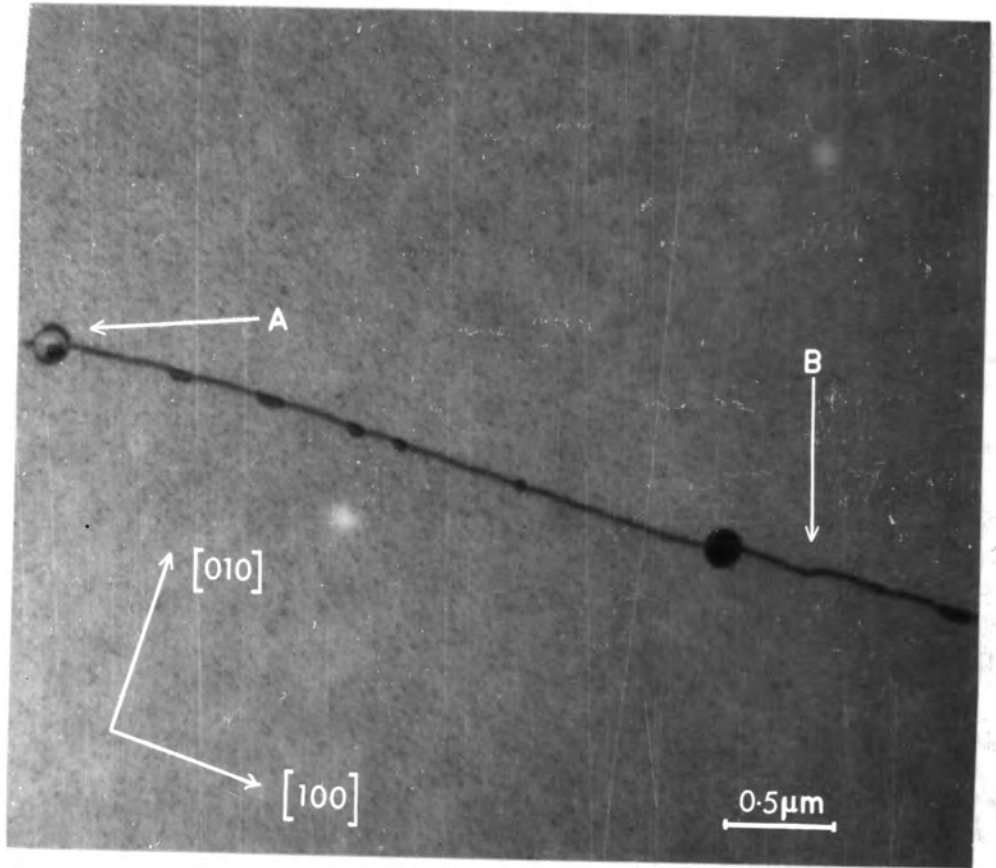


Figure 5.9: A precipitate at A exhibiting an unusual contrast effect

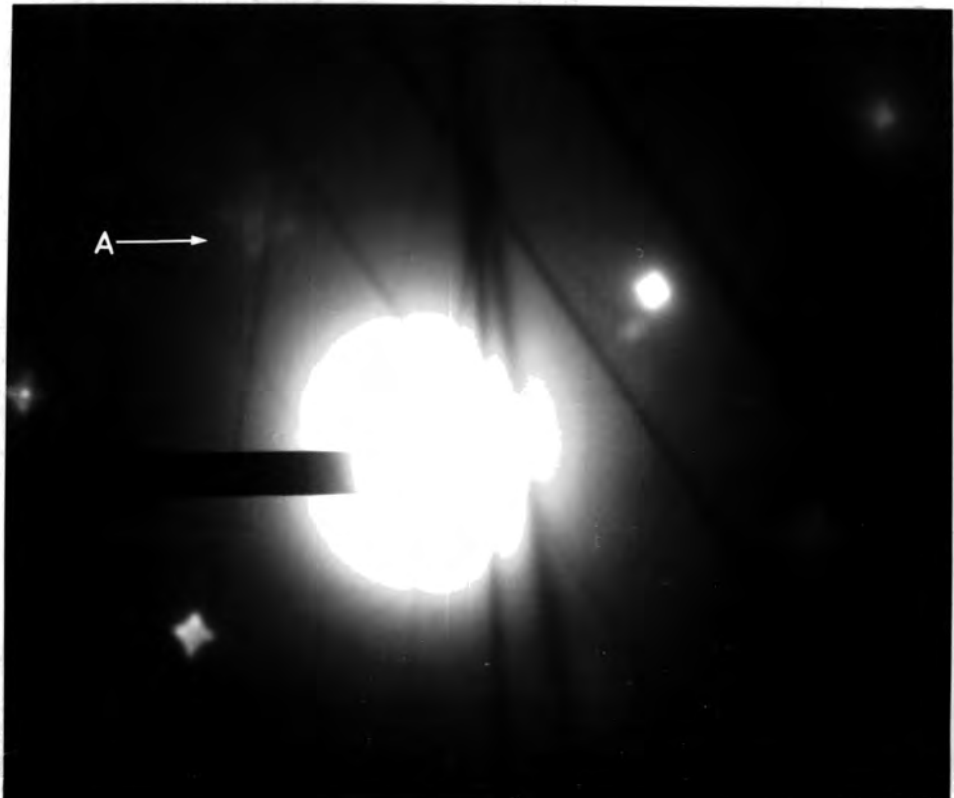


Figure 5.10: A  $\langle 100 \rangle$  diffraction pattern containing spots showing 'fine structure'.

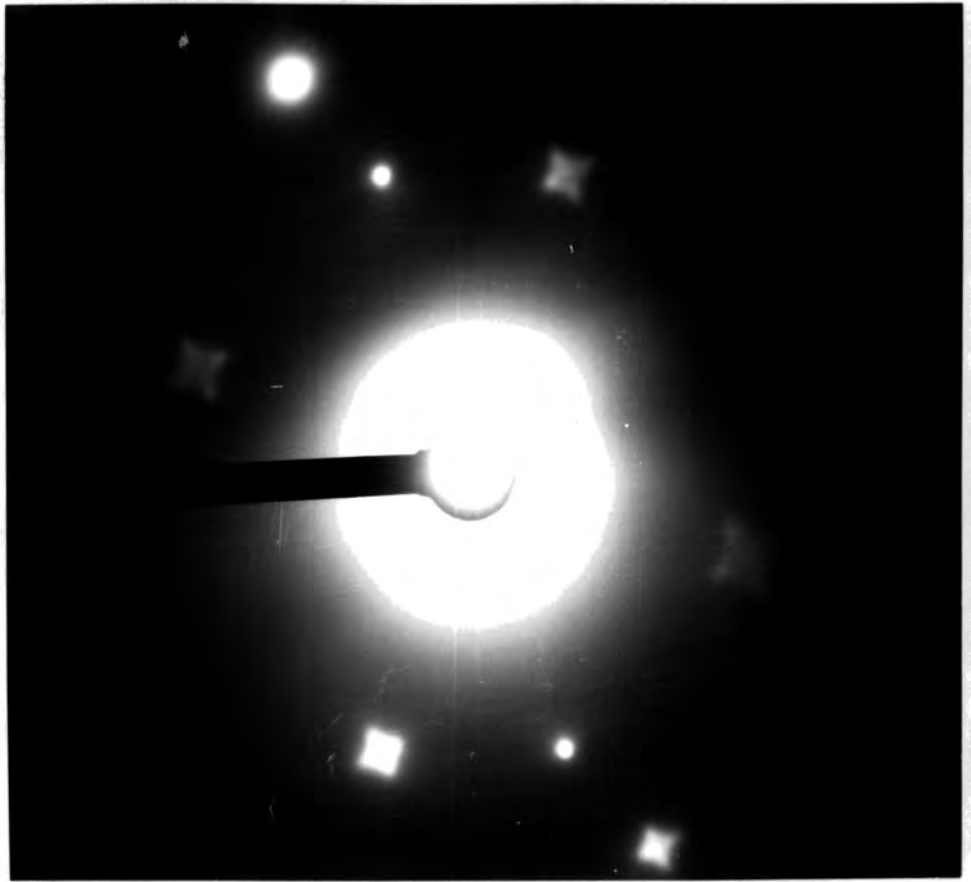


Figure 5.11: Diffraction from two overlapping crystals

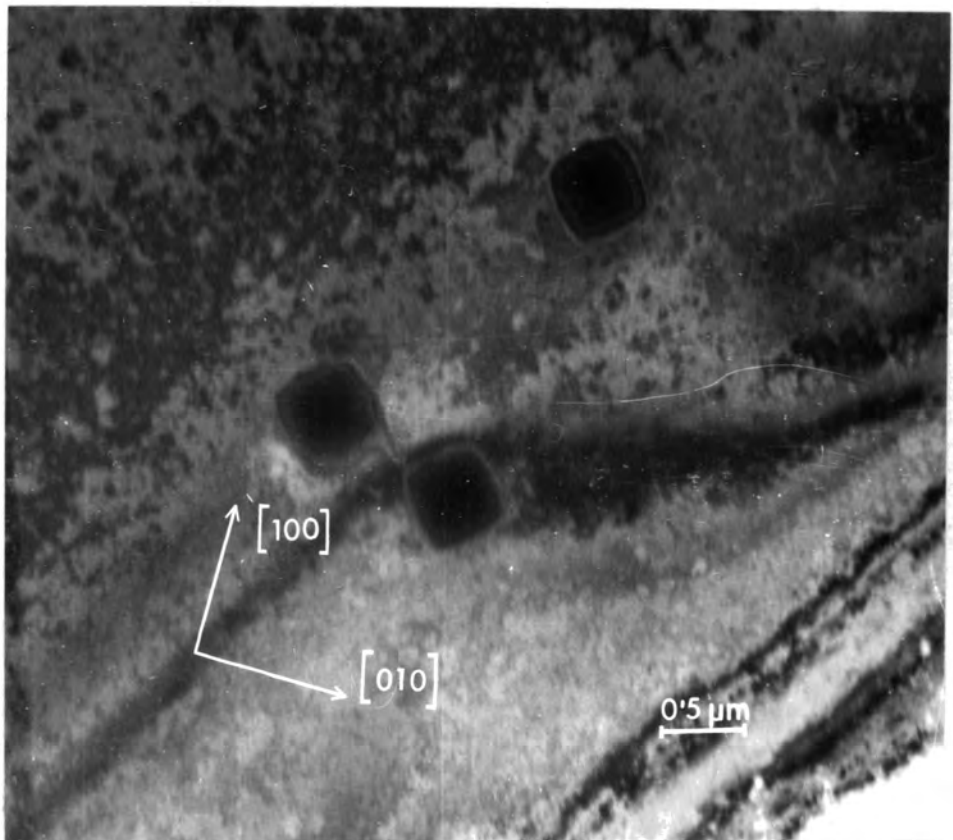
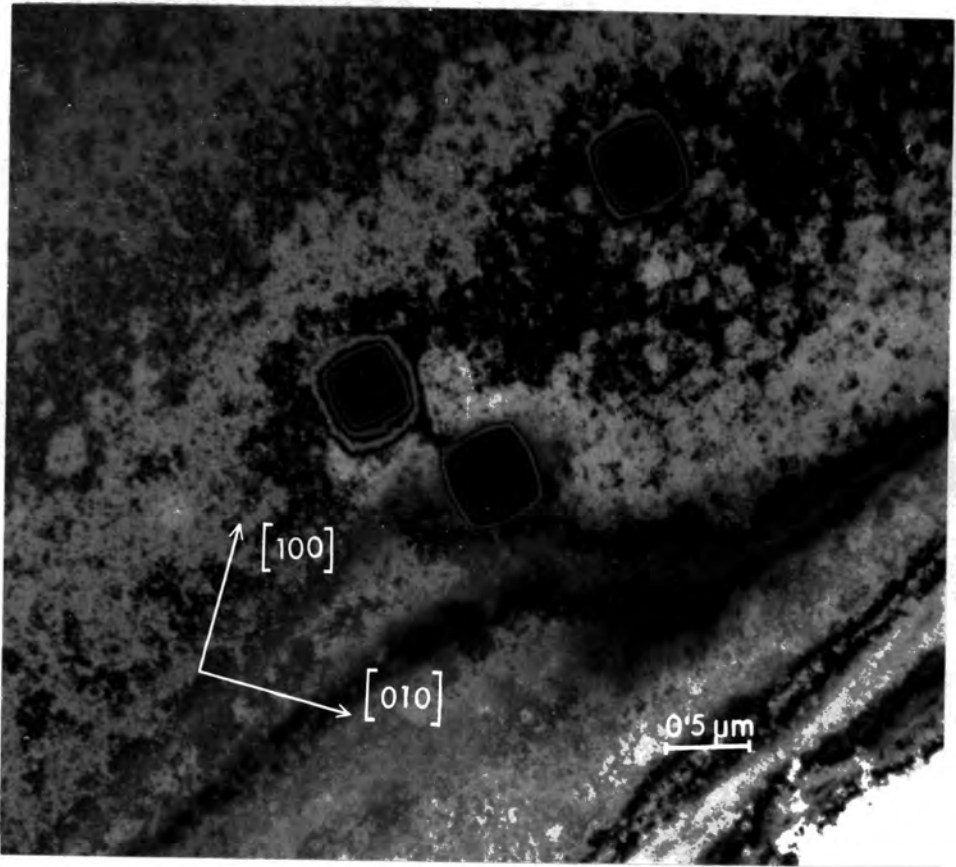
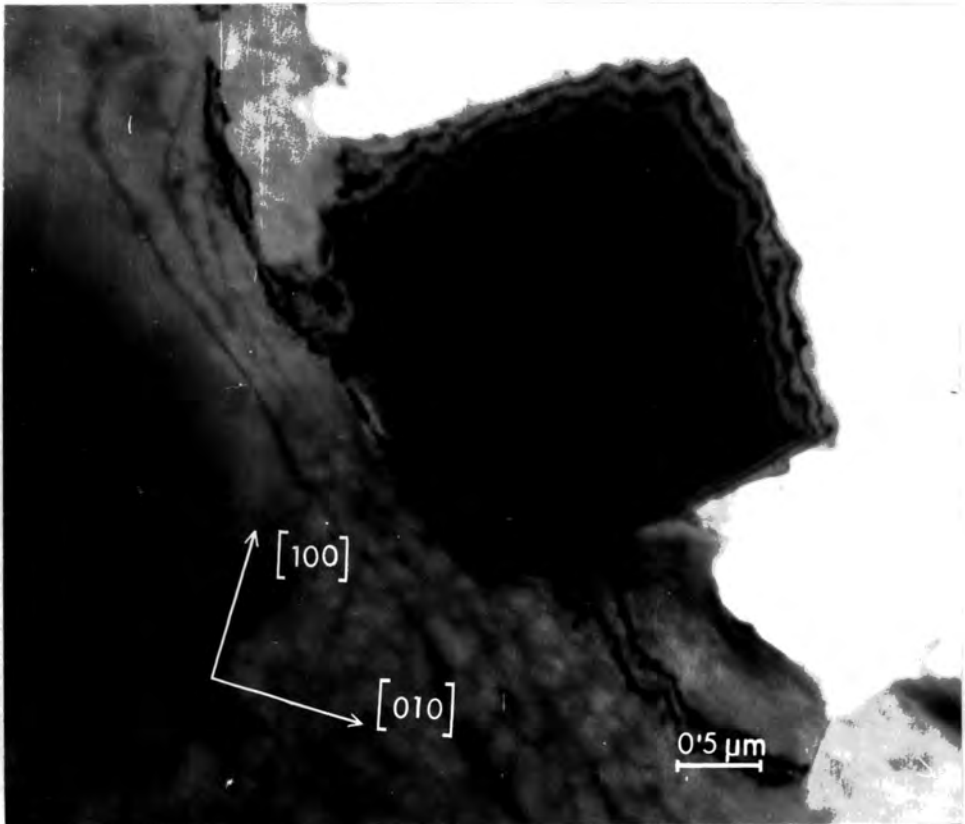


Figure 5.12: Etch hillocks revealed by absorption contrast



**Figure 5.13:** The same hillocks as in Figure 5.12 exhibiting diffraction contrast



**Figure 5.14:** An etch hillock at the edge of a thin specimen

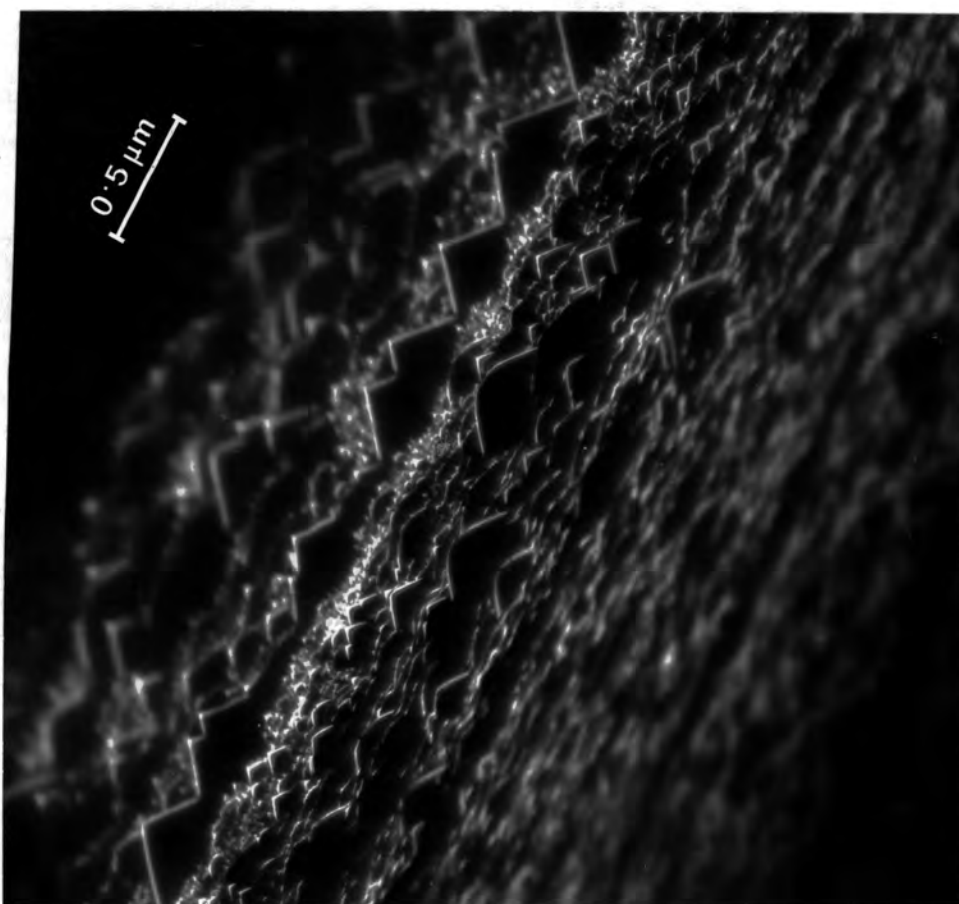


Figure 5.15: Reflection electron micrograph showing pyramidal etch hillocks

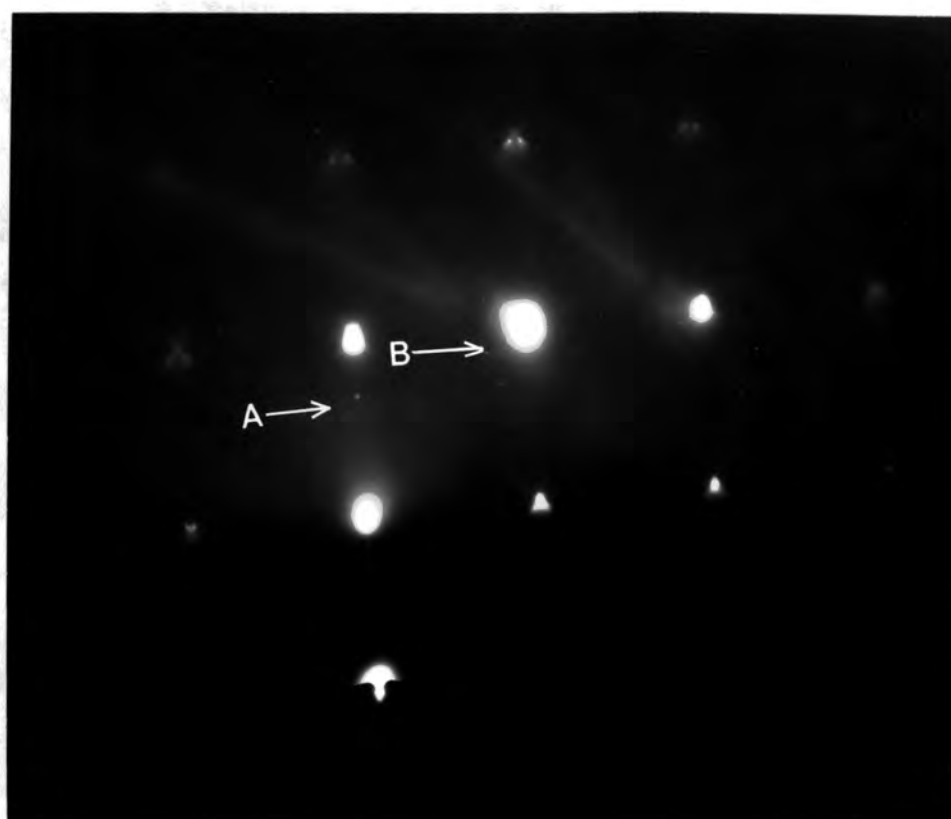


Figure 5.16: Reflection electron diffraction pattern taken from the region shown in Figure 5.15

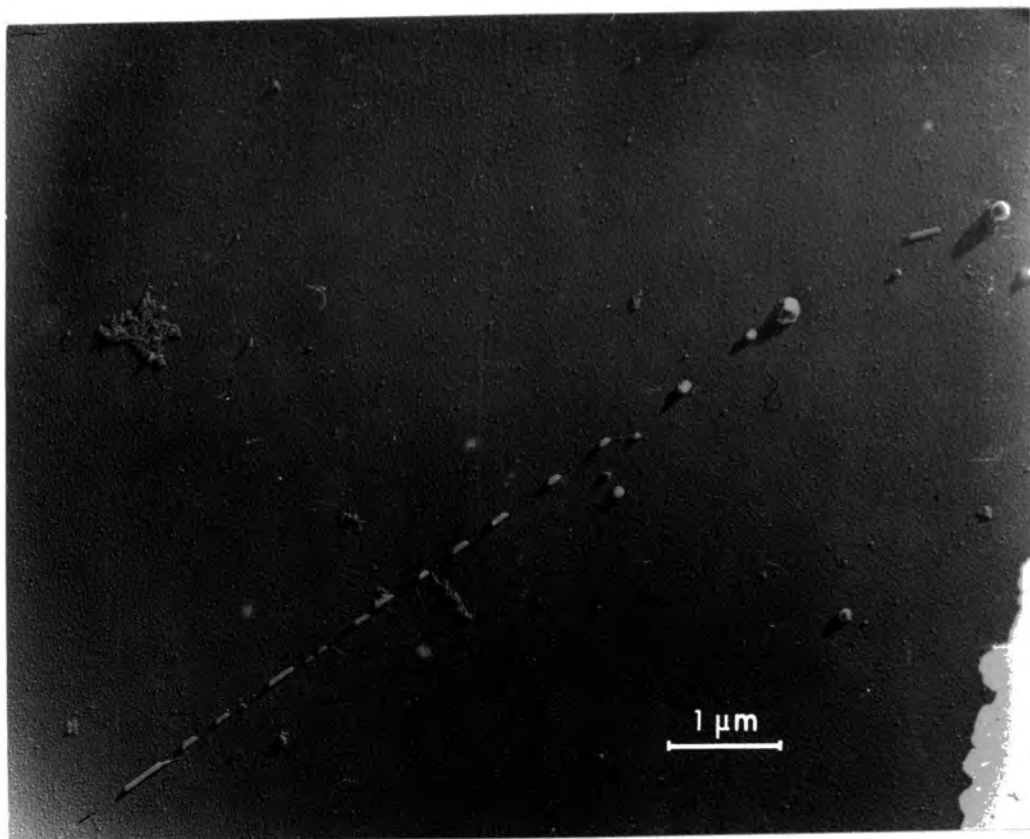


Figure 5.17: A shadowed extraction replica showing a linear array of precipitates

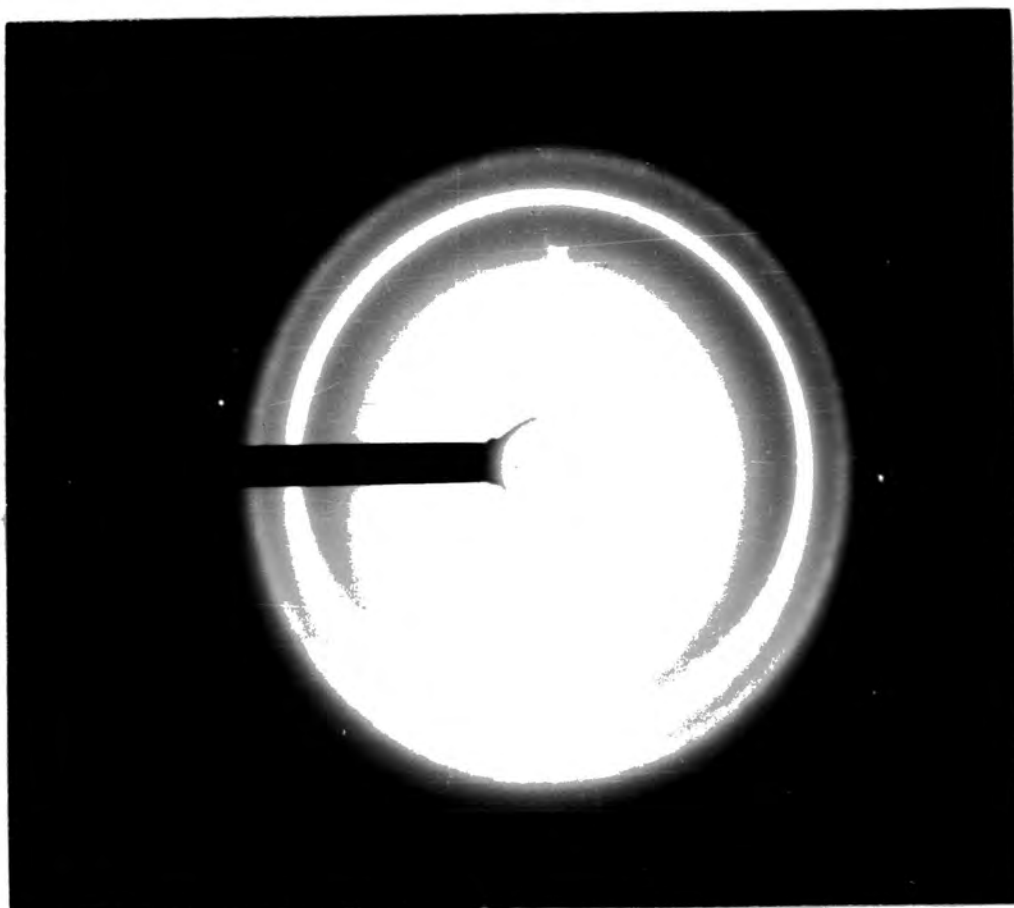


Figure 5.18: A diffraction pattern from extracted platelet shaped precipitates

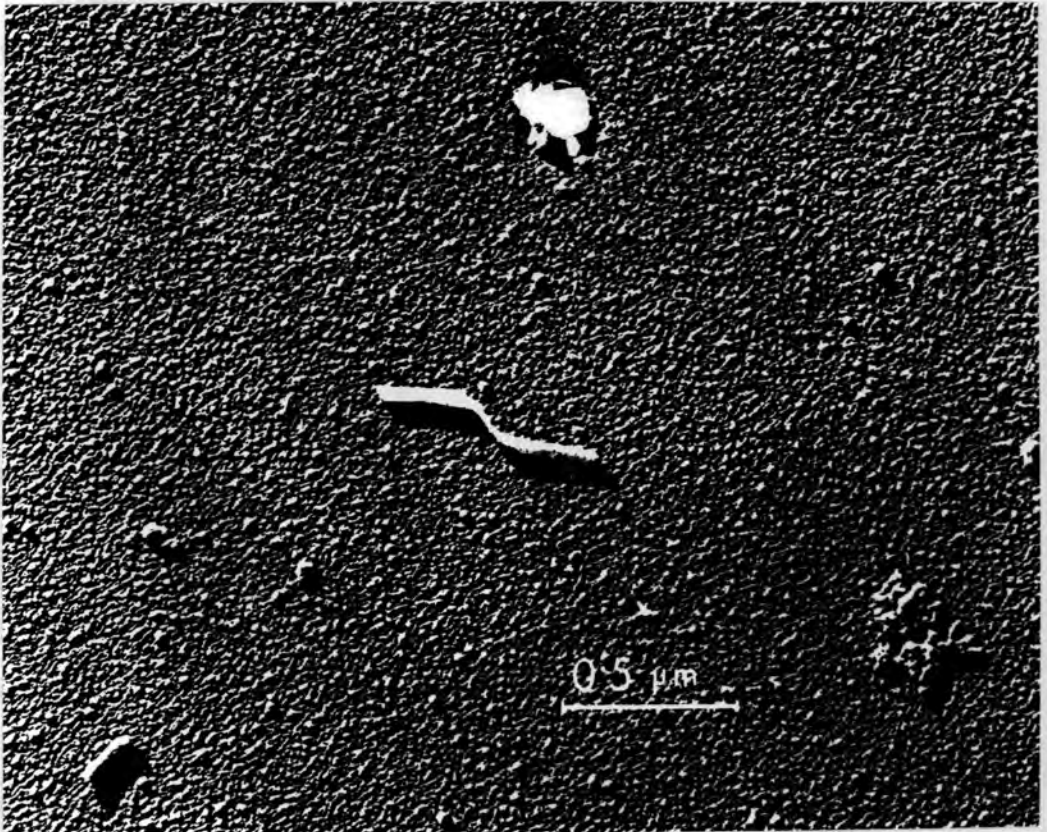


Figure 5.19: An extracted platelet precipitate with a characteristic morphology

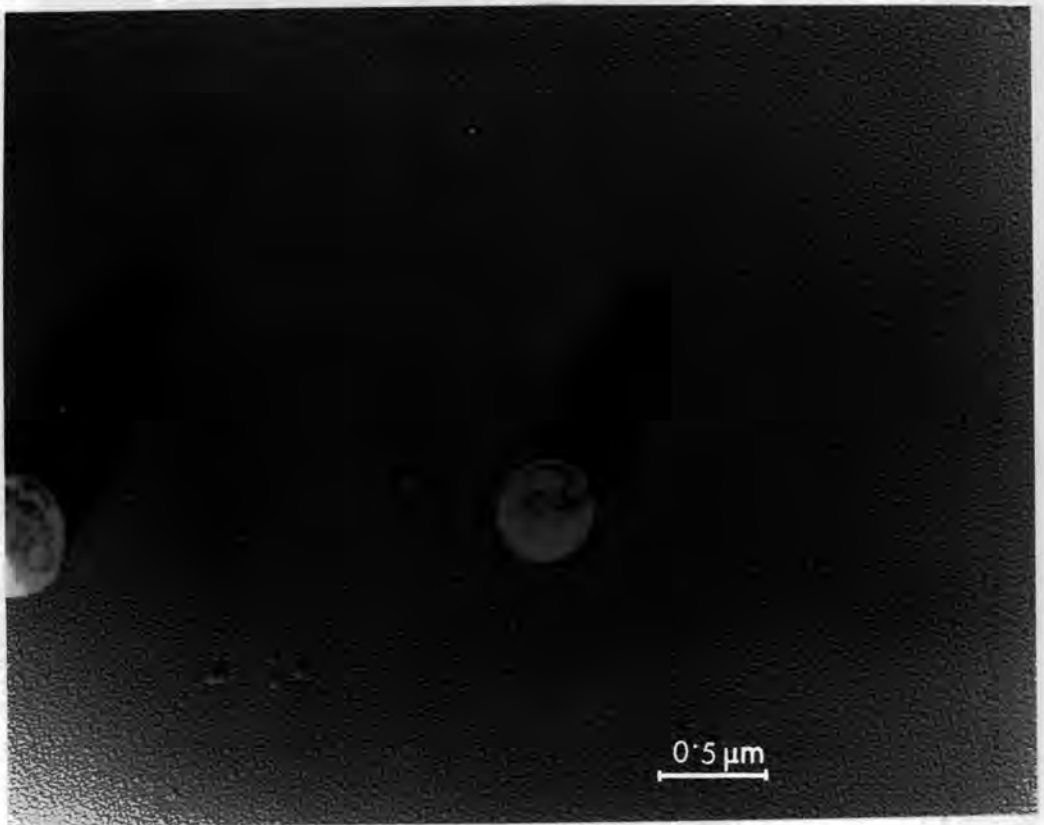


Figure 5.20: An extracted precipitate exhibiting an unusual contrast effect

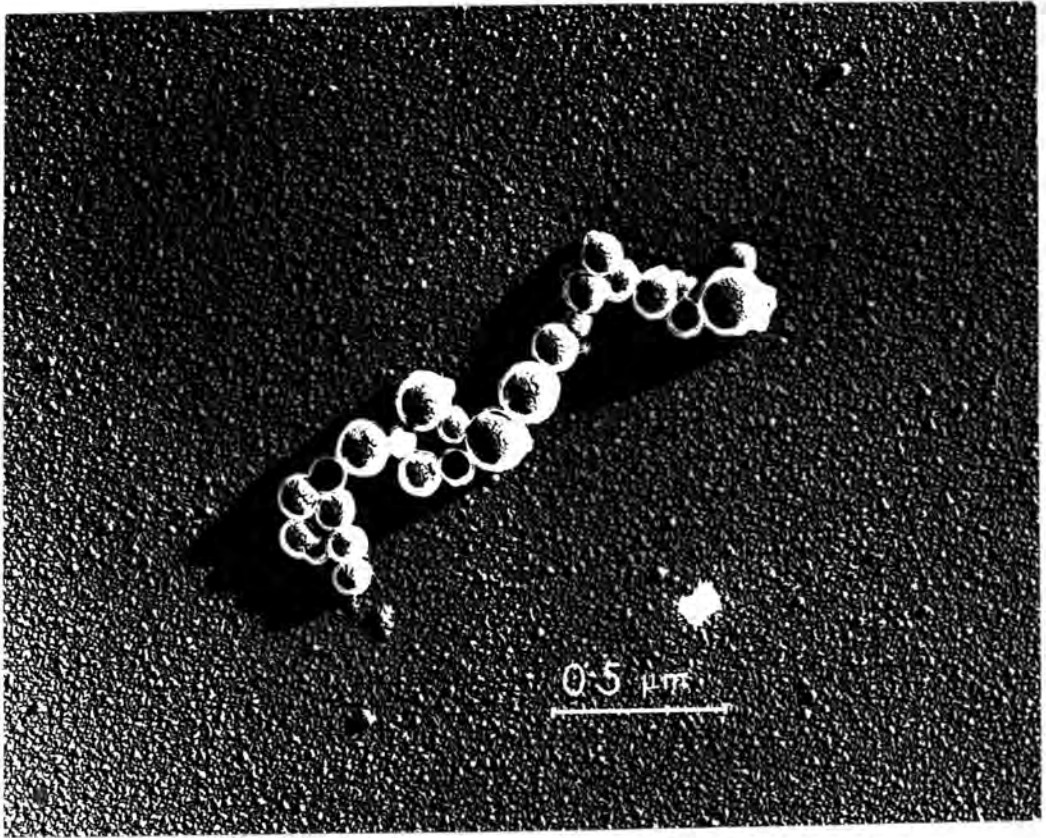


Figure 5.21: A cluster of extracted spherical precipitates

CHAPTER 6

NEUTRON IRRADIATED AND ANNEALED MAGNESIUM OXIDE

6.1 GENERAL INTRODUCTION

At present non-fissile oxide ceramics are not generally used in nuclear reactors. However as the efficiency of reactors, particularly the gas cooled type, increases at higher operating temperatures it is necessary to investigate the possibility of replacing metals in reactor cores by refractory materials. To this end extensive studies of neutron irradiated ceramics have been carried out over the past decade. MgO is of particular interest in this respect in that it has a relatively high melting temperature, and further its constituent elements do not lead to the formation of any long-lived radioactive species after irradiation by fast neutrons. It is therefore a potential candidate for use as an oxide fuel dispersant, or as a material for fuel element sleeves. For either application its behaviour after being subjected to large neutron doses and high temperatures must be evaluated.

When this study began, much was known about the properties of as-irradiated material and of its annealing characteristics up to temperatures of about 1400°C (Groves and Kelly 1963, Bowen and Clarke 1964). However little was understood about the processes involved in the formation of rectilinear cavities which are produced in material irradiated to doses exceeding  $10^{20}$  nvt by post-irradiation annealing treatments at temperatures greater than 1500°C (Morgan and Bowen 1967, Briggs and Bowen 1968). The principal aim of this study therefore was to try to achieve a better understanding of the mechanisms involved in the growth of these cavities especially with

regard to the known impurities present in as-grown MgO. However before embarking on such an investigation, it is first necessary to establish a clear background of all of the factors involved. Thus the theory of the damage produced by neutron irradiation is discussed and the observations made during a brief study of as-irradiated material are described as are the effects on the damage of annealing treatments at progressively increasing temperatures below that necessary to nucleate cavities.

## 6.2 THEORY OF NEUTRON DAMAGE

Compared with the alkali halides MgO is relatively insensitive to ionising radiations. For instance, exposure to x-ray and electron beam irradiations which causes extensive displacement of ions in certain alkali halides has little or no effect on MgO. Comparable damage can be produced in this material however by irradiation with fast neutrons with energies exceeding 1 MeV. Such neutrons can penetrate relatively large thicknesses of crystal, typically a few cm before interacting with ions in the lattice. The interactions can be of two kinds; in one case an ion is displaced from its lattice site in a Newtonian-type collision, while in the other, the nucleus of a host atom captures a neutron with the result that a transmutation of the atom occurs. These processes will now be considered separately in more detail.

### 6.2.1 Ionic Displacement

The fact that neutrons can penetrate matter so easily compared with other particles can be attributed to their small size and their electrical neutrality. In fact they can typically pass up to  $10^8$  atoms before colliding with one (see for instance Clarke et al 1963). Most

such collisions are elastic and a fraction of the energy of the neutron is transferred to the struck atom. In a collision there is an equal probability of a neutron imparting any energy between zero and a maximum value,  $E_m$ , to the atom. This maximum transfer of energy occurs in a direct head-on collision for which it can be shown, by application of the laws of conservation of momentum and energy, that:

$$E_m = \frac{4 M_1 M_2}{(M_1 + M_2)^2} E_i \quad \dots \quad \dots \quad \dots \quad (6.1)$$

where  $M_1$  is the mass of the neutron  
 $M_2$  is the mass of the ion in the lattice, and  
 $E_i$  is the energy of the impinging neutron.

If the transferred energy is greater than a threshold value called the displacement energy,  $E_d$ , then the struck atom or primary knock-on, will be removed from its lattice site, taking with it the energy it received in excess of  $E_d$  and leaving a vacant site behind. The value of  $E_d$  is a function of several parameters including atomic mass and the type and strength of bonding between atoms, and it consequently varies from one material to another. Seitz and Koehler (1956) suggested that  $E_d$  was of the order of 30 eV for most materials and more recently Pooley (1966) has calculated a value in excess of 40 eV for MgO. Assuming this value to hold for magnesium and oxygen ions in MgO, then equation 6.1 shows that the minimum energies required by a neutron to displace magnesium and oxygen ions are 260 eV and 180 eV respectively. Thus all fast neutrons can produce displacements and furthermore provide the primary knock-on with a large amount of energy. The role of this knock-on atom in the radiation damage process will be discussed next.

If we consider a 1 MeV neutron colliding with a magnesium ion, equation 6.1 shows that the maximum energy that can be imparted to the ion is about  $10^5$  eV. In contrast to the neutron, this primary knock-on is physically relatively large and electrically charged. Consequently it only moves a small distance in dissipating its energy. The way in which it does this is determined to a large extent by the magnitude of its energy,  $E_p$ . For interactions involving ions with energies exceeding about  $5 \times 10^4$  eV, energy loss by ionisation processes is favoured. However at energies below this, the dominant process is elastic collision with other ions which results in their displacement. This process forms part of a cascade of displacements which terminates when the ion at the end of the "chain" receives an energy by momentum transfer which is less than  $E_d$ . Displacement cascades account for most of the defects produced by neutron irradiation. The number of displaced ions,  $N_d$ , that can be produced from a single fast neutron collision has been determined theoretically by Kinchin and Pease (1955a). They showed that for  $E_p \gg E_d$

$$N_d = \frac{E_p}{2 E_d} \dots \dots \dots (6.2)$$

When displacement cascades are examined more closely, a number of new concepts have to be introduced. A few of the more important of these will now be outlined briefly.

Firstly Kinchin and Pease (1955b) introduced the idea of replacement collisions. In these, the impinging ion which displaces a stationary ion from the lattice is left with insufficient energy to escape from the lattice site and thus replaces the displaced ion. This mechanism is important in a structure like that of MgO which contains more than one type of atom, because atoms of one type can now be replaced by those of another type. In addition to destroying the

regularity of the crystal structure in local regions, such a replacement can also lead to a difference between the concentration of interstitials of one type of atom and the concentration of vacancies of the same type.

Another concept is that of thermal and displacement spikes. A thermal spike is produced when the energy given to a struck ion is insufficient to displace it. This leads to the excess energy being dissipated through lattice vibrations as heat. Although this thermal effect is confined to a small region containing only a few thousand ions and lasts for only about  $10^{-10}$  to  $10^{-11}$  seconds (see for instance Brooks 1956), it is possible that it could give rise to some agglomeration of vacancies. A displacement spike is a heated region at the end of a cascade process initiated by a primary knock-on. Brinkman (1954) has shown that at the end of such a cascade the distance between displacement collisions is of the order of the atomic spacing and, as in the case of the thermal spike, very local heating of short duration is experienced. He suggests that in this case, damage can be produced in the form of dislocation loops.

To explain the observed nucleation of dislocation loops in the region of displacement spikes, it is necessary for there to be a mechanism which removes interstitials from this vicinity more efficiently than thermal diffusion, thereby preventing recombination with the nucleus of vacancies present at the core of the spike. One such process is focussing (see for instance Silsbee 1957, Nelson and Thompson 1961). This mechanism is based on the replacement collision concept outlined above, where one of the knock-on atoms is an interstitial located near a displacement spike. By a succession of replacement collisions, such an interstitial can be "transported" away from the region of the spike.

This process is called focussing because at each succeeding collision a larger fraction of the diminishing momentum is transferred to the next ion, so the collisions become nearer to the head-on type and the energy is transmitted along crystallographic directions.

The final mechanism to be mentioned in connection with the cascade process is that of channelling. This is the passage of an energetic knock-on in a particular crystallographic direction characterised by an open structure. Thus, a knock-on ion can pass down a hollow core in the crystal structure without producing displacements.

The effect of the processes just described is to reduce the total number of displacements produced by a primary knock-on to a value below that given by equation 6.2. One of the more realistic estimates of the number of displacements is that due to Brinkman (1964):

$$N_d = K \left[ k' \frac{E_p}{E'_d} \right]^{(1-p)} \dots \dots (6.3)$$

where  $K$  represents the fraction of a thermal annealing

$E'_d$  is the energy at which cascade multiplication ceases and is thus similar to  $E_d$

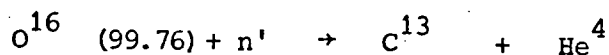
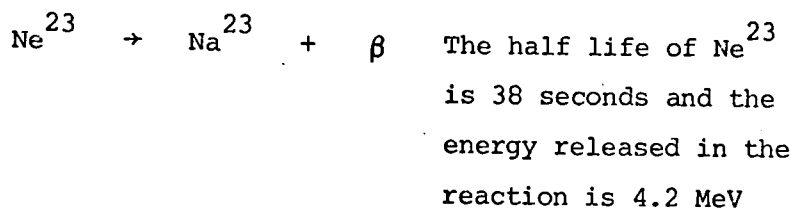
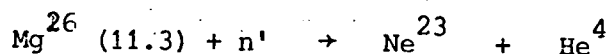
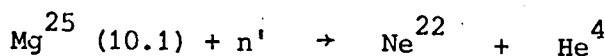
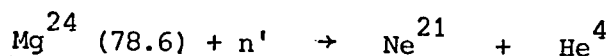
$k'$  represents the fraction of collisions which are not of the hard sphere type, and

$p$  is the sum of the probabilities of channelling from a lattice site and for an incident ion. This parameter also takes inelastic energy loss into account.

### 6.2.2 Transmutations

In addition to producing ionic displacements neutrons can cause transmutations of the nuclei of host ions. In this process, which constitutes another fraction of neutron irradiation damage in MgO,

a neutron is absorbed by the nucleus of a magnesium or an oxygen ion with the result that another isotope of the parent nucleus is formed. In each case the new nucleus is unstable and therefore subsequently disintegrates with the emission of an  $\alpha$ -particle as shown by the following reactions, where the figures in parenthesis denote the natural abundances of the particular isotopes as percentages.



In these (n, $\alpha$ ) reactions an amount of kinetic energy,  $Q$ , which is equal to  $\Delta m c^2$  is released or absorbed, where  $\Delta m$  is the change in the total mass as a result of the reaction and  $c$  is the velocity of light. In general, transmutations caused by thermal neutrons give rise to exothermic reactions, while those produced by fast neutrons result in endothermic ones. Of the four (n, $\alpha$ ) reactions above, only the one involving the  $\text{Mg}^{25}$  nucleus is exothermic.

Wilks (1966) calculated the total number of inert gas atoms produced by these reactions and compared it with the number of displacements expected theoretically at 0 K. His calculations show that the expected displacements at this temperature exceed the number of atoms produced by transmutation by about six orders of magnitude.

He suggested then that even allowing for recombination which would occur at 100°C and which would reduce the effective number of displacements, the concentration of defects would still be greater than the number of inert gas atoms produced by a factor of about  $10^4$  (see for instance McDonald 1963, Pryor et al 1964). Thus he concluded that the atoms produced by transmutation contribute only a minor fraction to the neutron damage.

When irradiation is carried out at low temperatures the inert gas atoms formed remain evenly distributed throughout the crystal lattice. In this state they have little effect on the physical properties which are important in reactor design. It is only when the irradiation is carried out at high temperatures where the mobility of the gas atoms is sufficient to allow their agglomeration, that their presence can have adverse effects on the mechanical properties.

### 6.3 EXPERIMENTAL DETAILS

The single crystals used in the radiation damage study were supplied by Semi-Elements Inc., Saxonburgh, Pa. Cleaved specimens with dimensions of about  $10 \times 4 \times 0.5 \text{ mm}^3$  were given a heat treatment for 18 hours at 1300°C in an ambient of hydrogen before being irradiated to doses of  $6.0 \times 10^{19}$  and  $3.66 \times 10^{20}$  nvt in the Harwell Dido reactor. The irradiation temperature was about 150°C.

The samples irradiated with a dose of  $6.0 \times 10^{19}$  nvt were given post-irradiation annealing treatments, each of one hour duration, at temperatures of 1050 and 1450°C in an atmosphere of argon. Samples subjected to higher doses were treated similarly except that the annealing was carried out over a range of temperatures at 50°C intervals between 1475 and 1775°C.

Electron spin resonance (ESR) spectra were obtained from most of the annealed specimens in magnetic fields with flux densities corresponding to the g-value of the free electron. All measurements were made at 77 K with a 35 GHz spectrometer. The samples were placed in the cavity such that a  $\langle 100 \rangle$  axis of the crystal was as nearly as possible parallel to the direction of the magnetic field. The field was calibrated by measuring the absorption of a trace of D.P.P.H., the g-value of which was taken to be 2.0037. This supplemented the electromagnet calibration obtained employing the proton/lithium resonance technique.

After examination in the microwave spectrometer the samples were cleaved and the resultant flakes were further reduced in thickness by chemical polishing as described in Section 5.2.1. The thinned samples were then examined in the electron microscope. To determine the distribution in size of the cavities, which were observed in the samples irradiated to a dose exceeding  $10^{20}$  nvt and annealed at temperatures greater than  $1500^{\circ}\text{C}$ , a number of micrographs were recorded from different areas for each annealed specimen. The sample orientation was close to a  $\langle 100 \rangle$  direction in all cases.

#### 6.4 TRANSMISSION ELECTRON MICROSCOPE OBSERVATIONS

##### 6.4.1 As-Irradiated Material

The neutron irradiation damage which was discussed theoretically in Section 6.2 appeared as small dots of dark contrast when irradiated samples were examined by TEM. A micrograph taken from a sample irradiated with a dose of  $6.0 \times 10^{19}$  nvt is shown in Figure 6.1, where the damage can only be resolved clearly in the very thin region close to the edge of the sample. The density of the

defects is such that at only a short distance away from the edge of the hole, where the specimen thickness is probably less than  $1000 \text{ \AA}$ , superposition of images from more than one defect cluster occurs and consequently the resolution of individual defects is impaired.

Although the damage appears at first to have the nature of a random distribution of dots, closer inspection suggests the presence of some loop-like images as at A. The observation of Groves and Kelly (1963) that some of the dots moved discontinuously in straight lines when the strength of the electron illumination of the microscope was increased provides further support for the contention that some of the damage in Figure 6.1 is in the form of glissile dislocations.

While it is not possible to make an accurate measurement of the concentration of the defect clusters from a micrograph such as this, their concentration was found to be about  $5 \times 10^{16}$  clusters/cm<sup>3</sup> by counting the dots within a known area near to the specimen edge where they could be resolved and by taking the mean sample thickness in this region to be about  $1000 \text{ \AA}$ . This estimate is comparable with that made by Groves and Kelly (1963) for similarly irradiated material. They showed that the observed number of clusters, assuming an average cluster to be a loop of  $30 \text{ \AA}$  diameter, was about two orders of magnitude smaller than the total number of displacements calculated using equation 6.3. They therefore concluded that magnesium and oxygen ions displaced during irradiation can return to their normal lattice sites even at temperature below  $200^\circ\text{C}$ .

When a sample irradiated with a neutron dose of  $3.66 \times 10^{20}$  nvt was thinned for TEM, the damage was found to be much coarser than that in Figure 6.1 and the concentration of the clusters was too large to enable individual clusters to be resolved, even in the thin edges of the samples.

#### 6.4.2 Samples Annealed Below 1500°C

The effect of annealing neutron irradiated material is to coarsen the damage structure. The degree of coarsening is mainly determined by the temperature and time of the anneal, but the gas ambient can also have an effect. In this section, TEM observations made on samples given annealing treatments at temperatures of 1050 and 1475°C in an atmosphere of argon for a period of one hour are described and the mechanisms involved in the annealing process are discussed.

On annealing at 1050°C the damage structure of a sample irradiated to a dose of  $3.66 \times 10^{20}$  nvt appears as shown in Figure 6.2. It is seen to consist of dislocation tangles with many small loop-like features in the background as at A. In the dark field image corresponding to the same area as shown in Figure 6.2, which was obtained using the (200) reflection, some of these features can be clearly resolved as dislocation loops as for example at A in Figure 6.3. The effect of increasing the annealing temperature of a similarly irradiated specimen to 1450°C is shown in Figure 6.4, where it can be seen that the dislocation tangles have increased in length and that the large number of loop-like features in samples annealed at the lower temperature, have been replaced by a small number of much larger dislocation loops (note the difference in the print magnification when comparing Figures 6.2 and 6.4). These observations are in qualitative agreement with those of Bowen and Clarke (1964) on similarly irradiated and annealed material. They showed that the mean loop diameter increased with annealing temperatures from about 250 Å at 1100°C to about 800 Å at 1300°C, as the loop concentration decreased. In a similar investigation, Groves

and Kelly (1963) also reported an increase in loop diameter with increasing annealing temperature, although they observed the damage to recover at lower temperatures. This was attributed by Bowen and Clarke (1964) to the different ambients which were used in the two independent annealing studies. Bowen and Clarke carried out their annealing in an atmosphere of argon, while Groves and Kelly used air. The former workers suggested that the difference in temperature at which the damage was observed to recover could be explained in terms of the postulate of Wertz et al (1962) that heating in oxygen causes positive ion vacancies to move into the crystal. While vacancies of both kinds are required to annihilate interstitial loops, the presence of those of one kind is probably sufficient to give rise to the observed difference in the temperatures at which the damage recovers.

The growth of loops was attributed by Henderson and Wertz (1968) to the interaction of loops of the same character, lying on the same {110} slip plane, by a dislocation glide mechanism. The interaction of loops on different {110} slip planes which occurs by the same glide process is responsible for the formation of dislocation tangles. The implication of the suggested mechanism of loop growth is that the loops are predominantly of one character. This was indeed confirmed by both Groves and Kelly (1963) and by Bowen and Clarke (1964) who reported in their independent studies of damage annealing that only interstitial dislocations were observed. It is thus necessary to enquire where the vacancies in annealed samples are located and what form they take. The best evidence for the presence of vacancies is provided by the x-ray lattice parameter measurements of Bowen and Clarke (1964), Hickman and Walker (1965) and Briggs and Bowen (1968). All of these workers showed that the lattice parameter decreased to

a value below that of an unirradiated sample after annealing above about 1100°C. This effect is attributed to lattice relaxation around vacancies or small vacancy clusters at the stage during the annealing process when most of the interstitials have migrated to dislocation loops. In fact the coincidence of the recovery of the lattice parameter to the unirradiated value with the nucleation of cavities on annealing at temperatures in excess of 1500°C is regarded as confirmation of this suggestion. Further evidence for the presence of vacancies in the form of small clusters is provided by the experiments on cold neutron scattering by Martin (1967). He concluded that approximately spherical vacancy clusters containing up to about 100 vacancies were present in specimens irradiated with a similar dose and annealed in the same temperature region as the samples under discussion. Thus, it can be concluded that small vacancy clusters approximately 5 Å in diameter are present in specimens irradiated to about  $10^{20}$  nvt after annealing at temperatures just below 1500°C for one hour, but they are not detected by TEM because of their small size and the absence of associated strain fields sufficiently large to produce observable contrast effects.

#### 6.4.3 Samples Annealed above 1500°C

While no evidence for the presence of vacancies in samples annealed below 1500°C was obtained by TEM, all samples irradiated with a dose in excess of  $10^{20}$  nvt and annealed above this temperature contained cuboidal cavities. These features of radiation damage in MgO were first observed by Morgan and Bowen (1967) who attributed their origin to the condensation of vacancies. The cavities thus provide direct microscopic evidence of the presence of vacancies in irradiated MgO. In this section some characteristics of the cavities are described,

together with the results of a study of their size distribution as a function of annealing temperature.

The appearance of the cavities which were observed in all the samples irradiated with a dose of  $3.66 \times 10^{20}$  nvt and annealed at a temperature greater than  $1500^{\circ}\text{C}$  is illustrated in Figure 6.5. The light and dark contrast exhibited by these features in the micrograph can be attributed to the operating diffraction conditions and to the depth of the cavities in the foil. The cavities were bounded by  $\{100\}$  planes and were approximately cuboidal with an edge dimension ranging from about 50 to  $350 \text{ \AA}$ . Morgan and Bowen also pointed out that the voids were nearly cuboidal in that the ratio of the length of the sides of these defects varied between 1.0 and 1.25. In examining a large number of cavities, for the statistical purposes described below, it has been noticed that those cavities for which the ratio of the lengths of the sides deviated significantly from unity tended to be the smaller ones, like those marked A in Figure 6.6. Cavities such as these are not thought to be representative of an early stage in the growth of all the larger cuboidal cavities. Three possible mechanisms which could lead to the rectilinear shape are as follows. The first is related to localised constraints on cavity growth by impurity ions which are believed to play an important role in the cavity growth process as discussed in Section 6.6. The second involves the migration and subsequent coalescence of smaller cuboidal cavities during annealing as observed in metal foils (see for instance Barnes and Mazy 1963, 1964). The third is simply that cavities nucleated only a few hundred  $\text{\AA}$  apart coalesce during their growth. The first two of these proposed mechanisms are equally lacking in supporting evidence. The postulate that the presence of localised impurity ions is responsible for rectilinear rather

than cuboidal cavities can only be speculative because for this mechanism to be operative, it would be necessary for there to be locally high concentrations of these ions and to the writer's knowledge there is no evidence that this is the case. With regard to the second proposed mechanism, it is to be noted that the attempts of Morgan and Bowen to induce migration of cavities by pulse heating with the electron beam in the electron microscope were unsuccessful. Thus it is suggested that the third mechanism involving coalescence of cavities nucleated only a few hundred Å apart is responsible for the small rectilinear cavities. In fact the cavity at B in Figure 6.6 is believed to provide direct evidence for the existence of this process. The reason why only the smaller cavities exhibit this morphology can be attributed to the fact that the cavities grow by the collapse of small defect clusters in their immediate vicinity (see Section 6.6). Consequently the probability of two large cavities existing sufficiently close together to coalesce is expected to be negligibly small.

Another feature of cavities which was frequently observed was their association with segments of interstitial dislocations which were still present after annealing at temperatures above 1500°C. This association was observed by Morgan and Bowen (1967) who noted that these features of radiation damage were often located at cusps in dislocation lines. The present study has shown that these dislocations were usually pinned by the corners of cavities and that in the region close to these defects the orientation of the dislocations approximated to a  $\langle 110 \rangle$  direction. This is demonstrated by the examples shown in Figures 6.7 and 6.8. While the cavity at A in Figure 6.8 is clearly located at a cusp in the dislocation with

which it is associated, the same cannot be said for the one at A in Figure 6.7. However closer inspection of the latter micrograph reveals that the section of dislocation on the left hand side of the cavity appears to stop short indicating that a large component of its length must be parallel to the direction of observation. This is confirmed by the oscillatory contrast of this section. In contrast, the section of the dislocation on the right hand side of the cavity is longer and does not exhibit the same oscillatory contrast. It seems reasonable therefore to suggest that the cavity is located at a cusp in a dislocation which is in a plane perpendicular to the plane of the specimen.

The origin of the association of cavities with dislocations is believed to be as follows. When an interstitial loop, which is still present in a sample after annealing for an hour at temperatures above  $1500^{\circ}\text{C}$ , moves through the crystal, its interaction with the cavities present will result in the partial annihilation of the loop by absorption of vacancies from the cavities. The motion of the parts of the loop in the vicinity of the cavities will consequently be impeded. It is further suggested that the observed  $\langle 110 \rangle$  orientation of dislocations in the proximity of cavities is related to a favourable energy configuration for the annihilation process to occur. This is associated with the fact that in the NaCl structure the uninterrupted rows of anions and of cations in  $\langle 110 \rangle$  directions make diffusion of vacancies of either type more likely in these directions than in others.

The size distributions of the cavities as a function of annealing temperature are shown in the histograms in Figure 6.9. These results were derived from at least ten micrographs taken from different areas

for each annealed sample. The histograms show that the maximum cavity size increases dramatically on annealing above some temperature between 1575 and 1625°C. Annealing at higher temperatures does not lead to any further increase in size or significant change in the size distribution.

The total cavity volume per unit volume of crystal, and the concentration of cavities for each annealed sample have also been estimated and are shown in Table 6.1.

TABLE 6.1

Temperature of anneal (°C)	1525	1575	1625	1675	1725	1775
Ratio of cavity volume/ crystal volume (x 10 <sup>4</sup> )	1.8	1.4	13.5	11.5	11.9	16.2
Number of cavities per cc (x 10 <sup>-14</sup> )	0.95	0.51	1.38	0.83	1.00	1.64

For the purpose of these calculations a mean specimen thickness for the total area from which the size distributions were derived was taken to be 1000 Å, a typical sample thickness for TEM. Accepting the crudeness of this approximation, inspection of Table 6.1 shows that the large increase in cavity size which occurs at 1625°C is accompanied by a correspondingly large increase in the ratio of the total cavity volume per unit volume of crystal. The cavity concentration however remains more or less unchanged. The origin of this cavity growth will be discussed later in Section 6.6.

#### 6.5 ELECTRON SPIN RESONANCE

The ESR spectra from the different annealed samples exhibited several common features. The main trend is shown in the three spectra

of Figures 6.10 to 6.12 which were obtained from samples annealed at 1475, 1575 and 1625°C. In examining these it is to be noted that some data on other MgO crystals made by the same supplier (Semi-Elements Inc.) has been given by Martin (1968) whose results showed that the major paramagnetic impurity was iron at about 100 wt. p.p.m.: it is also generally accepted from analytical evidence on other MgO crystals that both manganese and chromium are often present at low trace levels.

Figure 6.10 shows the spectrum obtained with the magnetic field parallel to  $\langle 100 \rangle$  for the specimen annealed at 1475°C which contained interstitial loops but no cavities, (c.f. Figure 6.4). The prominent features are (a) six lines marked A, (b) a line B having  $g = 1.9785$  and (c) a line C having  $g = 2.0034$ . Features A and B were identified by comparison with the data of Henderson and Wertz (1968) as arising from the  $+\frac{1}{2} \rightarrow -\frac{1}{2}$  transition of  $Mn^{2+}$  and from  $Cr^{3+}$  respectively. The origin of line C is in some doubt. Further measurements showed that it was isotropic, indicating that it could not be ascribed to an interstitial atom with an associated vacancy; although the  $g$ -value is reasonably close to that of the  $+\frac{1}{2} \rightarrow -\frac{1}{2}$  transition of  $Fe^{3+}$  in octahedral symmetry, this interpretation is precluded because the  $-\frac{3}{2} \rightarrow -\frac{1}{2}$  and  $+\frac{3}{2} \rightarrow +\frac{1}{2}$   $Fe^{3+}$  transitions are absent; and finally the  $g$ -value does not fit with any of those of the impurities listed in the review by Henderson and Wertz. Evidence given later suggests that line C may arise from an electron trapped in a vacancy to form a centre persistent even at the annealing temperatures used.

In the spectra obtained from specimens annealed at both 1525°C and 1575°C, i.e. just above the temperature necessary to nucleate cavities, new features were observed. These are shown in Figure 6.11 which

refers to a specimen annealed at 1575°C. The most important change is the occurrence of the new lines marked D and E; the g-value of 2.0031 for the D transition, together with the observed anisotropy of the E lines, fit well with reported data on Fe<sup>3+</sup> (see for example Low, 1958) and enable them to be identified as the  $-\frac{1}{2}$  to  $+\frac{1}{2}$  and  $\pm\frac{3}{2} \rightarrow \pm\frac{1}{2}$  transitions respectively of Fe<sup>3+</sup> in octahedral symmetry, i.e. Fe<sup>3+</sup> occupying a magnesium site. The other differences appear to be associated with localised detailed changes in the manganese environment; they include additional transitions close to each of the six A lines and also transitions F situated midway between the A lines. The transitions F are of low intensity and have the same separation as the A lines.

The spectra of specimens annealed above 1575°C (e.g. Figure 6.12) differ from those just described in two major respects. In the first place there is no indication of the D and E lines corresponding to Fe<sup>3+</sup> in octahedral symmetry; secondly, the additional lines in Figure 6.11 which were attributed to Mn<sup>2+</sup> are much less pronounced. Comparison of all the spectra shows that the intensity ratio of the Mn<sup>2+</sup> hyperfine and Cr<sup>3+</sup> lines remained approximately constant throughout all the annealing treatments and consequently the hyperfine components of Mn<sup>2+</sup> could be used as an intensity reference (see for example King and Henderson, 1967). On this basis it appears that in Figure 6.12 the intensity of line C has increased by approximately two times, indicating that annealing at 1625°C produces a twofold increase in the number of centres responsible for line C.

## 6.6 DISCUSSION OF CAVITY GROWTH

An important conclusion of Morgan and Bowen (1967) from their studies of neutron irradiated and annealed MgO was that to nucleate

cavities it was necessary to anneal samples irradiated to a dose in excess of  $10^{20}$  nvt at a temperature greater than  $1500^{\circ}\text{C}$  in an ambient of argon. This minimum critical temperature was attributed to the activation energy associated with vacancy mobility. In addition, the results of the annealing studies reported here concerning the nucleation and growth of cavities would suggest that another critical temperature for the growth exists in the temperature range of  $1575$  to  $1625^{\circ}\text{C}$ . While annealing above some temperature within this range does not produce any significant change in the concentration of cavities, the ratio of total cavity volume to unit volume of crystal increases by an order of magnitude. This must similarly be accounted for by the movement of vacancies and consequently it is proposed that, following the nucleation of cavities, some mechanism exists which impedes further growth of these defects until another critical temperature (for an hour annealing period) is exceeded. An indication of the nature of this mechanism can be inferred from the results of the ESR measurements as will be discussed next.

The ESR results show that the nucleation of cavities, in the samples annealed at  $1525^{\circ}\text{C}$  and  $1575^{\circ}\text{C}$ , is accompanied by the appearance of  $\text{Fe}^{3+}$  in octahedral symmetry. As mentioned earlier, analysis of material made by the same supplier has shown that iron was present in the specimens (see Martin, 1968). Due to the pre-irradiation heat treatment in hydrogen it is most likely that any iron present will be in the divalent state (see for instance Davidge, 1967); this view is supported by the absence of  $\text{Fe}^{3+}$  lines in specimens annealed at temperatures below  $1500^{\circ}\text{C}$  (Figure 6.10).

As the post-irradiation annealing took place in an inert atmosphere the cation vacancies necessary for the conversion of  $\text{Fe}^{2+}$  into  $\text{Fe}^{3+}$

on increasing the annealing temperature from  $1475^{\circ}\text{C}$  to  $1525^{\circ}\text{C}$  must have come from within the crystal. An adequate supply of vacancies is known to be produced when the vacancy clusters, which are about  $7 \text{ \AA}$  in diameter and which are present in similarly treated specimens, suddenly collapse on annealing at about  $1500^{\circ}\text{C}$  (see Martin, 1966). The disappearance of the  $\text{Fe}^{3+}$  lines at temperatures above  $1625^{\circ}\text{C}$  could be explained either by a reduction of  $\text{Fe}^{3+}$  into  $\text{Fe}^{2+}$  by the outward diffusion of cation vacancies, (see for example Wertz et al, 1962) or by the trapping of vacancies near the  $\text{Fe}^{3+}$  sites, creating an  $\text{Fe}^{3+}$  - vacancy complex (see Henderson et al, 1971), whose ESR would probably fall in the low magnetic field region outside the present range of measurement. Since the subsequent growth of the cavities indicates that a large number of vacancies are retained in the crystal the outward diffusion explanation appears unlikely and the trapping mechanism more probable.

In view of the ESR evidence, it is envisaged that the cavity nucleation and growth proceeds by stages as follows. On annealing just above  $1500^{\circ}\text{C}$  a critical vacancy mobility is exceeded and small cavities are nucleated in the manner suggested by Morgan and Bowen (1967). Simultaneously there is a conversion of iron to  $\text{Fe}^{3+}$  in octahedral symmetry at magnesium sites; this conversion uses vacancies released when clusters collapse at about  $1500^{\circ}\text{C}$  which then form charge compensating centres for the  $\text{Fe}^{3+}$  ions. After nucleation negligible cavity growth occurs until an annealing temperature of  $1625^{\circ}\text{C}$  (for one hour) is reached, see Figure 6.9. This behaviour is attributed to mobile vacancies being trapped near the  $\text{Fe}^{3+}$  sites in preference to condensation at cavities. A calculation, based on the observed cavity growth between the annealing temperatures of  $1575^{\circ}\text{C}$  and  $1625^{\circ}\text{C}$  and an

iron impurity level of 100 wt. p.p.m., shows that the number of vacancies required to associate with all the  $\text{Fe}^{3+}$  is some two orders of magnitude less than the number required to account for the cavity growth. When this stage is complete, cavity growth can proceed. It is suggested that the presence of iron is not expected to alter the magnitude of ultimate growth significantly. However, the extent to which growth is impeded, and hence the annealing temperature necessary for the last growth stage, would be expected to increase with iron concentration. Further evidence which indicates that cavity growth is incomplete when annealing at  $1500^{\circ}\text{C}$  is provided by the measurements of Bowen (1966), who recorded the density variation with annealing temperature for similarly treated MgO. These show a discontinuity at about  $1625^{\circ}\text{C}$  and consequently his results suggest that cavity formation is a two stage process, as our studies using a different technique (TEM) have confirmed to be the case. In addition, the high precision X-ray measurements of Briggs and Bowen (1968) showed that complete recovery of the lattice parameter to the unirradiated value did not occur until the annealing temperature reached about  $1750^{\circ}\text{C}$ . However, interpolation of their data would suggest that most of the recovery had occurred at about  $1650^{\circ}\text{C}$ . So, allowing for the fact that their material was irradiated to more than twice the dose of that used in this study, it is concluded that there is a reasonable correlation between the minimum temperature at which it has been necessary to anneal to produce most of the cavity growth and that reported by Briggs and Bowen to obtain almost complete recovery of the lattice parameter. To the writer's knowledge the influence of an impurity on the movement of vacancies in cavity growth in neutron irradiated MgO, has not previously been

reported. Here it appears that iron plays a significant role (see Russell et al, 1976). It is possible that other impurities may act in a similar way, but this remains to be established.

#### 6.7 CONCLUSIONS

While the observations made on neutron irradiated MgO before and after annealing treatments at temperatures up to 1500°C only confirm conclusions drawn from work done earlier, principally by members of the Materials Development Division, A.E.R.E., Harwell, the proposed role of iron in the growth of cavities in neutron irradiated and annealed MgO is a novel idea (Russell et al, 1976). Davidge (1968) has previously shown that the valence state of iron influences resistance to annealing of the hardening of single crystal MgO, however his work was concerned with the role of iron in material irradiated with lower neutron doses and annealed at much lower temperatures. Both the density measurements of Bowen (1966) and the x-ray lattice parameter results of Briggs and Bowen (1968) suggested that the cavity growth mechanism was more complex than a simple vacancy condensation process occurring at a single temperature (Morgan and Bowen 1967). However no mention was made in either of these works of the possible role of impurities. Thus the mechanism for cavity growth (in the temperature range of 1500 to 1775°C) which has been proposed here provides an explanation for the observed behaviour of the density and lattice parameter in terms of a specific impurity ion which has been identified.

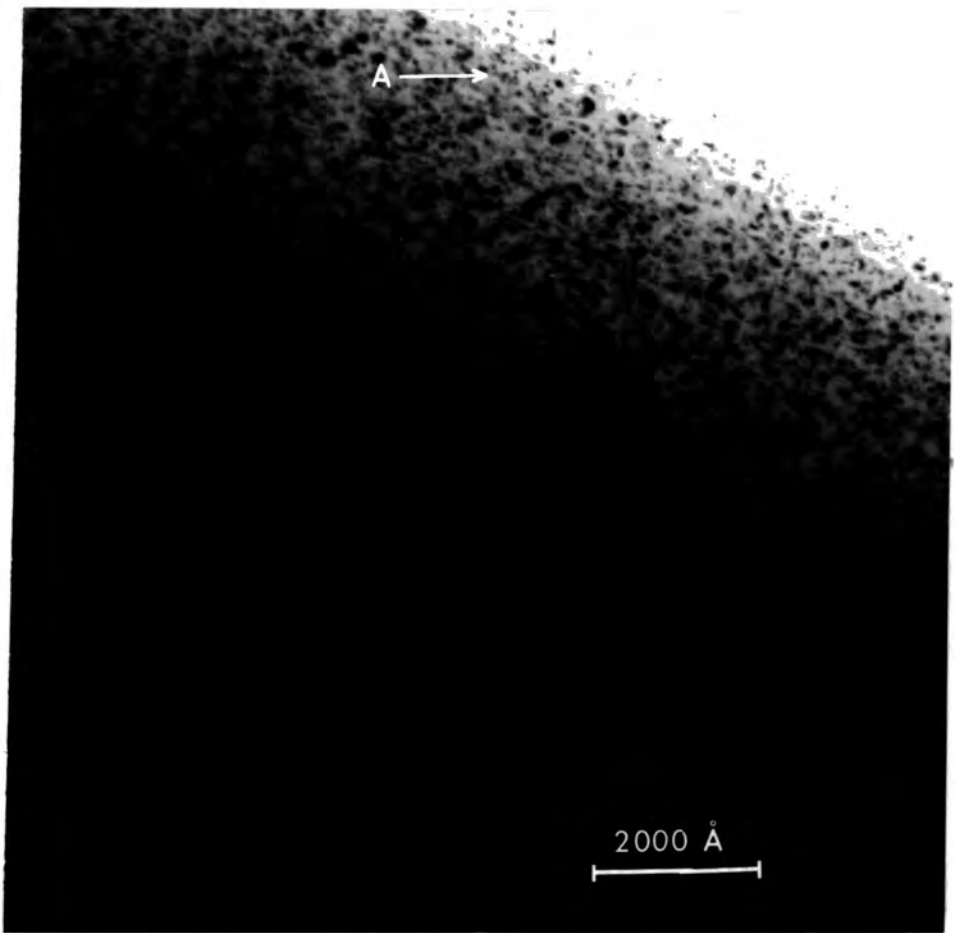


Figure 6.1: Defect clusters in MgO irradiated with a dose of  $6.0 \times 10^{19}$  nvt

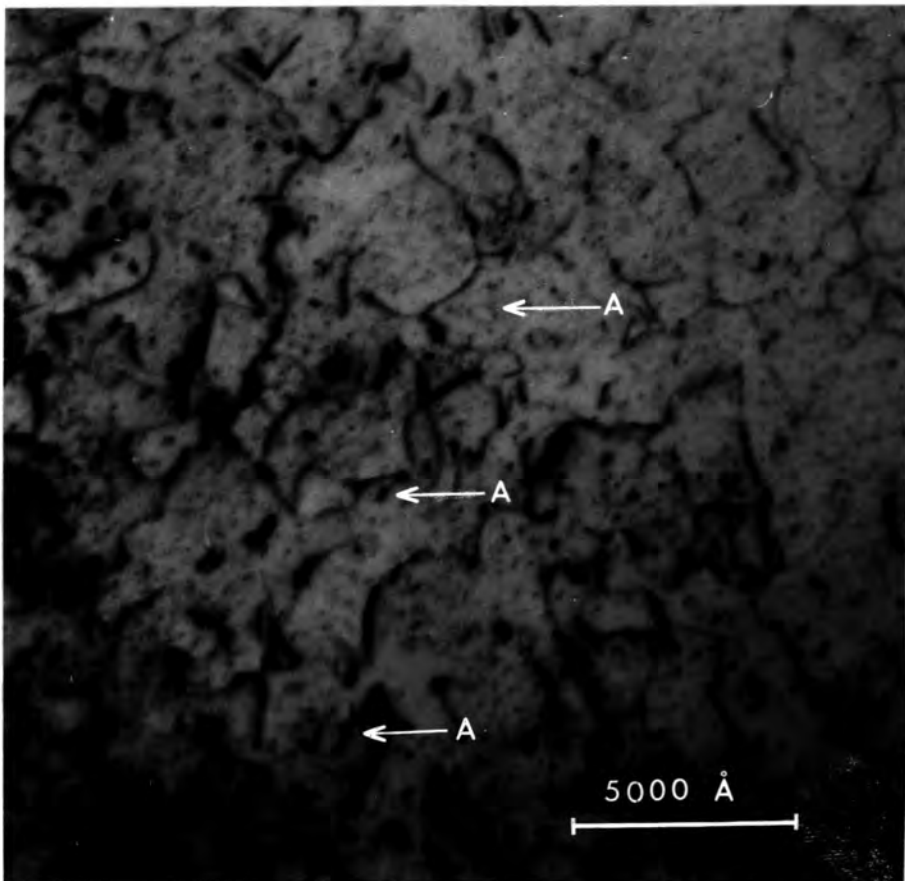


Figure 6.2: Dislocation tangles and small loops in MgO irradiated with a dose of  $3.66 \times 10^{20}$  nvt and annealed at  $1050^{\circ}\text{C}$

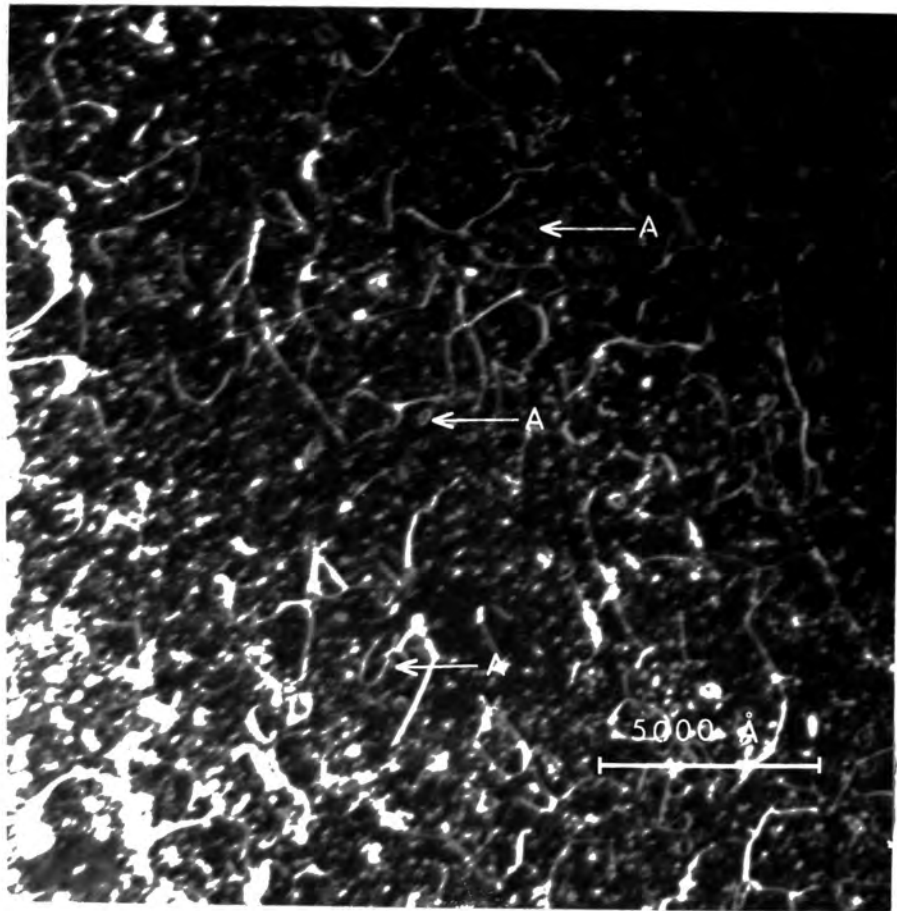


Figure 6.3: A dark field image of the region in Figure 6.2 taken using a  $\{200\}$  diffracted beam

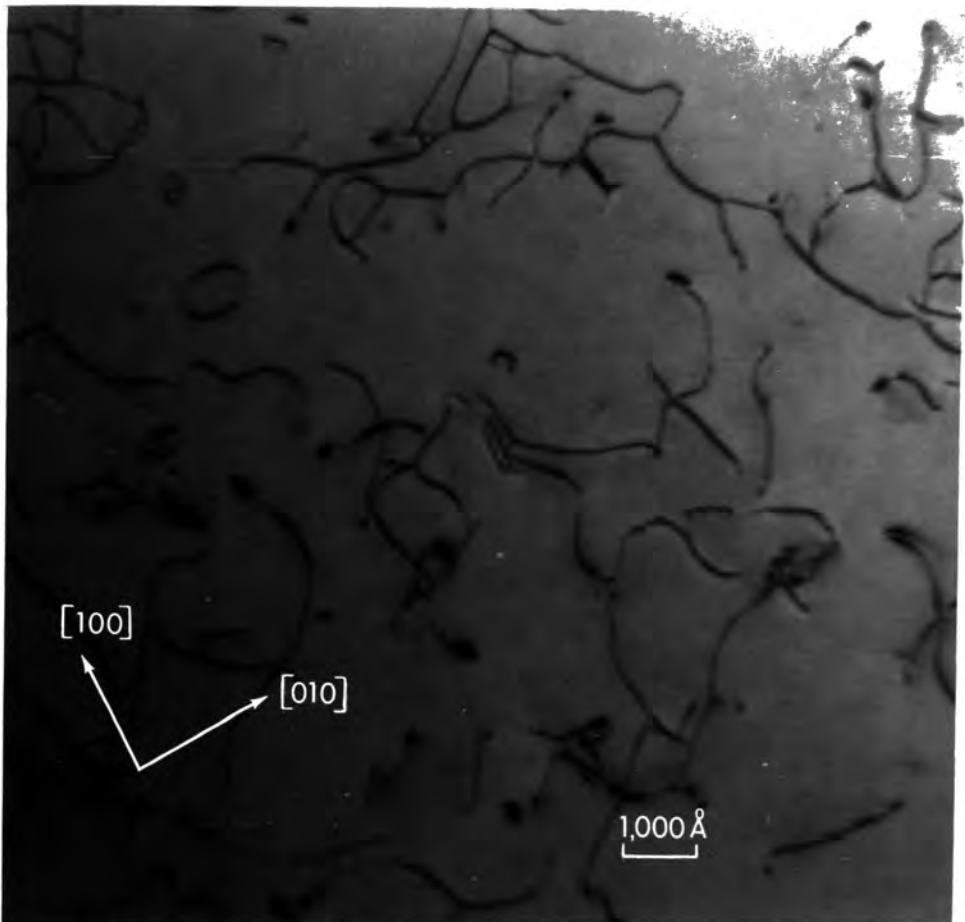


Figure 6.4: Dislocation tangles and loops in MgO irradiated with a dose of  $3.66 \times 10^{20}$  nvt and annealed at  $1450^{\circ}\text{C}$

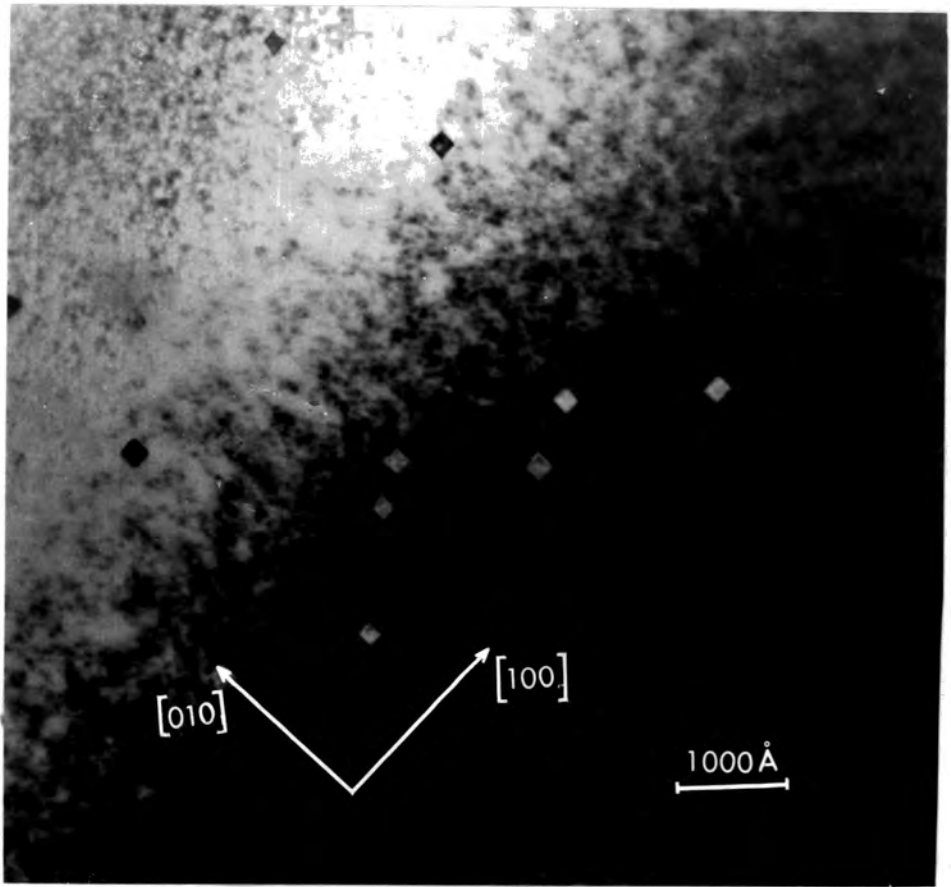


Figure 6.5: Cavities showing light and dark contrast in MgO irradiated with a dose of  $3.66 \times 10^{20}$  nvt and annealed at 1525°C

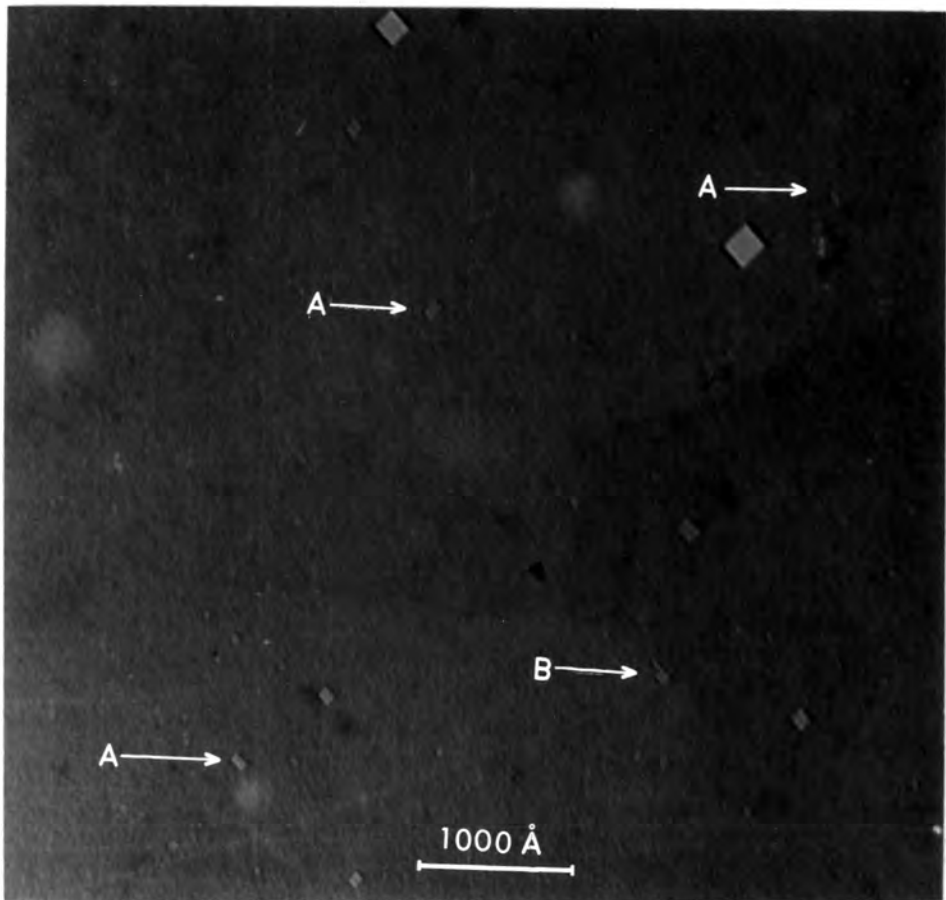


Figure 6.6: Cavities which are rectilinear rather than cuboidal in a sample treated similar to that shown in Figure 6.5

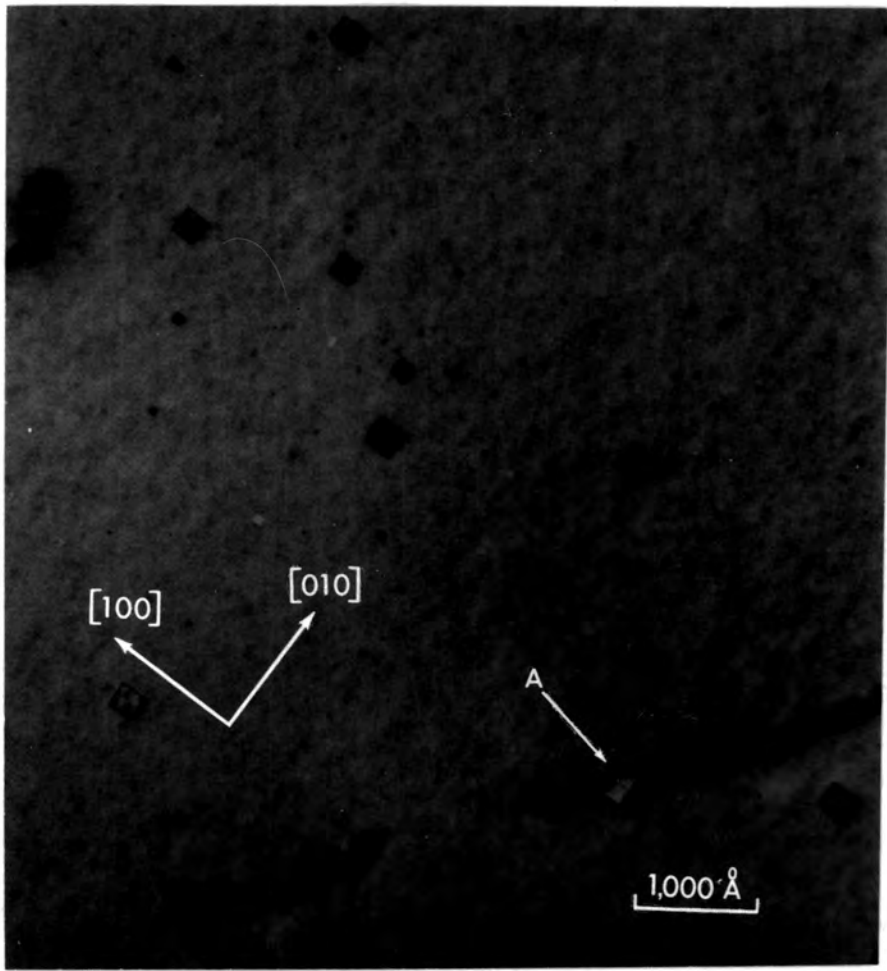


Figure 6.7: The interaction of an interstitial dislocation with a cavity

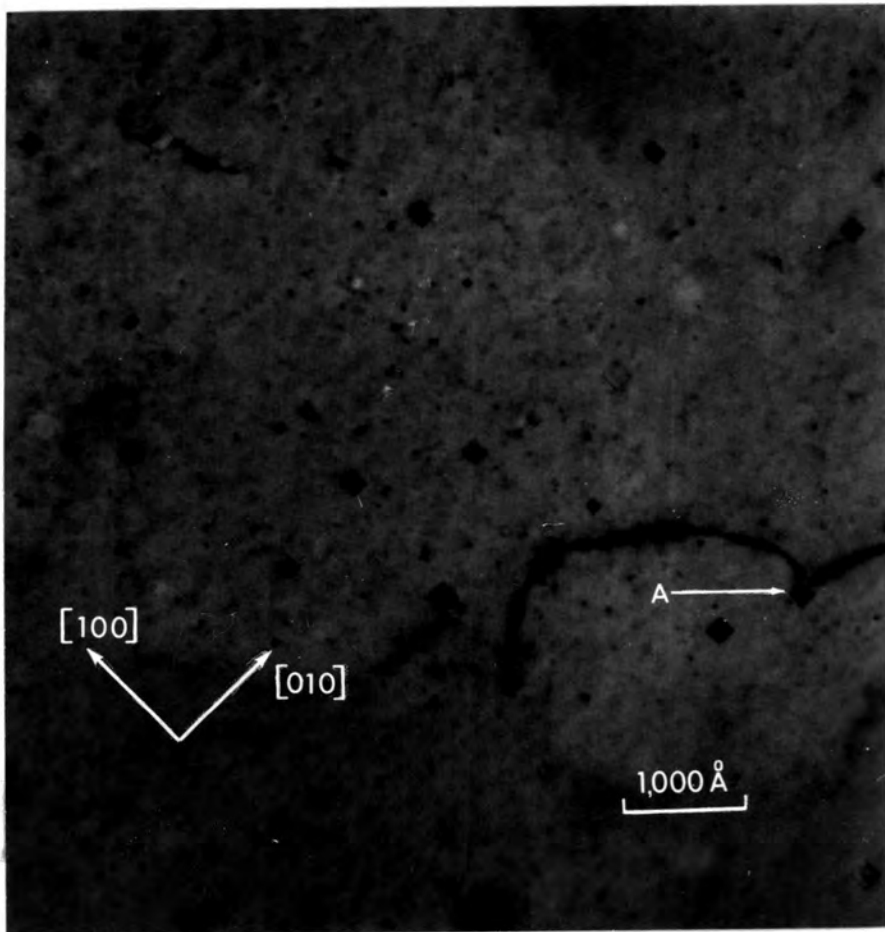


Figure 6.8: As in Figure 6.7, but in this case showing the location of a cavity at a cusp in a dislocation

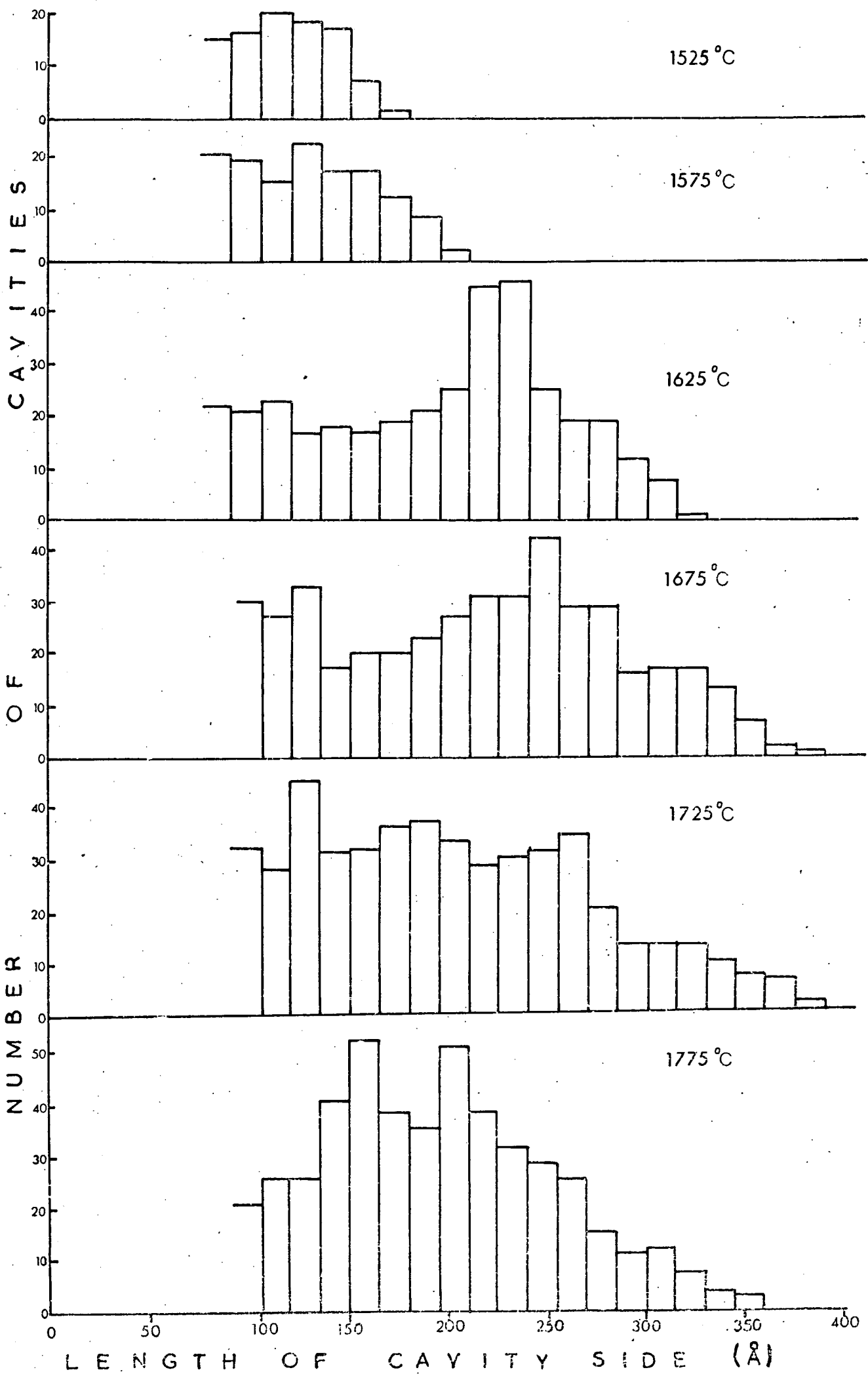


FIGURE 6.9 VARIATION OF CAVITY SIZE WITH ANNEALING TEMPERATURE

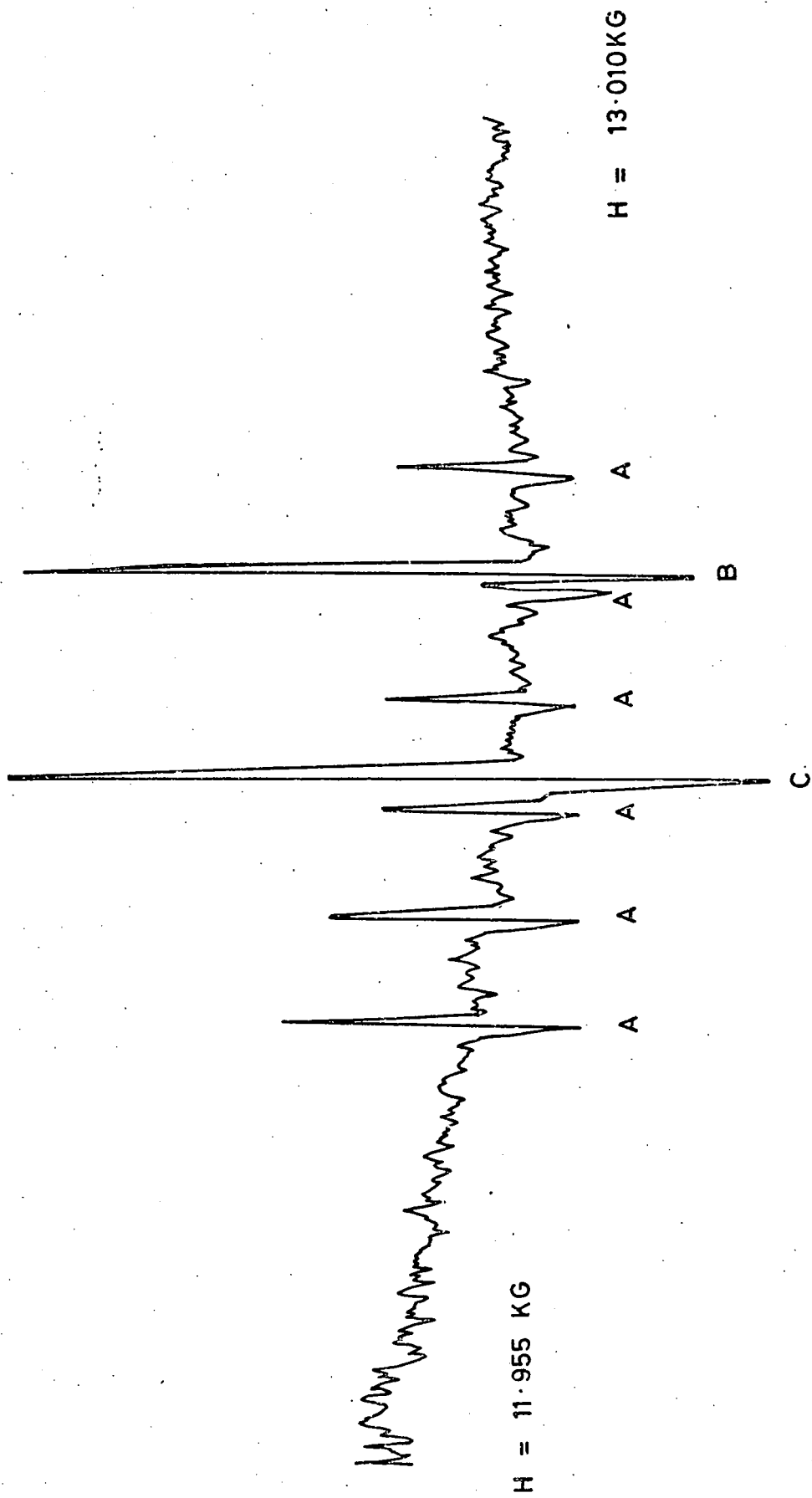


FIG 6.10 E.S.R Spectrum of the Sample Annealed at  $1475^{\circ}\text{C}$

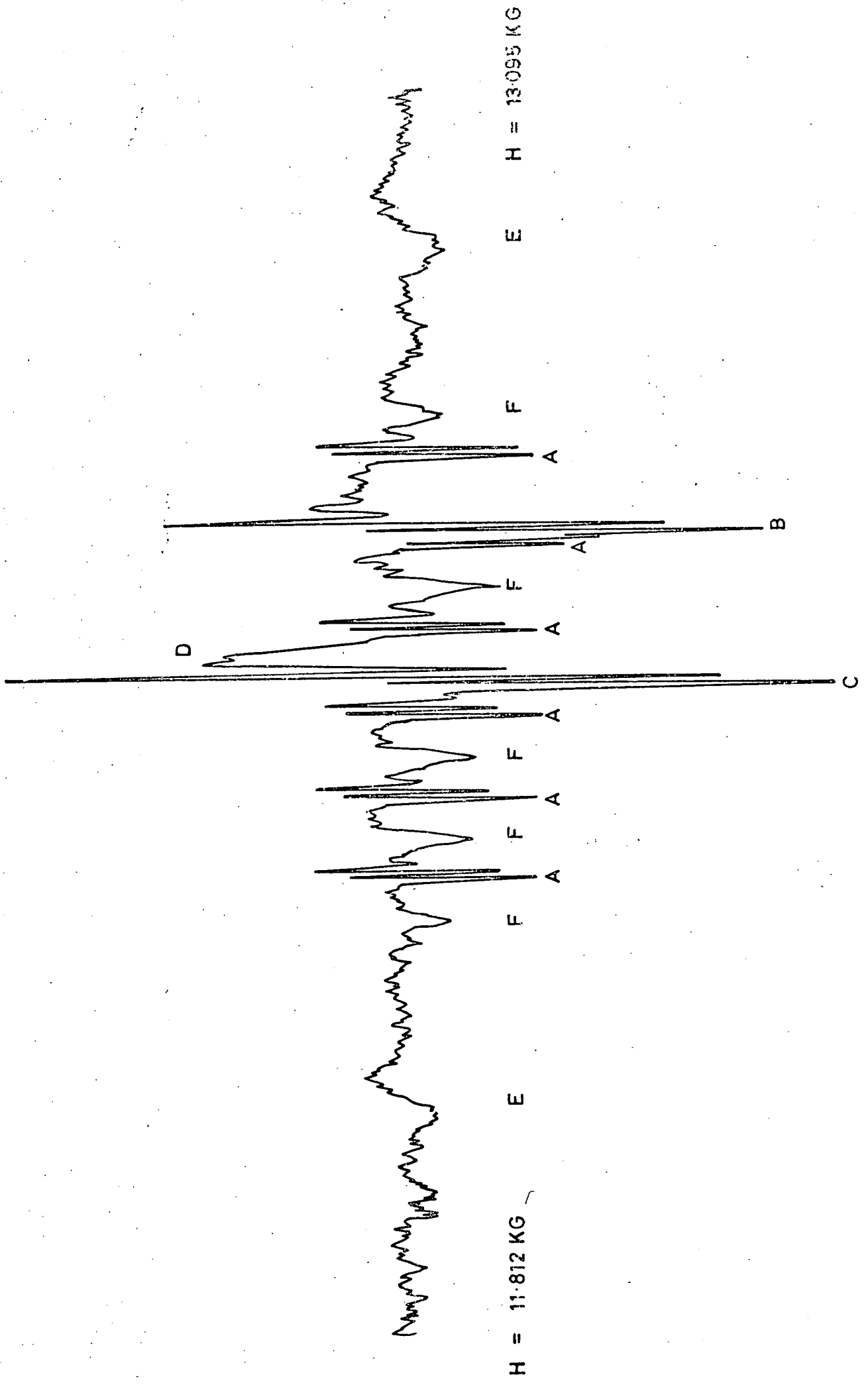


FIG 6.11 E.S.R. Spectrum of the Sample Annealed at 1575 °C

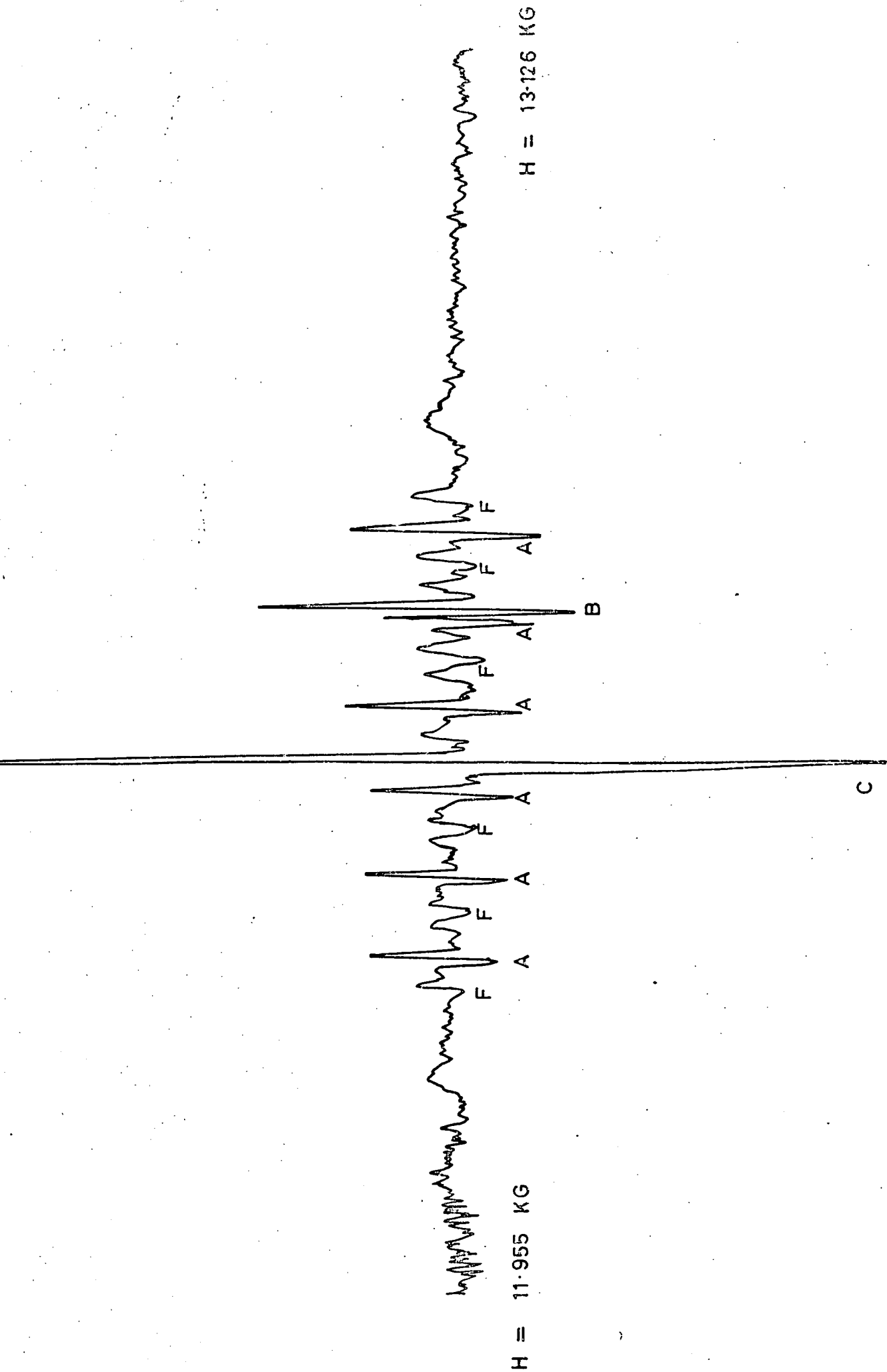


FIG 6.12 E.S.R. Spectrum of the Sample Annealed at 1625 °C

CHAPTER 7

AS-GROWN ZINC SELENIDE AND ZINC SULPHO-SELENIDE

7.1 GENERAL INTRODUCTION

ZnSe is a II-VI compound semiconductor which has become of importance in recent years as single crystals with the purity essential for electronic device application have become available. ZnSe has a band gap of 2.67 eV at room temperature and a high luminescence efficiency in the visible range. Extensive studies of its photo- and electroluminescent properties have been made previously (see for instance Morehead 1967). In addition, its optical properties are such that it transmits light of wavelength in the range 0.5 to 22  $\mu\text{m}$  with very little attenuation. This, in conjunction with its inherent mechanical strength and chemical stability (ZnSe is non-hygroscopic), makes it ideally suitable for use as a material for infra-red laser windows.

In spite of the increasing technological interest in this material, only a small amount of work has been done on its defect structure, and that which has been reported has mainly been confined to defects in single crystal platelets (see for instance Gezci and Woods 1972). The defect structure of single crystal boules was expected to differ from that of freely grown platelets mainly because of the constraints of the silica wall of the growth tube on the growing boule. The purpose of the TEM studies of ZnSe and  $\text{ZnSe}_{0.4}/\text{S}_{0.6}$  which are reported in this chapter was to obtain a better knowledge of the defect structure of single crystal boules. It was hoped that this might lead to a better understanding, not only of the mechanism of crystal growth, but also of the electronic processes associated with certain forms of luminescence; for instance, Williams and Yoffe (1968)

have demonstrated the effects that twins and stacking faults in ZnSe have on cathodoluminescence, by comparing transmission electron micrographs with cathodoluminescence from the same areas of specimens in a scanning electron microscope. In this chapter, the main defects observed in ZnSe and in  $\text{ZnSe}_{0.4}/\text{S}_{0.6}$  are described and a mechanism to account for their origin is suggested. Some preliminary results of the damage observed in ion thinned samples are also reported and discussed.

## 7.2 SPECIMEN PREPARATION

### 7.2.1 Crystal Growth

The basic technique used in this laboratory to grow large single crystal boules of ZnSe is that developed by Burr and Woods (1971). With this method a charge of the required compound is sublimed, in a temperature gradient, from one end to the other of a vertical silica capsule. As growth proceeds the capsule is pulled through the furnace at a rate comparable to the advance of the crystal interface at about 1 mm/hr. The stoichiometry of the vapour in the growth capsule is controlled by connecting the capsule to a reservoir containing one of the elemental constituents via a narrow orifice. By controlling separately the temperatures of the charge and the reservoir, the partial pressures of the constituents of the binary (zinc, selenium) system at the growth interface are uniquely determined. In this way boules of ZnSe 1 cm in diameter and up to 5 cm in length are produced.

When the above method is used to grow a ternary compound such as  $\text{ZnSe}_{0.4}/\text{S}_{0.6}$ , one degree of freedom remains in the vapour. The

only attempt made to prevent serious segregation of sulphur and selenium was to pre-anneal the charge. This was done by holding the growth capsule in the furnace in a position such that the tip of the capsule, where the crystal was ultimately to grow, was at the hottest part of the furnace for a period of three days. After coalescence and sintering of the charge had occurred the capsule was pulled through the furnace in the same manner as used for the growth of ZnSe.

### 7.2.2 Chemical Polishing

Slices of ZnSe or ZnSe<sub>0.4</sub>/S<sub>0.6</sub>, 1 cm in diameter and about 0.5 mm thick, were obtained by cutting boules at right angles to their long axes using a diamond saw. The edges of these slices were coated with an acid resistant lacquer and then the samples were chemically thinned in a polish termed H.P.C. (see Hemmatt and Weinstein 1967). This consists of one part of a saturated solution of chromium tri-oxide in phosphoric acid with two parts of hydrochloric acid. On preparing this mixture, chlorine from the hydrochloric acid complexes with chromium producing globules of red liquid, probably a chromyl chloride, which float to the surface of the brown polish. In this state the mixture acts as a good chemical polish. However, within 20 to 30 minutes from mixing, the hydrolisation of the chromyl chloride to form the chromate ion results in the polish turning to a dark green colour and the mixture subsequently etches rather than polishes. Thus the change to the dark green colour can be used as an indication that the polish should be discarded.

H.P.C. was chosen as a polish after a few others which were recommended in the literature had been investigated. These included a 1% solution of bromine in methanol (Sagar et al 1968) and potassium



permanganate dissolved in sulphuric acid (Rowe and Forman, 1968). The first of these was found to etch rather than polish, while the second polished, but its rate of removal of material was too slow to make its use practicable here.

During chemical polishing the sample was constantly agitated and the progress of the thinning was followed by periodically removing the specimen from the polish, washing it successively in distilled water and in absolute alcohol and examining the dried sample in reflected light in an optical microscope. In the final stages of thinning, the acid resistant lacquer was carefully removed using tweezers, in order to promote better flow of the polish over the specimen surface. When the sample became very thin, as indicated by the increase in its translucency, it was repeatedly dipped in and out of the opaque polishing solution so that continuous visual inspection of the surface could be made. When a hole appeared in the specimen, polishing was stopped and the sample was washed as described above. It was subsequently examined in the optical microscope and, in the event that no interference fringes around the edge of the hole could be resolved at a magnification of about 50 x, the chemical polishing was re-started until another hole appeared. In this way, by making a few examinations of the thinned area of the sample in an optical microscope, a suitable specimen for TEM could be assured.

### 7.2.3 Ion Beam Thinning

The apparatus used for ion beam thinning was purchased from Ion Tech, Teddington, U.K. It is a single gun system of a very simple design with no facilities for rotating or tilting the specimen with respect to the orientation of the ion beam or for cooling the sample

to reduce radiation damage. The whole arrangement, which is shown schematically in Figure 7.1 was mounted in a conventional 12" vacuum coating unit. A power supply delivered an accelerating voltage in the range from 0 to 10 KV to the anode and inert gas was bled into the system via a needle valve. A hole in the anode allowed some of the accelerated ions to pass through and these were collimated into a beam by an arrangement of apertures. This beam was incident on the specimen normally to its surface. When a hole was eventually produced in a sample, the transmitted ions were collected by a high energy ion detector. The magnitude of the resultant ion current gave an indication of the size of the perforated specimen area and the current measuring circuit was adjusted so that when a pre-set current level was reached the H.T. would be tripped.

As the quoted thinning rate of the apparatus was about 20  $\mu\text{m}$  per hour for most materials, the following procedure for sample preparation was adopted. Slices of material were cut from boules and were chemically polished as described in Section 7.2.2 until their thickness was not greater than a few tens of  $\mu\text{m}$ . They were then washed and dried, after which they were fractured into sections of a size suitable for mounting in the sample holder of the ion beam thinning apparatus. The sections were such that the maximum dimension in any direction was less than 3 mm but nevertheless the 2 mm diameter aperture in the sample holder was completely covered (see Figure 7.1).

The chemically polished sections were loaded into the sample holder and after evacuating the bell jar to  $1 \times 10^{-5}$  torr, the system was flushed with argon. The bell jar was then re-evacuated again to about  $1 \times 10^{-5}$  torr at which pressure the H.T. was switched on and the needle valve was opened slightly to admit argon into the system.

By making suitable adjustment of the pressure in the region of  $1 \times 10^{-4}$  torr, an ion beam current of about 30 to 40  $\mu\text{A}$  was obtained at a selected accelerating voltage in the range from 4 to 6 KV. After thinning for about 15 to 20 minutes, the bombardment was stopped, the system was let up to air and the sample was inverted. In this way, by subsequently continuing the ion thinning from the opposite side of the specimen until perforation occurred, a foil for TEM was obtained. Two obvious advantages of this procedure were, (1) that any possible surface contamination from chemical polishing was eliminated and (2) that by producing an indentation on both sides of the section until the surfaces met at the edge of a hole, the resultant "wedge angle" was reduced and the sample was therefore more suitable for TEM, than one produced by making a single indentation from one side of the section.

It is to be noted that in an attempt to reduce the ion beam damage, experiments were carried out in which argon atoms with a mass of 40 amu were replaced firstly by diatomic nitrogen, with molecular mass 28 amu and secondly by diatomic hydrogen, with molecular mass 2 amu. This was achieved by simply interchanging the gas cylinders connected to the needle valve of the vacuum system.

### 7.3 OBSERVATIONS OF DEFECTS

#### 7.3.1 As-Grown Zinc Selenide

The dominant defects observed in ZnSe were narrow twins extending completely across thin regions of samples as shown in Figure 7.2. Although some of these twins exceeded 1  $\mu\text{m}$  in width, the majority were slightly narrower than this and were usually found close together in small groups which were separated by larger

regions of untwinned material. With the wider twins, where the boundaries were well separated, some irregularity was apparent at the edge of the specimen at the intersections with twin boundaries. This is illustrated in Figure 7.3 and is attributed to differential etching of the different crystallographic faces of the twinned and untwinned material. Electron diffraction patterns from regions containing twins showed that twinning occurred on  $\{111\}$  planes in all samples.

As discussed in Section 4.4, there are two types of twins which can occur on  $\{111\}$  planes in the sphalerite structure, namely the ortho- and the para-twin. The ortho-twin is not associated with any change in polarity across the  $\{111\}$  twinning plane, whereas the para-twin is. In order to identify the nature of the twins in ZnSe the following experiment was performed. A boule containing large grains was selected and a slice was cut from it so that the large area surface of one of the grains lay close to a  $\{111\}$  plane on which twinning occurred. Since the cut was made at an angle of a few degrees to the  $\{111\}$  plane, the twin boundaries intersected the cut surface at this low angle. After mechanical and chemical polishing with diamond paste and H.P.C., the slice was etched in a 1% solution of bromine in methanol for about one minute. The choice of this etchant was based on the work of Gezci and Woods (1972) who showed that it gave rise to triangular pits on the (111) zinc faces, and conical pits on the  $(\bar{1}\bar{1}\bar{1})$  selenium faces. The result of this etching experiment is shown in Figure 7.4, which is a photomicrograph of the zinc surface of the etched slice. The fact that the etch pits within the twin band traversing the photomicrograph, exhibit the same threefold symmetry on either side of the twin boundaries indicates that there

is no reversal of polarity across the twin boundaries. Thus the twin in Figure 7.4 is an ortho-twin, as were all of the others observed within this large grain. The  $180^\circ$  rotation of the etch pits within the twin band relative to those outside it is consistent with this identification.

Although very few other defects have been observed in the ZnSe slices examined by TEM, the micrograph in Figure 7.5 does illustrate one interesting grain boundary which is worth recording. A knowledge of the orientations of the two grains, at the top and bottom of the micrograph, together with the information that the boundary lies approximately parallel to the [100] direction in the upper grain, suggests that the fault is a tilt boundary with a  $\langle 100 \rangle$  axis, of the type described by Holt (1964). Such a grain boundary, in contrast to an ortho-twin boundary for example, contains an array of wrong bonds which makes the fault a favourable site for the formation of precipitates. In fact small regions of dark contrast are seen along this boundary, as in Figure 7.6 and these are believed to be such precipitates.

The incidence of dislocations in the as-grown crystals of ZnSe was very low, and apart from the twinning described above, very few crystallographic defects were observed. Many of the diffraction patterns however did exhibit extensive streaking, as shown in Figure 7.7. This effect is attributed to thermal diffuse scattering which is observed in many materials with the diamond or zincblende structure (see for example Honjo et al 1964). The diffuse streaking was most prominent in diffraction patterns where the zone axis was close to a  $\langle 100 \rangle$  direction as in Figure 7.7. In contrast to the streaking associated with stacking faults and planar defects, which

is very sensitive to specimen orientation, the streaking associated with thermal diffuse scattering is maintained as the crystal is tilted through several degrees with respect to the incident beam,

The reason why the thermal diffuse scattering produces streaking which is most prominent in diffraction patterns with a  $\langle 100 \rangle$  zone axis is that the 'zig-zag' chains in  $\langle 110 \rangle$  directions which connect nearest neighbour atoms, and which give rise to 'intensity walls' in reciprocal space perpendicular to their length, are perpendicular to the direction of the electron beam in this orientation. In other orientations where the zig-zag chains are not perpendicular to the electron beam, the intensity walls intersect the Ewald sphere at an angle inclined at less than  $90^\circ$  to the direction of the electron beam and the streaking is less pronounced.

### 7.3.2 As-Grown Zinc Sulpho-Selenide

The defect content of  $\text{ZnSe}_{0.4}/\text{S}_{0.6}$  differed from that of ZnSe mainly in the degree of stacking disorder. The first indication of this came from the fact that many more twins were observed in the mixed material and these were less wide than those in ZnSe. A typical region containing such faults is shown in Figure 7.8 which once again suggests that the twins occur in groups, while most of the area shown in the micrograph remains of the same crystallographic orientation. The selected area diffraction pattern from a region similar to that in Figure 7.8 is recorded in Figure 7.9. This pattern has been indexed in Figure 7.10 which shows that the extra spots arise from thin twins with the orientational relationships:

(111) Twin parallel to  $(\bar{1}\bar{1}\bar{1})$  matrix, and

$[0\bar{1}\bar{1}]$  Twin parallel to  $[01\bar{1}]$  matrix .

The diffraction streaks which pass through some of the matrix reflections in Figure 7.9 are attributed to the thin nature of the twins.

Further evidence for the greater stacking disorder of  $\text{ZnSe}_{0.4}/\text{S}_{0.6}$  was provided by the presence of groups of long stacking faults similar to those shown in Figure 7.11. Their occurrence in groups and the fact that within a group all faults had the same displacement vector suggests that these faults owe their origin to slip processes. The nature of the faults was determined by relating the direction of the diffraction vector operating to the asymmetry of the corresponding dark-field image (see for example Gevers et al 1963). The application of this method is illustrated in Figures 7.12 to 7.14 which show the bright and dark field images of a single stacking fault and the corresponding two-beam diffraction condition that was operative. The diffraction pattern has been corrected to account for relative rotation of the image (see Section 2.5.3) and the strong diffracted beam arises from a set of  $\{220\}$  planes. For such a reflection Gevers et al (1963) have shown that if the origin of the  $\underline{g}$  vector is placed at the centre of the dark-field image of the fault,  $\underline{g}$  points away from the light fringe if the fault is intrinsic and towards it if it is extrinsic. Thus inspection of Figures 7.13 and 7.14 shows that this fault is intrinsic. In fact all of the faults examined in this way in  $\text{ZnSe}_{0.4}/\text{S}_{0.6}$  have been of this nature.

It is worth noting that not all the stacking faults observed were confined to one  $\{111\}$  plane. A few which slipped from one  $\{111\}$  plane to another have been observed (see Figure 7.15). However, faults such as these are thought to originate from the same source as the longer faults confined to a single  $\{111\}$  plane.

In addition to the readily identified twins and stacking faults, crystals of  $\text{ZnSe}_{0.4}/\text{S}_{0.6}$  also contained a few small regions where the concentration of planar faults was very high as illustrated in Figure 7.16. It has not been possible absolutely to identify individual defects in such heavily faulted regions as this, but the degree of stacking disorder suggests that thin lamellae of hexagonal or polytypic material may be present. Evidence for the presence of polytypes is provided by the closely spaced diffraction spots of low intensity such as that at A in Figure 7.17 which is a selected area diffraction pattern taken from the region shown in Figure 7.16. However the irregularity of the spacing of the diffraction spots even within the group at A does not permit a specific polytype to be identified. On the other hand, the presence of a hexagonal phase in one sample has been firmly established by electron diffraction. In the sample examined, the hexagonal material was in the form of a thin layer in the plane of the foil. The consequent overlapping of the layers of wurtzite and zinblende gave rise to the moiré fringes shown in Figure 7.18. The variation in orientation and spacing of these fringes is attributed to different diffraction conditions and changes in orientation of the phase boundary in different regions of the specimen. A selected area diffraction pattern from this area is recorded in Figure 7.19, in which the reflections of low intensity around the central spot arise from the hexagonal phase, while the more intense spots are produced by the larger amount of cubic material present in the same region. This pattern shows that the orientational relationship between the cubic and hexagonal phases is as follows:

the (111) cubic plane is parallel to the  $(10\bar{1}0)$  hexagonal plane and the  $[211]$  cubic direction is parallel to the  $[0001]$  hexagonal direction.



while that of the hexagonal was between  $\text{ZnSe}_{0.45}^{\text{S}}_{0.55}$  and  $\text{ZnSe}_{0.22}^{\text{S}}_{0.78}$  depending on whether the value of  $a_0$  or  $c_0$  is taken into consideration. The uncertainty in the lattice parameters derived from electron diffraction patterns really permits of a qualitative conclusion only, namely that this particular boule contained a higher molar proportion of sulphur than selenium and indeed was a solid solution with a composition not too far removed from that of the charge from which it was grown.

### 7.3.3 Ion Beam Thinned Zinc Selenide

All of the samples prepared as described in Section 7.2.3 were found to contain defects which were not present in chemically polished samples from the same crystal boules. In an attempt to eliminate this ion beam damage the accelerating voltage was reduced from 6 to 3 KV when thinning samples using argon ions. As this produced no noticeable improvement, other attempts were made to reduce or exclude the damage by replacing argon firstly by nitrogen and secondly by hydrogen. However these efforts were similarly unsuccessful, although the use of hydrogen, while prolonging the thinning period, did perhaps slightly reduce the extent of the damage. Thus this section is concerned principally with the nature of the damage in ion beam thinned samples and no attempt is made to compare the thinning conditions with the extent of the damage.

A bright field image of an ion beam thinned sample is shown in Figure 7.20. At first glance no interesting features can be identified, not even in the vicinity of extinction contours. However closer inspection does reveal a suggestion of some fringe contrast over small areas as at A. On the other hand, the selected area diffraction pattern taken from this region and recorded in Figure 7.21 yields much

more definite information and is very different from patterns obtained from chemically thinned samples. The diffraction streaks, passing through the matrix reflections of this  $\langle 110 \rangle$  zone axis pattern and lying in  $[1\bar{1}1]$  and  $[1\bar{1}\bar{1}]$  directions, were not associated with the thermal diffuse scattering described in Section 7.3.1 for the following reasons. Firstly the streaks in Figure 7.21 were relatively more intense making it possible to take dark field micrographs from them, and secondly they exhibited a variation in intensity along their lengths which showed a strong orientational dependence and which gave rise to intensity maxima at positions displaced by approximately  $\frac{1}{3} \langle 111 \rangle$  from matrix reflections. A dark field image of the region in Figure 7.20 was made from one of these intensity maxima and is shown in Figure 7.22. This shows a large number of thin features of light contrast with their long dimension approximately parallel to  $[1\bar{1}2]$ . This observation would be consistent with their identification as planar defects lying on the  $(1\bar{1}\bar{1})$  plane as will be discussed further in Section 7.4.2. Another dark field micrograph taken from an intense portion of a streak in the  $[1\bar{1}\bar{1}]$  direction revealed the presence of a similar set of defects lying on the  $(1\bar{1}1)$  plane. Further it is suggested that the satellite spots displaced from several of the matrix reflections in the  $[002]$  and  $[00\bar{2}]$  directions as at B in Figure 7.21 can be attributed to the intersection of the Ewald sphere by diffraction streaks in the  $[111]$  and  $[1\bar{1}\bar{1}]$  directions arising from further sets of planar defects on the  $(111)$  and  $(1\bar{1}\bar{1})$  planes respectively. To illustrate this suggestion a reciprocal lattice construction for a  $[110]$  zone axis is given in Figure 7.23a, while Figure 7.23b shows the mechanism by which the satellite spots might be produced. Further support for the suggestion that these planar defects are present on all four  $\{111\}$  planes is

provided by a diffraction pattern recorded close to a  $\langle 100 \rangle$  zone axis and shown in Figure 7.24. In this orientation thin planar defects on all four  $\{111\}$  planes are expected to give rise to the presence of four satellite spots around the positions of several of the matrix reflections as indeed is observed to be the case.

Finally it should be emphasised that none of the several attempts to obtain a dark field image of the planar defects, when they are inclined to the direction of the electron beam as they are in the orientation in Figure 7.24, has been successful. This is attributed to the thin nature of the defects which results in their low contrast in all orientations except that where they are observed nearly edge on.

#### 7.4 DISCUSSION

##### 7.4.1 As-Grown Zinc Selenide and Zinc Sulpho-Selenide

The observations recorded in Sections 7.3.1 and 7.3.2 show that in as-grown ZnSe the major defects are narrow ortho-twins extending completely across grains, while in  $\text{ZnSe}_{0.4}\text{S}_{0.6}$  a larger concentration of narrower twins occur in some grains and groups of intrinsic stacking faults are found in others. Further evidence for the increase in the stacking disorder in the sulpho-selenide relative to the selenide is provided by the presence of a few polytypic regions in this material. It thus remains to account, as far as is possible, for the origin of these defects, i.e. are they introduced into the crystals during growth or do they arise from post growth stress?

Consider first the possibility that the twins form while the crystals are being grown. During the etching experiments in which it was established that the twins in ZnSe were of the ortho-type, it was also found that the surfaces of most of the grains on the growth face

lay within about  $20^\circ$  of the  $(\bar{1}\bar{1}\bar{1})$  or selenium surface. From this it was inferred that the growth of these boules was strongly polar in nature. This is in agreement with the findings of Parker (1971) who investigated the growth of epitaxial layers of ZnSe on GaAs and found that the growth rate of the  $(\bar{1}\bar{1}\bar{1})$  selenium face was two and a half times that of the (111) zinc face. Now as a grain of ZnSe grows in a fast  $\langle\bar{1}\bar{1}\bar{1}\rangle$  direction at a small angle to the axis of the capsule, see Figure 7.25, twinning may well occur to preserve the overall axial growth direction. If the twin boundary is of the ortho-type, the  $180^\circ$  rotation of the twinned region about an axis perpendicular to the twinning plane, with respect to the rest of the crystal, results in the growth interface having opposite polarity on either side of the twin boundary. As the metal face thus produced at the growth interface grows much more slowly than the adjacent non-metal face, this is an inherently unstable situation so that the crystal would rapidly twin back to establish the original fast growing interface. It is suggested that this mechanism could account for some of the long, thin twins observed in ZnSe and  $\text{ZnSe}_{0.4}\text{S}_{0.6}$ . However it cannot be responsible for all of them because some are found lying perpendicular to the growth axis and the origin of these cannot be explained by this growth mechanism.

As to the possibility that the twins are introduced by post-growth stress, it seems unlikely that stress due to the differential contraction of the crystal and the silica capsule during cooling will be significant. This is because the coefficients of thermal expansion of ZnSe and ZnS are substantially larger than that of silica glass, as evidenced by the fact that the crystal boules usually become completely free from the walls of the growth capsule during the cooling

process following growth. However sticking sometimes occurs and then differential contraction leads to stress. In addition there is some evidence to suggest that the walls of evacuated silica glass capsules creep slowly at  $1200^{\circ}\text{C}$  under external atmospheric pressure. For example, capsules with cross sections which are initially circular are sometimes found to have become slightly elliptical in section after ten days at this temperature. The gradual collapse of the walls of the capsule could therefore readily introduce stress into the growing boule. While the two sources of stress just mentioned were only known to be operative on rare occasions, another source was always present and this arises from the radial temperature gradient which exists between the core and the periphery of the boule when cooling from about  $1100^{\circ}\text{C}$  to room temperature over a period of three days. Further, the fact that boules are cooled in a position in the furnace corresponding to the termination of pulling means that a temperature gradient exists along the length of the boule. Thus it is possible that the rate of cooling might vary along the length of the boule and thereby constitute a further source of stress.

So far only the formation of twins in ZnSe and in  $\text{ZnSe}_{0.4}\text{S}_{0.6}$  has been considered and, on the basis of the above discussion, it would appear that a post-growth stress rather than a growth mechanism is responsible for most of these defects. When describing the long stacking faults, which were only observed in  $\text{ZnSe}_{0.4}\text{S}_{0.6}$ , it was pointed out that some appeared to slip from one {111} plane to another. This, taken in conjunction with the fact that all of the faults studied were found to be of intrinsic character, would suggest that these defects also owe their origin to slip processes. Thus it is thought that the stacking faults in  $\text{ZnSe}_{0.4}\text{S}_{0.6}$  and the twins in ZnSe are closely

related in that both kinds of defect owe their origin to post growth stress. Further it is proposed that the reason for the occurrence of different defects in the two materials is associated with the slight difference in the degree of ionicity of the bonding of ZnSe and  $\text{ZnSe}_{0.4}\text{S}_{0.6}$ . This is based on the assumption that the sulphur content of  $\text{ZnSe}_{0.4}\text{S}_{0.6}$  is expected to modify the bonding to a nature similar to that of ZnS.

To understand the mechanism of formation of these defects by slip processes, consider the stacking of double atom layers along a  $\langle 111 \rangle$  axis of the zincblende structure. In the notation used in Section 4.1 this can be represented as

$$\text{A}\alpha \text{ B}\beta \text{ C}\gamma \uparrow \text{A}\alpha \text{ B}\beta \text{ C}\gamma \text{ A}\alpha \text{ B}\beta \text{ C}\gamma \dots \dots (7.1)$$

A stress nucleated dislocation will split into two partials separated by an intrinsic stacking fault, and one partial will sweep across a  $\{111\}$  plane in a position such as that marked by the arrow in the stacking sequence (7.1) above. The stacking fault energy of ZnS is very low, or even negative, so that the fault extends across the complete plane. Following the passage of the partial dislocation, the stacking sequence becomes

$$\begin{matrix} \leftarrow \text{hexagonal} \rightarrow \\ \text{A}\alpha \text{ B}\beta \text{ C}\gamma \text{ B}\beta \uparrow \text{C}\gamma \text{ A}\alpha \text{ B}\beta \text{ C}\gamma \text{ A}\alpha \dots \dots (7.2) \end{matrix}$$

The intrinsic stacking fault in this sequence can be regarded as containing four double layers of hexagonal material with a stacking sequence  $\text{B}\beta \text{ C}\gamma \text{ B}\beta \text{ C}\gamma$ . This configuration will be particularly stable in ZnS and in  $\text{ZnSe}_{0.4}\text{S}_{0.6}$ , because the higher ionicity of the bonding in ZnS favours the formation of the wurtzite structure. Thus to relieve thermal stress a large number of partial dislocations must



(7.3) the double layers to the left of the arrows (and the double layer to the left of the right-hand arrow in (7.4)) are in an immediately hexagonal environment. The covalent nature of ZnSe ensures that this is a relatively unstable arrangement so that there will be an inherent weakness on the planes marked with arrows. Stress relief will consequently occur preferentially on these planes with the result that the twins widen in preference to the formation of random stacking faults. Energy considerations make this point clearer. The passage of three partial dislocations on successive  $\{111\}$  planes leads to the configuration in (7.4) with two 3-layer hexagonal regions marked H. On the other hand if the three partial-dislocations had passed across three  $\{111\}$  planes at random, a total of twelve double layers with the hexagonal stacking would have been formed. This is clearly energetically less favourable in a crystal with a high proportion of covalency in its bonding. The disparity between the energies required to form wider twins or random stacking faults increases with the number of partial dislocations required to accommodate the strain.

In conclusion therefore it is suggested that the relief of thermal stress leads to the formation of ortho-twins in ZnSe. It is perhaps worth recording that crystals of ZnTe, which is more covalent than ZnSe, are usually heavily twinned (see for example Lorenz 1967), while the more ionic ZnS crystals are found to contain predominantly stacking faults (see for instance Blank et al 1962). In the case of  $\text{ZnSe}_{0.4}\text{S}_{0.6}$ , the replacement of selenium by sulphur atoms results in an increase in the ionicity of the bonding and in the corresponding tendency to take up the wurtzite modification. Thus, this is expected to lead to the formation of random stacking faults as a stress relieving mechanism, particularly if microscopic homogeneity is not

strictly maintained, as appears to be the case from the presence of polytypic growth in some regions (see Cutter et al, 1976).

#### 7.4.2 Ion Beam Damage in Zinc Selenide

In all of the samples prepared for TEM by ion beam thinning, planar defects lying on all four  $\{111\}$  planes were observed as described in Section 7.3.2. The planar nature of these faults was seen by viewing them edge-on and the fact that the thickness of some was only a few atomic layers, was evidenced by the occurrence of continuous streaks in  $\langle 111 \rangle$  directions passing through matrix reflections of a  $\langle 110 \rangle$  zone axis diffraction pattern. The presence of intensity maxima at positions displaced  $\frac{1}{3} \langle 111 \rangle$  from matrix spots in such patterns enabled these faults to be identified as micro-twins (see for instance Pashley and Stowell 1963). No other maxima at positions displaced  $\frac{1}{6} \langle 111 \rangle$  from matrix reflections were observed in these patterns so it appears that no thin regions of hexagonal material lying on  $\{111\}$  planes were present (see Holt 1969). This is consistent with the above discussion of defects in as-grown ZnSe in that the formation of twins, in this case micro-twins, rather than thin layers of material having the wurtzite structure is preferred on energy considerations.

The formation of micro-twins in ion beam thinned samples is thought to arise from re-ordering processes following the displacement of atoms. Although it was not possible to measure the actual temperatures of the surface being bombarded with ions, the fact that the stainless steel specimen holder reached a temperature which was in excess of  $100^{\circ}\text{C}$  would suggest that the temperature at the surface of the specimen was likely to be somewhat higher than this. In

addition, in a study of the annealing behaviour of ion implanted ZnSe platelets having the wurtzite structure, Olley et al (1970) reported that an annealing treatment at  $500^{\circ}\text{C}$  produced a phase transformation from the wurtzite phase to that of zincblende, which is the stable structure below about  $700^{\circ}\text{C}$ . To produce the re-ordering required in this case, it was necessary for a large number of partial dislocations to pass completely across the platelet between every second close packed double atomic layer (see for instance Williams and Yoffe 1972). It seems plausible therefore to suggest that the micro-twins observed here similarly owe their origin to re-ordering processes.

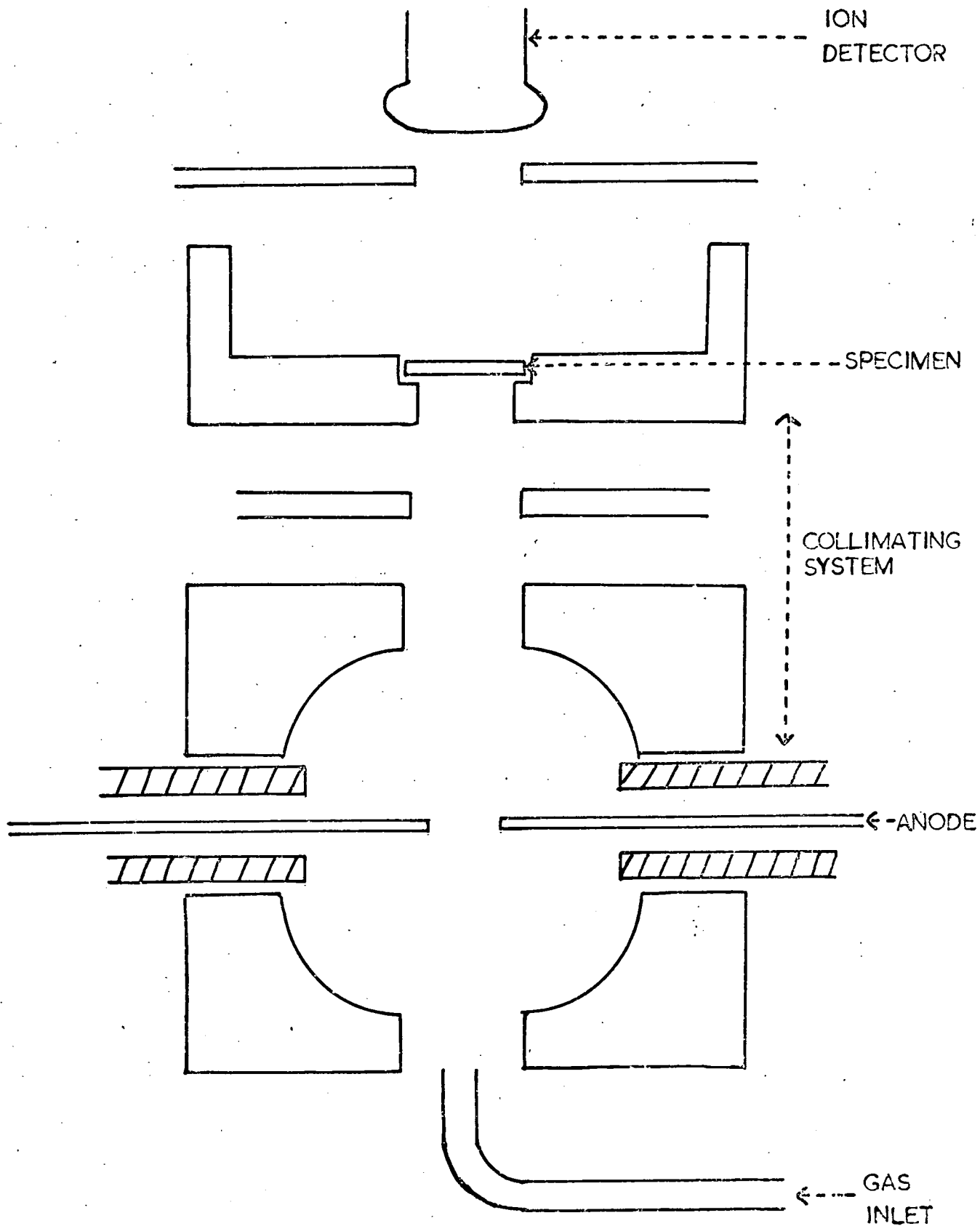


FIGURE 7.1 SCHEMATIC DIAGRAM OF ION BEAM THINNING APPARATUS

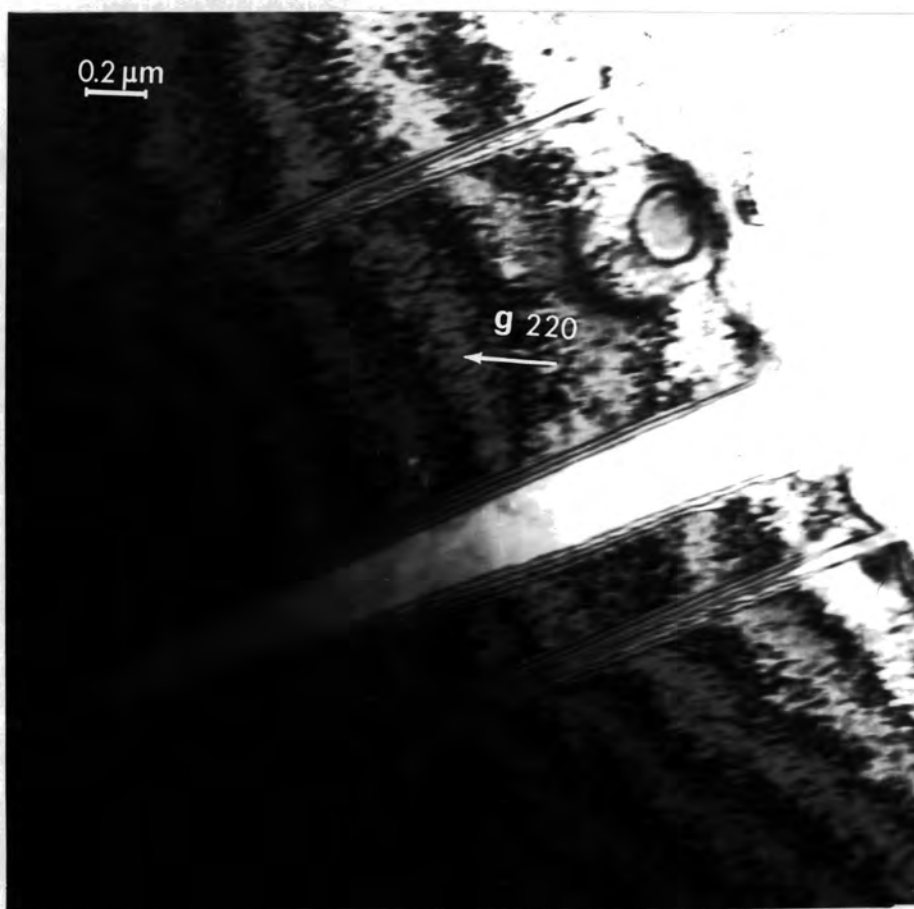


Figure 7.2: A group of narrow twins in ZnSe

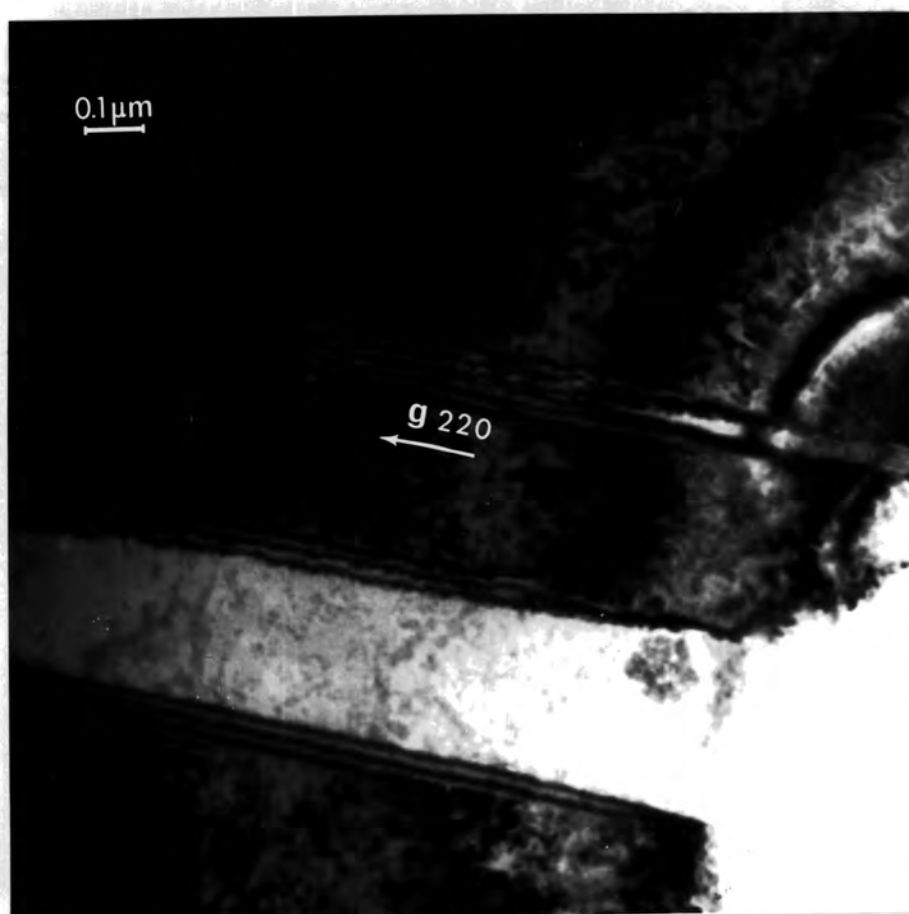


Figure 7.3: An irregularity in a specimen edge at a twin boundary

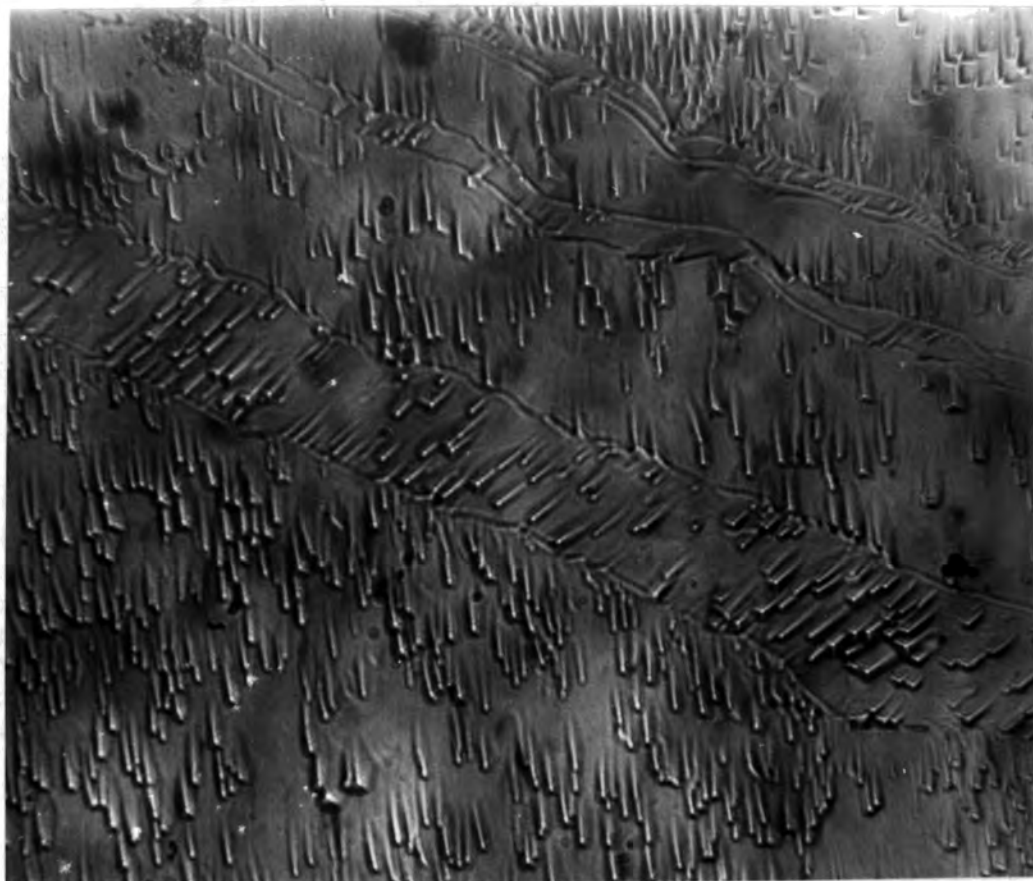


Figure 7.4: A photomicrograph of the Zn surface of an etched ZnSe sample demonstrating no change in polarity across twin boundaries x 200

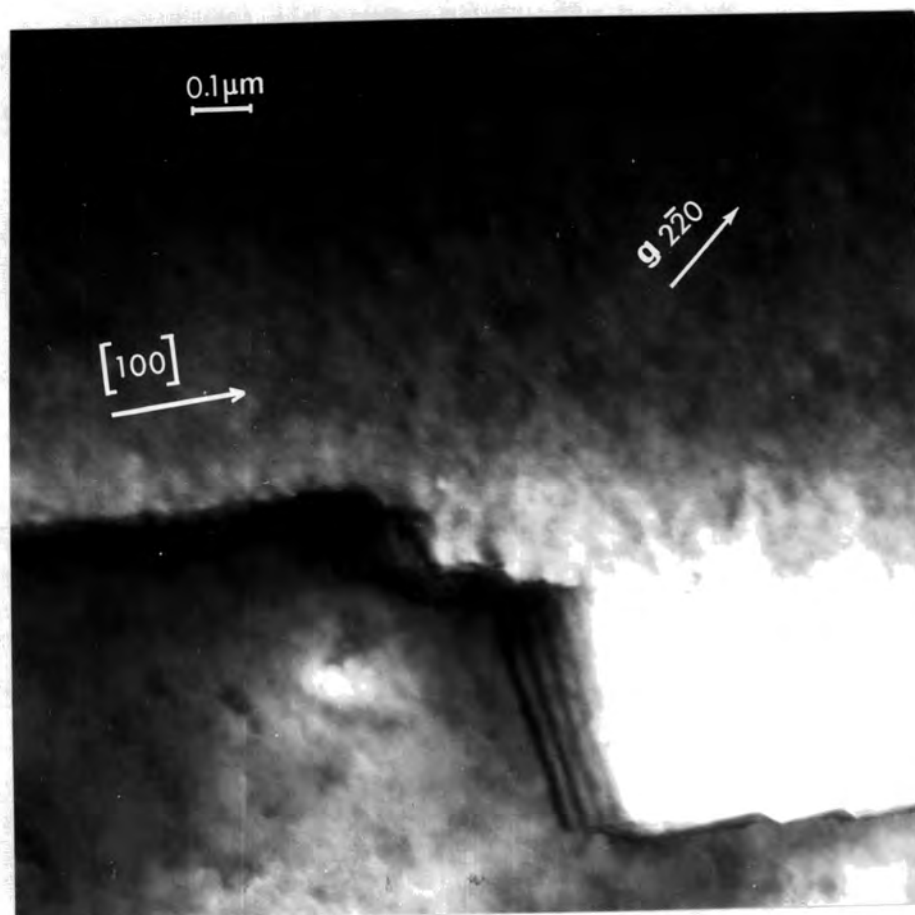


Figure 7.5: Fringe contrast at a  $\langle 100 \rangle$  tilt boundary in ZnSe

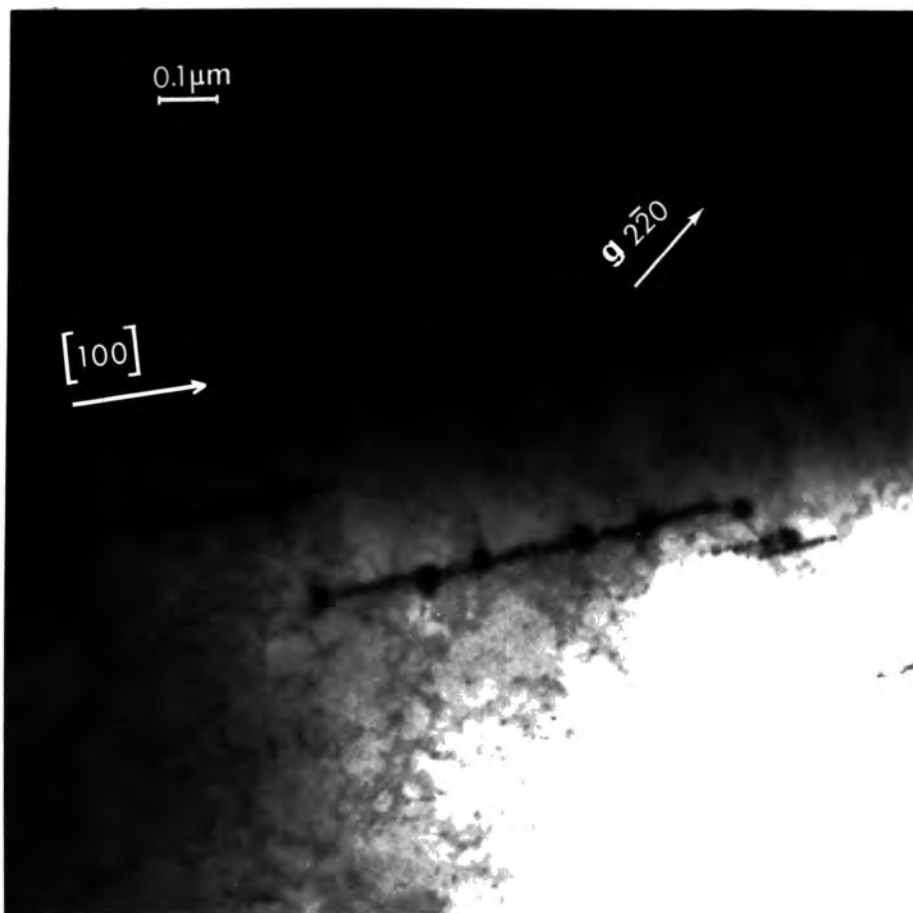


Figure 7.6: Another region of the boundary in Figure 7.5 after tilting through a few degrees

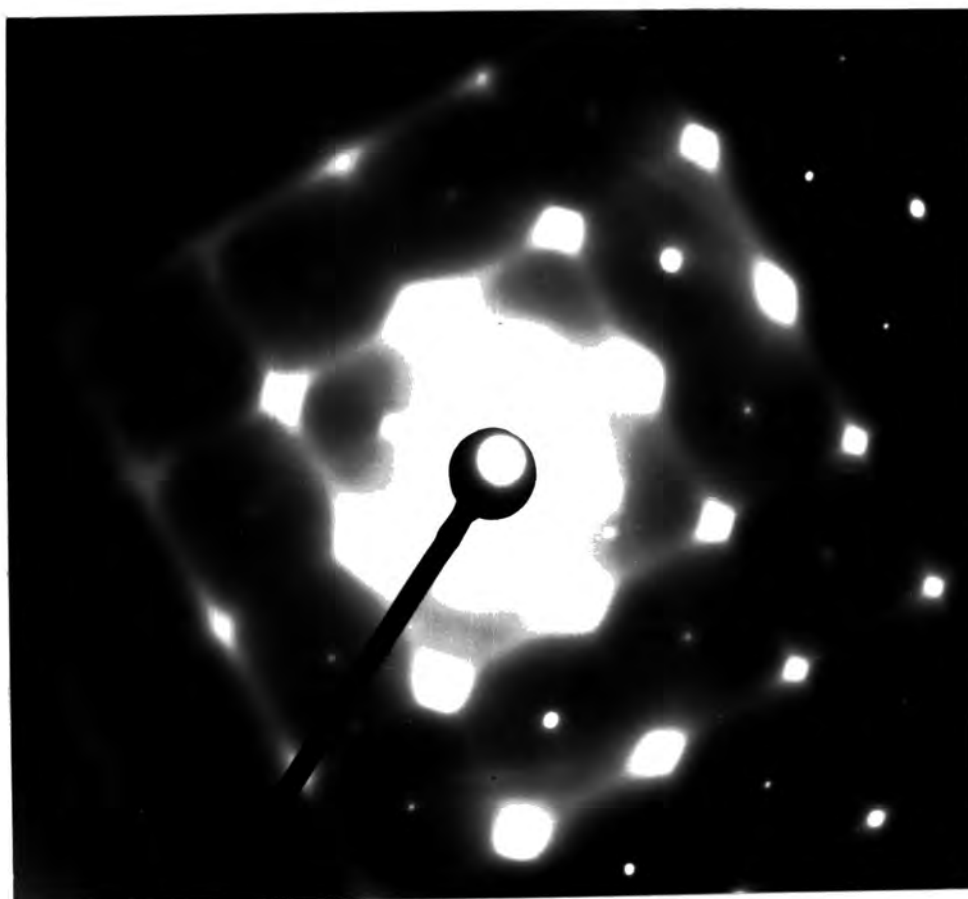


Figure 7.7: Selected area diffraction from a  $\langle 100 \rangle$  zone axis of ZnSe using 100 KV electrons

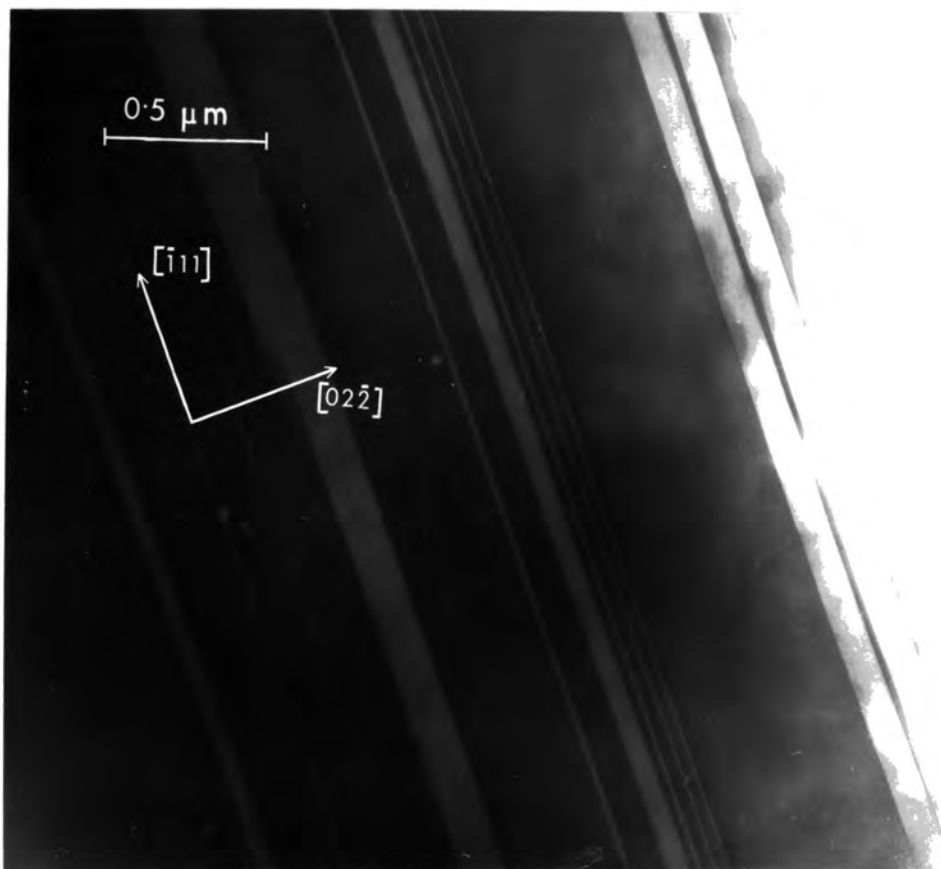


Figure 7.8: A group of thin twins in  $\text{ZnSe}_{0.4}\text{S}_{0.6}$



Figure 7.9: The selected area diffraction pattern from a similar region to that in Figure 7.8

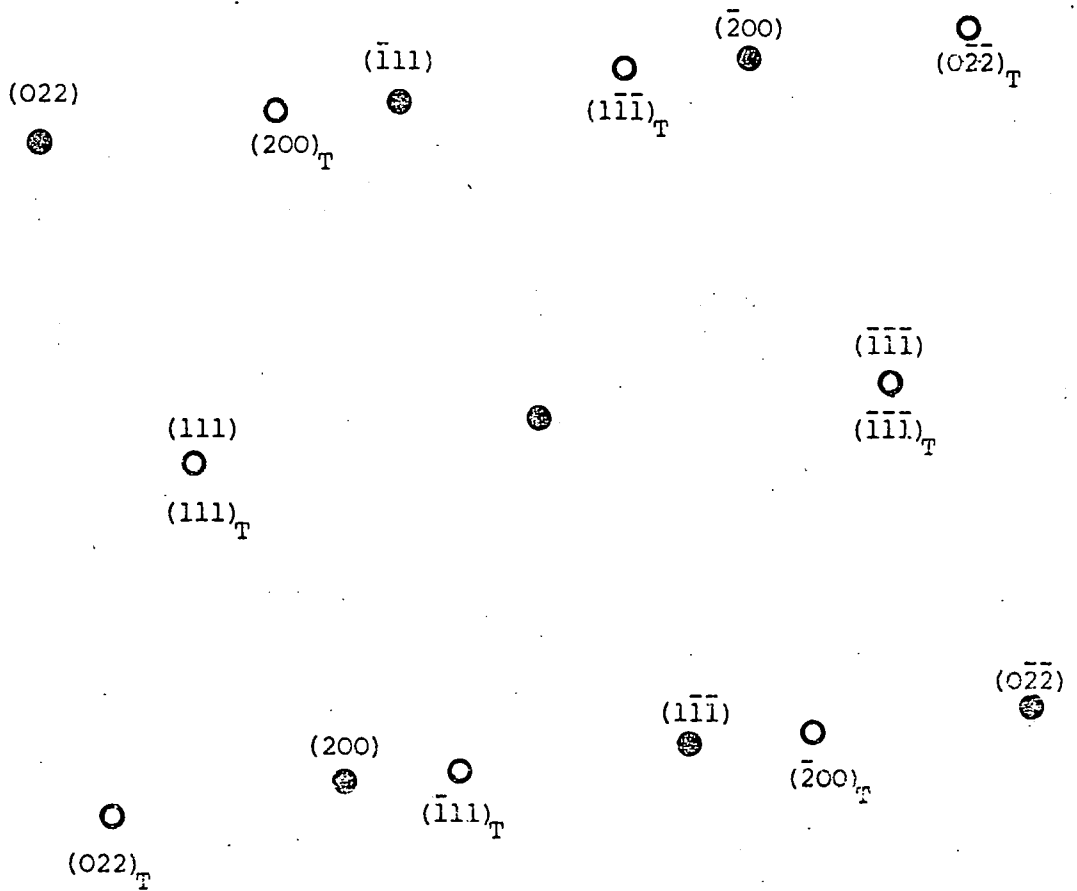


FIGURE 7.10

The indexing of the diffraction pattern shown in Fig.7.9

● (hkl) ≡ matrix reflection

○ (hkl)<sub>T</sub> ≡ twin reflection

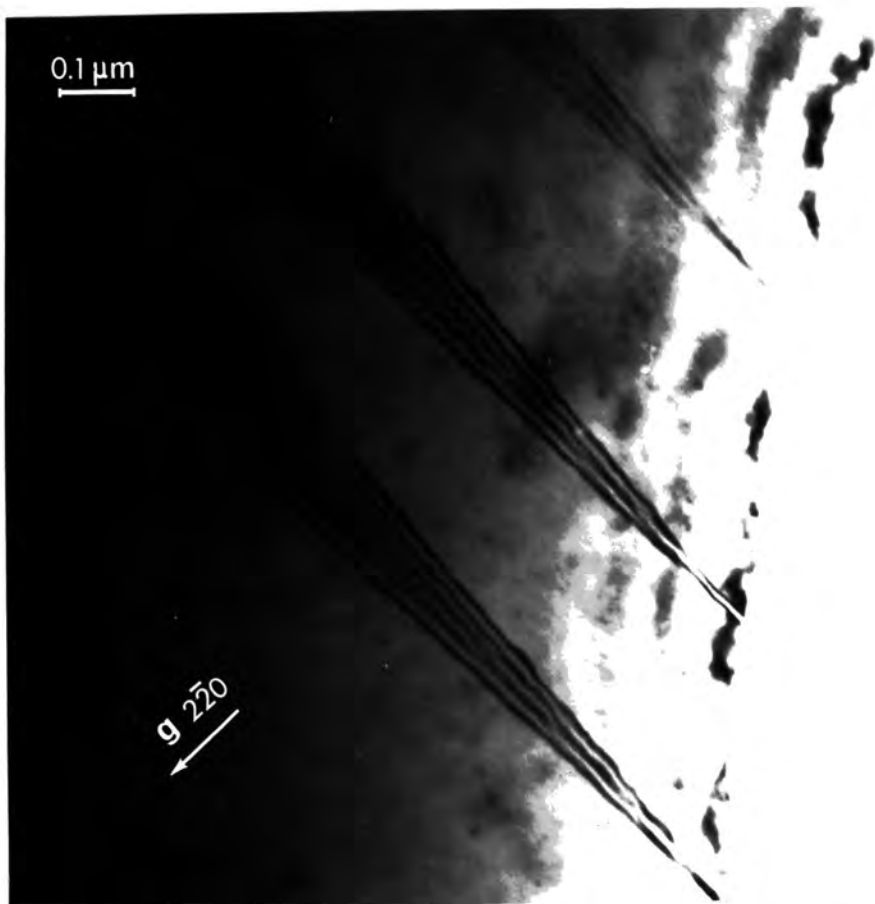


Figure 7.11: A group of long intrinsic stacking faults in  $\text{ZnSe}_{0.4}\text{S}_{0.6}$

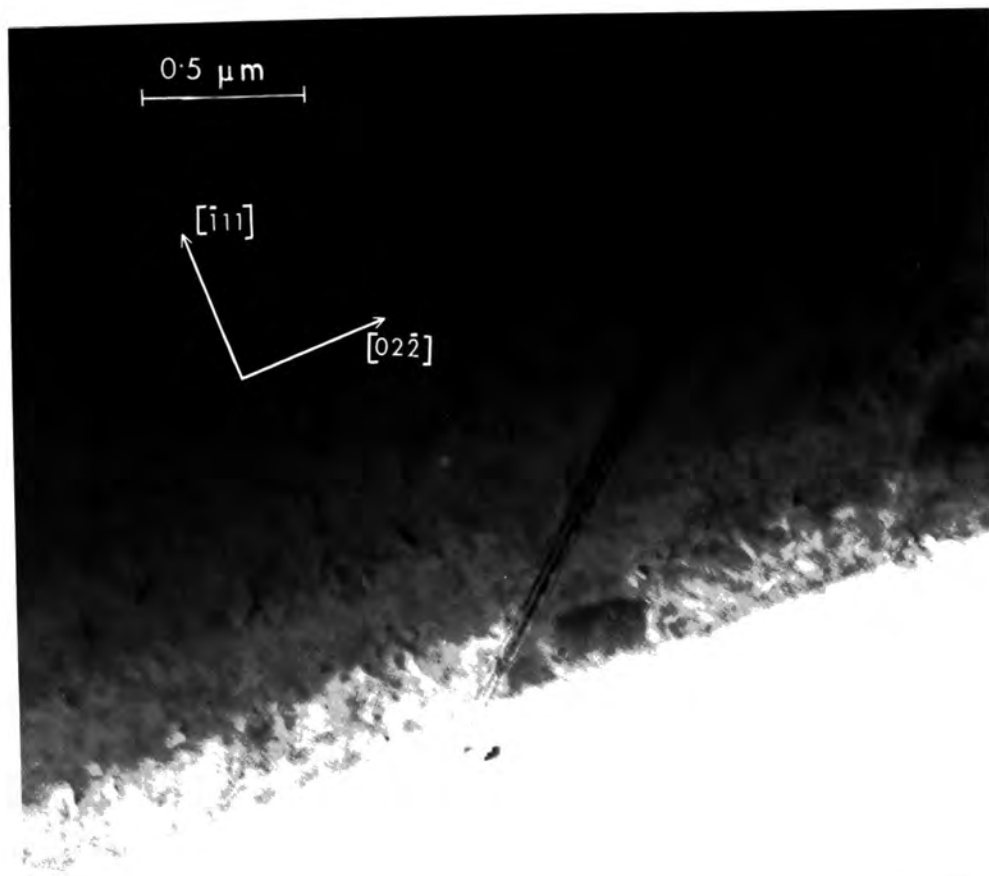


Figure 7.12: The bright field image of a single stacking fault in  $\text{ZnSe}_{0.4}\text{S}_{0.6}$

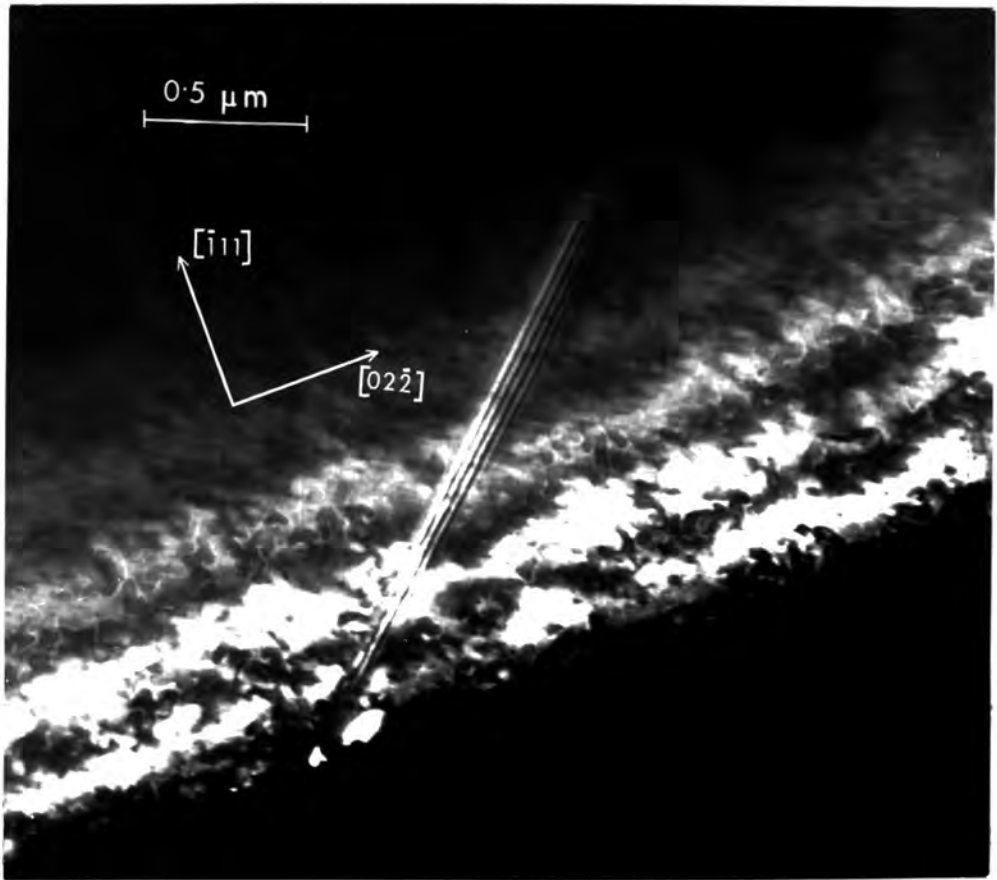


Figure 7.13: The dark field image of the stacking fault shown in Figure 7.12 recorded using the strong diffracted beam in Figure 7.14



Figure 7.14: The selected area diffraction pattern illustrating the diffraction conditions operative when recording Figures 7.12 and 7.13

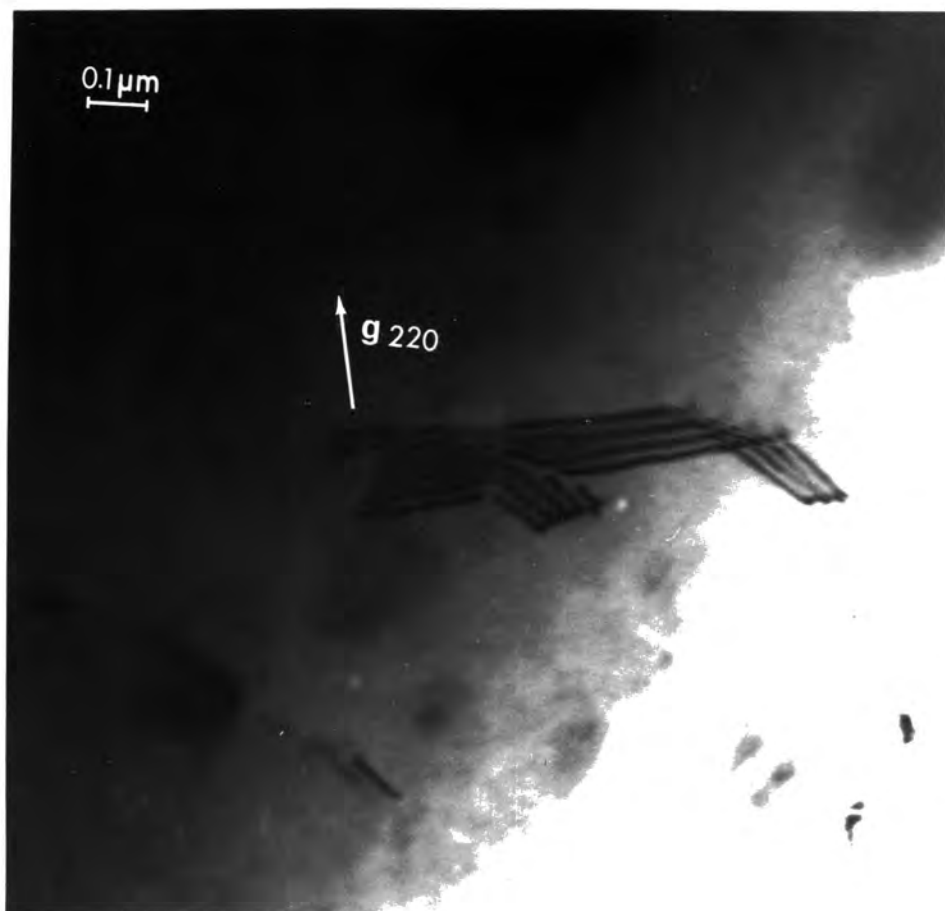


Figure 7.15: A stacking fault that has slipped from one  $\{111\}$  plane to another

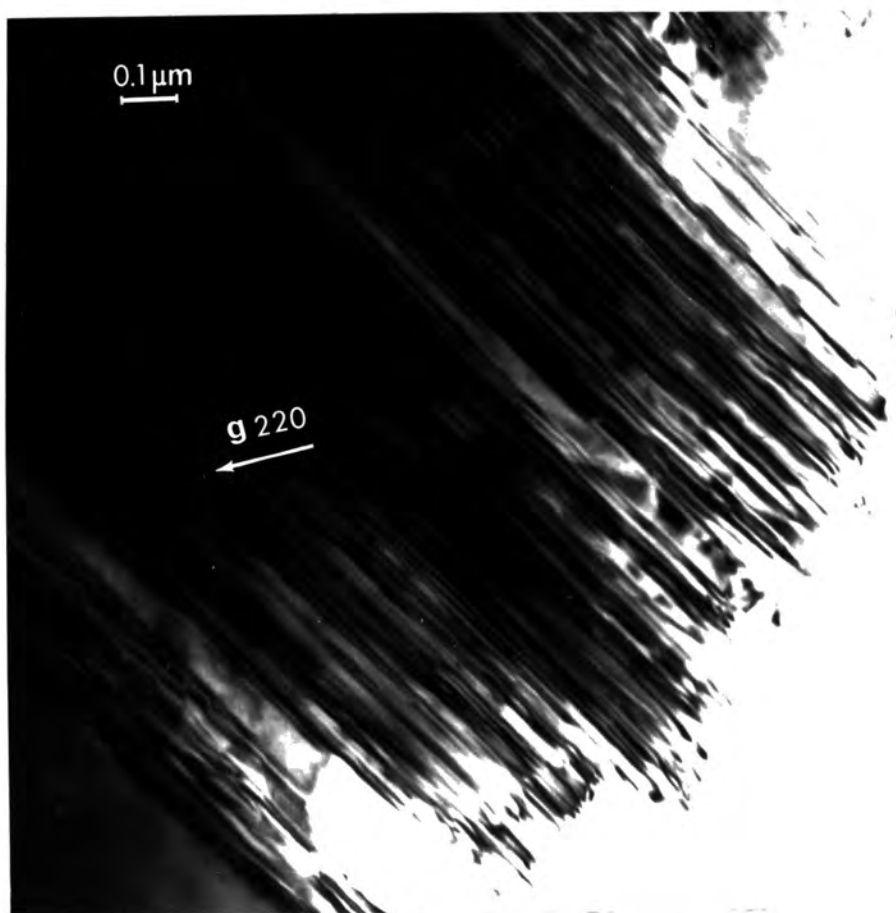
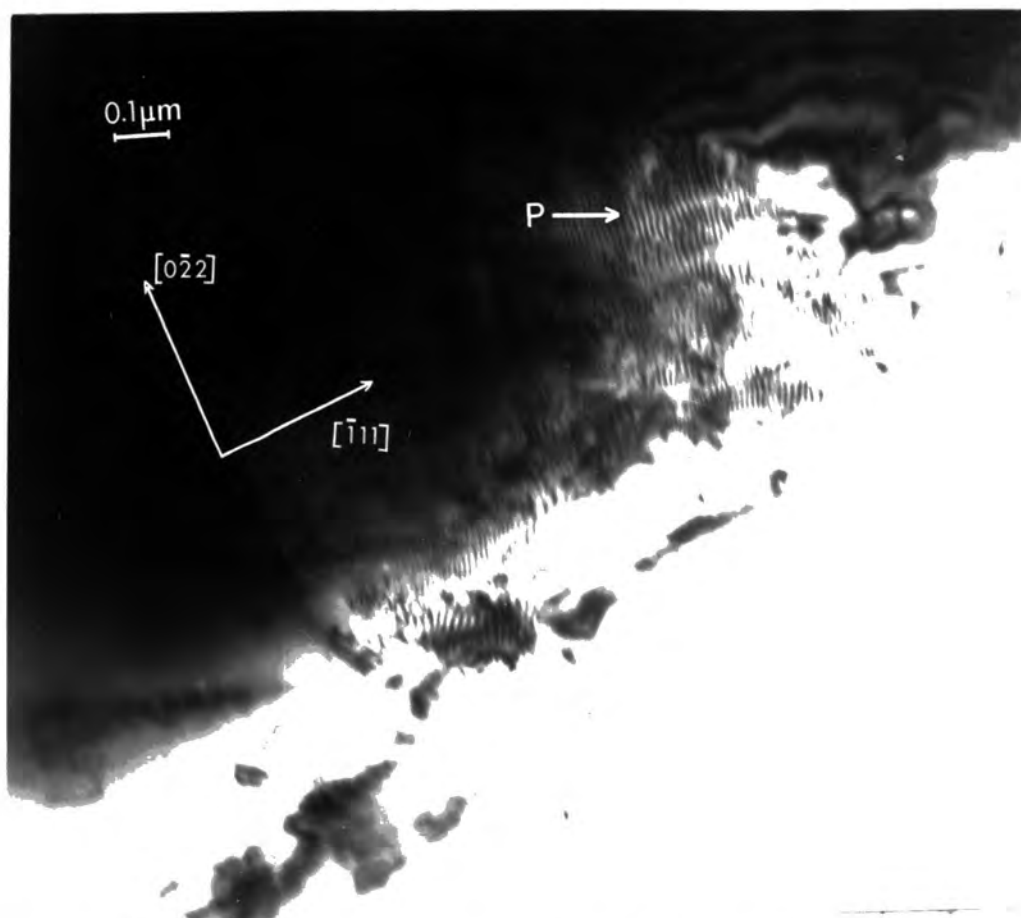


Figure 7.16: A large number of very thin overlapping planar faults in  $\text{ZnSe}_{0.4}\text{S}_{0.6}$



**Figure 7.17:** Selected area diffraction pattern from the region in Figure 7.16



**Figure 7.18:** Overlapping layers of wurtzite and sphalerite structures giving rise to moiré fringe contrast in  $\text{ZnSe}_{0.4}\text{S}_{0.6}$

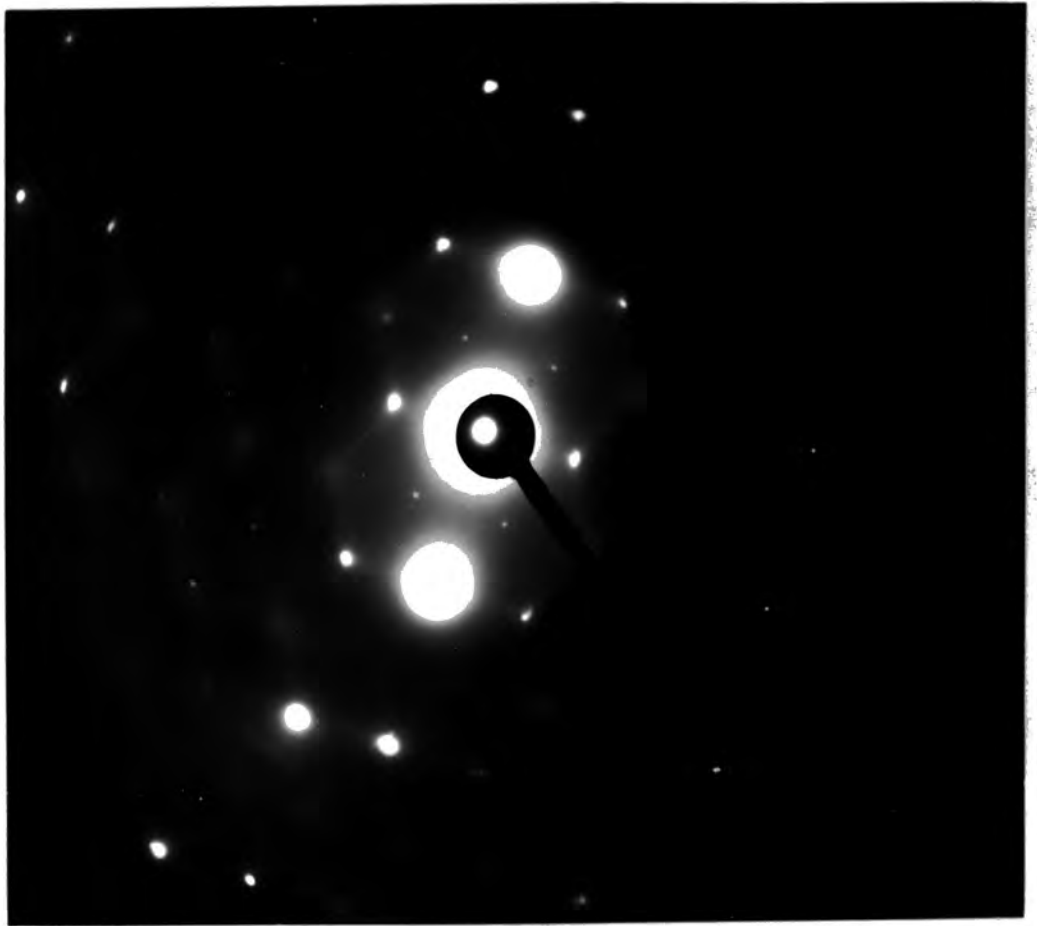


Figure 7.19: Selected area diffraction pattern from the region in Figure 7.18

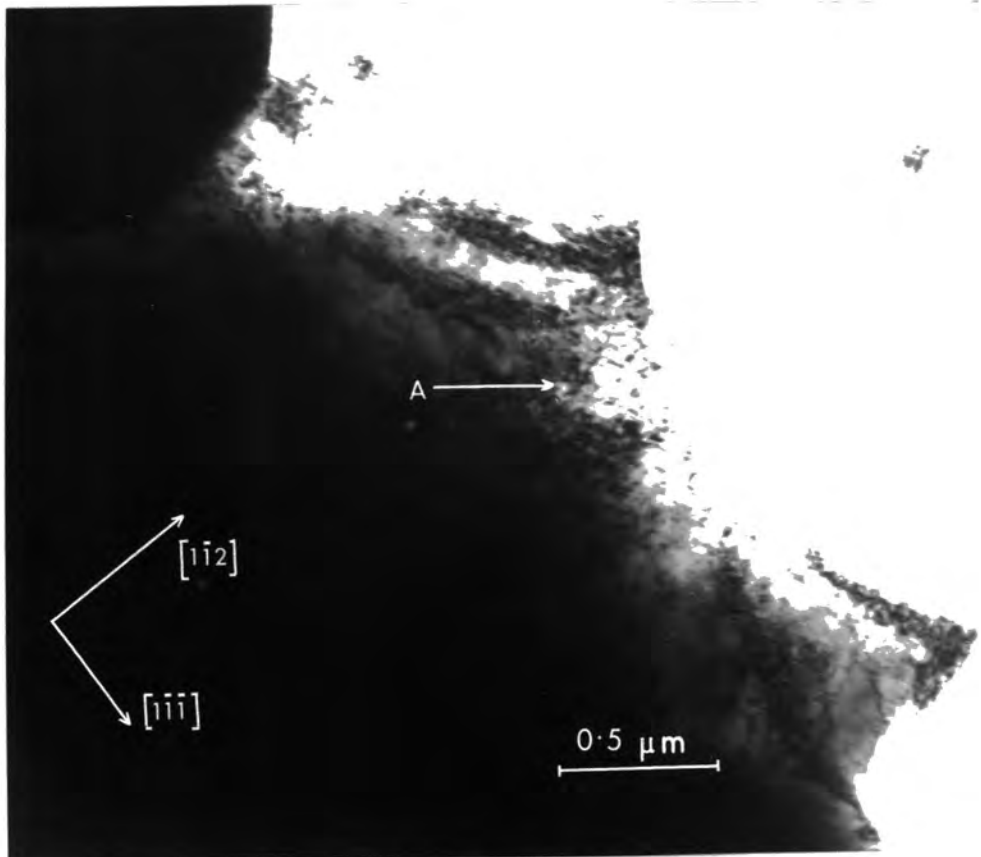


Figure 7.20: A bright field image of an ion beam thinned sample of ZnSe

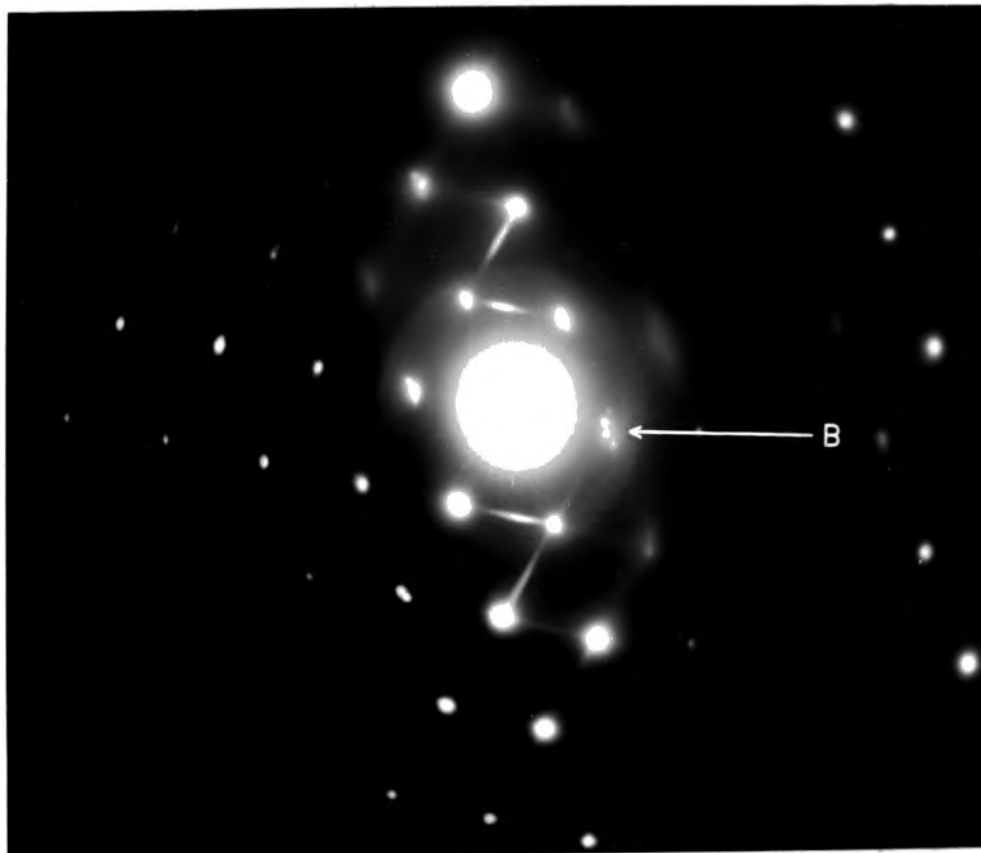


Figure 7.21 The selected area diffraction pattern from the region in Figure 7.20

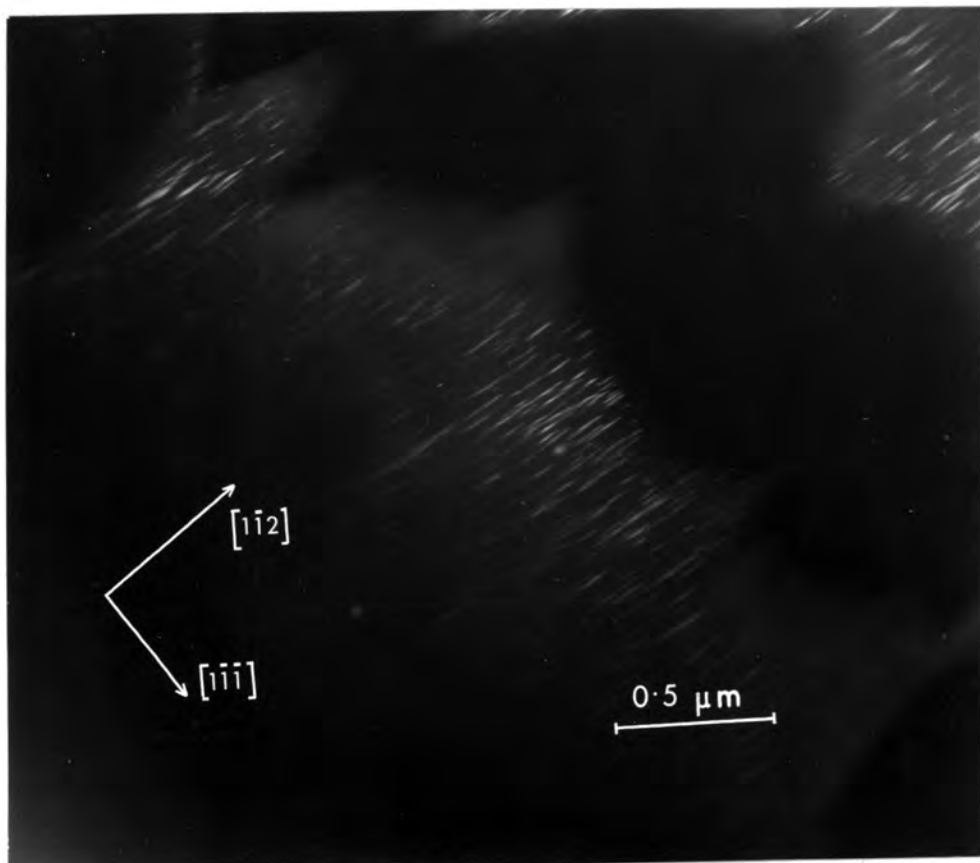
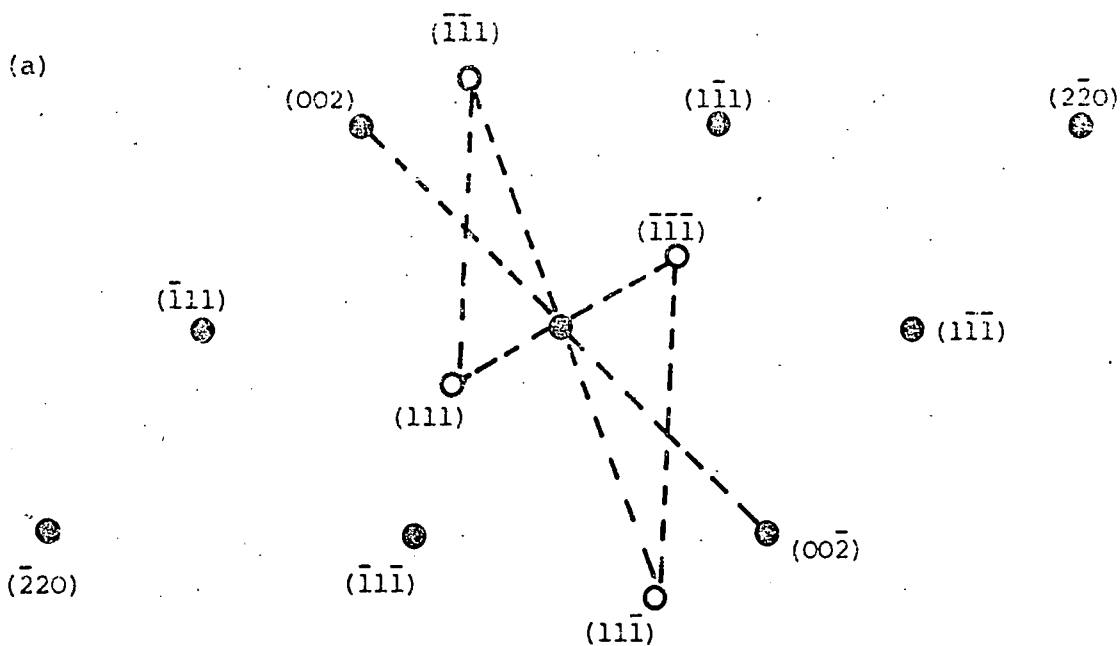
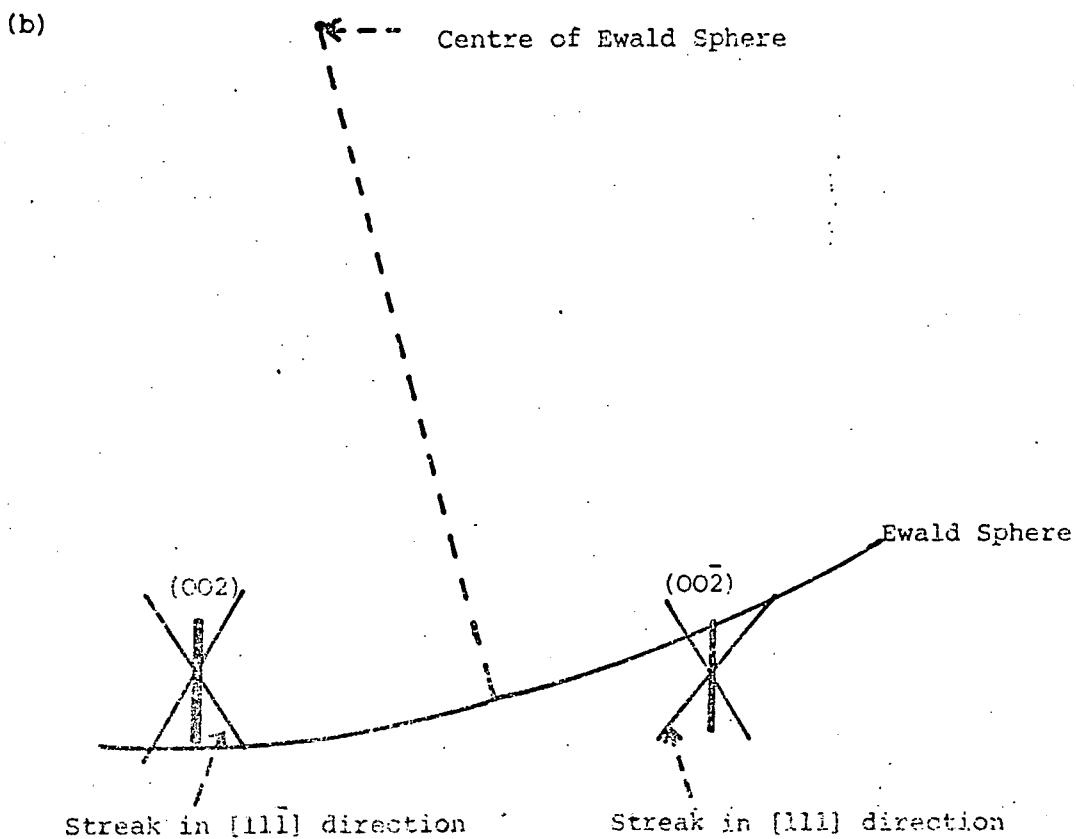


Figure 7.22: A dark field image of the region shown in Figure 7.20 taken using one of the intensity streaks in Figure 7.21



(a) Reciprocal lattice construction for  $[110]$  zone axis showing all  $\{111\}$  reflections.



(b) Diagram showing the mechanism thought to be responsible for the satellite spots displaced in  $[002]$  and  $[00\bar{2}]$  directions from matrix reflections in

Fig. 7.21



Figure 7.24: Selected area diffraction from a  $\langle 100 \rangle$  zone axis of an ion beam thinned ZnSe specimen

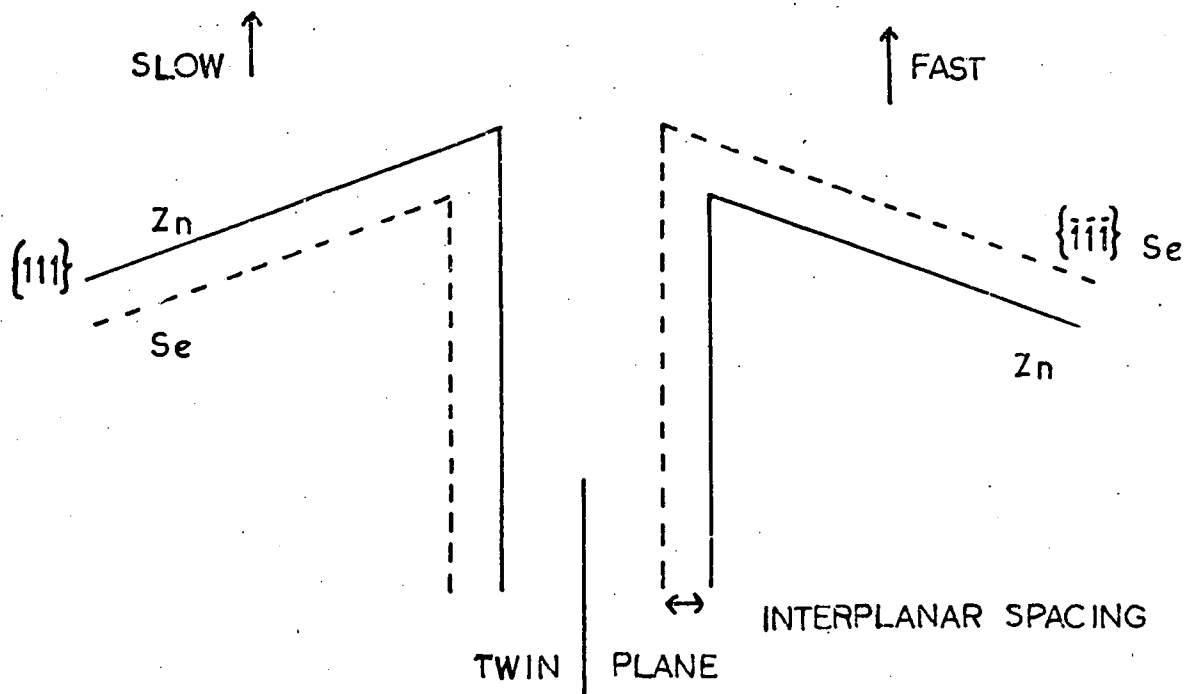


FIGURE 7.25a FAST AND SLOW GROWING FACES ON EITHER SIDE OF A TWIN BOUNDARY

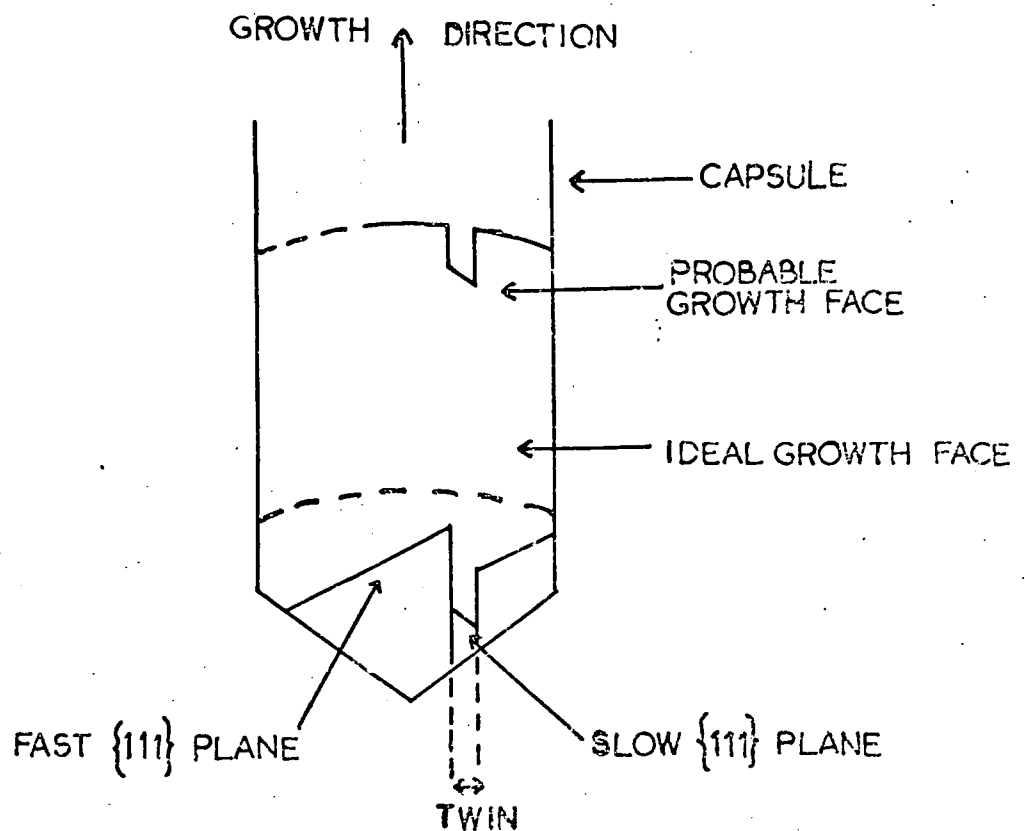


FIGURE 7.25b A POSSIBLE GROWTH MECHANISM OF AN ORTHO-TWIN

CHAPTER 8

SUMMARY OF CONCLUSIONS

8.1 AS-GROWN AND NEUTRON IRRADIATED MAGNESIUM OXIDE

The main aim of the study of MgO was to achieve a better understanding of the processes involved in the nucleation and growth of the cuboidal cavities formed by annealing neutron irradiated material. Some preliminary unpublished work of Bowen had suggested that heterovalent impurities might have been involved, so in the first instance a fairly detailed study of as-grown MgO was made with a view to establishing a clear background of the impurities present.

The principal findings of the study just mentioned were recorded in Chapter 5 and concerned the precipitates that decorated as-grown dislocations in various configurations, one of which has not previously been reported. These precipitates were of two different morphologies, namely rod shaped and spherical. The former were identified as calcium stabilised zirconia (in agreement with earlier published work) from electron diffraction patterns taken from extraction replicas. The spherical precipitates however did not give rise to any diffraction effects and they thus remain unidentified. Another observation, which may be of significance with regard to the formation and growth of cavities, was of diffraction patterns that contained spots of a square nature. These were attributed to the presence of partially coherent precipitates which were not detected by TEM.

By employing the technique of ESR to supplement the microscopic study of irradiated and annealed material containing cavities, it has been possible, as shown in Chapter 6, to identify an impurity

ion in MgO which plays an important role in the cavity growth process. The ion involved is that of iron which is indeed heterovalent as predicted by Bowen. In fact the work described in this thesis has indicated that the presence of iron as an impurity appears to impede the growth of cavities in this material. The pre-irradiation annealing treatment of samples in hydrogen ensured that most of the iron was in the divalent state. However when the post-irradiation annealing treatment in argon was carried out at a temperature just exceeding  $1500^{\circ}\text{C}$ , in addition to the nucleation of the cavities first reported by Morgan and Bowen (1967), oxidation of some of the iron ions to the trivalent state was observed. Microscopic examination showed that the presence of trivalent iron in octahedral symmetry was accompanied by little growth of the cavities. However, after annealing a sample for the same period at  $1625^{\circ}\text{C}$ , the transitions of  $\text{Fe}^{3+}$  in octahedral symmetry sites were no longer present in the E.S.R. spectrum. The same sample exhibited about a tenfold increase in the volume of the crystal occupied by cavities. It was therefore concluded that the presence of iron in the trivalent state and in octahedral symmetry constituted an impediment to the motion of vacancies and thus delayed the growth of the cavities. It has been suggested that this delay is likely to increase with increase in iron impurity content.

A further interesting observation concerns the interaction of cavities with segments of interstitial dislocation loops still present in samples annealed above  $1500^{\circ}\text{C}$  for one hour. Morgan and Bowen (1967) noted that cavities appeared to be pinned by such dislocations, but in this work it has further been suggested that this pinning arises from the partial annihilation of the interstitial dislocation loops by vacancies diffusing from cavities. This is probably associated with the observed  $\langle 110 \rangle$  orientation of dislocations in the region of cavities.

Finally, for the sake of completeness, it is to be noted that the original proposal for the investigations to be pursued for this thesis contained a suggestion that diffraction contrast effects, which were observed to be associated with cavities in some preliminary independent work carried out at A.E.R.E., Harwell, should be studied. It was hoped that this might yield some further information relating to the morphology of cavities. Unfortunately however it transpired that the alleged diffraction contrast effects were characteristics associated with over-focussed images suffering from objective lens astigmatism, and were therefore of no significance.

## 8.2 ZINC SELENIDE AND ZINC SULPHO-SELENIDE

The purpose of the TEM studies of these materials was to establish an understanding of their defect structures with a view, firstly to improving crystal quality and secondly to relating electroluminescent behaviour to defect content. In Chapter 7 it has been demonstrated that the dominant faults in ZnSe are narrow twins which extend completely across grains and which etching studies have shown to be of the ortho type. From the etching experiments it has also been concluded that the growth of ZnSe is strongly polar in that grains grow preferentially in a  $\langle \bar{1}\bar{1}\bar{1} \rangle$  direction, with the growth axis often lying close to the geometric axis of the crystal boule. The defect structure of  $\text{ZnSe}_{0.4}\text{S}_{0.6}$  differed from that of ZnSe mainly in the degree of stacking disorder. This was evidenced by the presence of narrower twins and groups of long intrinsic stacking faults. In addition, the observation of a few polytypic regions in this material was taken as an indication that the microscopic homogeneity was not strictly maintained throughout these crystals.

The origin of most of the defects mentioned above, other than polytypes, in both of these materials has been attributed to post growth stress arising from the unavoidable temperature gradients incurred when cooling crystal boules. The occurrence of different faults in the two separate materials has been ascribed to a slight difference in the degree of ionicity in their bonding. Thus, strain is accommodated by the passage of partial dislocations across adjacent double atomic {111} layers in ZnSe thereby producing ortho-twins and minimising the number of less energetically favourable boundary regions of hexagonal material formed. In contrast, the nature of the bonding of  $\text{ZnSe}_{0.4}\text{S}_{0.6}$  is more ionic being closely related to that of ZnS and the passage of partial dislocations across {111} planes results in many more regions of hexagonal structure being produced in the form of intrinsic stacking faults and a larger number of twin boundaries.

The study of samples of ZnSe prepared by ion beam thinning has shown that all of the specimens prepared by this technique have contained microtwins lying on all four {111} planes. As expected on energy considerations, no regions of hexagonal material have been found in these samples. The origin of the microtwins has been attributed to the re-ordering of the primary damage at an elevated temperature of a few hundred °C produced by the incident ion beam. Attempts to eliminate this damage, firstly by reducing the operating accelerating voltage of the ion gun and secondly by using gases other than argon, including nitrogen and hydrogen, were unsuccessful.

### 8.3 FUTURE WORK

The primary objective of the study of neutron irradiated and annealed MgO has been fulfilled in that a specific impurity species

has been identified and associated with the discontinuities in the variations of density, lattice parameter and cavity volume with annealing temperature. However one question has been raised by this investigation and this relates to the origin of a transition in the ESR spectra from irradiated and annealed samples. As this transition was observed to undergo a twofold increase in intensity in the same sample as that which showed a tenfold increase in cavity volume, it appears to be associated with a vacancy. So far, however, it has not been possible to identify it with any of the colour or impurity centres reported in the literature. Thus, further work is necessary on this problem and, in the first instance, it is proposed that a much more accurate determination of the g-value of this line be made. This could be obtained by repeating the measurements carried out at Q-band over a much smaller range of magnetic field centred on this line. This would allow an investigation of any possible small degree of anisotropy of this centre that may have been too small to detect in the measurements recorded here.

From the studies of ZnSe and  $\text{ZnSe}_{0.4}\text{S}_{0.6}$  it was concluded that the defects in stacking sequence in both materials could be ascribed to the movement of partial dislocations to accommodate post-growth strain in crystal growth. Further, it is to be noted that preliminary attempts (not recorded in this thesis) to introduce damage by heating ZnSe samples in the electron beam have shown that stacking faults can be produced. These presumably owe their origin to the locally induced thermal stresses. Thus, in an effort to further the knowledge of the processes involved in the deformation of this material, it is proposed to perform three-point bend tests on as-grown material over a range of temperatures, so that faults

introduced in a controlled manner may be studied.

To date, only little attention has been paid to the preparation of ZnSe for TEM by ion beam thinning. While the damage introduced into samples by the ion beam has been shown to consist mainly of microtwins, little is known about the re-ordering processes involved in the formation of these defects. In an attempt to obtain a better understanding of this damage it is expected that this study will be extended to include the preparation of other related materials, in particular ZnS and ZnTe. The elimination of the formation of microtwins in ZnSe seems unlikely, although the possibility of re-designing the ion gun assembly to allow for the sample to be cooled to liquid nitrogen temperature must be investigated. The study of this damage is considered to be of particular importance because beams of inert gas ions are currently used for "cleaning" surfaces in the preparation of electroluminescent diodes based on this material. Further, this damage presents the interesting opportunity for the study of the effect of microtwins on the electroluminescent behaviour of ZnSe.

REFERENCES

- A W Agar (1965) in 'Techniques for Electron Microscopy' Oxford Blackwell 28
- R S Barnes and D J Mazy (1963) Proc. Roy. Soc. A 275 47
- R S Barnes and D J Mazy (1964) Proc. Third European Regional Conf. on Electron Microscopy, Czechoslovak Academy of Sciences Prague 197
- C S Barrett (1943) in 'The Structure of Metals' New York McGraw-Hill Book Co. Inc.
- C S Barrett and T B Massalski (1966) in 'The Structure of Metals' New York McGraw-Hill Book Co. Inc. 626
- H Blank, P Delavignette and S Amelinckx (1962) Phys. Stat. Sol. 2 1660
- D H Bowen (1962) Proc. Sixth Saclay Metallurgical Colloquium 151
- D H Bowen (1963) Trans. Brit. Ceram. Soc. 62 771
- D H Bowen and F J P Clarke (1963) Phil. Mag. 8 1257
- D H Bowen and F J P Clarke (1964) Phil. Mag. 9 413
- D H Bowen (1966) U.K.A.E.A. Rep. No. R5269 461
- D E Bradley (1965a) in 'Techniques for Electron Microscopy' Oxford Blackwell 66
- D E Bradley (1965b) *ibid* 136
- A Briggs and D H Bowen (1968) 'Mass Transport in Oxides' National Bureau of Standards Special Publication 296 103 (Washington: US Government Printing Office)
- J A Brinkman (1954) J. Appl. Phys. 25 961
- J A Brinkman (1964) U.K.A.E.A. Rep. No. R4694 48
- L de Broglie (1924) Phil. Mag. 47 446
- H Brooks (1956) Ann. Rev. of Nucl. Science 6 215
- P J Brown and J B Forsyth (1973) 'The Structure and Properties of Solids' London Arnold

- K F Burr and J Woods (1971) J. Mat. Sci. 6 1007
- H Busch (1926) Ann. Physik 81 974
- F J P Clarke, D H Bowen and R S Wilks (1963) Trans. Brit. Ceramic Soc. 62 83
- A L Companion (1964) in 'Chemical Bonding' McGraw-Hill Book Co. New York 90
- A V Crewe (1972) Proc. Fifth European Congress on Electron Microscopy Manchester 14
- J R Cutter, G J Russell and J Woods (1976) J. Crystal Growth 32 179
- R W Davidge (1967) J. Mat. Sci. 2 339
- R W Davidge (1968) J. Nucl. Mat. 25 75
- P Duwez, F Odell and F Brown (1952) J. Am. Ceramic Soc. 35 107
- M L Fuller (1929) Phil. Mag. 8 658
- S Gezci and J Woods (1972) J Mat. Sci. 7 603
- T K Ghosh and F J P Clarke (1961) Brit. J. Appl. Phys. 12 44
- G W Groves and A Kelly (1962) J. Appl. Phys. Supplement to Vol. 33 No.1 456
- G W Groves and A Kelly (1963) Phil. Mag. 8 1437
- K J Hale and J Batson (1965) Brit. J. Appl. Phys. 16 85
- J S Halliday and R C Newman (1960) Brit. J. Appl. Phys. 11 158
- R D Heidenreich (1949) J. Appl. Phys. 20 993
- N Hemmatt and M Weinstein (1967) J. Electrochem. Soc. 114 851
- B Henderson (1964) Phil. Mag. 9 153
- B Henderson and J E Wertz (1968) Advances in Physics 17 749
- B Henderson, J E Wertz, T P P Hall and R D Dowsing (1971) J. Phys. C : Solid St. Phys. 4 107
- B Henderson (1972) 'Defects in Crystalline Solids' London Arnold

- B S Hickman and D G Walker (1965) Phil. Mag. 11 1101
- P B Hirsch, A Howie and M J Whelan (1960) Phil. Trans. Roy. Soc.  
A 252 499
- P B Hirsch, R W Horne and M J Whelan (1956) Phil. Mag. 1 677
- P B Hirsch, A Howie, R B Nicholson, D W Pashley and M J Whelan  
(1965a) in 'Electron Microscopy of Thin Crystals' London  
Butterworths 1
- P B Hirsch et al (1965b) *ibid* 156 and 195
- P B Hirsch et al (1965c) *ibid* 90
- P B Hirsch et al (1965d) *ibid* 499
- P B Hirsch et al (1965e) *ibid* 195
- D B Holt (1962) J. Phys. Chem. Solids 23 1353
- D B Holt (1966) J. Mat. Sci. 1 280
- D B Holt (1964) J. Phys. Chem. Solids 25 1385
- D B Holt (1969) J. Mat. Sci. 4 935
- G Honjo, S Kodera and N Kitamura (1964) J. Phys. Soc. Japan  
19 351
- G H Kinchin and R S Pease (1955a) Rep. on Prog. in Phys. 18 1
- G H Kinchin and R S Pease (1955b) J. Nucl. Energy 1 200
- R D King and B Henderson (1967) Proc. Brit. Ceramic Soc. 9 63
- M R Lorenz (1967) in 'Physics and Chemistry of II-VI Compounds'  
eds. M Aven and J S Prener Amsterdam North-Holland Publishing  
Co. 103
- W Low (1958) Ann. New York Acad. Sci. 72 69
- D G Martin (1966) U.K.A.E.A. Rep. R5269 243
- D G Martin (1967) U.K.A.E.A. Rep. R5521
- D G Martin (1968) J. Phys. C (Proc. Phys. Soc.) Series 2 Vol. 1 333
- D L McDonald (1963) Appl. Phys. Letters 2 175

- G D Miles (1965) J. Appl. Phys. 36 1471
- F F Morehead (1967) in 'Physics and Chemistry of II-VI Compounds'  
eds. M Aven and J S Prener Amsterdam North-Holland Publishing  
Co. 640
- C S Morgan and D H Bowen (1967) Phil. Mag. 16 165
- J Narayan and J Washburn (1972) Crystal Lattice Defects 3 91
- J Narayan (1973) J. Appl. Phys. 44 3436
- R S Nelson and M W Thompson (1961) Proc. Roy. Soc. A 259 458
- J A Olley, P M Williams and A D Yoffe (1970) Proc. of the Conf.  
on Ion Implantation Reading 148
- E Orowan (1934) Z. Physik 89 634
- S G Parker (1971) J. Cryst. Growth 9 177
- D W Pashley and M J Stowell (1963) Phil. Mag. 8 1605
- M Polanyi (1934) Z. Physik 89 660
- J B Le Poole (1947) Philips Tech. Rdsch. 9 33
- A Pooley (1966) Proc. Phys. Soc. 87 257
- A W Pryor, R J Tainsh and G K White (1964) J. Nucl. Materials  
14 209
- W L Roth (1967) in 'The Physics and Chemistry of II-VI Compounds'  
eds. M Aven and J S Prener Amsterdam North-Holland Publishing  
Co. 139
- J E Rowe and R A Forman (1968) J. Appl. Phys. 39 1917
- G J Russell and J Woods (1976) J. Phys. E : Scientific  
Instruments 9 98
- G J Russell, E A E Ammar and J S Thorp (1976) To be published
- A Sagar, W Lehmann and J W Faust Jr. (1968) J. Appl. Phys. 39  
5336
- J H Schulman and W D Compton (1963) 'Colour Centres in Solids'  
Oxford Pergamon Press

- F Seitz and J S Koehler (1956) Solid State Physics 2 447
- J Sherman (1932) Chem. Revs. 11 92
- R H Silsbee (1957) J. Appl. Phys. 28 1246
- G I Taylor (1934) Proc. Roy. Soc. A 145 362
- G Thomas (1964a) in 'Transmission Electron Microscopy of Metals'  
New York John Wiley and Sons. Inc. 79
- G Thomas (1964b) *ibid* 100
- G Thomas (1964c) *ibid* 57
- G Thomas (1964d) *ibid* 9
- J D Venables (1961) Phys. Rev. 122 1388
- J D Venables (1963) J. Appl. Phys. 34 293
- B Von Borries and E Ruska (1939) Z. wiss Mikroskop 56 317
- J Washburn, G W Groves, A Kelly and G K Williamson (1960)  
Phil. Mag. 5 991
- J E Wertz, J W Orton and P. Auzins (1962) J. Appl. Phys. Suppl.  
to Vol. 33 No.1 322
- R S Wilks (1966) J. Nucl. Materials 19 351
- P M Williams and A D Yoffe (1968) Phil. Mag. 18 555
- P M Williams and A D Yoffe (1972) Phil. Mag. 25 247

